# Large-Eddy Simulations of Helix Active Wake Control
## Sensitivity, Robustness and Advanced Actuator Line Modelling

Taschner, Emanuel

**DOI**
10.4233/uuid:2fa33fc4-4467-4d52-9390-0c8f6c52b66b

**Publication date**
2025

**Document Version**
Final published version

**Citation (APA)**
Taschner, E. (2025). *Large-Eddy Simulations of Helix Active Wake Control: Sensitivity, Robustness and Advanced Actuator Line Modelling.* [Dissertation (TU Delft), Delft University of Technology]. https://doi.org/10.4233/uuid:2fa33fc4-4467-4d52-9390-0c8f6c52b66b

**Important note**
To cite this publication, please use the final published version (if applicable).
Please check the document version above.

# Large-Eddy Simulations of Helix Active Wake Control

## Sensitivity, Robustness and Advanced Actuator Line Modelling

Emanuel Taschner

# Large-Eddy Simulations of Helix Active Wake Control

Sensitivity, Robustness and Advanced Actuator Line Modelling

# Large-Eddy Simulations of Helix Active Wake Control

## Sensitivity, Robustness and Advanced Actuator Line Modelling

**Dissertation**

for the purpose of obtaining the degree of doctor
at Delft University of Technology,
by the authority of the Rector Magnificus prof. dr. ir. H. Bijl,
chair of the Board for Doctorates,
to be defended publicly on
Monday 9 February 2026 at 15:00 o'clock

by

**Emanuel TASCHNER**

Master of Science in Engineering Mechanics,
KTH Royal Institute of Technology, Sweden,
born in Leonberg, Germany.

This dissertation has been approved by the promotors.

Promotor: Prof. dr. ir. J.W. van Wingerden
Promotor: Dr. ir. R.A. Verzijlbergh

Composition of the doctoral committee:

| | |
|---|---|
| Rector Magnificus, | chairperson |
| Prof. dr. ir. J.W. van Wingerden, | Delft University of Technology |
| Dr. ir. R.A. Verzijlbergh, | Delft University of Technology |
| *Independent members:* | |
| Prof. dr. S. Ivanell, | Uppsala University, Sweden |
| Prof. dr. dipl.-ing. S. Kenjereš, | Delft University of Technology |
| Dr. ir. R.J.A.M. Stevens, | University of Twente |
| Prof. dr. N.J. Wei, | University of Pennsylvania, US |
| Prof. dr. S.J. Watson, | Delft University of Technology, reserve member |
| *Other members:* | |
| Dr. L.A. Martínez-Tossas, | National Renewable Energy Laboratory, US |

Dr. L.A. Martínez-Tossas has contributed significantly to the preparation of this dissertation as co-author of Chapters 4 and 5.


*Keywords:* wind farm flow control, helix active wake control, large-eddy simulation, actuator line modelling, unsteady aerodynamics

*Printed by:* Gildeprint

*Style:* TU Delft House Style, with modifications by Moritz Beller
`https://github.com/Inventitech/phd-thesis-template`

*Funding:* This Ph.D. project was part of the Hollandse Kust Noord wind farm innovation program, where CrossWind C.V., Shell, Eneco, Siemens Gamesa and GROW are teaming up; funding for the PhDs and PostDocs was provided by CrossWind C.V. and Siemens Gamesa.



ISBN 978-94-6518-181-3

An electronic version of this dissertation is available at
`http://repository.tudelft.nl/`.

*Für Tilde und Andreas*

# Contents

# Summary

The current change of the Earth's climate necessitates actions to strongly reduce the human carbon footprint. For the energy sector, this implies moving to renewable energy sources like wind. The wind resource is spatially heterogeneous, where wind speeds and power densities are particularly favourable offshore. The favourable offshore wind resource, together with the limited availability of onshore land area for wind energy, motivates the move to offshore wind energy generation. Economic, spatial and environmental considerations suggest clustering wind turbines offshore into wind farms.

Wind turbines clustered in a wind farm operate on average at a lower efficiency than they would achieve in isolation. One major source of this efficiency loss is wake interaction. As wind turbines extract kinetic energy from the wind, they leave behind a region of low wind speed, the so-called wake. When wakes generated by upstream turbines impinge on downstream turbines in the farm, they reduce their power output and thus the overall farm efficiency. In the design phase, the wind farm layout is optimised to minimise wake losses; however, even in an optimal layout wake losses are significant. From the desire to further mitigate the remaining wake losses, the field of wind farm flow control (WFFC) arose, which aims to reduce wake losses by farm-wide coordinated control of the wind turbines.

Wind farm flow control strategies differ based on their working mechanism, e.g. control strategies aim to either reduce the initial wake deficit of upstream turbines by reducing the turbine thrust or redirecting wakes past downstream turbines by intentionally misaligning upstream turbines with the incoming wind direction. A newer category of strategies for WFFC is active wake control (AWC). Compared to the former quasi-steady strategies, AWC strategies are inherently dynamic as their working mechanism relies on unsteady actuation, which aims to trigger underlying instability modes of the wake flow. One of the most recently developed AWC strategies is helix active wake control. It makes use of the individual pitch control capabilities (IPC) of modern wind turbines in order to intentionally force the first instability mode of the wake.

This thesis is concerned with high-fidelity modelling of helix active wake control using large-eddy simulation (LES) of the atmospheric flow, where the effect of IPC is captured by representing the turbine in the LES by means of the actuator line model (ALM). Judging the potential of helix active wake control requires (i) quantifying the arising power-load trade-off, (ii) comparing it to established WFFC strategies like wake steering, and (iii) ultimately testing it in realistic transient atmospheric boundary layers. To this end, the overall objective of this thesis is to

> *"Assess the performance of helix active wake control in quasi-steady atmospheric boundary layers and develop actuator line model capabilities for its study in coarse grid real weather large-eddy simulations."*

In a first step, the sensitivity of helix active wake control to the amplitude of the pitch actuation is quantified for a full wake overlap scenario. It is found that the activation of the control leads to a trade-off between power gain and additional turbine loading in terms of the incurred damage equivalent loads (DEL). While the power gain monotonically increases for pitch amplitudes between one and six degrees, the same trend is observed for the DELs of the actuated turbine. Hence, the value of activating the control and selecting its pitch amplitude setpoint will need to be determined based on a higher-level metric like the current electricity price.

In a second step, the sensitivity of the power gain achieved with helix active wake control to varying degrees of wake overlap and turbine spacing is compared to wake steering. It is found that wake steering outperforms the helix except for dense spacing combined with full wake overlap. However, when considering a varying wind direction around full wake overlap without an immediate control response, the results suggest that the power gain achieved by the helix control setpoint is more robust.

The previous finding suggests that time-varying wind directions are important for selecting the best control strategy. Hence, in a third step, an actuator line model is implemented into an atmospheric LES code, which allows for driving microscale LES with mesoscale forcing derived from numerical weather prediction models in order to include additional time scales in the problem. The correctness of the ALM implementation is verified with reference to results from four other research LES codes. Additionally, the emphasis is on ensuring accurate thrust and power predictions on coarser LES grids. To this end, the filtered lifting line correction is included in the ALM implementation.

Current corrections for coarse grid ALM-LES, e.g. the filtered lifting line correction, do not consider the complete unsteady problem. Thus, as a last step, we take the IPC actuation underlying helix active wake control as an opportunity to formally investigate unsteadiness in the ALM for scenarios corresponding to unsteady attached flow below stall. By deriving a semi-analytical solution for the two-dimensional "ALM" its connection to Theodorsen theory is established. Further, this solution allows for determining the optimal kernel width for the unsteady ALM, which is approximately 40% of the chord length and determining bounds of its validity. Importantly, we find that even when using the optimal kernel width, the magnitude of the unsteady force cannot be accurately captured anymore by the ALM if the reduced frequency exceeds $k > 0.2$.

In summary, this thesis contributed to the understanding of under which circumstances the application of helix active wake control for the mitigation of wake effects might be a viable option. Given that the benefits and drawbacks of the helix are at least partially complementary with wake steering control, both control strategies could be seen as pieces of a more comprehensive toolbox of wind farm flow control strategies. The activation of a respective control strategy would then happen only during periods corresponding to its identified favourable conditions. Hence, the model development conducted in the second part of this thesis aims towards building a simulation environment — spanning from mesoscale effects down to airfoil aerodynamics — within which such a selection process of WFFC strategies can be studied in realistic weather conditions.

# Samenvatting

De huidige verandering van het klimaat op aarde maakt maatregelen noodzakelijk om de menselijke CO2-voetafdruk sterk te verminderen. Voor de energiesector betekent dit een overstap naar hernieuwbare energiebronnen zoals wind. Het windklimaat is ruimtelijk heterogeen, waarbij de windsnelheden en vermogensdichtheden op zee bijzonder gunstig zijn. Het gunstige windklimaat op zee, in combinatie met de beperkte beschikbaarheid van landoppervlak voor windenergie, motiveren de overstap naar windenergie op zee. Bovendien pleiten economische, ruimtelijke en milieuoverwegingen voor het clusteren van windturbines in windparken op zee.

Windturbines die in een windpark zijn geclusterd, werken gemiddeld minder efficiënt dan wanneer ze afzonderlijk zouden staan. Een belangrijke oorzaak van dit rendementsverlies is het zogeffect. Wanneer windturbines kinetische energie uit de wind halen, laten ze een gebied met lage windsnelheid achter, het zogenaamde zog. Wanneer het zog dat door bovenwinds gelegen turbines wordt gegenereerd in aanraking komt met benedenwinds gelegen turbines in het park, verminderen ze het vermogen van deze turbines en daarmee het totale rendement van het park. In de ontwerpfase wordt de opstelling van het windpark geoptimaliseerd om zogverliezen tot een minimum te beperken, maar zelfs bij een optimale opstelling zijn de zogverliezen aanzienlijk. Vanuit de wens om de resterende zogverliezen verder te beperken, is het onderzoeksgebied van windparkstromingsregeling ontstaan, dat tot doel heeft zogverliezen te verminderen door middel van een gecoördineerde regeling van de windturbines in het hele park.

De strategieën voor stromingsregeling in windparken verschillen op basis van hun werkingsmechanisme. Zo zijn er bijvoorbeeld strategieën die erop gericht zijn het initiële zog van bovenwindse turbines te verminderen door de stuwkracht van de turbine te verlagen of door het zog om benedenwindse turbines heen te leiden door de bovenwindse turbines opzettelijk niet goed uit te lijnen met de inkomende windrichting. Een recentere categorie strategieën voor windparkstromingsregeling is actieve zogregeling. In vergelijking met de vroegere quasi-stationaire strategieën zijn strategieën voor actieve zogregeling inherent dynamisch, aangezien hun werkingsmechanisme berust op tijdsafhankelijke aandrijving, die tot doel heeft de onderliggende instabiliteitsmodi van de stroming te activeren. Een van de meest recent ontwikkelde strategieën voor actieve zogregeling is helix actieve zog regeling. Deze maakt gebruik van de individuele bladhoekregeling van moderne windturbines om opzettelijk de eerste instabiliteitsmodus van de stroming te forceren.

Dit proefschrift gaat over modellering van helix actieve zogregeling met behulp van large-eddy simulatie (LES) van de atmosferische stroming, waarbij het effect van de individuele bladhoekregeling wordt meegenomen door de turbine in de LES weer te geven met behulp van het *actuator line model* (ALM). Om het potentieel van helix actieve zogregeling te beoordelen, is het nodig om (i) de ontstane trade-off tussen vermogen en belasting te kwantificeren, (ii) deze te vergelijken met bestaande strategieën voor wind-

parkstromingsregeling zoals zogsturing, en (iii) deze uiteindelijk te testen in realistische transiënte atmosferische grenslagen. Daartoe is het algemene doel van dit proefschrift om:

> *"Het potentieel in kaart te brengen van helix actieve zogregeling in quasi-stationaire atmosferische grenslagen en om een actuator line model te ontwikkelen voor grove resolutie large-eddy simulatie van realistisch weer."*

In een eerste stap wordt de gevoeligheid van de helix actieve zogregeling voor de amplitude van de bladhoekactivering gekwantificeerd voor een scenario met volledige zogoverlap. Er wordt vastgesteld dat de regeling leidt tot een trade-off tussen energiewinst en extra turbinebelasting in termen van de opgelopen equivalente belasting (*damage equivalent loads*). Terwijl de energiewinst monotoon toeneemt voor bladhoekamplitudes tussen één en zes graden, wordt dezelfde trend waargenomen voor de equivalente belastingen van de geactiveerde turbine. Daarom moet de waarde van het activeren van de regeling en het selecteren van de instelwaarde voor de bladhoekamplitude worden bepaald op basis van een andere maatstaf, zoals de huidige elektriciteitsprijs.

In een tweede stap wordt de gevoeligheid van de energiewinst die wordt bereikt met helix actieve zogregeling bij verschillende mate van zogoverlap en turbineafstand vergeleken met zogsturing. Er is vastgesteld dat zogsturing beter presteert dan de helix, behalve bij een dichte afstand in combinatie met volledige zogoverlap. Wanneer echter rekening wordt gehouden met een variërende windrichting rond om de richting van volledige zogoverlap en het feit dat de reactie van de zogregeling niet instantaan is, suggereren de resultaten dat de energiewinst die wordt bereikt met de helix regeling robuuster is.

De hierboven beschreven bevinding suggereert dat tijdsafhankelijke windrichtingen belangrijk zijn voor het selecteren van de beste regelstrategie. Daarom wordt in een derde stap een ALM geïmplementeerd in een atmosferische LES code, waardoor het microschaal LES model kan worden geforceerd met mesoschaal data afgeleid van numerieke weermodellen om grotere tijdschalen in het probleem op te nemen. De juistheid van het geïmplementeerd ALM wordt geverifieerd aan de hand van resultaten van vier andere LES codes. Daarnaast ligt de nadruk op het waarborgen van nauwkeurige voorspellingen van stuwkracht en vermogen op grovere resolutie LES. Daartoe wordt de benadering van de zogenaamde *filtered lifting line correction* opgenomen in de implementatie van de ALM.

Huidige correcties voor grove resolutie ALM-LES zoals de *filtered lifting line correction* houden echter geen rekening met het volledige tijdsafhankelijke probleem. Daarom nemen we als laatste stap de activering van de individuele bladhoekregeling die ten grondslag ligt aan helix actieve zogregeling als een kans om de tijdsafhankelijkheid in de ALM formeel te onderzoeken voor tijdsafhankelijke aangehechte stroming. Door een semi-analytische oplossing voor de tweedimensionale "ALM" af te leiden, wordt het verband met de theorie van Theodorsen vastgesteld. Verder maakt deze oplossing het mogelijk om de optimale kernbreedte voor de tijdsvariante ALM te bepalen, die ongeveer 40% van de koorde bedraagt, en om de grenzen van de geldigheid ervan te bepalen. Belangrijk is dat we vaststellen dat zelfs bij gebruik van de optimale kernbreedte de omvang van de tijdvariante kracht niet meer nauwkeurig kan worden vastgelegd door de ALM als de gereduceerde frequentie $k > 0.2$ overschrijdt.

Samenvattend heeft dit proefschrift bijgedragen aan het inzicht in de omstandigheden waaronder de toepassing van helix actieve zogregeling voor het verminderen van zogeffec-

ten een haalbare optie kan zijn. Aangezien de voor- en nadelen van de helix ten minste gedeeltelijk complementair zijn aan zogsturing, kunnen beide regelingsstrategieën worden gezien als onderdelen van een uitgebreidere toolbox van strategieën voor de regeling van de stroming rond windparken. De activering van een bepaalde regelingsstrategie zou dan alleen plaatsvinden tijdens periodes die overeenkomen met de geïdentificeerde gunstige omstandigheden. Daarom is de modelontwikkeling in het tweede deel van dit proefschrift gericht op het bouwen van een simulatieomgeving — variërend van mesoschaaleffecten tot aerodynamica van vleugelprofielen — waarin een dergelijk selectieproces van strategieën voor windparkstromingsregeling onder realistische weersomstandigheden kan worden bestudeerd.

# Acknowledgements

Four years ago at the end of my Master thesis, I felt that searching for optimal perturbations to trigger bypass transition above flat plates on the one hand kept speaking to the theorist deep inside me, which is still there to this day, but on the other hand my four years younger I seemingly felt the urge to continue with some work slightly closer to what people outside of academia generally refer to as "real life". This wish led me to the field of wind energy, where I could keep working on fluid dynamics, but with elevated chances to actually explain my family and friends what I spend my work days with (not sure I succeeded when it comes to that). However, I somewhat naively decided to continue from now on with fluid dynamics research in a department for systems and control. This decision caused at the same time some of the most joyful and also frustrating moments of the past four years. While I managed to get some research working now and then, I mostly feel very lucky to have met so many kind people along the way whom I would like to thank below, since they were the most important reason why this PhD journey has been overall a very enjoyable one.

First of all, I would like to thank my two supervisors Jan-Willem and Remco. As a supervisory team the two of you were complementing each other very well. Jan-Willem, I cannot forget the moment we met for the first time online during the Covid pandemic, which already seems to be so far in the past. It was the first round of the interviews for the PhD position, and you seemed very exited, for sure about the helix, but also very much because it just started snowing outside your window in the Netherlands (at the end of April!). Having a very good feeling about the position, the group, and the supervisor after this meeting, one thing led to another and four months later I moved to Delft. During the PhD, our meetings very often started with a chat about Austria (apparently your favourite vacation destination and my second home), since we seemingly shared the common understanding that a minimum exposure to mountains of a couple of weeks per year is absolutely required for mental well-being. During the last four years you provided a great deal of scientific freedom (way more than some of the initial project milestone plans suggested) and it was very rare to hear a "no" from you when the opportunity to pursue a new idea came by (actually I cannot remember any at all). You also showed that almost any disagreement can be solved with persistence, negotiation and compromise. It took us some time, but I feel we were successful in the last four years to learn each others "scientific languages" of control and fluid dynamics: You accepted these rather lengthy sections in the papers about ABL precursors (sorry sometimes they really need to be that long), and taught me some intuition for control theory in return (the last paper even includes a transfer function!). Remco, thank you for sharing your blend of research and industry perspective during the last four years, your very helpful advice on effective writing and communication, and for always keeping the bigger picture in mind, and of course for one or the other nudge to maybe consider slightly more pragmatic and realistic scenarios than fully controlled double-periodic LES domain setups, 2D unsteady analytical modelling and

"switched-off" inflow turbulence... Your mantra to just take the opportunity when a good one comes by made decisions on where to go with the research way easier for someone like me who likes to overthink things. You are an inspiration that the gap between fundamental science and industry can be way smaller than it sometimes might seem, and letting me experience this first-hand by hosting me at the Whiffle offices during the first year of my PhD.

Secondly, I would like to thank the committee for their time to read the thesis, their feedback, and their opposition during the defence. Thank you Sasa Kenjereš for venturing into wind energy research. Thank you Nathaniel Wei, Richard Stevens and Stefan Ivanell: It is an honour that the people I knew only from all these papers I read during the last four years agreed to read some of mine and ask a few tricky questions about them. And lastly of course thank you Tony for being the 5th (certainly not independent) committee member. Certain colleagues (you know who you are!) used to make fun of my slightly excessively structured email folders, but for once I can claim that they come in handy as I still find the email with the subject "Regarding the data for the figures in your paper 'Comparison of four large-eddy simulation research codes...' " (sent on the 03.11.2021). One of the most impactful connections during my PhD was getting to know you by pure coincidence. What started with this small question about data availability only two months after I started my PhD, developed into a collaboration enduring the rest of it. You co-authored both of my journal articles and as highlight you hosted me for a two month research stay at NREL in Boulder. These weeks have been the best ones of my entire PhD (the ESTA got maxed out until the last day), both in terms of research and living at the foothills of 14,000 feet tall mountains with seemingly never ending sunshine weather. The view of the front range during the coffee breaks on the terrace certainly helped to solve some of the tricky integrals we were starring at for quite some time back then (although Mathematica contributed its fair share, too). Your suggestions for tours with the road bike also kept me busy during the weekends and turned out to be quite challenging, this ascend to Ward is so steep (especially for someone adapted to cycling at 5 m below and not 3000 m above sea level)! The time that you have spent working on our shared research despite being not involved in any formal way in my PhD project and doing this as free time hobby is outright crazy.

A very big thanks to my paranymphs Amr and David for all their support during the last four years and the defence. Thank you Amr, you were the one truly welcoming me to the group with your openness and kindness in these first few weeks of my PhD when I was doubting if choosing this PhD thing really has been a good idea. Our shared dinners were a cherished tradition throughout the four years and I forgot how much shawarma and konafa we ate in Delft, Amsterdam, during our travel to the VKI course in Brussels, or elsewhere. You invited the entire group to your wedding in Morocco (tinitus of my life!) and we travelled together to our first conference abroad to the US (whenever I was waking up during night you seemed to prefer debugging Matlab code over sleep). Together with AMR-Wind you have been a constant in this PhD. Thank you David (or should I say Domingos as the Portuguese do?!): The first time we really talked for longer must have been somewhere in Brooklyn after we decided that 40$ entrance fee for an evening bouldering session seemed reasonable for some New Yorkers, but slightly excessive to us. It is impossible to not get infected by your positive spirit which you spread in and outside the office. Thank you for converting any conference travel we could into a van trip to

the best climbing spots nearby (trad climbing in the peak district, midnight hikes in the Scottish highlands, bouldering in the Rockies and surviving this treacherous rain weather in Val di Mello). I am happy that the hammock will keep its deserved spot in the rebuilt van and I am looking forward to all the trips which are still to come!

Collaboration is a great help in doing good research while also having a lot of fun in the process. Hence, I am very grateful to my collaborators from the last four years. Thank you to the Whiffle team for welcoming me to your team. It was a pleasure to observe your take-off from a small startup with a few desks to a company that probably most people in the wind business know by now. In particular, thank you Mikko and Pim: Mikko, I am convinced that the code which you can not compile and get running still needs to be written! Your relaxed attitude makes it almost impossible to be stressed around you, no matter how close the deadline or how long the error logs. Pim, thank you for making the miracles of ASPIRE seem less miraculous, being a living code documentation, and challenging one or the other promise of wind farm flow control in your humorous way. Also thank you to the NREL group: Yorgos for co-hosting and knowing everything that there is to know about CFD, Garret for your regular check-ins on Mehtab's and my wellbeing at NREL, Michael for translating whatever Tony and I came up with into AMR-Wind source code that actually works, and Alex for introducing me to slacklining in North Boulder Park. Further, many thanks to this PhD from a remote Swedish island in the Baltic Sea who decided to do LES differently than anyone else. Henry, thank you for the shared conference experiences, all the discussions about LES/ALM/Lattice-Boltzmann, for simply being a great example why it has been so enjoyable to work in the wind energy science community, and for showing up with cake to my conference presentation at 8:40 in the morning after the conference dinner in an otherwise veeeery empty room, because beyond conservation of mass, momentum, and energy, the conservation of cake is the law which truly matters in science: $\mathrm{D}N_{\mathrm{Cake}}/\mathrm{D}t = \mathrm{D}N_{\mathrm{AcceptedPaper}}/\mathrm{D}t$ (it might miss a sink term for all the cake eaten, but I leave that for future work).

I consider myself very lucky that I got the chance to do a PhD in Jan-Willem's group with its welcoming and supportive spirit. Thank you Marcus and Jonas, two of the fellow Kartoffeln in the group, there is something special to having home also nearby while living abroad for so long. Thank you for the countless hours spent together for research, free time and in-between: the community lunches (do you like mushrooms by now Marcus?), the van trips, all the climbing, and your positive attitude towards any problem. These ideas from chats at the coffee machine, from running after work, or from the latest van trip, sometimes kept us more occupied that one or the other project plan considered, but I think that's not too bad. And of course I learned that the control engineers' "Größenwahnsinn" knows no limits, "sure we can control the atmosphere..." (Marcus, you would probably cite Deichkind: "Denken sie groß!"). Thank you Unai, for the surprise visits from Bilbao in the office, for providing me with a one week intro to life in Boulder, and of course for inviting us to Mallorca this year. Thanks Maarten, for showing how to work efficiently and more importantly for exploring together the Atlas mountains all the way up to the peak of Jbel Toubkal before Amr's & Wassima's wedding. Thank you to the fellow HKN researchers Mees and Marion for all the discussions about the helix and of course the Paris trip. Thank you Daniel, we share our sometimes slightly pessimistic view on the world:); Livia, for regularly sharing samples of our latest baked cakes; Claudia, for being the only

other person in this department interested in the ALM rather than control; Daan and Atin, for being the "Ruhepol" of the group; Sander and Tim, for the padel games; Jaques, Paul and Guido, for the tours with the road bikes (I am still waiting for any draft Paul); Jesse, for taking scientific plots for as important as one should; Sachin and Fafa, for carrying on with the cluster wake project; Leendert, for teaching control theory to me while I was teaching the students; Robin and Fritz, for teaching me some basic sailing skills; Sam, Gianpietro, Filippo and Alex for the after-work climbing sessions; and Rogier, Matteo, Tristan, Alexandra, Sebastiaan, Jean, Bert, Twan and Tushar for the fun discussions during coffee breaks, lunch or whenever a little bit of time for procrastination was needed. Thank you to my former two Master students Louis and Swen, for showing up every week with new (surprising) results and for asking the questions, which got us thinking if we actually understood things. And of course thank you to the DCSC staff, in particular, Francy, Sandra, Wim, and Will, for always helping and finding solutions, be it with bureaucracy, finances, or docker images on GPUs...

Whenever the Bode plots became too overwhelming or the LES output stopped making any sense at all, there was luckily an aerospace faculty close by: Anand, I admire your persistence despite all the challenges life has in stock for you. Thank you for your delicious Indian dinners, the talks about life and LES, the cycling tours, and for inviting me to Rouen and showing me around Normandy. Mehtab, thank you for discussing gravity waves while enjoying some chai (I will keep bothering you when starting my new job...), the great time in Boulder when visiting NREL, approving the pumpkin which I introduced to your legendary lamb stew, hiking almost to the top of Longs peak wile starting at 11:00 (absolutely realistic!), the volleyball sessions in the park, getting lost in Colorado (who could know they would miss us after only one day), and for venturing into sailing while casually mentioning right before that you actually can not swim. I am sure a visit to Hunza is only a matter of time! Dries, thank you for taking so much time to explain ABL physics and your inspiring attitude towards doing rigorous research. You are deeply missed.

Via aerospace, Marcus, Jonas and I were also lucky to get to know Sebastiano, the LES wizard! Thank you for being open to some new crazy ideas, for making cluster wake control practically happen, and visiting in Boulder. Koen, it is unfortunate to have met you only so late during the PhD despite Leuven and Delft being not actually that far apart, thank you for all your humorous stories and giving us a nudge in the right direction for actually understanding cluster wake control. While the coursework required by the graduate school sometimes might have felt like an undesired distraction, it was a good chance to meet new people: Thank you Harika and Santosh, for your hospitality in Breda and Delft, all the very spicy food, the board game nights, and sharing your experiences with life in the US. The stay in Boulder has been also very special because of Anna and Brian: Thank you for being some of the most welcoming people I have ever met, for borrowing me a bike for 8 weeks such that I could cycle around Boulder like I used to in Delft, for showing the best outdoor bouldering and climbing spots, and for introducing me to country music up on Gold Hill. And we almost made it for a flight session along the front range before a snowstorm stopped us, a good reason to visit again! Finally, a steady supply of good coffee and cookies made most of this thesis happen, thank you Mateusz for being the best barista on campus and a great climbing buddy for some weekend escapes to Belgium and Luxemburg.

Living abroad in different countries has been often a pleasure, but sometimes it also felt difficult to stay in touch. Even more so I am glad that I somehow still managed to visit Sweden regularly in winter and summer (the wake conference also providing a convenient excuse): Thank you Rogelio for reigniting my passion for climbing and exploring the local crags around Stockholm. Martin, thank you for caring and regularly asking how I am doing when I had vanished again for too long, the summer escapes to Gotland and Öland to forget about papers and deadlines at least once a year, and being a cycling buddy for life! Alex & Alex, ihr begleitet mich schon gefühlt seit immer, vielen Dank für stundenlange Spaziergänge durch den Schwarzwald um die verpassten Monate aufzuholen, eure ehrliche Meinung zu jedem kleineren oder größeren Problem, und dafür, dass Silvester ein Fixpunkt im Jahr ist, egal was die anderen zwölf Monate passiert ist. Vielen Dank Rudi, dich in Österreich in der Nähe der Berge zu besuchen war immer eine gute Zeit um die Uni etwas zu vergessen und stattdessen radfahrend über Kameras und das Leben zu philosophieren. Danke, Albert und Helga, ich hoffe, dass ich in der Zukunft wieder öfters zu Besuch kommen kann, die Wochen die ich während des PhD's bei euch im Burgenland arbeiten konnte waren immer sehr entspannend und produktiv zugleich. Und zuletzt natürlich vielen Dank an meine Eltern, Tilde und Andreas, und meinen Bruder Jakob. Danke Tilde und Andreas, dass Jakob und ich immer unserer Neugierde haben folgen können, für eure Unterstützung ins Ausland zu ziehen, meine doch manchmal niedrige Besuchsfrequenz zu akzeptieren, und wenn es dann wirklich mal zu lange war einfach in den Niederlanden vorbeizukommen oder einfach ja zu einem relativ spontanen Roadtrip durch die USA zu sagen. Danke!

*Emanuel*
*Delft, November 2025*

# 1 Introduction

Worldwide greenhouse gas emissions continue to rise and challenge the goal of limiting long-term average global warming to 1.5°C compared to pre-industrial levels. Despite this danger, current national policies are insufficient to achieve this goal, as there is a disparity between ambition and the actions taken. However, there is the chance of closing this gap by realising the mitigation potential across all major sectors, including the energy, agriculture, forestry, industry, transport and building sectors, by taking firm action. In particular, the energy sector holds great potential for reducing greenhouse gas emissions by deploying solar and wind energy plants [1]. The key role of these two renewable energy sources is also highlighted by the International Energy Agency (IEA) in their *Net Zero by 2050: A roadmap for the global energy system* strategy [2]. As of now, wind energy stands at an installed capacity of 1000 GW with additions of 116 GW in 2023, whereof 107 GW were achieved by onshore projects [3]. Further expansion on a similar scale is expected for 2024, with an estimated capacity increase of 119 GW [4]. At the United Nations COP28 climate summit, about 130 countries also agreed to triple contributions from renewable energy [5], and wind energy is a crucial puzzle piece to achieve this goal [3]. The feasibility of this goal is challenging since growth models for the expansion of wind and solar energy in countries across the globe do not support these assumed growth rates. National growth rates were found to follow S-curves, and the corresponding maximum growth rates are insufficient to realise scenarios compatible with the 1.5°C goal. In particular, later adopting countries of the new technology did not achieve higher growth rates than the early adopting ones [6]. Nevertheless, there are also more optimistic studies which show that the optimised large-scale deployment of wind and solar energy can achieve net-zero targets in 2040 [7]. While this thesis is concerned with technological improvements to both improve the absolute production and the efficiency of wind energy in support of the outlined deployment goals, it is also worthwhile to consider that achieving the net-zero $CO_2$ strategy in 2050 goes way beyond a sole focus on the supply side. An increasing focus on sufficiency and efficiency measures on the electricity demand side aids the climate ambitions and mitigates the risk of a sole focus on the transformation of the supply side [8].

When considering the scale of the required wind energy deployment, a first natural

1

question might be the one of how large the global wind resource actually is. Global wind resource estimates vary since, for example, the assumed rated power (and height) of the hypothetical turbines extracting the power varies between studies. In fact they were often assumed to be of sizes like 1.5 MW turbines in [9], 2.5 & 3.5 MW turbines in [10] and 5 MW turbines in [11], which are all significantly smaller than today's wind turbine standard. Further accounting for changes of power curves with altitude and excluding regions because of factors like accessibility, missing grid connection or sea ice concentration influences the estimates [12]. Despite these variations between the estimates, the former studies suggest that from a global perspective, the wind resource is abundant [9, 10, 11, 12]. However, the availability of the wind resource is spatially heterogeneous, where topography and climate are important factors. Offshore sites feature lower surface roughness, which leads to higher wind speeds [9] and mean power densities, where the latter is proportional to the mean air density and the mean of the cube of the wind speed [13]. A map of the mean power density at 100 m above ground for central and western Europe is shown in Figure 1.1. The map displays that the potential for wind energy lies especially offshore, where the mean power densities are distinctly higher than onshore, which is visually demonstrated by the fact that the coastlines can be identified solely by the gradient of the colour map without any need for explicitly marking them. While selecting this specific region for demonstration purposes, the offshore potential is not limited to Europe and extends worldwide, e.g. to California [14] and China [15]. Beyond the raw wind resource, there are also additional arguments for offshore wind energy. Given the rapid growth of wind energy in general, it increasingly has to compete for land surface with

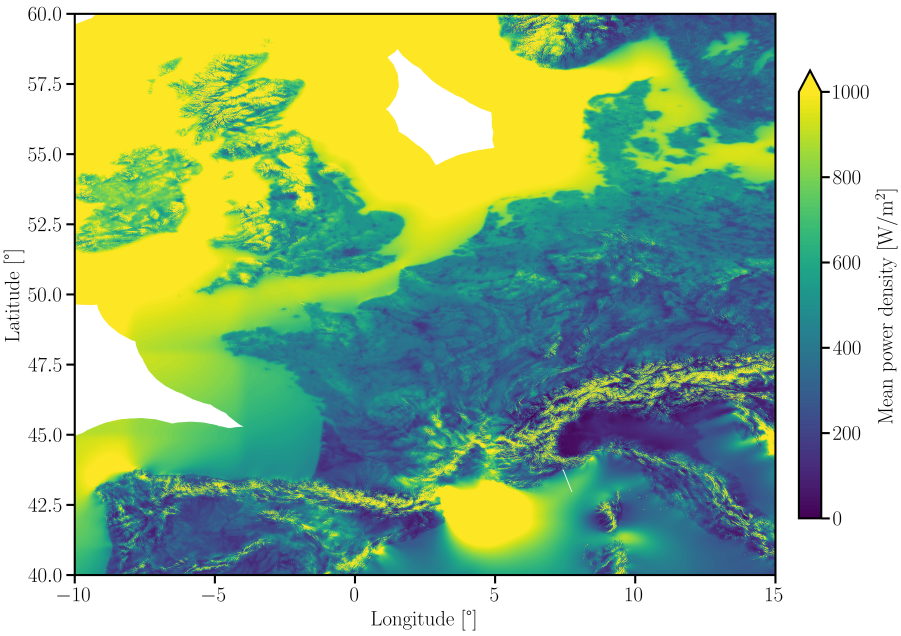


Figure 1.1: Mean power density at 100 m above the surface for central and western Europe. The raw data is taken from the global wind atlas (`https://globalwindatlas.info/en/`). Regions without data are shown in white.

all other stakeholders in our society and economy. Thus, offshore wind energy unlocks additional surface for energy generation purposes [16]. Moving offshore also alleviates onshore transportation constraints, which allows for the design and deployment of larger wind turbines with higher rated power [17].

## 1.1 Wind farms — The enabler of offshore wind energy

When moving offshore, economic [18, 19] and environmental [20] considerations suggest the clustering of wind turbines in proximity to each other, thus forming a wind farm. These considerations include cabling costs for the intra-turbine and land connections; construction cost; maintenance cost; and the constraint of the surface dedicated to wind energy generation, since offshore, different stakeholder interests need to be balanced, too (e.g. shipping routes, fishing, natural reserves). Modern offshore wind farms contain from a few dozen up to more than a hundred wind turbines, where each wind turbine on its own constitutes one of the largest rotating machines built by humankind to date. For reference, it takes two to three times the wingspan of an Airbus A380 to cover the rotor diameter of these wind turbines [17]. In the following two sections, we present the physical scales which impact the performance of these gigantic farms and introduce an unfortunate drawback of clustering wind turbines into farms.

### 1.1.1 The scales impacting wind farm performance — From the airfoil to the mesoscale weather system

Wind farms operate in the turbulent winds occurring in the lowest part of the Earth's atmosphere, where they are impacted by physical processes spanning a very wide range of spatial and temporal scales [21]. The wind energy-relevant scales of the atmospheric flow cover processes from the mesoscale down to the Kolmogorov microscales. The latter characterise the smallest turbulent motions in the flow, which dissipate energy, i.e. transform kinetic energy into internal energy [22]. Their length scale, $\eta$, in the turbulent atmospheric flow is on the order of one millimetre with a corresponding time scale, $\tau_\eta$, on the order of a fraction of a second [23]. In contrast, towards the upper end of the relevant range, mesoscale atmospheric systems span distances from a few up to several hundred kilometres with temporal dynamics on the order of hours. These larger mesoscale dynamics then force the microscale atmospheric flow and provide the boundary conditions for its temporal evolution [24, 25]. However, not only the atmospheric physics, but also the scales of the human-made wind energy extracting machinery span several orders of magnitude from a small airfoil up to the length of an entire wind farm. To build an intuition for this coupled natural-technical system, it helps to divide it into four characteristic scales, where we use the geometric scales of the turbine/farm as a guide. These scales of course merge into one another and interact, but they are still helpful to structure the system (Figure 1.2):

- **Airfoil scale:** Airfoils are the two-dimensional cross sections from which a turbine blade is made up. They are a crucial part of the wind turbine since they harness the forces of the wind, which turn the wind turbine's rotor. The airfoil dimensions are on the order of the chord length $c$ (the length of the airfoil), which for airfoils near the blade tip is $\mathcal{O}(c) \approx 1\,\mathrm{m}$. Airfoils located at the outer part of the blade towards the tip experience local flow speeds of up to $U_c \approx 100\,\mathrm{m/s}$ such that the local characteristic

time scale, $\tau_c$, is on the order of $\mathcal{O}(\tau_c) = c/U \approx 0.01\,\mathrm{s}$ (the time it takes an air parcel to travel across the airfoil). The airfoils leave behind a wake in the flow with vortex structures of similar size to the chord length.

- **Turbine scale:** The kinetic energy extracted from the wind is converted to electricity at the scale of an individual turbine. A modern offshore wind turbine reaches diameters, $D$, on the order of $\mathcal{O}(D) \approx 200\,\mathrm{m}$ where the time for one revolution of the turbine rotor is on the order of $\mathcal{O}(\tau_D) = 10\,\mathrm{s}$. A large coherent vortex system forms immediately downstream of the wind turbine, consisting of tip and root vortices originating from the outer and inner ends of the turbine blades.
- **Wind farm scale:** A large offshore wind farm can contain on the order of ten rows of wind turbines, where turbines are spaced typically $5-10\,\mathrm{D}$ apart. Hence, the length (and also width) of such a wind farm is on the order of $\mathcal{O}(L) \approx 10-20\,\mathrm{km}$. The incoming wind in front of the farm attains speeds of $\mathcal{O}(U_\infty) \approx 10\,\mathrm{m/s}$ and thus the time it takes the flow to cross the farm is on the order of $\mathcal{O}(\tau_L) \approx 1000-2000\,\mathrm{s}$, i.e. tens of minutes.
- **Wind farm clusters and mesoscale:** The actual atmospheric microscale conditions encountered by a wind farm are the result of forcing from the larger mesoscale weather systems introduced above, which span up to several hundred kilometres. These spatial scales are also encountered when considering clusters of multiple wind farms.

The performance of a wind farm is impacted by all four of the scales described above. Hence, we return to them in Section 1.3, where suitable modelling approaches will be discussed.

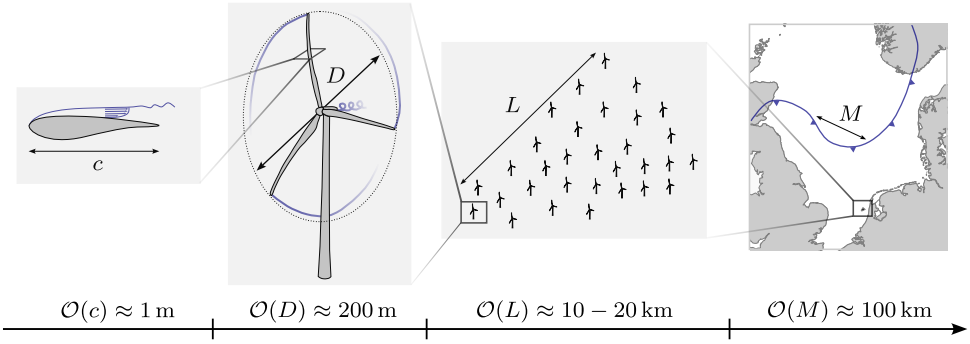


Figure 1.2: The range of characteristic scales impacting wind farm performance: airfoil scale, turbine scale, wind farm scale and wind farm cluster/mesoscale.

### 1.1.2 Efficiency losses — The cost of clustering wind turbines into wind farms

In this section, the goal is to introduce the drawbacks of clustering wind turbines into a large farm from a phenomenological and intuitive standpoint. Each wind turbine in the

farm converts parts of the kinetic energy contained in the incoming wind into electrical energy. Since the overall energy is conserved (the sum of kinetic energy in the wind, electrical energy and losses due to energy conversion), this implies that a positive electrical power output of the turbine results in a reduction of the kinetic energy contained in the wind behind the turbine, which translates to a reduced wind speed. What does this imply for the power output of a very long column of wind turbines? Would the wind, as it moves through the column, eventually slow down to a standstill? Fortunately, this is not the case, as the air moves downstream between two turbines, its kinetic energy is partially replenished. This is due to turbulent fluctuations in the wind, which act to transport kinetic energy from the more energetic surrounding winds from above and the sides back to the region between the turbine. If we now consider many long columns of turbines stacked next to each other, the neighbouring winds are depleted of energy, too, and hence energy is mostly replenished from the top, except for turbines which are located towards the front or side of the farm. Nevertheless, the replenishment of kinetic energy implies that the wind not only slows down as it passes each turbine, but it also accelerates again afterwards. That the atmospheric winds are indeed influenced on such a fundamental level by the wind turbines/farm is beautifully visualised by an image taken from the Sentinel-2 satellite on the 16$^{th}$ April 2018 (top panel of Figure 1.3). The image captures the Sandbank and DanTysk wind farms operating within a cloud cover at the border of the Danish-German North Sea. While the actual turbines can hardly be spotted (the very small white dots in the inset), the low wind speed regions behind them are very prominent due to the distinctly different structure of the cloud cover. These structures also evidently impinge on the downstream turbines and superpose. Further, the fine-grained topology of these structures indicates a second property of the low-speed regions behind the turbines, which are elevated levels of velocity fluctuations, i.e. an elevated level of turbulence intensity added by the turbines. These two properties — the wind speed deficit and the higher levels of turbulence — are the two defining properties of the region behind each turbine, which is called the wake [26]. While it would be speculative what caused the "atmospheric wake visualisation" in this specific case, it certainly requires suitable atmospheric conditions [27].

The wind speed deficit of wakes gradually recovers as they move downstream, where the exact process and rate depends on the ambient turbulence level in the atmosphere, the boundary layer height, the wind shear, the stratification and the wind veer (the last two terms refer to the vertical variation of temperature and wind direction in the ABL, respectively) [28, 29, 30, 31, 32]. However, wake recovery takes time, which translates to streamwise distance. This distance is limited within a wind farm. Hence, downstream wind turbines generally encounter lower wind speeds than front row turbines, resulting in a reduced power output. The efficiency losses depend on the wake recovery rate (see above) and the effective turbine layout (which is a function of the wind direction), where field experiments found that wake losses on the order of 10% can occur [33, 34, 35, 36]. Wakes are only one component of the entire wind farm flow topology (see mid panel of Figure 1.3). The entirety of the turbines in the farm presents an obstacle to the incoming flow. The flow thus slows down in front of the farm and partially deflects around the farm. This phenomenon is called global blockage and causes even front row turbines to produce less power than one would expect from an individual turbine [37]. Furthermore, in a

1

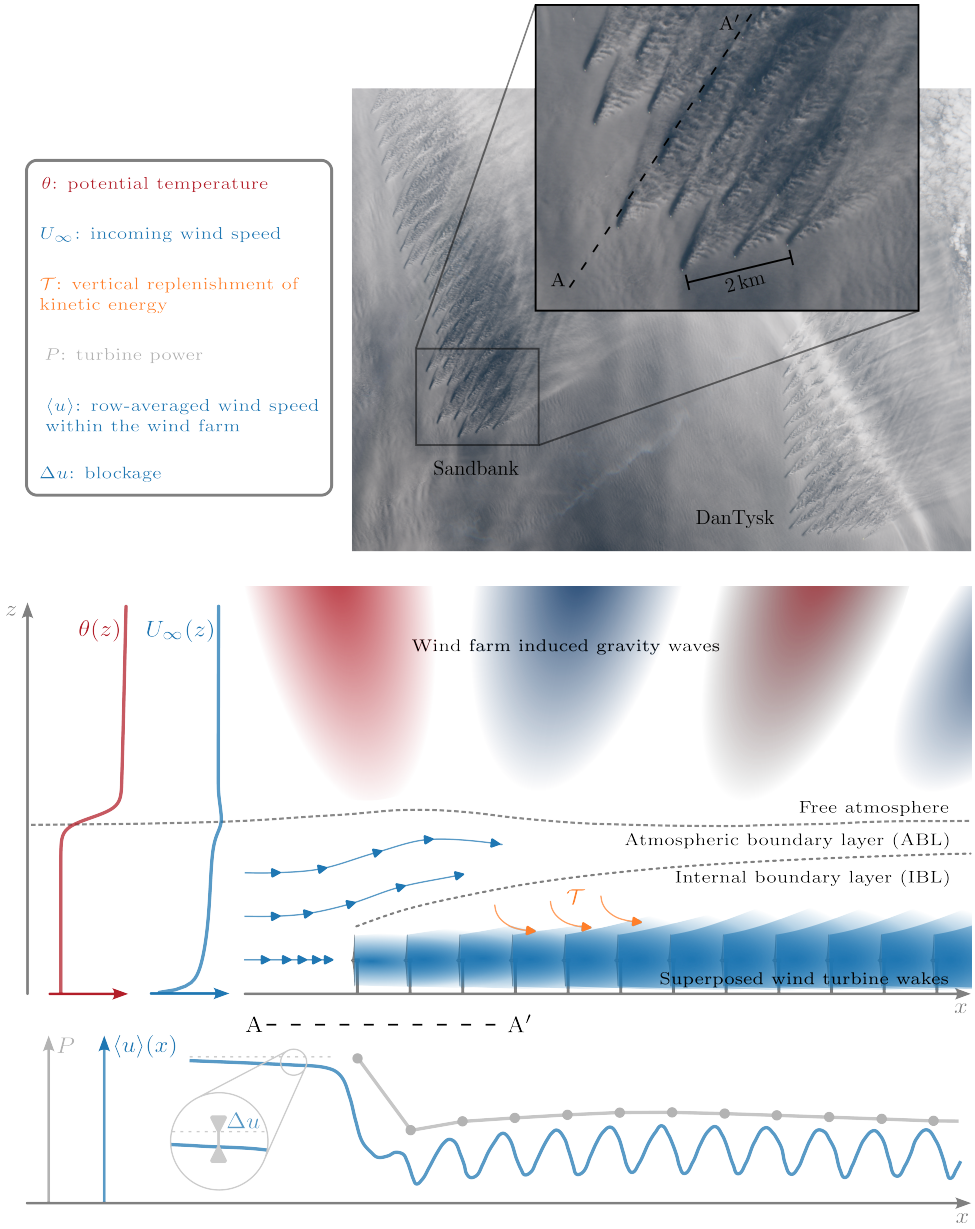


Figure 1.3: The Sandbank and DanTysk wind farms in the North Sea observed from the Sentinel-2 satellite on the 16th April 2018 (top panel). Credit: European Union, contains modified Copernicus Sentinel data (2025). Qualitative visualisation of the flow physics associated with a large wind farm operating in the atmospheric boundary layer (mid panel, adapted from [26]). Qualitative visualisation of the global blockage effect, the turbine power output, and the streamwise evolution of row-averaged wind speed in the wind farm (bottom panel).

stratified atmosphere, the flow deflection around the top can cause gravity waves. These gravity waves induce additional pressure gradients in the wind farm, which superpose onto the driving large-scale background pressure gradient. These additional pressure gradients cause local flow acceleration and deceleration, which modify the turbine's power production, too [38]. Another wind farm flow feature is the development of an internal boundary layer above the farm, which could reach a fully developed state for a very long wind farm [39, 38, 26]. All these features together result in a case-dependent evolution of the mean streamwise velocity and turbine power output through the farm, which are shown qualitatively in the bottom panel of Figure 1.3. Its important features are the major deceleration in the first few rows and the recurring acceleration/deceleration pattern of the wakes in between turbines. The resulting overall lower wind speed across the farm results in, on average, reduced efficiency of the clustered turbines compared to their counterparts operating in isolation. The quantitative attribution of these efficiency losses to either large-scale farm-atmosphere interaction (blockage, gravity waves and limits to the vertical replenishment of kinetic energy in the farm from faster winds above) and internal turbine interaction via wakes is still the subject of ongoing research [40, 41, 42, 43]. However, wakes are certainly a big piece of the puzzle.

## 1.2 Wind farm flow control — The quest for increasing farm efficiency

The preceding section detailed the sources of efficiency losses encountered in wind farms. From there, the question arises whether these losses need to be accepted as they are or if there is potential for mitigation using optimised design and control. The former is done during the wind farm planning stage to identify farm layouts which minimise wake losses and thus is inherently static in the sense that it considers the statistical distribution of the wind speed and direction at a site [44]. The latter is employed during the operation of a wind farm with a given layout. In fact, the degrees of freedom of modern three-bladed variable pitch wind turbines provide a large playground to exploit them for dedicated actuation, which aims at controlling and enhancing the recovery of the wake flow. From this opportunity, the research field of wind farm flow control (WFFC) arose. It should be noted that the objectives of WFFC go beyond an elevated energy extraction. Objectives can also reduce structural loading, power tracking, O&M services and mitigate environmental impact [45]. Furthermore, there is also an effort to optimise energy extraction beyond the sole focus on wakes by accounting for wind farm-atmosphere interaction [46]. In this thesis, we are, however, concerned with WFFC in the narrow sense of increasing power extraction via the reduction of efficiency losses due to wakes.

### 1.2.1 An overview of wind farm flow control strategies — Derived from the turbine's degrees of freedom

Let us consider a wind turbine of radius, $R$, sweeping across an area, $A = \pi R^2$, while operating in an incoming air flow with speed, $U_\infty$, and density, $\rho$. The turbine experiences a force normal to the rotor, which is the thrust force, $T$, and extracts the power, $P$, which in terms of the local wind speed normal to the rotor, $U_r$, is given by $P = T * U_r$. Using the characteristic scales of the system ($U_\infty$, $R$, and $\rho$) one can define the rotor induction

1

$a_r = 1 - U_r/U_\infty$ and the non-dimensional power, $C_P$, and thrust, $C_T$, coefficients

$$C_P = \frac{P}{\frac{1}{2}\rho A U_\infty^3}, \quad C_T = \frac{T}{\frac{1}{2}\rho A U_\infty^2} \quad \rightarrow (1 - a_r) C_T = C_P. \tag{1.1}$$

Theory can now relate $C_T$ and $C_P$ to the induction in the rotor plane and predict maximum $C_P$ with the corresponding $C_T$ setpoint [47, 48]. The $C_T$ setpoint can be adjusted utilising the degrees of freedom of modern wind turbines, namely the pitch angle, $\beta$, the yaw angle, $\gamma$, and the generator torque, $Q$, where the last one can be used to regulate the rotational speed, $\Omega$, which is expressed as the non-dimensional tip-speed ratio $\lambda = \Omega R/U_\infty$. A turbine which is agnostic of its neighbours acts in a greedy manner; thus, it aims to maximise its own extracted power. To this end, the greedy turbine controller adjusts the tip speed ratio and blade pitch angle to adjust $a_r$ to the setpoint of maximum $C_P$ [47]. For simplicity, this assumes the case of uniform inflow and thus $\gamma = 0^\circ$ to be optimal. The resulting relationship between $\lambda$, $\beta$, $C_T$ and $C_P$ is shown in Figure 1.4 for the IEA 15 MW reference turbine.

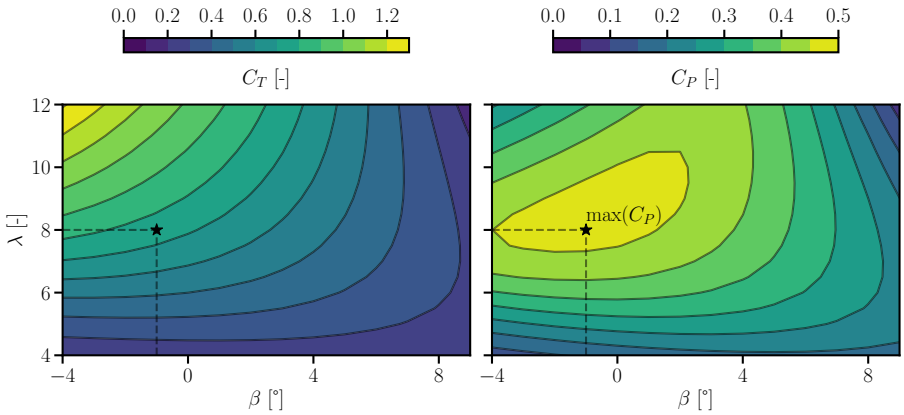


Figure 1.4: Thrust coefficient (left) and power coefficient (right) of the IEA 15 MW reference turbine as a function of the blade pitch angle, $\beta$, and the tip-speed ratio, $\lambda$ [49]. The stars indicate the setpoint $(\beta, \lambda)$, which maximises $C_P$.

Within the interval $a_r \in [0, 1]$ (corresponding to the windmill and turbulent wake states), the relation between $C_T$ and $a_r$ is a monotonically increasing one [48, 50]. Hence, thrust and induction are interlinked and an increasing thrust force results in an increased initial wake deficit. Conversely, when speeding up the recovery of the wake deficit is the goal, the modification of the thrust is the required actuator to do so. Deviating from the optimal greedy thrust set-point implies power losses on the actuated turbine (left panel of Figure 1.4), which need to be compensated for by increased power extraction of downstream turbines. Any successful WFFC strategy then needs to find a favourable balance between additional power loss due to actuation and power gain due to an enhanced wake recovery. An overview map of WFFC strategies can be intuitively derived from the different available turbine degrees of freedom, which can be exploited to modify the turbine

thrust. Such an admittedly subjective map is presented in the following (see Figure 1.5). For an extensive literature review, the interested reader is referred to [51].

For the greedy turbine, the thrust coefficient is given by $C_T(\lambda, \beta, \gamma = 0^\circ)$. Hence, the most simplistic strategy one could think of would reduce the rotor induction and thus $C_T$ in a static manner by adjusting either the tip-speed ratio or the collective blade pitch angle. This strategy is called static induction control and was already proposed in 1988 by Steinbuch *et al.* [52]. However, the potential gains of this strategy have turned out to be small across numerical, wind tunnel and full-scale studies [45]. When also the turbine's yaw angle is considered, one obtains $C_T(\lambda, \beta, \gamma)$. Misaligning the rotor with respect to the incoming flow ($\gamma \neq 0^\circ$) results in yaw angle offsets. These offsets were observed to cause wake deflection (lateral displacement of the wake) in experiments [53] and LES [54]. The cause for this deflection is a lateral force exerted onto the flow by the turbine operating with yaw offsets. Larger yaw offsets lead to decreased $C_T$, $C_P$ and wake velocity deficit, but increase the wake deflection. Further, a counter-rotating vortex pair forms behind the misaligned turbine and leads to a characteristic kidney-shaped wake [55]. The intentional use of yaw offsets on wind turbines in a farm allows then to steer wakes past downstream turbines, which provides them with larger inflow wind speed and thus increases their power production. The resulting WFFC strategy is called wake steering, and the potential for power gains was already demonstrated in multi-month field experiments at a utility-scale wind farm [56].

The two strategies above — static induction control and wake steering — can be classified as quasi-steady control in the sense that the control set-points are only adapted to slow temporal variations of the mean wind speed and direction. Therefore, the efficacy of these strategies does not inherently rely on dynamic actuation. In contrast, there is a relatively new branch of control strategies with working principles which inherently rely on the dynamic system response. The umbrella term for these strategies is active wake control (AWC). In order to define the time scale of AWC, $\tau_a$, a non-dimensional frequency known as the Strouhal number is convenient. It is defined as $St = f_a D/U_\infty$, where $f_a = 1/\tau_a$ is the actuation frequency. It is also noteworthy that the Strouhal number for an actuation frequency which matches the rotor's rotational speed $f_a = f_r = \Omega/(2\pi)$ is directly related to the tip-speed ratio as $St_r = \lambda/\pi$.

Active wake control strategies can target two different Strouhal regimes. The first regime is on the order of $\mathcal{O}(St_r = \lambda/\pi) \approx 3$ and includes strategies which aim at triggering/accelerating the tip vortex instability in the turbine near-wake [57, 58, 59, 60]. These strategies are motivated by the observation that the tip vortex system inhibits wake recovery [61] and thus its destabilisation could benefit the power production of downstream turbines.

The second regime concerns AWC actuation with lower frequencies of $\mathcal{O}(St) = [0.1, 0.5]$, which create large coherent structures in the wake with spatial scales on the order of the rotor diameter. As such, this kind of actuation aims to artificially force phenomena which are already naturally present in wind turbine wakes or forced by the incoming ABL turbulence [62]. An example is wake meandering, a term denoting the slow lateral oscillation of the wake due to large-scale turbulent structures in the incoming ABL flow and instabilities of the wake shear layer [63, 64]. By imposing an oscillatory yaw angle signal (which is not in response to a changing wind direction), the thrust coefficient is now time-dependent ac-

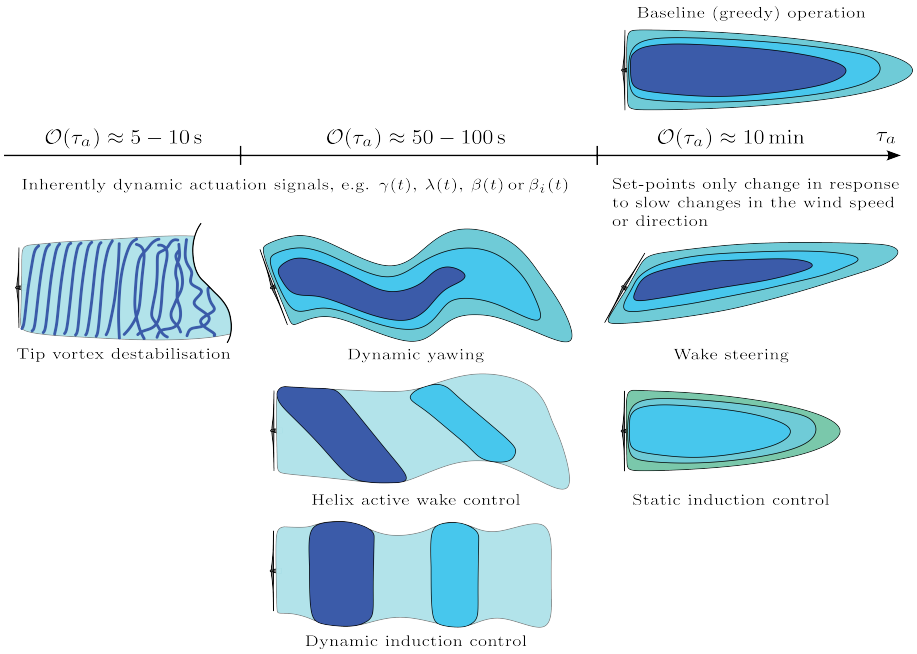


Figure 1.5: An overview of wind farm control strategies classified by the time scale of the actuation.

cording to $C_T(\lambda, \beta, \gamma(t))$. This WFFC strategy is called dynamic yawing and actively forces downstream wake meandering [65]; however, the power gains diminished in conditions with higher ambient turbulence intensity [66].

Even in the absence of atmospheric turbulence, studies conducted in water/wind tunnels with negligible to small inflow turbulence levels detected sustained low-frequency motions in the wake. These motions corresponded to the precession of a helical vortex [67] and were linked to an unstable helical mode predicted by linear stability analysis [68]. Linear stability analysis of wind turbine wakes revealed that both the zeroth (vanishing azimuthal dependence) and the first (azimuthal wavelength corresponds to full circle, i.e. 360°) instability modes of a wind turbine wake have significant growth potential, whereby their deliberate excitation offers the potential to enhance wake recovery through increased turbulent transport of mean kinetic energy into the wake [69].

The zeroth instability mode can be actively forced by applying a time-varying thrust force $C_T = f(\lambda(t), \beta(t), \gamma = 0^\circ)$ through actuation of the rotor speed and/or the collective pitch angle. This leads to the WFFC strategy of dynamic induction control (DIC). Adjoint optimisation allowed to identify DIC actuation signals which maximise wind power extraction by optimising the turbine-ABL interaction [70, 71]. Analysis of these actuation signals allowed to derive a simplified DIC strategy by parameterising the $C_T(t)$ variation with a sinusoid. As a result, optimising DIC does not require finding the optimal time series for $\lambda(t)$ and/or $\beta(t)$, but only selecting the optimal amplitude and frequency (in terms of $St$). Applying this parameterised DIC actuation leads to the periodic excitation of large-scale vortex rings in the wake, which increase wake recovery [72]. Due to this

flow feature, the parameterised DIC is also colloquially referred to as the pulse.

Modern wind turbines with individual pitch control (IPC) capabilities also allow for intentionally forcing the first instability mode. This requires the creation of an azimuthally non-uniform thrust distribution which additionally rotates as time progresses. In contrast to any of the aforementioned wind farm flow control (WFFC) strategies this requires individual blade pitch actuation $\beta_i(t)$ with $i \in \{1;2;3\}$ and hence $C_T = f(\lambda, \beta_i(t), \gamma = 0^\circ)$. In this manner, the first instability mode manifests itself as a helical coherent structure in the wake [73]. This WFFC strategy is called helix active wake control — also referred to as the helix approach or simply the helix. It is one of the newest proposed WFFC strategies and the subject of the present thesis.

### 1.2.2 Helix active wake control — Leveraging individual pitch actuation for wind farm flow control

What distinguishes helix active wake control from the other AWC strategies mentioned in the previous section is the fact that it involves both target Strouhal number regimes, namely $\mathcal{O}(St_r = \lambda/\pi) \approx 3$ and $St \approx [0.1, 0.5]$. As stated earlier, it forces the first instability mode of the wake in the frequency range $St \approx [0.1, 0.5]$. However, there is a distinct difference to e.g. DIC for which the frequency of the collective pitch actuation matches the forcing frequency of the wake. This does not hold true for the helix, which causes its own new set of modelling challenges as will become clear later in Section 1.3. To achieve the creation of the azimuthally non-uniform thrust distribution which rotates with $St \approx [0.1, 0.5]$ an individual pitch actuation on the order of the rotor's rotational speed, $\mathcal{O}(St_r = \lambda/\pi)$, is required. This can be intuitively understood by following a blade once around the full circle. At each azimuthal location, the blade pitch is slightly adjusted to create the non-uniform thrust and induction distribution. If this forced distribution were supposed to stand still, this would lead to an individual blade pitch actuation frequency of exactly $St_r = \lambda/\pi$. However, the non-uniform thrust distribution is supposed to rotate either clockwise (CW) or counter clockwise (CCW) with $St \approx [0.1, 0.5]$ and thus an individual blade needs to pitch slightly faster or slower than the rotational speed of the rotor with a non-dimensional frequency of $St_r \pm St = \lambda/\pi \pm [0.1, 0.5]$ (where plus and minus sign lead to CCW and CW helix, respectively). This concept for the helix actuation is visualised in Figure 1.6.

The initial work proposing the helix with its above-introduced actuation scheme showed its potential compared to the pulse using large-eddy simulation [73]. This finding led to several experimental and numerical follow-up studies, which further matured the control strategy. Several studies focused on the underlying working mechanism. Investigations based on large-eddy simulations using the lattice Boltzmann method (LBM) and synthetic turbulence as inflow showed that the increase in streamwise momentum available to a downstream turbine stems both from increased radial turbulent transport of mean kinetic energy (colloquially referred to as "wake mixing") and an increased lateral displacement of the wake. The former mechanism was shown to dominate in the near wake, whereas further downstream the latter became more dominant [74]. The displacement contribution was shown to be due to the induced velocities of large-scale coherent vortices, which resulted from streamwise vorticity created in the near wake as a result of the helix actuation. These vortex structures displace and deform the wake, and notably, their interaction with the wake swirl explains the different efficacies of CW and CCW helix [75]. The formation,

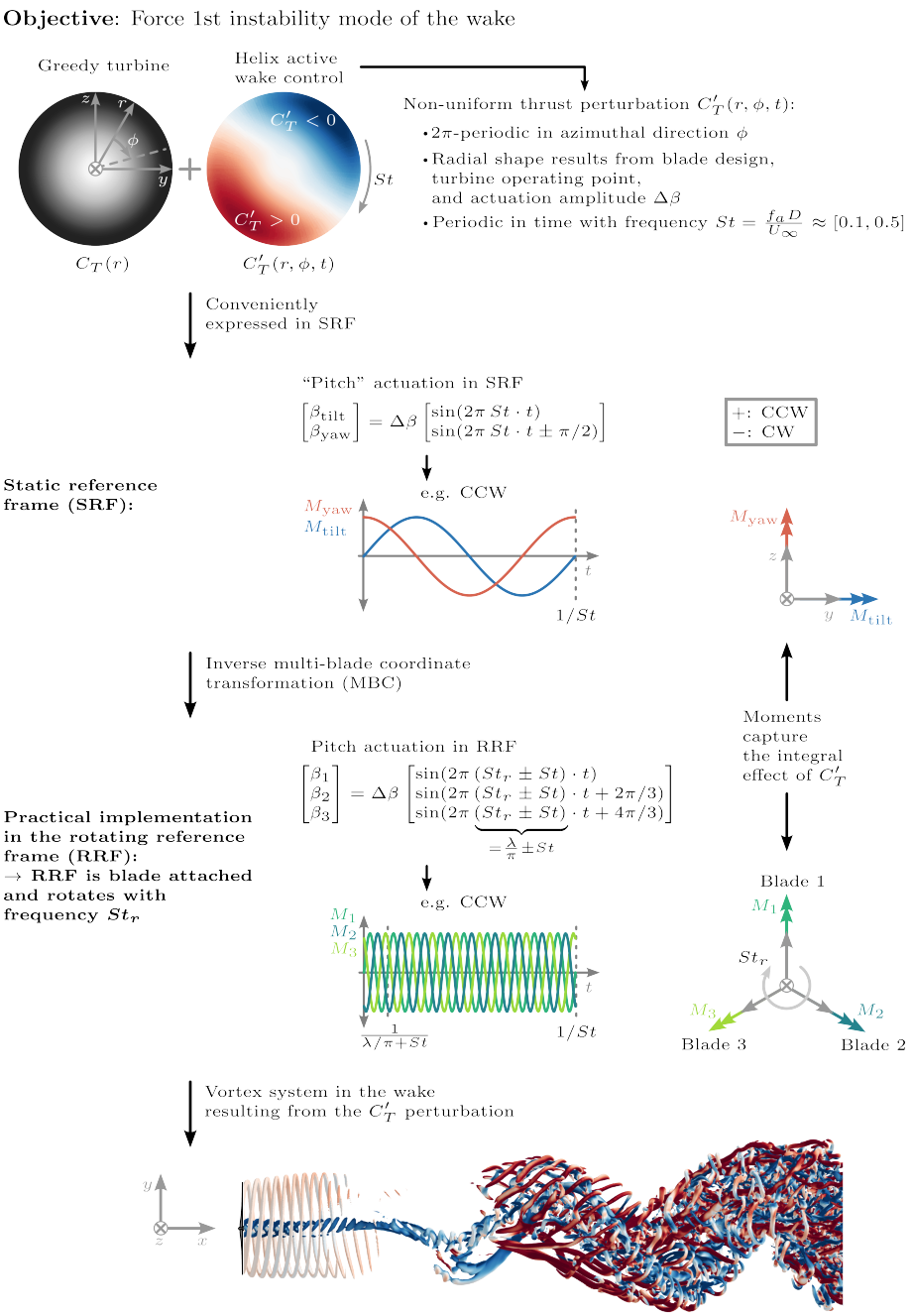


Figure 1.6: Formulation of the helix active wake control actuation signal in the static and rotating reference frames. The two reference frames are connected via the multi-blade coordinate transform (MBC) [76]. The bottom panel shows the resulting helical vortex system in the wake [77].

evolution and decay of the large-scale coherent vortices were further shown to contribute to the enhanced transport of mean kinetic energy into the wake. Further, CW and CCW actuation lead to stable and more unstable vortex system configurations, respectively [77]. The observed formation of a large-scale coherent vortex system can be seen as the manifestation of the underlying first instability mode of the system, which is triggered by the helix forcing at the rotor. As such, the frequency of the actuation (in terms of Strouhal number) has a great impact on the modal growth rate of the instability [69]. All the studies mentioned so far relied on numerical simulation using LES. However, the enhanced transport of mean kinetic energy has also been found experimentally. These experiments also noted an enhanced destabilisation of the tip vortices and an earlier onset of wake recovery [78, 79]. The latter study also examined a wide range of $St$ and found peaks of the total power extracted by the two-turbine wind farm around $St \approx 0.4$ (CW) and $St \approx 0.5$ (CCW).

The Strouhal number is one of the two required parameters to define the open-loop helix actuation signal, the other being the pitch amplitude. Their choice defines the power loss/gain and dynamic loading on the actuated and waked turbine. Hence, optimisation of these parameters is essential. An approach based on reinforcement learning (RL) achieved power gains of up to 7% for a three-turbine wind farm, but the control actions did not sustain the helix in the wake of the second turbine, and the computational effort was high due to the required long simulation times [80]. Computational optimisation of the actuation parameters remains expensive, given that, in principle, the single-harmonic helix actuation could be even extended to include higher harmonics [81]. For the single-harmonic case, a grid search across the feasible range of amplitudes and frequencies can be an alternative to RL. Such a search has been conducted with two scaled-down turbines in a wind tunnel with low levels of inflow turbulence ($\approx 2\%$) [82]. The experiments allow for mapping the entire search space, which would be computationally very expensive using numerical simulation. However, the power curve of the scaled-down turbines can cause different power loss characteristics in response to the helix actuation compared to utility-scale turbines, which influences the optimal pitch amplitude. Further, changing the inflow turbulence level or adding shear are expected to modify the optimal frequency given that they cause different mean flow wake profiles, which change the stability properties of the wake [69].

Identifying a setpoint $(\beta, St)$ which maximises power production is not sufficient, since the incurred load also needs to be considered. Aero-elastic simulations using synthetic turbulent inflow allow for the study of the load impact on the actuated turbine across a wide range of parameters. However, the load impact on the downstream turbine follows from wake interaction and needs computational fluid dynamics (CFD) solvers for modelling, which limits the studied operating points. Using both approaches, it is shown that for the helix, the upstream turbine's pitch bearing damage and flapwise blade root moments see the largest increase and are consequently the most important ones to consider in a load-power trade-off [83]. These two important load channels were shown to scale more strongly with an increase in pitch amplitude compared to frequency, allowing some tuning of the latter. In addition, the tower top fore-aft and tower torsional moments were also shown to see non-negligible increases in load [84]. Using measurement-derived large-eddy simulations of two-turbine wind farms, it was also shown that damage equiva-

1

lent load (DEL) increases of the helix are in general significantly larger compared to wake steering. In boundary layers with low levels of veer and shear, the helix compensates with larger power gains; however, in particular for larger levels of veer, wake steering is superior both in terms of power gain and DEL [85]. Based on the same set of LES cases, it was shown that veer impacts the effectiveness of the different major working mechanisms underlying the different WFFC strategies. Wake steering achieved the increase in mean kinetic energy in the wake mostly via mean advection, which proved to be more robust to increased wake skewing due to veered inflow compared to enhancing the turbulent transport of mean kinetic energy as the helix aims to do [86].

While most work on the helix focused on its working mechanism, parameter space, power/load impact and dependence on ABL conditions, a few works have also already moved towards reduced order modelling, where both data-driven approaches using dynamic mode decomposition [87] or spectral proper orthogonal decomposition [88] and approaches based on the governing equations (linearised perturbation NSE coupled to RANS) [89] are pursued. Apart from reduced order modelling which is necessary for further integration of the helix into the wind farm optimisation process (e.g. AEP optimisation), there are also efforts to extend the application of the helix past the first row of turbines in a farm via synchronisation [74, 90] and to implement the helix on floating wind turbines [91, 92], which unlock new offshore wind resources in deeper waters.

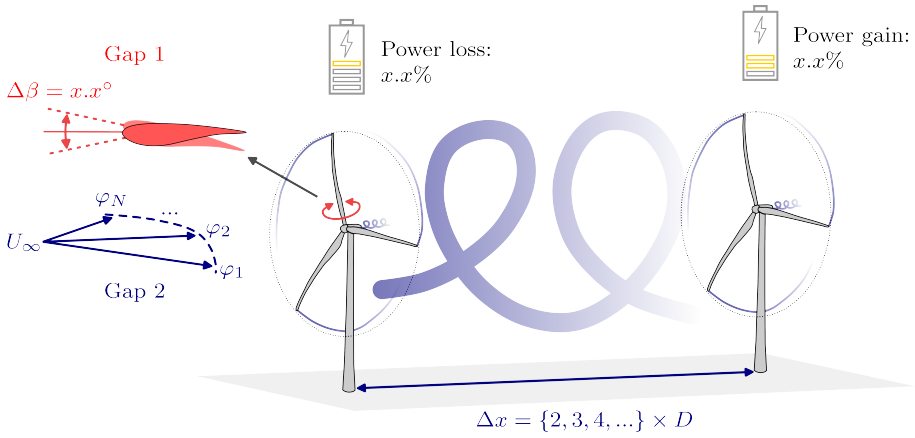


Figure 1.7: Identified research gaps for helix active wake control. Sensitivity of power gains to the pitch actuation amplitude (gap 1) and robustness to wind direction changes deviating from full wake overlap (gap 2).

From the outline of the current state-of-the-art, we note two gaps for helix active wake control (also see Figure 1.7):

1. The impact of varying the pitch amplitude for helix active wake control on the turbine response of the actuated and waked turbine in terms of power and DEL has not been assessed for ABL turbulence. Previous studies either considered only a single value for the amplitude or used scaled-down wind turbine models in wind tunnel flows with negligible shear.

2. The potential of helix active wake control compared to established methods like wake steering in terms of operating conditions (wake overlap and turbine spacing) and robustness to wind direction changes is still unclear.

To summarise, we have so far explored why wind turbines are clustered into wind farms; that clustering causes efficiency losses; and that a range of WFFC strategies have been developed to reduce these losses. We further identified two research gaps for the new WFFC strategy of helix active wake control. In the following, we will now focus on the associated modelling challenge posed by this control strategy.

## 1.3 The modelling challenge — A constant balancing act between fidelity and cost

In this section, we are concerned with the necessary modelling strategies to study WFFC strategies in general and more specifically helix active wake control. Section 1.1.1 already provided an overview of the wide range of scales impacting wind farm performance, i.e. scales reaching from the airfoil up to atmospheric flow features on the mesoscale. Hence, when trying to alter wind farm performance with wind farm flow control, one is presented with a formidable modelling challenge. Before making any modelling choices, it is helpful to define the requirements for model selection/development from a WFFC-oriented point of view:

- The performance of any WFFC depends on the atmospheric state, which is forced by the current mesoscale conditions and within which the turbine wakes evolve. An accurate model should either directly resolve or model effects like temperature stratification, turbulence, surface topology and the directional and magnitude change of the driving background pressure gradient.

- The performance of any WFFC strategy ultimately depends on the turbine response. In particular, one needs accurate power and load estimates for all, both the actuated and the affected, turbines in the farm in order to judge the efficacy of the applied control. Those depend on the turbine's control system and its aero-elastic behaviour.

These requirements treat the task of choosing an appropriate model for WFFC only as a matter of physical fidelity. However, WFFC-oriented modelling is done for an objective, and this objective defines a maximum acceptable computational cost. Hence, a modelling choice needs to balance physical fidelity with computational cost depending on the objective. Models with low fidelity are chosen when a single model evaluation should not exceed the order of seconds on a single CPU [93], e.g. where the objective involves optimising the wind farm's AEP with WFFC [94]. Higher fidelity is needed when optimisation of steady-state setpoints for WFFC is not sufficient, as the objective is to find an optimal dynamic control actuation accounting, e.g. for a time-varying inflow wind direction. For these applications, models need to capture the temporal evolution and propagation of wakes in a wind farm. An example is the FLORIDyn model [95], which has been employed for closed-loop model-predictive WFFC [96].

Even higher physical fidelity is needed when the objective is to study the underlying working mechanisms of WFFC strategies and to generate data which can be subsequently used for the development and validation of lower fidelity models as they were described above. Given their computational cost, this kind of model might only allow for a number of evaluations on the order of $\mathcal{O}(\text{evaluations}) \approx 10$. In this thesis, we are concerned with this class of models to address the research gaps for helix active wake control outlined at the end of Section 1.2.2. However, even within this class of models, the cost-fidelity trade-off remains since the physical fidelity requirements still span all four major scales introduced in Section 1.1.1, namely the airfoil, the turbine, the farm and the mesoscale.

A physically uncompromising numerical modelling approach would then need to resolve the smallest spatial and temporal processes on the airfoil scale while considering spatial domain sizes and time horizons large enough to account for the atmospheric mesoscale phenomena. In a very rough manner, one could estimate the degrees of freedom of such a discretised system as follows. When the discretisation of the airfoil scale requires $N^3$ spatial and another $N$ temporal points, the degrees of freedom for resolving the smallest scale are DOF = $N^4$ for a given resolution deemed sufficient. When additionally, the temporal and spatial scales of the turbine scale should be captured, this would require an increase of the spatial domain extent and simulated time horizon by at least one order of magnitude, i.e. the degrees of freedom would increase by at least a factor of $(10*10*10)*10 = 10^4$. However, the resolution $N$ is still constrained by the airfoil scale and thus the total number of degrees of freedom would be DOF = $N^4 * 10^4$. When further including the wind farm and mesoscale, one would obtain DOF = $N^4 * 10^4 * 10^4 * 10^4 = N^4 * 10^{12}$. Assuming a required resolution of $N \approx 100$ for the airfoil scale this results in DOF = $10^8 * 10^{12} = 10^{20}$. For reference, this might exceed the order of the largest computational fluid dynamics simulations of turbulence conducted at the time of writing this thesis (see e.g. [97]). This very rough estimate should simply illustrate why even "high-fidelity" WFFC-oriented modelling with practical relevance needs to make a choice of which scales and physical mechanisms are (a) directly resolved; (b) represented by an analytical/empirical/data-driven model; or (c) simply neglected. The particular choices made with respect to (a), (b) and (c) are described in the following two subsections for the modelling of the atmospheric/wake flow and the wind turbine, respectively.

### 1.3.1 Large-eddy simulation — Modelling the atmospheric flow

The flow physics relevant for wind energy concern the atmospheric flow and the therein embedded aerodynamic flow (fluid-body interaction, i.e. the flow around the turbine blade/tower with features like the airfoil boundary layer, the tip-hub vortex system and the turbine wake). For the latter, the fidelity is not only determined by the flow model, but notably also the fidelity of the turbine model, which will be discussed in the subsequent Subsection 1.3.2.

The atmospheric boundary layer (ABL) is the lowest layer of the atmosphere, which is nearest to the earth's surface [98], featuring an almost continuous presence of three-dimensional turbulence both in time and space [23]. To model this atmospheric turbulence, the highest fidelity of modelling needs to stay close to the governing equations. Within the framework of continuum mechanics and for a Newtonian fluid like air, this leads to the Navier-Stokes equations (NSE) as the set of underlying governing equations [22].

For the numerical modelling of the NSE with computational fluid dynamics (CFD) the candidates are simulation of the (unsteady) Reynolds-averaged Navier–Stokes equations (RANS), large-eddy simulation (LES) or direct numerical simulation (DNS). RANS modelling only considers the mean NSE. However, since we are interested in dynamics for helix active wake control, this would be too restrictive. Unsteady RANS modelling only resolves the low-frequency modes of the flow using temporal filtering and models the remaining turbulent fluctuations. As pointed out previously in Subsection 1.2.2, enhancing turbulent transport is one of the important working mechanisms for helix active wake control. An unsteady RANS approach would still mostly model and not resolve this turbulent transport, which is undesirable for our purpose. Hence, the candidate chosen in this work is large-eddy simulation (LES). An approach based on LES resolves all but the smallest scales of the turbulent flow by employing spatial filtering of the governing equations. The impact of the unresolved small scales on the resolved part of the turbulent spectrum is modelled with subgrid-scale models [99]. LES thus finds a balance between directly resolving most of the flow dynamics and limiting the computational burden compared to DNS.

LES has been fundamental for numerical modelling of wind farms. Since the primary works done for infinite wind farms [100, 101], LES has enabled many advancement for the study of wind farm flow, such as studying the impact of atmospheric stability and the Coriolis force on wind turbine wakes [30, 102]; the impact of boundary layer height and gravity waves on wind farm power extraction [31, 38]; the formation of wakes behind entire wind farms (in contrast to the individual wind turbine wakes within the farm) [103]; and attempts to actively control them [104]. LES has been also instrumental for the development and evaluation of WFFC strategies [45]. It, for example, played an important role in the evaluation of wake steering [105] and helix active wake control [73]. LES has also been combined with an optimal control framework to improve power extraction [70] and to identify optimal actuation signals for dynamic induction and wake steering WFFC [71, 66]. Furthermore, LES allows to test optimal closed-loop controllers for WFFC, e.g. for wake steering [106, 107, 96].

To this end, the wind energy fluid mechanics community has developed and maintains a range of state-of-the-art LES codes with a special focus on modelling of wind farms in the ABL: Examples are SOWFA [108], TOSCA [109], EllipSys3D [110, 111], AMR-Wind [112], Nalu-Wind [113], SP-Wind [100, 70], WiRE [114] and VirtualFluids [115]. These codes are well suited to study WFFC strategies in idealised statistically quasi-steady ABLs. They then enable to discern and single out the effect of a specific parameter, like boundary layer height or stratification. As such, these codes are also very well suited to generate large data sets of high-fidelity data for the development of lower-fidelity models. However, WFFC strategies ultimately need to show their benefit in realistic operating conditions where the mean ABL state varies in time and space and hence its energy spectrum contains additional contributions from low frequencies and long wavelengths, which might not be captured by the codes above [25]. These variations due to the diurnal cycle [116] and the mesoscale forcing [117] lead to transient ABLs which need to be accounted for when developing controllers for WFFC since they could also affect the selection of the most suitable control strategy (see the second identified gap in Subsection 1.2.2).

As more physical scales are essential for the modelling of WFFC, this calls for a new

approach to model development, which was also formulated in a more general sense for the entire wind energy community by Sanz Rodrigo et al. [25]. They noted that in the past, each of the major scales relevant for wind energy (see Section 1.1.1) was commonly studied by separate scientific communities, e.g. meteorologists, wind engineers, and aerodynamicists. This led, according to them, to

> *"... each one [community] developing their own community models with little interaction with the neighbouring ones (silo effect). The next generation of wind energy models will necessarily look for an integrated approach that can produce a more comprehensive characterisation of the modelling system."*

In this spirit, there is benefit in bridging the gap between LES codes designed for idealised quasi-stationary ABLs as introduced above and meteorological LES codes, which come with more extensive modelling capabilities for atmospheric physics and mesoscale to microscale coupling. Such codes are WRF-LES [118], PALM [119], FastEDDY [120] and GRASP/ASPIRE[1] [121, 122, 123]. For example, ASPIRE features the anelastic approximation and models not only the transport of momentum, but also heat and moisture. As such, it includes a radiation balance, cloud formation and precipitation, where all these processes in turn drive mesoscale fluctuations. The adaptation of open boundary conditions further allows for prescribing large-scale conditions from NWP models with spatial and temporal variation for all prognostic variables in the LES.

### 1.3.2 The actuator line model — Modelling the wind turbine

One approach to bridging the gap between the more idealised wind energy and the meteorological LES codes is to transfer the advanced turbine modelling capabilities from the former to the latter. Offshore wind turbines need to sustain static, periodic, transient and stochastic loading in response to gravity, wind, waves and controller actions. As such, the fields of aerodynamics, hydrodynamics, structural dynamics and control all need to be considered to model the dynamics of the turbine. To this end, a range of aero-hydro-servo-elastic codes have been developed [124], where popular examples are OpenFAST [125] or HAWC2 [126]. These codes also provide interfaces to include state-of-the-art reference controllers for both greedy turbine control, but also AWC strategies [127]. When used in a stand-alone mode, these models usually use synthetic turbulence as inflow, e.g. generated with tools like TurbSim [128]. They allow the calculation of the ultimate and fatigue loads (the latter, e.g. in terms of DELs) for all major turbine components and assess their sensitivity with respect to the inflow conditions [129, 130]. Hence, these aero-hydro-servo-elastic codes fulfil the second requirement defined for high fidelity WFFC modelling at the beginning of Section 1.3.

To address the first requirement, we outlined the need for LES in the previous subsection. Consequently, turbine models need to interface the flow computed with LES. To this end, most models are so-called actuator models; however, the different instances feature very different degrees of abstraction (see Figure 1.8). Actuator models do not attempt to directly capture the impermeable surfaces of the solid bodies (blades, tower, ...) and associated flow features like boundary layers. They instead mimic the effect of the solid bodies by computing discrete actuator forces, which are then imposed as body forces onto the

[1]The code was renamed from GRASP to ASPIRE. Note that Chapter 4 still uses the legacy name.

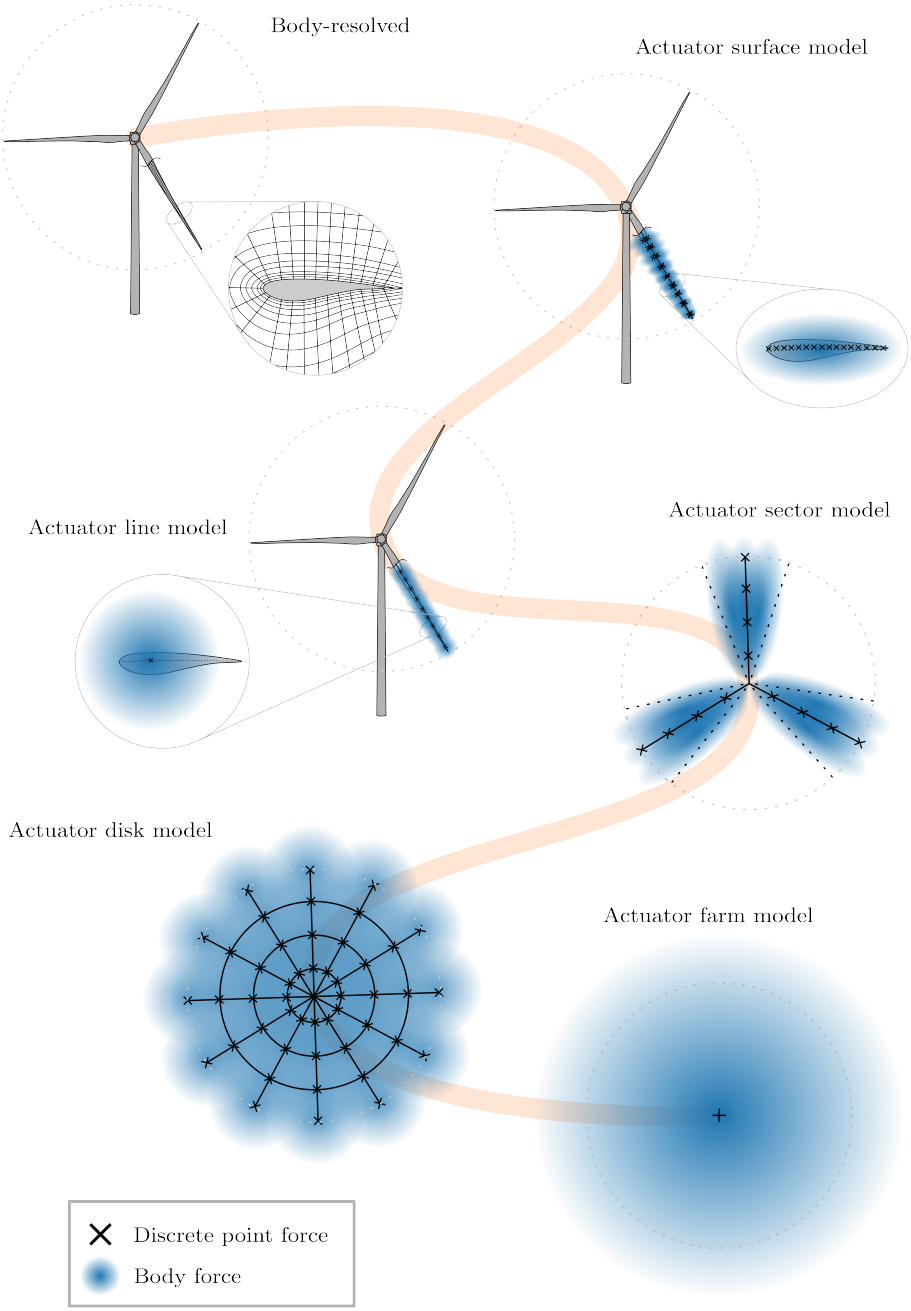


Figure 1.8: Fidelity hierarchy of wind turbine models suitable for representing turbines in large-eddy simulations.

flow via a projection using regularisation kernels. The detail considered in the computation of the discrete actuator forces, the number of required actuator points and the shape of the regularisation kernel lead to varying fidelity and LES grid resolution requirements, which in turn determine the computational cost [131].

Actuator farm models are a new development. They consider a single actuator point to model the turbine, which allows the use of very coarse grids, which makes them suitable for the study of wakes behind entire wind farms [132, 133]. In turn, the concept of the actuator disk model (ADM) routes back to Froude in the nineteenth century [134] and has been applied for wind turbine modelling early on [135]. One of the first combinations of the ADM with LES was done by [136], and as the name suggests, actuator points are distributed across the rotor swept disk. To determine the magnitude of the discrete actuator forces, the ADM approaches either rely on the integral thrust coefficient [136] or more detailed blade element information in terms of tabulated airfoil data for the lift and drag coefficients [114]. Airfoil specific tabulated lift and drag coefficients can also be used as the basis for the actuator line model (ALM) [137]. It considers actuator points distributed along lines representing the three turbine blades. As such, the ALM naturally captures the rotor footprint on the flow. There are also modifications to the ALM to either decrease or increase the fidelity. The former is done by distributing the actuator forces also in the azimuthal direction within a sector around the blade, which leads to the actuator sector model and relaxes the maximum allowed time step size [138]. The latter is done by extending the ALM such that the chordwise direction of the airfoil is represented by multiple rather than a single actuator point, which leads to the actuator surface model [139, 140]. Lastly, the turbine can also be directly represented by body-resolving approaches instead of employing actuator concepts [141, 142, 113].

As stressed earlier on even high fidelity modelling for WFFC needs to find a balance between physical detail and computational cost. Since we are in this thesis concerned with helix active wake control — which relies on individual blade pitch actuation — resolving the footprint of individual blades is important. While there is potential to mimic the non-uniform thrust distribution induced by the helix via a non-uniform ADM approach [143, 144, 145], this choice entails further simplifying assumptions for the unsteady aerodynamics on the airfoil/blade scale. Hence, for modelling helix active wake control in LES the ALM balances physical detail with cost and is the model of choice. It allows for a direct implementation of the pitch actuation signals and a coupling with the aforementioned aero-hydro-servo-elastic codes [108]. Further, it can be used to assess the load impact of wakes subject to helix control on downstream turbines [83], and it is compatible with synchronisation controllers, which extend the helix control to downstream turbines [90]. However, it is known that for practical applications like WFFC the width of the regularisation kernel employed for the ALM exceeds the optimal value by approximately an order of magnitude [146]. This is the case since the kernel width is constrained by LES grid resolution. However, large sub-optimal kernel widths lead to the overprediction of the actuator forces and thus the turbine power and thrust [147]. To this end, ALM corrections have been developed to still obtain accurate force predictions on coarser grids [148, 149, 150, 151, 152, 153]. These different corrections vary as they use different degrees of *ad-hoc* modelling, empirical assumptions or solutions to simplified versions of the governing equations. A comparison of two of the aforementioned corrections, namely [149]

and [150], showed that they are both effective in improving the accuracy of coarse grid ALM-LES results [154].

The introduced ALM corrections either directly rely on quasi-steady assumptions or neglect the spanwise shed vorticity, which would appear for unsteady blade loading. While unsteadiness is already inherently caused by the turbulent atmospheric flow, the structural deformations and operation of the rotor in veered/sheared flow, the use of unsteady actuation for WFFC strategies like helix active wake control motivates us to investigate the general ability and bounds of applicability of the ALM for unsteady aerodynamics. To quantify the degree of unsteadiness, one can make use of the reduced frequency $k = \pi f c/U$, which relates the local advection time scale of the flow ($c/U$) to the time scale of the actuation ($1/f$) [155]. In the case of a wind turbine blade, the chord, $c$, and the velocity, $U$, are functions of the span. Considering a realistic application of helix active wake control, we choose a CCW helix actuation with $St = 0.3$ at an incoming wind speed of $U_\infty = 8$ m/s. The resulting reduced frequency along the blade span, $k = \pi f_{\text{helix}} c(r)/U(r)$, is shown in Figure 1.9 for the NREL 5-MW ($R = 63$ m) and the IEA 15-MW ($R = 120$ m) turbines. Blade inwards the reduced frequencies exceed values of $k = 0.05$ and $k = 0.2$ beyond which the degree of unsteadiness is considered as unsteady and highly unsteady, respectively [155]. This motivates us to investigate how well the unsteady loading at these reduced frequencies is captured by coarse grid ALM-LES, in particular given that also higher harmonics of $f_{\text{helix}}$ will appear in the system response.

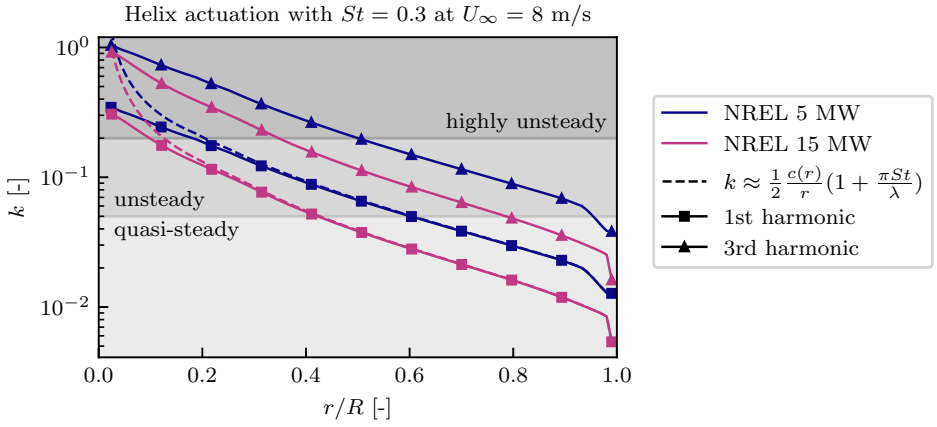


Figure 1.9: Reduced frequencies $k$ along the blade span of the NREL 5-MW and the IEA 15-MW turbines for actuation with the CCW helix at a Strouhal number of $St = 0.3$ and inflow wind speed of $U_\infty = 8$ m/s. The spanwise location $r$ is non-dimensionalised with the respective rotor radius $R$.

From the above outlined state-of-the-art for WFFC-oriented modelling, it is found that simulation environments which combine turbine simulations at "blade footprint" fidelity level with real weather atmospheric flow at affordable cost are scarce. Such capabilities could enable numerical tests of wind farm flow control leveraging individual blade pitch actuation in realistic operating conditions. In particular, the following two gaps are identified:

3. There is a trade-off between the fidelity of the turbine modelling and the inclusion of phenomena from the wind farm and mesoscale. There is a lack of tools to simulate at the intersection of aero-hydro-servo-elastic turbine models coupled to mesoscale-driven atmospheric boundary layer flow via the actuator line model (right-hand side of Figure 1.10).

4. The actuator line model is used to model unsteady actuation for helix active wake control. Especially on coarser LES grids, it is unknown how strongly the unsteady aerodynamic response predicted by the ALM is impacted and if corrections are necessary (left-hand side of Figure 1.10).

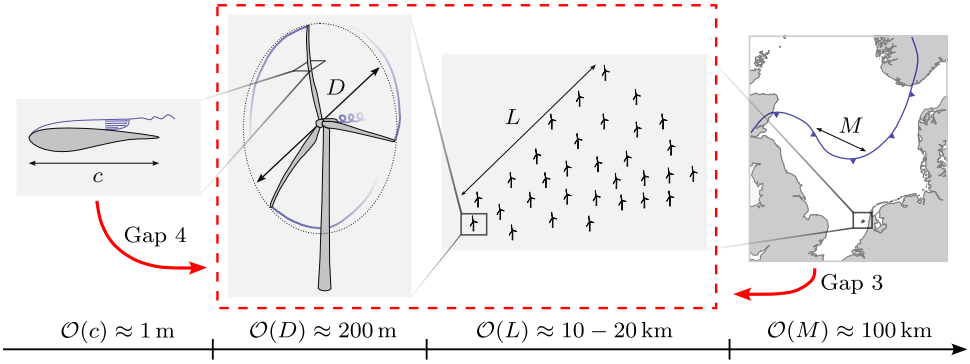


Figure 1.10: The range of characteristic scales impacting wind farm performance and their relation to the identified gaps for WFFC in general (gap 3) and helix active wake control specifically (gap 4).

## 1.4 Thesis objective — Joint-development of helix active wake control and tailored actuator line modelling

Wind farm flow control based on wake steering has already matured to an industrially viable option[2]. However, dynamic control strategies aiming at wake mitigation have emerged as a new alternative and are still relatively unexplored, in particular strategies leveraging individual pitch actuation like helix active wake control. In this thesis, the goal is to further assess this new control strategy and, alongside further develop the corresponding modelling strategies in order to address the gaps identified in Sections 1.2.2 and 1.3.2. To this end, the following overarching objective is formulated:

**Thesis Objective:** Assess the performance of helix active wake control in quasi-steady atmospheric boundary layers and develop actuator line model capabilities for its study in coarse grid real weather large-eddy simulations.

[2] https://www.siemensgamesa.com/global/en/home/press-releases/191126-siemens-gamesa-wake-adapt-en.html, Accessed 19/06/2025

### 1.4.1 Contributions

The potential power gain and the corresponding structural load impact of the helix have so far been mainly studied separately. Loads were assessed with aero-hydro-servo-elastic simulations relying on synthetically generated turbulent inflow and focused on the actuated turbine. The power gain was then studied separately using large-eddy simulations of two turbine wind farms. Further, the control input parameters — the amplitude and frequency — were not studied across a wide range. This leads to the first contribution of this thesis:

> **Contribution I:** Quantify the sensitivity of helix active wake control to the pitch amplitude control input in terms of the trade-off between wind farm power gain and structural turbine loading in a quasi-steady atmospheric boundary layer.

As a newly proposed control strategy, it is important to benchmark helix active wake control with respect to the established standard of wake steering. Here, the choice of the more performant control strategy can depend on the position of the wind turbine, i.e. its downstream distance and lateral offset. In addition, the robustness of the power gain at a given operating point with respect to wind direction changes influences the selection of the control strategy. The resulting contribution reads as:

> **Contribution II:** Compare the robustness of power gains achieved with helix active wake control to variations in turbine spacing and wake overlap with static wake steering.

The two former contributions consider small two-turbine wind farms operating in quasi-steady atmospheric boundary layers, i.e. ABLs with constant mean wind speed and direction. To bring wind farm control strategies to practice, their efficacy should also be demonstrated in conditions more closely resembling real-world conditions where the "mean" wind speed and direction are time varying. To this end, large-eddy simulations need the capability to be driven with mesoscale data. Furthermore, as domain sizes grow to accommodate larger wind farms while the grid size is still constrained by the fact that the actuator line model is needed to model the helix's individual pitch control actuation, the degrees of freedom of the resulting simulation can become computationally limiting or even prohibitive. As a remedy, corrections for the actuator line are needed to allow for the use of coarser LES grids while limiting the actuator line modelling error. Tackling these objectives leads to the third contribution:

> **Contribution III:** Develop a simulation environment to enable large-eddy simulations of helix active wake control in realistic weather scenarios, which ensures an accurate turbine response also on coarse grids.

Existing corrections for the actuator line model as implemented for the third contribution do not consider all vorticity components contributing to the unsteady response. Unsteady phenomena are abundant in wind energy, e.g. the turbulent inflow, shear, structural deformation or control actions. Here we take the use of an ALM with correction to model unsteady individual pitch control as the opportunity to study the effect of the so far neglected unsteady spanwise vorticity component on the unsteady aerodynamic response. Thus, the final contribution of this thesis is:

1

> **Contribution IV:** Derive a semi-analytical model, which quantifies the ability of the actuator line model to capture unsteady aerodynamic effects and identify bounds for its validity.

### 1.4.2 Thesis outline

The four introduced contributions are each addressed with a dedicated chapter. Each chapter consists of a previously published paper with its own introduction to the relevant literature, presentation of the underlying methods and specific conclusions. Thus, each chapter can also be read individually. The paper introductions reflect the state-of-the-art at the time of their writing, which might partially lack some of the newest literature presented in this thesis introduction.

**Chapter 2** assesses the performance of helix active wake control using large-eddy simulations of a two-turbine wind farm operating in a conventionally neutral boundary layer. The turbines are modelled with an aero-hydro-servo-elastic solver coupled to the flow solver via an actuator line model. The upstream turbine is actuated with pitch amplitudes of $1^\circ, 2^\circ, 3^\circ, 4^\circ$ and $6^\circ$. The power loss of the actuated turbine is related to the gain downstream. The actuation-induced increase in structural loading is quantified in terms of the damage equivalent load (DEL) of the main turbine components, and spectra of the blade root bending moments show the footprint of the control in the frequency domain. Analysis of the angle of attack at the actuated turbine provides insight into the cause of the upstream power loss.

> Chapter 2 is based on the following publication:
> E. Taschner, A. van Vondelen, R. Verzijlbergh, and J. W. van Wingerden. "On the performance of the helix wind farm control approach in the conventionally neutral atmospheric boundary layer". In: *Journal of Physics: Conference Series* 2505.1 (2023), p. 012006

**Chapter 3** compares static wake steering with helix active wake control using large-eddy simulations of a conventionally neutral boundary layer. A setup is developed which allows for estimating the control-specific power gain of a two-turbine wind farm across all relevant turbine spacings and levels of wake overlap with a single LES run. Thus, the number of simulations equals the number of studied control setpoints and makes the use of LES computationally feasible. The results allow for the selection of a suitable control strategy depending on the operating conditions and provide insight into the robustness of the control in case of wind direction variations.

> Chapter 3 is based on the following publication:
> E. Taschner, M. Becker, R. Verzijlbergh, and J. W. van Wingerden. "Comparison of helix and wake steering control for varying turbine spacing and wind direction". In: *Journal of Physics: Conference Series* 2767.3 (2024), p. 032023

**Chapter 4** develops a new simulation environment to allow for the study of wind farm flow control strategies based on individual pitch control in real weather conditions. To this end, a large-eddy simulation solver tailored for meteorological applications, including forcing with site-specific mesoscale data, is coupled to a multi-physics solver computing

the aero-hydro-servo-elastic turbine response. The coupling is achieved via an actuator line model and incorporates a correction for the use on coarse LES grids. The coupling is verified for a single turbine case with laminar inflow using data from four other commonly employed research LES solvers.

> Chapter 4 is based on the following publication:
> E. Taschner, M. Folkersma, L. A. Martínez-Tossas, R. Verzijlbergh, and J. W. van Wingerden. "A new coupling of a GPU-resident large-eddy simulation code with a multiphysics wind turbine simulation tool". In: *Wind Energy* 27.11 (2024), pp. 1152–1172

**Chapter 5** derives a semi-analytical model for the two-dimensional unsteady actuator line, i.e. an airfoil represented by a Gaussian body force. The model is formulated both in the time and the frequency domain and efficiently computes the unsteady loading without the need for performing actual LES. The model is verified with ALM-LES, and the impact of a range of actuation frequencies and signal types on the unsteady loading is studied. Finally, validation with Theodorsen theory and numerical/experimental reference data allows us to establish bounds of validity for the use of the ALM when modelling unsteady aerodynamics.

> Chapter 5 is based on the following publication:
> E. Taschner, G. Deskos, M. B. Kuhn, J. W. van Wingerden, and L. A. Martínez-Tossas. "Unsteady aerodynamic loads on pitching airfoils represented by Gaussian body force distributions". In: *Accepted for publication in Journal of Fluid Mechanics* (2025)

**Chapter 6** draws the overall conclusions as they pertain to the thesis objective and presents recommendations for future work.

# 2

# On the performance of the helix wind farm control approach in the conventionally neutral atmospheric boundary layer

*The performance of wind farms can substantially increase when their individual turbines deviate from their own greedy control strategy and instead also take into account downstream turbines operating in the wake. The helix approach is a recently introduced dynamic wind farm control strategy that tackles this issue by leveraging individual pitch control to accelerate wake recovery. Its effective implementation requires detailed knowledge about the scaling between control input and the resulting power gain and turbine loading across the farm. In the present work, this scaling is explored by means of large-eddy simulation of a two-turbine farm in the conventionally neutral atmospheric boundary layer. A parameter sweep for the amplitude of the helix is performed, showing a monotonic increase of the farm's power output with increasing pitch amplitude within the considered range of zero to six degrees. The scaling of the power gain suggests that a threshold amplitude should be exceeded for effective speed-up of the wake recovery, whereas the damage equivalent loads computed for the turbines indicate an upper limit for the amplitude despite increasing power gains.*

This chapter is based on the following publication:

[156] E. Taschner, A. van Vondelen, R. Verzijlbergh, and J. W. van Wingerden. "On the performance of the helix wind farm control approach in the conventionally neutral atmospheric boundary layer". In: *Journal of Physics: Conference Series* 2505.1 (2023), p. 012006

The LES input files and numerical data underlying the figures in this chapter can be downloaded from: `https://doi.org/10.4121/1232217b-eceb-481e-a560-c03423287bf2.v1`.

## 2.1 Introduction

Wind turbines are commonly clustered in farms to allow for cost-effective power extraction, as e.g. cabling, maintenance, and installation costs can be shared. However, this clustering implies an inherent coupling between turbines due to wake interaction, which renders conventional control approaches optimising isolated turbine performance suboptimal on the wind farm level. As a result, wind farm control approaches have been developed which seek to optimise the overall power extraction and turbine loading across the entire farm [45]. Recently, especially dynamic control approaches have gained attention, including dynamic induction control (DIC). Actuation signals for DIC were developed leveraging optimal control combined with large-eddy simulations (LES) [71], its physical working mechanism was studied in [160], and steps towards the practical implementation were undertaken using simplified parameterised signals [72]. These works demonstrated increased wake recovery and overall power extraction. However, significant thrust and power fluctuations were found, too [161].

To mitigate these variations, a new dynamic control approach using individual pitch control (IPC) called the helix was introduced and benchmarked against DIC in [73]. This proof of concept showed promising gains in power extraction for the helix studying a two-turbine wind farm using LES. Nevertheless, there are still knowledge gaps regarding the impact of the helix on the flow physics in the wake, the performance in different atmospheric boundary layer (ABL) conditions and the optimal actuation signal in terms of amplitude and frequency (usually expressed as Strouhal number $St$) [51]. Attempts to optimise the helix signal are limited. For the initial proof of concept, the frequency is derived from DIC as $St = 0.25$, and the influence of the amplitude is analysed for two levels [73]. A study for a single amplitude, but four different Strouhal numbers suggested that the optimal frequency might deviate from $St = 0.25$, although only considering uniform inflow [162]. In [80] reinforcement learning was applied to optimize the helix amplitude for a three-turbine wind farm ($St = 0.25$) reporting an overall power gain of 6.8%.

Looking beyond the sole optimisation of the power gain, further investigations were conducted to evaluate the impact of the helix approach on turbine components. The results showed that DIC had a significant effect on the turbine tower compared to the helix approach, while the difference between both methods on the blades was minimal [83]. Another work performed a more comprehensive sensitivity analysis and found that the tower fore-aft, blade flapwise, and pitch bearing are particularly sensitive to a high-amplitude helix actuation signal, while other components are less affected [84]. Since the performance increase of the helix approach becomes more significant with amplitude, a balance should be found between the increased load and power gains. As of yet, no study has explicitly examined the amplitude scaling of power increase versus load increase for a two-turbine setup.

The objective of the present work is, therefore, to obtain a more detailed insight into the amplitude scaling by conducting a parameter sweep using LES of a two-turbine farm. In terms of atmospheric conditions, we focus on the neutral ABL and in particular its most common type in the atmosphere: the conventionally neutral atmospheric boundary layer (CNBL) [163]. This study thereby informs future research on the optimal actuation signal and provides a baseline for the assessment of the amplitude-power gain scaling in different atmospheric conditions.

## 2.2 Methodology

This section outlines the methodology to simulate the flow in the ABL and the wind turbine dynamics. Further, the helix controller and the approach for the load analysis are introduced.



### 2.2.1 AMR-Wind and OpenFAST

The flow in the ABL is modelled using the LES code AMR-Wind [112]. AMR-Wind solves the filtered incompressible Navier-Stokes equations where the subgrid-scale stresses are modelled using the kinetic energy one-equation turbulence model [164]. The code uses the Boussinesq approximation in order to include the effect of density gradients on buoyancy. At the lower boundary, a wall shear stress model using Monin-Obukhov similarity theory is employed following [164]. At the top of the domain, a slip wall is specified for the velocity and a fixed gradient for the potential temperature. AMR-Wind solves the governing equations on Cartesian block-structured grids, which can be locally refined either statically or dynamically. More details on the numerical implementation of AMR-Wind can be found in the work of [165], which examined the stable northeastern United States marine boundary layer. AMR-Wind further provides a coupling to OpenFAST, which is used in this work and was previously employed to evaluate the performance of wind farms operating in low-level jet events [166].

OpenFAST is a multi-physics wind turbine simulation tool capable of simulating the entire wind turbine including its structural, hydro-, aero- and control dynamics [125]. In this study, the OpenFAST model for the fixed-bottom monopile variant of the IEA-15 MW turbine is employed [49], which is representative of the next generation of offshore turbines. OpenFAST is coupled to the LES simulation using a standard actuator line model (ALM) [137].

### 2.2.2 Turbine controller

The control actions are implemented using the reference open-source controller (ROSCO), where the IPC routine of ROSCO is extended to include the additional pitch actuation required for the helix [127]. The key idea of the helix is to impose slowly periodically varying tilt and yaw moments on the turbine, thereby deflecting the wake in a helical shape and facilitating wake recovery [73]. The signals for these moments are designed in the turbine's non-rotating blade coordinate system using the corresponding yaw $\beta_{yaw}(t)$ and tilt $\beta_{tilt}(t)$ pitch angles. They are given by the relations $\beta_{tilt} = \beta \sin(\omega_e t)$ and $\beta_{yaw} = \beta \sin(\omega_e t + \psi)$, where $\beta$ is the pitch amplitude and the actuation frequency $\omega_e = 2\pi f_e$ can be expressed as non-dimensional Strouhal number $St = f_e D/u_H$. The rotor diameter is denoted as $D$ and $u_H$ is the mean inflow wind speed at hub height. A counterclockwise (CCW) helix is obtained for a phase offset of $\psi = \pi/2$, whereas a clockwise (CW) helix results from the offset $\psi = -\pi/2$. For the implementation on the actual turbine, the designed signals still have to be transformed to three blade pitch actuation signals $\beta_i(t)$ $(i = 1, 2, 3)$ expressed in the rotating blade-attached coordinate system using the inverse Multi-Blade Coordinate transform (MBC) [76]. The frequency of the resulting pitch actuation signals for a CCW helix is then given by $\omega_\beta = \omega_r + \omega_e$ $(\omega_e \ll \omega_r)$ for a wind turbine operating in below-rated conditions with constant rotor speed $\omega_r$ and collective pitch $\beta_0 = 0$ [73].

### 2.2.3 Fatigue analysis

Fatigue is a type of damage that occurs in structures as a result of repeated loading over time. This damage typically manifests as small cracks that gradually grow until the structure fails. The magnitude of the response to cyclic loading is governed by structural parameters such as damping and natural frequencies, which means that knowing these parameters is essential for designing structures such as wind turbines that must withstand cyclic loading for extended periods [167]. In the next paragraphs, the two measures for fatigue used in this study are presented: the damage equivalent load (DEL) and pitch bearing damage (PBD).

**Damage equivalent load**

One way to model the damage caused by cyclic loading on a structure is through the use of the S-N (or Wöhler) curve, which indicates the number of cycles a structure can endure before failure for a given stress level [47]. The slope of the S-N curve is specific for each type of structure and is used to calculate the damage equivalent load (DEL), which condenses the total fatigue damage experienced by a structure to a single number. To use the S-N curve, it is necessary to have information on the ranges and frequencies of the different load cycles, which can be collected from a load signal using rainflow counting. The means of these cycles must then be corrected to a single mean value using the Goodman correction, which is given by:

$$A_i^{\mathrm{RF}} = A_i * ((A^{\mathrm{u}} - |A^{\mathrm{fm}}|)/(A^{\mathrm{u}} - |A_i^{\mathrm{m}}|)) \tag{2.1}$$

where $A_i^{\mathrm{RF}}$ is the Goodman-corrected range, $A_i$ is the range, $A^{\mathrm{m}}$ is the mean of the i-th cycle, $A^{\mathrm{u}}$ is the ultimate load, and $A^{\mathrm{fm}}$ is the fixed mean load, which is set as the mean of the entire signal. The DEL is then calculated using the following formula:

$$DEL = ((\sum_{i=1}^{N} (A_i^{\mathrm{RF}})^m * n_i)/n_{eq})^{\frac{1}{m}} \tag{2.2}$$

where $N$ is the total number of cycles, $m$ is the inverse Wöhler slope (conventionally taken as 5 for the tower and 10 for the blades), $n_i$ is the number of cycles with range $A_i$, and $n_{eq}$ is the equivalent cycle, which is set as 1. The calculations were performed using NREL's MLife toolbox [168]. Furthermore, the DELs in this work are calculated for the blade root (BR) moment (edgewise, flapwise, and torsional direction), the tower top (TT) moment (fore-aft, side-side, and torsional direction) and the tower base (TB) moment (fore-aft and side-side direction). The computational expense of AMR-Wind simulations limits the loads analyses performed in this work to 35 minutes of suitable simulation data for DEL calculation. This is less than a typical loads analysis, which uses either six 10-minute datasets with different turbulence seeds or a single 1-hour dataset [169]. The fatigue results presented in this work should therefore be considered as preliminary.

**Pitch bearing damage**

Pitch bearings accumulate damage differently due to their dynamic character [170]. Fatigue develops in radial positions on the bearing rings due to movement and the blade moment acting on the bearing. Both these components are taken into account in the pitch

bearing damage (PBD) calculation, which differs from the conventional DEL. The standard used in this study is one prescribed by bearing manufacturers and given by the following equation:

$$PBD(\phi) = \sum_{k=1}^{N} \delta\theta(k)(\max(\cos(\phi)M_{\text{flap}}(k) + \sin(\phi)M_{\text{edge}}(k), 0))^m, \tag{2.3}$$

where $k$ denotes the OpenFAST time step, $\delta\theta$ is the pitch difference, $\phi$ is the radial position of the inner bearing on the outer ring, $M_{\text{flap}}$ is the flapwise blade root bending moment, $M_{\text{edge}}$ is the edgewise blade root bending moment, and $m$ is the inverse Wöhler slope, taken here as 3. In our analysis, the radial position with the largest damage is considered.

## 2.3 Setup of the numerical simulations

This section presents the setup of the precursor simulation, which generates a developed turbulent ABL state, and the subsequent turbine simulations, which use this state as an initial condition.

### 2.3.1 Precursor simulation

A CNBL including Coriolis forces is considered for the precursor where the ABL flow develops against a stably stratified free atmosphere with lapse rate $\gamma = 1\,\text{K/km}$. A capping inversion is employed to control the growth and height of the CNBL [31]. For the present study, a boundary layer height of $h = 1000\,\text{m}$ and a surface roughness of $z_0 = 0.0002\,\text{m}$ are considered. The value of the surface roughness is in agreement with offshore measurements made off the Dutch coast [171] and the latitude is chosen accordingly as $\phi_{lat} = 52.6^\circ$. Furthermore, a controller is used to drive the flow at turbine hub height ($z_H = 150\,\text{m}$) to a wind speed of $u_H = 10\,\text{m/s}$ and a direction of $\phi = 90^\circ$ aligned with the eastern direction (aligned with the x-axis of the rectangular domain). This choice places the operating point of the first-row turbine close to the upper limit of the below-rated control regime, where collective pitch control is still disabled.

The velocity profile is initialised with the desired hub velocity $u_H$. Further, the initialisation of the temperature profile is crucial to obtain the desired boundary layer height. The height of the inversion determines the point up to which the boundary layer can grow before its growth is restricted by the negative buoyancy forces in the inversion layer. The equilibrium strength for the capping inversion can be estimated as $h = A\theta_0 u_*^2/(g\Delta\theta)$ where $A \approx 500$ is a constant and $\Delta\theta$ is the inversion strength [172]. One can obtain the minimum required strength $\Delta\theta_{min}$ for equilibrium using a typical value for the friction velocity in offshore conditions $u_* = 0.28\,\text{m/s}$ [173] and a reference potential temperature of $\theta_0 = 288.15\,\text{K}$. The implemented inversion strength is then chosen as $\Delta\theta = 2.5K \approx 2\Delta\theta_{min}$. The complete temperature initial condition is designed using the function

$$\theta(z) = \theta_m + a\frac{\tanh(\eta) + 1}{2} + b\frac{\ln[2\cosh(\eta)] + \eta}{2}, \tag{2.4}$$

where $\eta = (z - l)/(c\Delta h)$ is a non-dimensional height, $\Delta h = 100\,\text{m}$ is the inversion depth, $\theta_m = \theta_0 = 288.15\,\text{K}$ is the potential temperature in the mixed layer and the parameters $a, b, c$

and $l$ are directly related to the inversion characteristics [174]. The domain size for the precursor simulation is $L_x = 4160\,\text{m}$, $L_y = 3200\,\text{m}$ and $L_z = 1600\,\text{m}$ required to accommodate two turbines and limit domain blockage. The domain is discretised with an isotropic grid of size $\Delta x = 10\,\text{m}$, which is in agreement with requirements for the CNBL [175, 176]. Using periodic boundary conditions in the horizontal directions (x and y) the flow is advanced for 16 hours to allow for the development of a quasi-stationary turbulent ABL state [177]. During the subsequent 45 minutes, instantaneous y-z planes are sampled at the inflow $x = 0\,\text{m}$ which are then stored as inflow boundary conditions for the turbine simulations.

### 2.3.2 Turbine simulations

The small wind farm considered here consists of two IEA-15 MW turbines located at $x = 5D$ and $x = 10D$ from the inflow, each centred at $y = L_y/2$ in the domain. The grid around the two turbines and their wakes is refined to $\Delta x = 5\,\text{m}$ in a box of size $L_{x,r} = 3840\,\text{m}$, $L_{y,r} = 960\,\text{m}$ and $L_{z,r} = 600\,\text{m}$ starting $4.5D$ upstream of the first turbine. In terms of rotor diameter, the resolution is $D/\Delta x = 48$, which allows for the use of the ALM. The simulation is advanced in time for 45 minutes using a constant time step of $\Delta t_{LES} = 0.025\,\text{s}$, which ensures that the tips of the blades pass less than one grid cell per time step. The boundary condition in the y-direction is still periodic, whereas in the x-direction, an inflow/outflow boundary condition based on the recorded precursor data is applied in order to avoid the recirculation of the wakes. The OpenFAST simulation uses a time step of $\Delta t_{OF} = 0.005\,\text{s}$ and active degrees of freedom for the generator, blades, tower and platform. The blades, tower and nacelle are represented with $N_B = 60/N_T = 72/N_N = 1$ actuator points, respectively, and the force projection onto the LES grid is done with a Gaussian kernel of width $\epsilon = 2\Delta x = 10\,\text{m}$.

Using the outlined setup, the parameter sweep for the pitch amplitude is performed considering the six cases $\beta \in \{0, 1, 2, 3, 4, 6\}^\circ$ (denoted as BL, HL1, ...) to explore the full range of dynamics. It should be noted that the default pitch rate limits of the IEA-15 MW turbine have to be increased if $\beta > 4^\circ$ in order to enable helix pitch actuation. All helix cases in this study use the most common helix actuation frequency of $St = 0.25$, but we do note that there is still uncertainty not only in the optimal amplitude but also frequency [162]. Note that the helix is only implemented for the upstream turbine (denoted as T1).

## 2.4 Results

This section first presents the characteristics of the precursor simulation. Subsequently, it is shown how the different helix actuation signals alter the turbine wake and the response of the turbines in terms of wake development, power extraction and loading.

### 2.4.1 Precursor simulation

The characteristics of the precursor simulation are shown in Figure 2.1, where the data is averaged across the time interval used as the inflow boundary condition for the turbine runs. As can be seen from the vertical wind speed profile, the wind controller successfully ensures a hub height wind speed of $u_H = 10\,\text{m/s}$. The local shear exponent defined as $\alpha = (z/u_{horiz})(du_{horiz}/dz)$ resulting from the wind speed profile is in the range of $\alpha = 0.07 - 0.085$ across the rotor except close to the bottom edge of the rotor disk where it

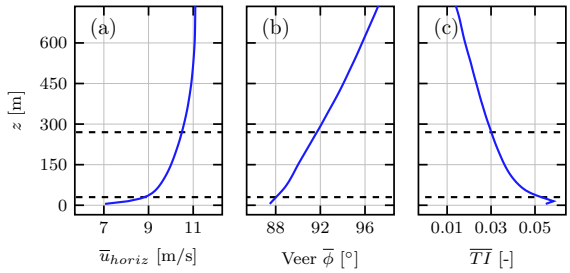


Figure 2.1: Vertical mean profiles of horizontal velocity magnitude (a), veer (b) and turbulence intensity (c) averaged across horizontal planes and the 45 minutes of the precursor inflow data. The rotor region is marked with dashed horizontal lines.

reaches up to $\alpha = 0.11$. The veer profile is nearly linear in the lower part of the ABL leading to a wind direction change of $\Delta\phi = 3.8^{\circ}$ across the rotor. The turbulence intensity is defined as $TI = (\frac{1}{3}\overline{u_i' u_i'}/\overline{u_i u_i})^{0.5}$ (where $u_i' = u_i - \overline{u}_i$ denotes the fluctuation around the temporal average and we use the Einstein summation convention) [161]. It reaches maximum values at the wall where turbulence is generated due to shear and decays with increasing height. The inflow TI level experienced by the rotor spans from 3% at the rotor top to 5.3% at the rotor bottom. The mean friction velocity is $u_* = 0.2855\,\mathrm{m/s}$, which closely matches the value assumed for the calculation of the inversion strength.

### 2.4.2 Turbine simulations: Wake development

The key concept of the helix control approach is to enhance the recovery of the wake behind the turbine. This is illustrated by comparing the vertical mean streamwise velocity profiles in the wake of turbine T1 for the baseline case and different helix signals (Figure 2.2). The mean profiles and quantities in the remainder of this article are obtained by averaging across the last 35 minutes of the simulation time, discarding the first transient 10 minutes of turbine start-up.

The initial wake behind the turbine consists of two regions of large velocity deficit separated by a low deficit region in the proximity of the nacelle. The deficit is superposed onto the incoming shear profile and during its downstream development the low deficit footprint of the nacelle diffuses. At $x/D = 3$ it is only visible for the BL and HL1 cases. There is a monotonic trend of larger helix pitch amplitudes leading to faster recovery of the wake, although differences between the BL and HL1 cases are minimal. We quantify the comparison by computing the relative increase of mean streamwise power integrated across the rotor area. At $x/D = 4$ the relative increase in power is 5.1% for the HL1 case, whereas the cases HL2, HL3, HL4 and HL6 lead to an increase of 16.2%, 29.3%, 48.8% and 86.6%, respectively.

The main trend found for the vertical mean velocity profiles also transfers to the turbulence kinetic energy $\overline{k}_{res}$ (TKE), where only the part directly resolved by the LES is considered (Figure 2.3). Higher helix pitch amplitudes lead to larger TKE levels at a fixed streamwise location. For all cases, the TKE level is especially elevated in the region of the upper and lower rotor tip and the nacelle region. However, for larger values of the pitch

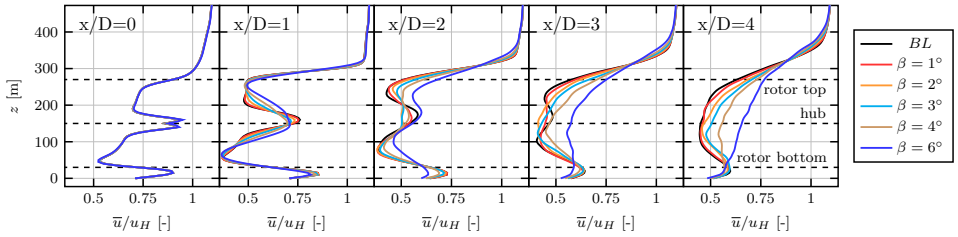


Figure 2.2: Vertical mean streamwise velocity profiles at the location of turbine T1 ($x/D = 0$) and four locations downstream in its wake. Note that at $x/D = 0$ all lines overlap.

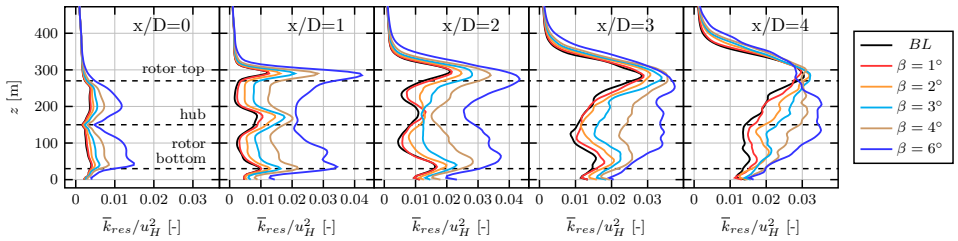


Figure 2.3: Vertical mean profiles of resolved turbulence kinetic energy at the location of turbine T1 ($x/D = 0$) and four locations downstream in its wake.

amplitude, the TKE level also saturates earlier upstream. Further downstream at $x/D = 4$ this leads to similar TKE levels at the upper edge of the rotor region for all cases including the baseline. Within the rotor region, there are still differences between the BL and HL6 cases of up to 300%.

We further compare the cases by analysing the wake meandering behaviour. The instantaneous wake centres in y-z planes are computed using the streamwise momentum deficit following [102]

$$y_c(t) = \frac{\int \Delta u^2(t,y,z) y \, dydz}{\int \Delta u^2(t,y,z) \, dydz}, \quad z_c(t) = \frac{\int \Delta u^2(t,y,z) z \, dydz}{\int \Delta u^2(t,y,z) \, dydz} \tag{2.5}$$

where $\Delta u(t,y,z) = u_{inflow}(y,z) - u(t,y,z)$ is the velocity deficit and the inflow is taken at $x = -2D$ upstream of T1. Using the mean wake centres $(\overline{y}_c, \overline{z}_c)$ as the origin of a polar coordinate system, the instantaneous wake centres are transformed to a radius $r_c(t)$ and angle $\gamma_c(t)$. Binning the angles into bins of size 15° and computing the average radius per bin results in the mean wake centre displacements $\overline{r}(\gamma)$ shown in Figure 2.4. Larger helix actuation amplitudes lead to larger vertical and horizontal wake centre displacement throughout the wake.

### 2.4.3 Turbine simulations: Turbine response

It is now studied how the trend of enhanced wake recovery with increasing helix pitch amplitude impacts the generated power of the farm (Figure 2.5 (a)). The second turbine's and the farm's cumulated power gain increase monotonously with $\beta$ and interestingly

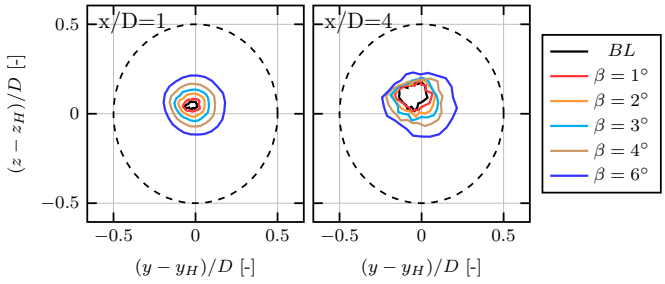


Figure 2.4: Binned mean wake center displacement $\overline{r}(\gamma)$ around the mean wake center $(\overline{y}_c, \overline{z}_c)$ in the wake of T1 at $x/D = 1$ and $x/D = 4$. The dashed line indicates the extent of the rotor. The axes are centred around the turbine's hub position.

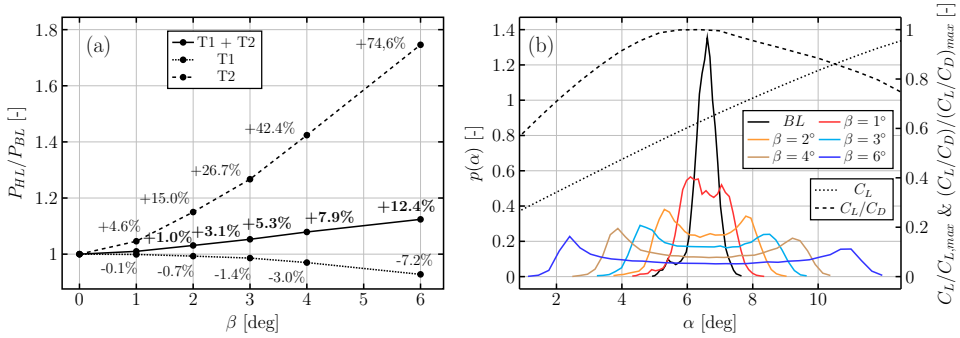


Figure 2.5: Relative power gain for the two-turbine wind farm with respect to the BL case (a) and PDF (normalised such that the respective integral equals unity) of the angle of attack for a blade section at 87% of the span (b). The dotted and dashed lines indicate the airfoil's lift coefficient and lift-to-drag ratio normalised with their maximum values, respectively.

scale superlinear for $\beta \in (0,2)^\circ$. It should be noted that even though the inflow wind speed for the upstream turbine is chosen close to the upper limit of the region II control regime, the second turbine still operates partially in control regime 1.5. In this regime, the turbine ensures that a minimum rotor speed constraint is fulfilled by collectively pitching the blades, but the achievable power coefficient is still lower than in region II. The time spent in region 1.5 increases with decreasing $\beta$. Nevertheless, the superlinear scaling is not the sole artefact of the change of control regimes since the above-reported increase in streamwise kinetic energy at $x/D = 4$ scales similarly to the power gain at T2. These results suggest that there is a threshold amplitude $\beta \approx 1^\circ - 2^\circ$, which should be exceeded in order to reach the more linear scaling regime of the cumulated power gain and thus fully capitalise on the helix actuation at T1. We also explore the upper end of the $\beta$ range, although these values are likely higher than the values which can be implemented in practice. Relative power losses at T1 become especially relevant for $\beta > 3^\circ$ but are still compensated for by the power gain at T2. The relative power gains are of the same order as literature results (DTU-10 MW turbine and $TI = 5\%$) that reported power gains of 3.4% ($\beta = 2.5^\circ$) and 7.5%

($\beta$ = 4.0°) using the same Strouhal number [73].

The impact of the helix actuation on the local aerodynamics at a blade section at 87% of the span is visualised in Figure 2.5 (b). It shows the probability density functions (PDFs) for the angle of attack and, in addition, the $\alpha - C_L$ & $\alpha - (C_L/C_D)$ characteristics of the airfoil. For the BL case, the airfoil is mainly operating in the proximity of the optimal lift-to-drag ratio. For the largest pitch amplitude $\beta = 6^\circ$, the angle of attack still does not reach the airfoil's static stall limit. However, the airfoil mostly operates in regions of suboptimal lift-to-drag ratio reaching values as low as $(C_L/C_D) = 0.6(C_L/C_D)_{max}$ for the HL6 case.

When judging the effectiveness of the helix approach, aerodynamic performance cannot be considered in isolation. The turbine loading of both the upstream and downstream turbines has to be taken into account. Figure 2.6 shows the power spectral densities (PSDs) of the out-of-plane blade moments (MOoPs) for T1 and T2. At T1, there is a strong peak visible at the 1P+St frequency, which is the helix pitch actuation frequency for a CCW helix in the rotating blade-attached coordinate system. At the downstream turbine T2, the comparison between the baseline and the helix cases shows that the upstream helix actuation still leaves a detectable footprint at the frequency of $St$ = 0.25.

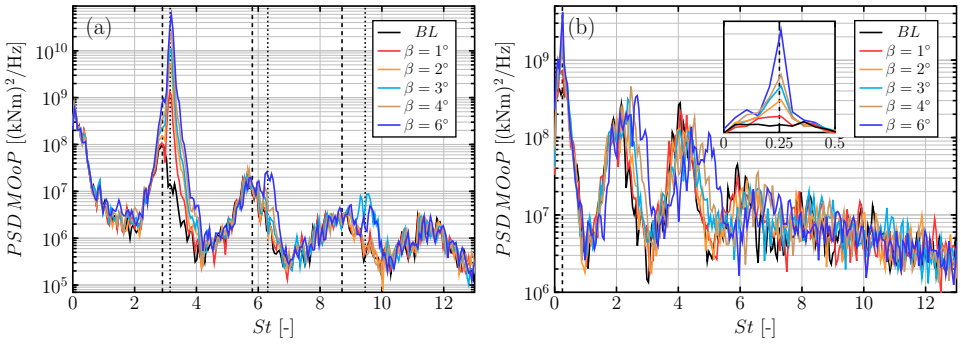


Figure 2.6: PSD of the MOoPs measured at the first blade of T1 (a) and T2 (b). In plot (a) dashed lines denote the 1P, 2P and 3P frequencies of the BL case and dashed lines the 1P+St, 2P+2St and 3P+3St frequencies. In plot (b), the dashed line indicates $St$ = 0.25.

The load impact of the helix on T1 and T2 can be quantitatively compared by computing the DEL for blades/tower and the PBD (Figure 2.7). The figure shows a trend of increased loading as amplitude increases for T1. Especially the blade root flapwise, tower top fore-aft, tower torsional, and pitch bearing damage are sensitive to increased amplitude, which aligns with previous research [84]. Interestingly, the downstream turbine does not seem significantly impacted by the helical-shaped wake, experiencing only slight increases in loading. This might also be explained due to the higher effective wind speed on the downstream turbine as a result of the faster wake recovery due to the helix.

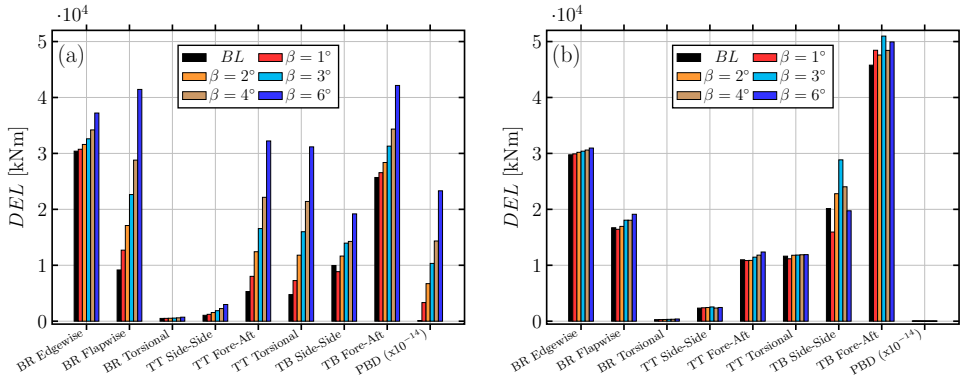


Figure 2.7: Damage equivalent loads and pitch bearing damage for T1 (a) and T2 (b). Note that the PBD is scaled with a factor of $10^{-14}$ to fit in the figure.

## 2.5 Conclusions

In this study, we analysed the performance of the helix wind farm control approach for a two-turbine farm operating in the CNBL. A parameter sweep was conducted for the pitch amplitude considering a CCW helix with $St = 0.25$. There was no saturation of the power gain detected within the considered range of pitch amplitudes. However, the DELs at the upstream turbine were sensitive to the helix actuation signal, thus imposing an upper limit for the actuation. A lower limit is suggested by the very small power gain found for $\beta = 1^{\circ}$. Therefore, the helix actuation amplitude should be chosen as a careful trade-off between the scaling of power gain and loading with $\beta$. Future work will focus on assessing how the power gain curve is affected by different ABL conditions, the optimisation of the actuation Strouhal number and a more robust calculation of the DEL using multiple turbulence seeds.

# 3



# Comparison of helix and wake steering control for varying turbine spacing and wind direction

*A variety of wind farm control strategies exist in order to reduce unfavourable wake effects in large wind farms. While strategies like wake steering have already reached a high maturity level, it is interesting to compare them to more recently proposed strategies. Such a comparison can form the basis for the development of a symbiotic wind farm control toolbox, from which a control strategy is chosen and activated depending on the operating conditions. The present study compares wake steering with helix control across a wide range of turbine spacings and wind directions using large-eddy simulation (LES). The size of the search space is made computationally tractable for LES by adopting a setup based on one physical upstream turbine and a distribution of virtual downstream turbines which do not exert any thrust force. It is found that helix control is beneficial for full wake overlap and turbine spacing of less than six rotor diameters, whereas wake steering proves to be optimal further downstream and for partial wake overlap. Furthermore, the results show that the helix control setpoint in the proximity of full wake overlap scenarios is less susceptible to wind direction variations. This finding indicates that the combination of wake steering and helix control has potential for the design of a wind farm controller which is more robust in full wake overlap scenarios and can reduce the need for large yaw offset adjustments.*

This chapter is based on the following publication:

[157] E. Taschner, M. Becker, R. Verzijlbergh, and J. W. van Wingerden. "Comparison of helix and wake steering control for varying turbine spacing and wind direction". In: *Journal of Physics: Conference Series* 2767.3 (2024), p. 032023

The LES input files, postprocessing code and numerical data underlying the figures in this chapter can be downloaded from:
`https://doi.org/10.4121/b64d4bf7-14fd-4703-bdb9-2e1011011c45.v1`.

## 3.1 Introduction

In today's large offshore wind farms, unfavourable wake interference induces additional losses in extracted wind power, which extend beyond the losses present for a single turbine. To mitigate these wake losses a wide range of wind farm control strategies have been proposed during recent years which can be broadly classified into quasi-steady and dynamic solutions [45]. Quasi-steady solutions include axial induction control to modify the strength of wakes and the steering of wakes using yaw offsets, where control setpoints are only adjusted on a long time scale. In contrast, dynamic solutions like dynamic induction control (DIC) and dynamic wake steering react to changes in operating conditions on a much shorter time scale or impose a periodically oscillating actuation around a quasi-steady control setpoint. The latter is the case for the helix, a very recently developed dynamic strategy based on individual pitch control (IPC), which showed promising results when compared to parameterised sinusoidal DIC (the pulse) [73].



The quasi-steady strategies have reached a higher maturity level to a point where, for instance, static wake steering is available as a commercial product (Wake Adapt from Siemens Gamesa). As more and more control strategies are proposed and progress in maturity, the questions arise how the different strategies compare, if they possess different strengths and weaknesses and ultimately if different strategies can be combined. This combination could be a toolbox from which a wind farm controller can choose from depending on the current operating conditions. In principle, this symbiotic approach could either encompass the simultaneous use of different control strategies for the same turbine or a switching logic between them. For example, static wake steering and induction control were combined [178], and seminal work compared/combined dynamic wake steering and DIC [66]. The latter study was further extended to compare the two strategies for different farm layouts, concluding that aligned and staggered layouts favour wake steering and induction control, respectively [179]. For the third introduced dynamic strategy - the helix - comparisons beyond the pulse control in a full wake overlap scenario are scarce, and thus, the potential for combination with other control strategies is not well known yet.

The present study explores this potential for the helix and static wake steering control. In the case of a switching logic, the identification of the regimes and boundaries within which the different control strategies play to their strength would be crucial, as any given constructed wind farm layout can be transformed into a variety of effective aligned/staggered layouts with different turbine spacing by just changing the wind direction. The potential of the helix is conjectured to be maximal in settings of dense turbine spacing and, in particular, full wake overlap. In these settings, the control strategy could also be extended by using synchronisation with downstream turbines [74]. In contrast, these particular settings would require the largest yaw offsets for wake steering, i.e. large deviations from the optimal orientation from a single turbine perspective [180]. Consequently, one can hypothesise that helix and wake steering can be combined into a wind farm control toolbox where each control strategy only operates within its most beneficial regime.

The main contribution of this work is a map that suggests a control strategy and setting based on both the lateral offset and the distance of a neighbouring downstream turbine. The map is derived based on turbulent large-eddy simulation (LES) data and distinguishes

between three control settings: baseline greedy control, helix control and wake steering control. Extending the map for a range of atmospheric boundary layer (ABL) conditions would then result in a steady state controller, but could also help with wind farm layout optimisation using control co-design as shown by [180]. In the subsequent sections, we first present the adapted LES methodology for the precursor ABL and the successor turbine simulations before concluding with the obtained map and its implications for the potential of a switching controller.

## 3.2 Simulation Methodology



The simulation methodology follows two steps: Firstly, the ABL flow is developed using a precursor simulation. This precursor simulation then provides the inflow for the subsequent successor simulations containing the wind turbine operating with different control strategies.

### 3.2.1 Precursor LES simulation: Conventionally neutral ABL (CNBL)

The ABL type is chosen to be a CNBL, i.e. a neutrally stratified boundary layer capped by a strongly stable inversion and a mildly stable free atmosphere aloft (the free lapse rate is $\gamma = 1\,\mathrm{K/km}$). This ABL type is frequently used for LES of wind farms (e.g. [31, 106]) and has also been used previously for an LES study of the helix [156]. Similar to the setup in the latter study, the surface roughness is chosen here representative for offshore conditions ($z_0 = 0.0002\,\mathrm{m}$) and the latitude is set to the Dutch North Sea coast ($\phi = 52.6^\circ$). The initial condition (IC) for the vertical potential temperature profile is determined by setting the inversion base height to $h_0 = 700\,\mathrm{m}$, estimating the required strength of the capping inversion for equilibrium [31] and using the Rampanelli-Zardi model [174].

The desired velocity profile should both attain a wind direction of $\varphi = 270^\circ$ (parallel to the x-axis of the LES domain) and a wind speed of $u_{horiz} = 10\,\mathrm{m/s}$ at a height of $z = 150\,\mathrm{m}$ (the turbine hub height), which places the upstream turbine in the successor simulations at the upper boundary of the control regime II where the rotor speed is still adjusted to track an optimal power coefficient $C_P$. These requirements are ensured by employing an ABL controller in the precursor, which adjusts the direction and magnitude of the driving pressure gradient accordingly. Since the equilibrium solution is an outcome of the chosen ABL setup and thus a priori unknown, it is not possible to initialise the velocity with a profile which fulfils the steady geostrophic wind balance (the momentum balance between pressure gradient and Coriolis force above the capping inversion). However, this leads to inertial oscillations of the wind speed and direction above the capping inversion, which are not damped as there is no turbulence present above the inversion [31]. Using a geostrophic wind forcing and geostrophic wind speed as IC would not give rise to these oscillations, but it does not provide any control of the hub height wind conditions. As a remedy, a modified controller was recently proposed which employs damping above the capping inversion [109]. Since this damping essentially resembles a Rayleigh damping layer with dynamically adjusted reference values, the present study follows this approach, but adapted in the following way for offline reference input (inspired by [181]).

Initially, the ABL turbulence is developed for eight hours using the ABL controller until the state within the boundary layer is quasi-steady and consequently also the con-

trolled driving pressure gradient. The pressure gradient is then sampled during the following hour and its average is converted into an equivalent geostrophic wind according to $u_g = -1/(f_c\rho)\,\partial\overline{p}/\partial y$ and $v_g = 1/(f_c\rho)\,\partial\overline{p}/\partial x$ [98], where the Coriolis parameter is given by $f_c = 2\sin(\phi)\Omega_z$ ($\Omega_z = 7.29 * 10^{-5}$ rad/s) and $\rho = 1.225\,\mathrm{kg/m^3}$ is the reference density. The geostrophic wind speed components are then set as references for a Rayleigh damping layer which spans the free atmosphere and decays to zero in the inversion layer according to a cosine function. The damping factor is chosen as $\alpha = 1$ for a critically damped system [109]. Subsequently, the simulation is then continued for twelve hours to dampen the inertial oscillation.



Using the outlined setup and procedure, the ABL flow is obtained with the open-source LES code AMR-Wind [112], which solves the filtered incompressible Navier-Stokes equations on block-structured Cartesian grids [165]. The domain size is chosen as $(L_x, L_y, L_z) = (4096, 3200, 1280)\,\mathrm{m}$ giving sufficient space for the development of ABL turbulence and later for capturing a range of wind directions and turbine spacings in the successor simulations. The grid resolution is uniform with $\Delta x_{LES} = 8\,\mathrm{m}$ and the constant time step of $\Delta t = 0.4\,\mathrm{s}$ sets a Courant-Friedrichs-Levy (CFL) number of CFL $\approx 0.6$.

Figure 3.1 (a) shows the development of the horizontal wind speed at four different heights within and above the boundary layer. It can be seen how the wind speed within the ABL reaches a quasi-stationary state while an inertial oscillation manifests for the horizontal wind speed in the free atmosphere, where the period is determined by the latitude (i.e. the Coriolis parameter). The Rayleigh damping is active from $t = 8 - 20\,\mathrm{h}$ as can be seen from the mitigated wind speed oscillation at $z = 1100\,\mathrm{m}$. The resulting vertical profiles of horizontal wind speed $\overline{u}_{horiz}$, wind direction $\overline{\varphi}$ and turbulence intensity $\overline{TI}$ (defined based on turbulent kinetic energy) averaged for the time interval $t \in (20 - 20.5)\,\mathrm{h}$ are shown in Figure 3.1 (b)-(d) across the rotor area. This half-hour interval is the period used as an inflow boundary condition for the successor simulations. The variations of TI level and local shear exponent $\alpha = (z/\overline{u}_{horiz})(d\overline{u}_{horiz}/dz)$ across the rotor are $\overline{TI} \in (3,5)\,\%$ and $\alpha \in (0.07, 0.1)$

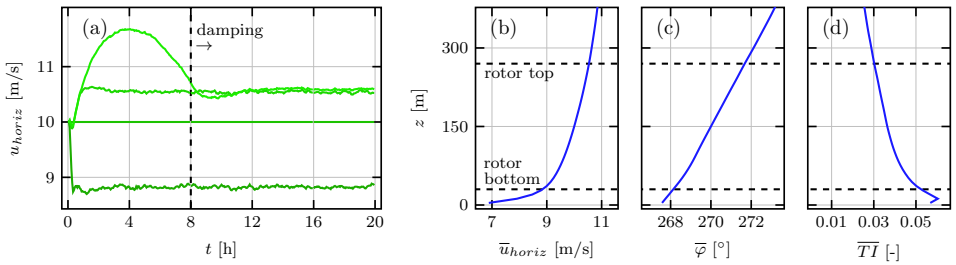


Figure 3.1: Development of the horizontal wind speed at $z \in (30, 150, 270, 1100)$ m in/above the ABL (darker green for decreasing $z$), where Rayleigh damping is activated at $t = 8$ h (a). Vertical mean profiles of horizontal velocity (b), wind direction (c) and turbulence intensity (d) averaged across $t \in (20 - 20.5)$ h.

### 3.2.2 Successor LES simulations: Greedy baseline, helix and wake steering control

The comparison of wake steering and helix is a high-dimensional optimisation problem since the effectiveness of each control strategy depends on the ABL condition and the given wind farm layout. The former point is addressed by choosing a single low turbulence ABL condition since wake control strategies are most likely to be employed therein. To tackle the latter point one requires an approach to reduce the degrees of freedom since a grid search for the optimal static yaw offset $\gamma_{Opt} = \gamma_{Opt}(S_x, \varphi)$ and additional helix/baseline simulations for each combination of streamwise spacing $S_x = \Delta x/D$ (non-dimensionalized with the rotor diameter $D$) and wind direction $\varphi$ are only feasible with engineering wake models, however, such a model is not yet available for helix control and thus this study resorts to LES. A brute force LES approach would become computationally prohibitive when comparing an increasing number of $(S_x, \varphi)$ combinations, but the use of LES can be made tractable by adopting a setup with one physical upstream turbine and a distribution of virtual turbines. The details of this setup are outlined in the following.

The adapted search space for the two control strategies spans the range of turbine spacings $S_x \in (2, 10)$ ($\Delta S_x = 1$) in order to cover the range within wake control might be in principle plausible. The range of wind directions is $\varphi \in (240, 300)^\circ$ at $S_x = 2$ and then decreases monotonously to $\varphi \in (258.2, 281.8)^\circ$ at $S_x = 10$, where at each $S_x$ station the wind direction range is discretized with seventeen points. This ensures that at each streamwise location the angular resolution is maintained in the area of interest, i.e. where wake overlap occurs. The level of wake overlap is also more intuitively given by the so-called view angle $\psi$, which is defined here as the difference between the downstream direction and the wind direction, i.e. $\psi = 270^\circ - \varphi$. Each $(S_x, \varphi)$ set is the location of a virtual downstream turbine, which does not exert any thrust force. Consequently, given a control actuation at the physical upstream turbine, one can estimate the power gain at a waked downstream turbine for all turbine spacings and wind directions with a single simulation. The total simulation count amounts then to one greedy baseline simulation, one simulation per set of helix control parameters and twelve wake steering simulations to discretize the search space of the yaw offsets $N_{Yaw} = (\gamma^+ - \gamma^-)/\Delta\gamma = (30^\circ - (-30^\circ))/5^\circ = 12$. The yaw offset is defined as the difference between the wind direction $\varphi$ and the turbine orientation $\theta$ as $\gamma = \varphi - \theta$. For this study we choose a single set of helix parameters, namely a blade pitch amplitude of $\beta = 3^\circ$ which provides a trade-off between power gain and additional loading [156] and an actuation frequency of $St = 0.3$, where the Strouhal number $St$ is a non-dimensional frequency $f$ defined as $St = f * D/\overline{u}_{hub}$. Thus, one can obtain an estimate for the optimal control strategy across the entire search space with a total of fourteen simulations. The setup, including all angle definitions, is also shown in Figure 3.2.

The physical upstream turbine is modelled using OpenFAST, which is a multi-physics wind turbine simulation tool capable of simulating the entire wind turbine, including its structural, hydro-, aero- and control dynamics [125] combined with the reference open-source controller (ROSCO) [127]. In this study, the OpenFAST model for the fixed-bottom monopile variant of the IEA-15MW turbine is used [49]. OpenFAST is coupled to the LES simulation using an actuator line model (ALM) [137], where the Gaussian kernel width for the force projection is chosen as $\epsilon = 2\Delta x_{LES}$. Given the still large number of required simulations, a grid refinement compared to the precursor simulation is computationally

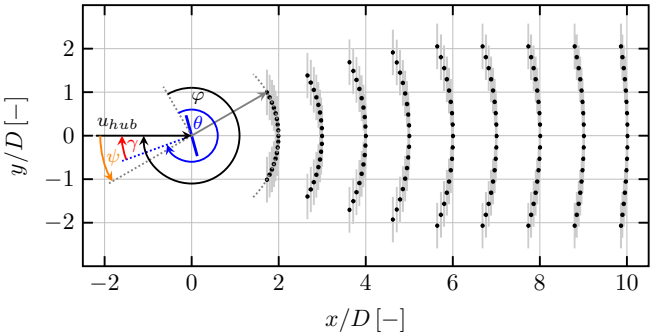


Figure 3.2: Positions of the physical turbine (blue) and virtual turbines (light grey) together with the definitions of the turbine orientation (blue), wind direction (black), yaw offset (red) and view angle (orange).

not feasible, and thus it is $\epsilon = 16\,\mathrm{m}$. The resulting ratio of LES grid points across the rotor radius is $R/\Delta x_{LES} = 15$, which falls into the category of coarse LES-ALM, which will cause the ALM to overestimate power. To remedy this effect the filtered lifting line correction (FLLC) is employed [149] and the rotor blades are discretized with $N_{Act} = 200$ actuator points, which requires the minimum allowable optimal Gaussian kernel width at the blade tip to be limited to $\epsilon_{Opt} = 1.2\,\mathrm{m}$. The choice of $N_{Act}$ is a trade-off between full convergence of the FLLC at the most outer three per cent of the blade and the computational slowdown of OpenFAST [158]. For reference a completely resolved FLLC is determined by the chord length $c$ at the blade tip and would require about $N_{Act} \approx 1000$ for the IEA-15MW blade which is not feasible with the constant actuator point spacing employed in OpenFAST ($N_{Act} = R/\min(\epsilon_{Opt}) = R/(0.25\,c_{tip})$). The time stepping further ensures that the CFL condition based on the turbine tip speed is below one. Using these settings, the fourteen successor simulations are advanced $T_{Sim} = 30\,\mathrm{min}$ in time, where the first ten minutes are discarded as start-up phase and the latter twenty minutes are the time interval $T_A$ utilised for the analysis.

The last component of the setup is an approach to obtain power estimates of the virtual turbines. The virtual turbines are two-dimensional velocity sampling planes which convert a time series of streamwise velocities $u_x(t, y, z)$ into mean power estimates $\overline{P}_{VT}(S_x, \varphi, C_i)$, where $C_i$ represents the control strategy (greedy baseline $C_B$, yaw $C_Y$ and helix $C_H$). Combined with the upstream ALM power estimate $\overline{P}_{OF}(C_i)$, one can then estimate the optimal farm control strategy for a given $(S_x, \varphi)$ set by calculating the power gain for each $C_i$:

$$G(S_x, \varphi, C_i) = \frac{\overline{P}_{OF}(C_i) + \overline{P}_{VT}(S_x, \varphi, C_i)}{\overline{P}_{OF}(C_B) + \overline{P}_{VT}(S_x, \varphi, C_B)}. \tag{3.1}$$

This transfer function is based on the $C_P$ look-up table for the IEA-15MW turbine, which is obtained from steady-state blade element momentum (BEM) theory. Since the instantaneous wakes in sheared/veered inflow behind a turbine subject to helix actuation or yaw misalignment show large spatial and temporal variations, we employ the concept of the rotor equivalent wind speed (REWS) to better capture this heterogeneity [182]. The REWS

is then used for the $C_P$ look-up table operation, and the entire transfer function for any virtual turbine is given as

$$u_{REWS}(t) = \sqrt[3]{\frac{1}{A_{Rotor}} \int_{A_{Rotor}} u_x^3(t,y,z)\,\mathrm{d}A}, \tag{3.2}$$

$$\overline{P}_{VT} = \frac{1}{T_A} \int_0^{T_A} \frac{1}{2} C_P(u_{REWS}(t)) \rho A_{Rotor} u_{REWS}^3(t)\,\mathrm{d}t. \tag{3.3}$$



# 3.3 Results – Identification of optimal control strategies and their sensitivities

Applying the outlined simulation methodology one obtains power gain maps for each control strategy $G(S_x, \psi, C_i)$ (Section 3.3.1), a map of the overall optimal control strategy and power gain $G(S_x, \psi, C_{Opt})$ (Section 3.3.2) and insight into the potential of a switching controller (Section 3.3.3).

## 3.3.1 Extracted power: Physical and virtual turbines

The power gain map for each individual $C_i$ is obtained by evaluating Equation 3.1 for each turbine spacing $S_x$ and wind direction $\varphi$. In the case of wake steering the upstream power scaling with the yaw offset angle $\gamma$ is well described by a cosine law $\overline{P}_{OF}(C_Y(\gamma)) = \overline{P}_{OF}(C_Y(\gamma = 0^\circ))\cos^{P_p}(\gamma)$ where $P_p = 1.7$. The power loss at the upstream turbine due to the helix actuation is 1.34% which is close to the 1.4% loss found in a study using the same turbine in a similar ABL condition and only slightly smaller Strouhal number $St = 0.25$, but a finer grid of $\Delta x_{LES} = 5\,\mathrm{m}$ and no FLLC [156]. Figure 3.3 shows the power gain maps for the helix and a selected wake steering case ($\gamma = +20^\circ$) to highlight the fundamental differences between the two control strategies. Wake steering leads to an antisymmetric power gain map with respect to a view angle of $\psi = 0^\circ$, whereas the helix leads to a more symmetric map. Furthermore, the power gain of $G(S_x = 5, \psi = 0^\circ, C_H) = 5\%$ is again found to be close to the observed 5.3% in [156], where also the downstream turbine was modelled with an ALM. This agreement goes to show that the developed physical-virtual turbine setup predicts gains of reasonable magnitude.

## 3.3.2 The overall optimal control map

The overall optimal control map is obtained by selecting the highest power gain and associated control strategy for each set $(S_x, \varphi)$ from the fourteen available individual power gain maps $G(S_x, \psi, C_i)$. The result of this selection process is shown in Figure 3.4. For wake steering, one can observe that the largest yaw offsets become optimal for dense spacing and full wake overlap scenarios. Increasing the turbine spacing $S_x$ or deviating further from a view angle of $\psi = 0^\circ$ then favours successively smaller yaw offsets. However, it is in particular interesting to see how the helix compares to the optimal wake steering solution. The helix maximises the power gain in a small subspace of the considered search space, e.g. it is favoured for full wake overlap ($\psi \approx 0^\circ$) and dense turbine spacing of $S_x < 6$ (the yellow region in the left panel of Figure 3.4). The resulting optimal power gain map $G(S_x, \psi, C_{Opt})$ (right panel of Figure 3.4) shows close to a symmetric shape around $\psi = 0^\circ$

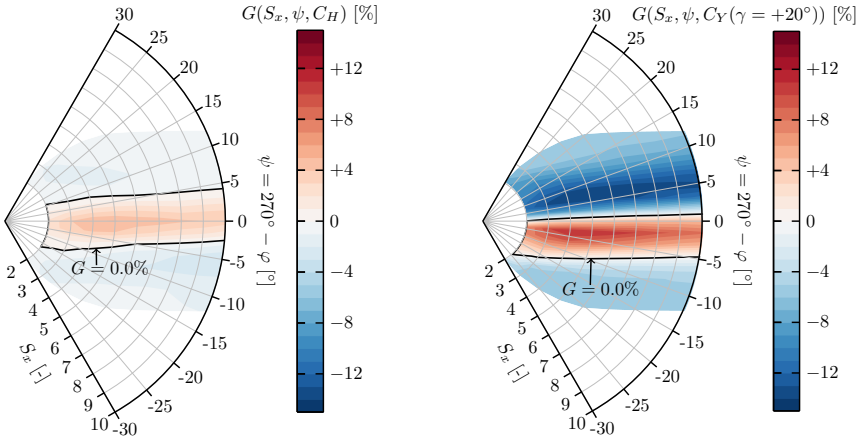


Figure 3.3: Overall power gain for the helix $G(S_x, \psi, C_H)$ (left) and a selected yaw offset angle $G(S_x, \psi, C_Y(\gamma = +20^\circ))$ (right) as function of turbine spacing and view angle.

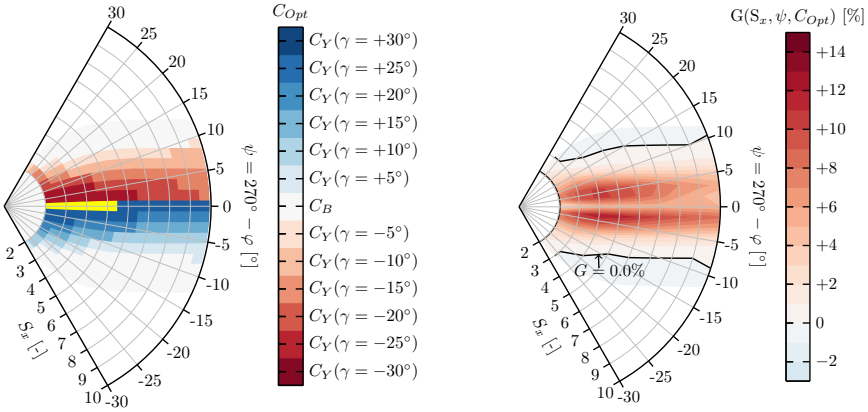


Figure 3.4: Optimal control strategy $C_{Opt}$ and setting as function of turbine spacing and view angle, where helix control is represented by a yellow region (left) and the respective achievable optimal overall power gain $G(S_x, \psi, C_{Opt})$ (right).

with a local minimum at the centre. In fact, the potential for maximum power gains is at $(S_x, \psi) \approx (4, \pm 5^\circ)$ achieved by large yaw offsets. Further deviating to larger absolute values for the view angle leads to a smooth transition to baseline greedy control being the optimal strategy. In contrast, this transition is not yet appearing in the downstream direction, e.g. at $S_x = 10$, wake steering is still favoured against baseline control. This should be seen in the light of the utilised ABL condition with low TI level, and a further increase is expected to shift the transition upstream towards smaller $S_x$.

### 3.3.3 The potential for a switching controller

The introduced map of optimal control strategies is derived for a steady wind direction at hub height, thus any movement in the map due to the in reality varying wind direction is not captured, yet. As soon as $\varphi = \varphi(t)$, the sensitivity of a particular optimal solution for a set $(S_x, \varphi)$ becomes relevant. To study this idea further, assume variations $\Delta\varphi(t) = \pm 5^\circ$ where the turbine controller does not react yet. This means that the turbine orientation is constant, which in turn results in induced changes of the yaw offset angle const $= \theta = \varphi(t) - \gamma(t)$. The resulting setpoint change of the upstream turbine can impact the neighbouring downstream turbine already after a few minutes, while the update period of the controller might be based on ten-minute averaged data, which essentially means that the turbine array now operates at a different setpoint, which can be suboptimal for the new wind direction. Interestingly, even in conditions where the turbine initially only operates with helix control, the $\Delta\varphi(t)$ variation will automatically induce a superposed non-zero yaw offset. In order to assess this scenario, we perform an additional four LES with $C_H$ and

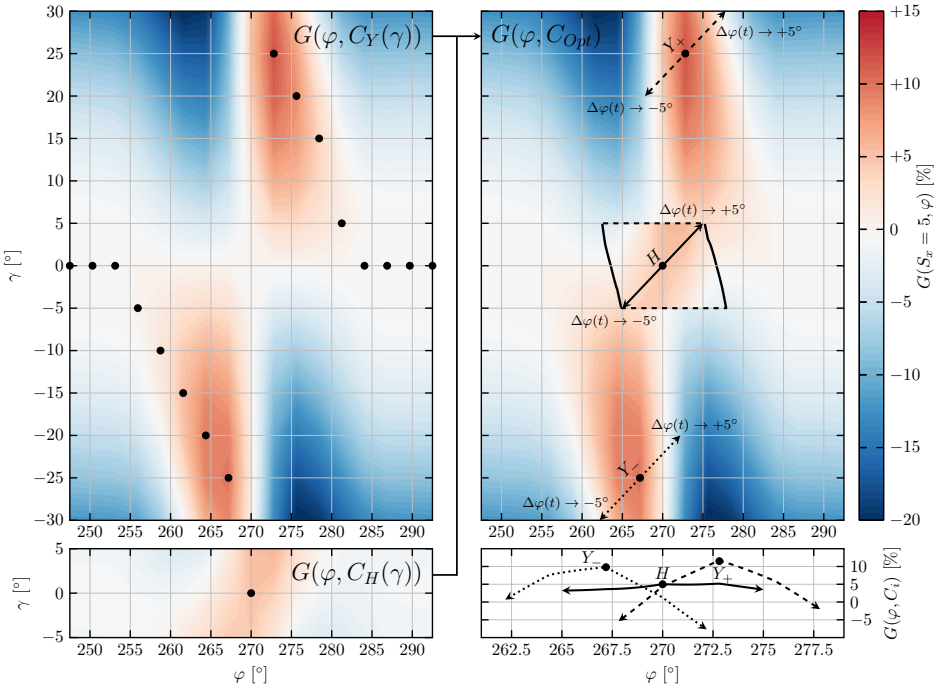


Figure 3.5: Comparison for $S_x = 5$: Wake steering power gain $G(\varphi, C_Y(\gamma))$ (left top) and helix power gain $G(\varphi, C_H(\gamma))$ (left bottom) as function of wind direction and yaw offset, where black dots indicate the optimal $C_{Opt}$ from Figure 3.4. Combined map of optimal gain $G(\varphi, C_{Opt})$ with the helix being the optimal strategy within the inset bounded by the solid/dashed black lines (right top) together with the optimal helix ($H$•) and two selected optimal yaw offset setpoints ($Y_-$•/$Y_+$•). The three arrows indicate trajectories resulting from wind direction variations $\Delta\varphi(t) = \pm 5^\circ$ without any control update ($\theta = \text{const} = \varphi(t) - \gamma(t)$). The right bottom panel shows the power gain $G(\varphi, C_i)$ when starting at the three selected optimal setpoints ($H$•/$Y_-$•/$Y_+$•) and moving along the trajectories caused by the wind speed variation $\Delta\varphi(t) = \pm 5^\circ$ (the three arrows in the top right panel).

small yaw offsets $\gamma \in (-5, -2.5, 2.5, 5)^\circ$ to study the helix performance in the light of a small yaw offset induced by a variation $\Delta\varphi(t)$.

In the following, we focus on a spacing of $S_x = 5$. The resulting separate power gain maps for wake steering $G(\varphi, C_Y(\gamma))$ and helix $G(\varphi, C_H(\gamma))$ are shown in the left column of Figure 3.5. In both plots, the black dots indicate the optimal control setpoints for any considered $\varphi$ bin at $S_x = 5$ (as previously shown in the left panel of Figure 3.4). These two maps are then further combined to obtain the overall optimal gain $G(\varphi, C_{Opt})$ (top right of Figure 3.5). It can be seen that helix control increases the achievable gain along the saddle connecting the two power gain maxima in the wake steering map. Furthermore, the discontinuities in vertical direction in the combined map when transitioning from helix to wake steering (indicated horizontal dashed lines) show that an initial control setpoint combining helix and yaw offsets has potential as the overall optimal control strategy for $\psi \approx 0^\circ$. In the present study the combined control is not taken into account for the overall optimization, but is used to assess the sensitivity of the different control strategies in the region of $\psi \approx 0^\circ$ (equals $\varphi \approx 270^\circ$) when moving along the trajectories caused by $\pm\Delta\varphi(t)$ (the three arrows) starting at the respective optimal helix and the two neighboring optimal yaw offset setpoints. The power gain along these trajectories is shown in the bottom right panel of Figure 3.5, highlighting two key observations. The differences in power gain at $\psi \approx 0^\circ$ are small, and trends might change in the light of the approximations made for the simplified LES setup. However, independently of the former observation, it can be seen that the helix power gain along the trajectory is more robust than the wake steering solutions, e.g. in order to outperform helix control, the wake steering controller has to switch from one extreme setpoint to the other. This requires either significant and timely yaw actuator travel, or if not executed due to load, hysteresis, or actuator constraints, leads to power losses compared to both baseline greedy and helix control. From this analysis, one can conclude that helix control could be used to avoid large yaw offsets and could make a wind farm wake steering controller more robust to wind direction variations in full wake overlap scenarios.

### 3.3.4 Limitations of the physical-virtual turbine setup

The preceding analysis identifies a potential for a helix-wake steering switching controller. While this is an interesting result, the accurate bounds of regions where a strategy is optimal and the estimate of the power gain are subject to uncertainty due to the made approximations, which are summarised here. Firstly, the value of the "correct" extracted power is unknown, and both coarse grid LES with an ALM-FLLC and the $C_P$ table look-up approach are expected to deviate from this value. Secondly, wake interaction occurring deeper in the farm, e.g. lateral interaction, helix synchronisation and secondary steering effects for wake steering are not captured. Thirdly, the study considers a single low TI CNBL condition with small values of veer.

## 3.4 Conclusions

For the first time, partial wake overlap scenarios were studied for the helix control approach and were compared to wake steering for a wide range of turbine spacings and wind directions. The qualitatively emerging picture is twofold. Firstly, from a power gain

perspective, the helix is only competitive with wake steering in full wake overlap scenarios and denser spacing $S_x \lesssim 6$ where exact bounds are subject to the uncertainties summarised in Section 3.3.4. However, a closer look revealed that, independent of the exact optimal gain, the helix holds potential for full wake overlap scenarios since it provides more robust power gains in the light of wind direction changes. More importantly, it covers this range with a single unmodified control setting while wake steering might be, in principle, more favourable, but requires large yaw offset adjustments of $\Delta\gamma = 50^\circ$. This highlights the potential for a wind farm switching controller. Finally, what this study only touched upon is the simultaneous use of helix and wake steering for the same turbine. In terms of power gain, this approach might hold potential, while trends for the sensitivity of the gain and turbine loads could be problematic. Anyways, it is an interesting question to study the resulting wake dynamics of simultaneous helix-wake steering control.

# 4

# A new coupling of a GPU-resident large-eddy simulation code with a multi-physics wind turbine simulation tool



*The development of new wind farm control strategies can benefit from a combined analysis of flow dynamics in the farm and the behaviour of individual turbines within one simulation environment. In this work, we present such an environment by developing a new coupling between the large-eddy simulation (LES) code GRASP and the multi-physics wind turbine simulation tool OpenFAST via an actuator line model (ALM). In addition, the implementation of the recently proposed filtered actuator line model (FALM) within the coupling is described. The new ALM implementation is cross-verified with results from four other commonly used research LES codes. The results for the blade loads and the near wake obtained with the new coupling are consistent with the other codes. Deviations are observed in the far wake. The results further indicate that the FALM is able to reduce the lift and power overprediction from which the traditional ALM suffers on coarse LES grids. This new simulation environment paves the way for future wind farm simulations under realistic weather conditions by leveraging GRASP's ability to impose data from large-scale meteorological models as boundary conditions.*

---

This chapter is based on the following publication:

[158] E. Taschner, M. Folkersma, L. A. Martínez-Tossas, R. Verzijlbergh, and J. W. van Wingerden. "A new coupling of a GPU-resident large-eddy simulation code with a multiphysics wind turbine simulation tool". In: *Wind Energy* 27.11 (2024), pp. 1152–1172

The numerical data underlying the figures in this chapter can be downloaded from:
`https://doi.org/10.4121/5f4a8fdb-6a7b-4c17-8449-8f16186b5872.v1`.
The AspFAST coupling code developed as part of this work is available on GitLab:
`https://gitlab.com/whiffle-public/aspfast`.

## 4.1 Introduction

Wind turbines and their aerodynamic behaviour have been of great interest for many years [183, 184]. However, the turbine is only one part of a large complex dynamical system. This dynamical system possesses spatial scales ranging from the turbine blade boundary layer up to global weather systems and temporal scales spanning from fractions of a second to slow seasonal variations [21]. While the performance of previous turbines could be analysed in a more isolated state, modern wind turbines are now often clustered in large farms, allowing for the generation of wind energy at low cost. The physics of these farms are governed by the flow in the atmospheric boundary layer (ABL), the dynamics of individual turbines and the inherent aerodynamic coupling between turbines due to their wakes [26, 185].



The efficient harvesting of the wind resource in these farms requires optimised control algorithms. Control algorithms developed for single turbines aim to increase individual power capture from the incoming wind and to reduce turbine loads [186]. Within the wind farm setting, the control problem is not only limited to the optimisation of individual turbine performance but also encompasses the maximisation of the overall power capture [187, 45]. The interaction of the turbines through their wakes is at the heart of this problem. The wakes, characterised by a velocity deficit and increased turbulence intensity, both reduce the power capture and increase the loads of turbines located downstream [26]. At the same time, however, wakes also offer an opportunity since existing turbine control degrees of freedom like rotor yaw and blade pitch can be utilised to modify the direction and development of the wakes. New (dynamic) wind farm control algorithms search for yaw and pitch actuation signals, which lead to optimal wake development in terms of power and load distribution across the entire farm [70, 161, 73, 83]. Therefore, the successful development of these algorithms relies crucially on the accurate quantification of their impact on the flow as well as the turbine dynamics that motivates the combination of the respective state-of-the-art simulation tools.

State-of-the-art numerical analysis of the flow dynamics in the ABL relies on large-eddy simulation (LES) [100, 188]. LES solves the filtered Navier-Stokes equations where only the smallest scales of the flow are modelled. It thereby provides insight into a wide range of temporal and spatial turbulent scales [22]. Wind turbines are included in these simulations mostly either via actuator disk models (ADM) or actuator line models (ALM), which both avoid the need for fully blade-resolving meshes [141, 189]. However, the ALM captures the footprint of individual turbine blades — in contrast to the ADM — thus enabling the analysis of individual pitch control algorithms [137]. During the last two decades, the ALM has become a prominent method for the representation of wind turbines in LES simulations and has been the subject of continuous development [190, 191].

One key component of the ALM is the spreading of the blade forces using a Gaussian kernel of width $\epsilon$. In particular, the choice of the value of $\epsilon$ has been the subject of active research. It has been shown that the optimal value for $\epsilon$ should be around 25% of the blade's local chord length [146]. However, this finding would imply very fine LES grid resolutions, making the simulation of larger wind farms computationally unfeasible. Simply using coarser grid resolutions and consequently also larger-than-optimal Gaussian spreading leads to the overprediction of blade lift and thus the turbine's power generation. Therefore, corrections were proposed for cases where optimal Gaussian spreading is com-

putationally too restrictive. The choice of correction is an ongoing research topic, and a variety of approaches have been proposed [150, 151, 152]. A recently proposed approach is the filtered actuator line model (FALM), which adds a subfilter correction to the LES velocity sampled for the ALM [149]. On the one hand, it was shown that FALM can indeed improve the prediction of lift and power generation for a wind turbine [192], whereas on the other hand, the impact of the FALM on the wake still needs further research [193].

The previous outline so far only concerned the analysis of the flow in a wind farm, but as motivated above, the development of new wind farm control algorithms also needs insights into the dynamics of individual wind turbines. These dynamics are analysed with dedicated multi-physics turbine simulation tools like OpenFAST or HAWC2, which simulate the turbine's aerodynamics, hydrodynamics, structural dynamics and control system [125, 126]. In addition, these tools provide a standardised interface for the inclusion of the most recent wind turbine reference controllers [127]. Therefore, the coupling of LES code, a turbine simulation tool and a turbine controller can provide combined physical insights into the dynamics relevant for the development of the next generation of dynamic wind farm control algorithms. The coupling of OpenFAST and HAWC2 to LES codes has been investigated by several scholars, where, for example, an initial approach by Storey et al. focused on a coupling via an ADM [194]. Later, the feasibility of couplings relying on ALM or actuator sector methods (ASM) was demonstrated, too [108, 138, 195, 196].



The progress in the development of new aero-servo-elastic couplings is accompanied by the growing importance of high-performance computing (HPC) architectures, which employ not only central processing units (CPUs) but also graphical processing units (GPUs). This development also affects the field of LES for wind farms, as it requires the adaptation or redesign of codes for optimal usage of the GPU architecture [197]. A very recent example of this trend is the work by Sprague et al. [198], which presented a coupling between OpenFAST and the LES code Nalu-Wind aiming for an effective use of GPUs.

In summary, the development of new dynamic wind farm control strategies asks for a simulation environment that enables the combined analysis of the complex ABL flow through wind farms and the performance of individual turbines, while ensuring the accuracy of the turbine power predictions also on coarser LES grids. Furthermore, this environment has to be compatible with the next generation of GPU-based HPC architectures. The main contribution of the present study is to develop a new simulation environment that meets these needs by coupling the GPU-resident LES code GRASP (GPU-Resident Atmospheric Simulation Platform) with OpenFast via an ALM and the FALM correction. The detailed contributions of this study are:

1. The extensive cross-verification of the new LES-OpenFAST coupling and its FALM correction, considering two benchmark cases with reference data from four other research LES codes;

2. An in-depth study of the FALM's impact on a wing & wind turbine rotor and their wakes, including the assessment of its convergence behaviour and implications for runtime.

The newly established simulation environment hence paves the way for the development of new dynamic wind farm control strategies under realistic weather conditions by lever-

aging GRASP's ability to impose data from large-scale meteorological models as initial and boundary conditions.

The remainder of this paper is structured as follows. First, an overview of GRASP, the new coupling and its subcomponents, including the ALM and FALM implementation, is given in Section 4.2. Secondly, Section 4.3 introduces the three considered wing and wind turbine cases, and Section 4.4 discusses the results. The cross-verification of the new ALM implementation is documented in Section 4.4.1. Subsequently, the FALM's impact on rotor and wake is assessed by using a simple translating wing (Section 4.4.2) and the NREL 5-MW reference wind turbine (Section 4.4.3). We conclude with a summary and an outlook in Section 4.5.



## 4.2 The simulation environment

The objective of this work is the coupling of the LES code GRASP with the turbine simulation code OpenFAST and the subsequent verification of the coupled simulation environment. The two main codes are described in Sections 4.2.1 and 4.2.2. The coupling between the codes is implemented via an actuator line model or a filtered actuator line model. The specifics of this coupling are presented in Section 4.2.3.

### 4.2.1 The large-eddy simulation code: GRASP

The fluid flow is simulated using the LES code GRASP. GRASP solves the filtered three-dimensional Navier-Stokes equations. The core structure of the code is based on the Dutch Atmospheric Large Eddy Simulation model (DALES), which is described in Heus et al. [121]. Details about the implementation of DALES on GPUs can be found in Schalkwijk et al. [122]. Furthermore, a proof of concept was delivered with a multi-GPU setup [123]. The GRASP model departs from the DALES formulation as it implements an anelastic approximation [199]. The governing equations for mass and momentum, including the anelastic approximation, are given by

$$\frac{\partial \rho_b \tilde{u}_j}{\partial x_j} = 0, \tag{4.1}$$

$$\rho_b \frac{\partial \tilde{u}_i}{\partial t} + \frac{\partial \rho_b \tilde{u}_i \tilde{u}_j}{\partial x_j} = -\frac{\partial \tilde{p}'}{\partial x_i} + \rho_b b \delta_{i3} - \frac{\partial \tau_{ij}}{\partial x_j} + \epsilon_{ij3} f_c (\tilde{u}_j - u_j^g) + f_i^{WT} + f_i^{Fringe}, \tag{4.2}$$

where $i \in \{1,2,3\}$ according to the Einstein summation convention, $\rho_b = \rho_b(x_3)$ is the specified reference density profile, $\tilde{u}_i$ is the filtered velocity, $b$ the buoyancy term $b = -g(\rho'/\rho_b)$ ($g$ being the gravitational constant and $\rho' = \rho - \rho_b$ the density fluctuation), $\tilde{p}'$ is the filtered pressure fluctuation $\tilde{p}' = \tilde{p} - \langle \tilde{p} \rangle$ ($\langle \cdots \rangle$ denotes the horizontal mean), $f_c$ is the Coriolis parameter, $u_j^g$ is the geostrophic wind, $f_i^{WT}$ are the body forces from the wind turbines, $f_i^{Fringe}$ denotes additional forcing terms (e.g. to drive the flow or impose large scale tendencies) and $\tau_{ij}$ is the subgrid-stress tensor. In the following, we use the Cartesian coordinate system $(x_1, x_2, x_3) = (x, y, z)$ when dealing with LES variables, where spatial directions are referred to as streamwise, lateral and vertical, respectively.

Using the symmetric part of the resolved velocity gradient tensor $\tilde{S}_{ij} = 0.5(\partial \tilde{u}_i / \partial x_j +$

$\partial \tilde{u}_j / \partial x_i$), the subgrid-stress tensor can be written as

$$\tau_{ij} = -\rho_b K_m \left( \frac{\partial \tilde{u}_i}{\partial x_j} + \frac{\partial \tilde{u}_j}{\partial x_i} \right) = -2\rho_b K_m \tilde{S}_{ij}. \tag{4.3}$$

In this study, the eddy viscosity $K_m$ is modelled using the Smagorinsky subgrid model

$$K_m = (C_s \Delta)^2 \sqrt{2\tilde{S}_{ij}\tilde{S}_{ij}}, \tag{4.4}$$

where $C_s$ is the Smagorinsky constant and the subgrid filter scale is denoted as $\Delta = (\Delta_x \Delta_y \Delta_z)^{1/3}$ [200]. For the remainder of this article, we omit the tilde sign for filtered variables for convenience. Spatial discretisation in GRASP uses the Arakawa C-grid, which is a spatially staggered grid. The cell centres and cell faces are referred to as full and half levels, respectively. All prognostic variables reside at the cell centre except the three velocity components. For example, consider the direction $i = 1$. The velocity component $u_x$ resides on the half level of the grid in the $x$ direction, whereas it is located on the full levels in the remaining two directions, $y$ and $z$. The advection scheme uses second-order central differences [121]. The time stepping can be done both with variable and fixed time step value $\Delta t$. A third-order Runge-Kutta scheme is used for explicit time integration of the governing equations [201]. Due to the periodicity of the streamwise and lateral directions, a pressure solver based on a fast Fourier transform can be employed, which acts on the periodic pressure fluctuation field $\tilde{p}'$. It ensures that the continuity equation is satisfied by computing the corresponding pressure fluctuations.

The main application of the LES code is for both weather hindcasting as well as operational forecasting. For example, Gilbert et al. [202] delivered a proof of concept using Grasp for operational forecasting at the Horns Rev I wind farm site. An application of GRASP for hindcasting purposes is presented in Schepers et al. [203]. They carried out a year-long hindcasting LES simulation with GRASP in order to study the effect of extreme events on the aero-elastic loads of a 10-MW wind turbine. Both of these studies use LES with periodic horizontal boundary conditions forced with tendencies from large-scale weather models. This approach requires additional source terms in Equation 4.2 representing large-scale subsidence, large-scale pressure gradients (expressed as geostrophic wind), large-scale advective tendencies and a relaxation term to avoid model drift (for details see Schalkwijk et al. [204]). GRASP enables the simulation of multiple nested LES domains in parallel, where the solution of an outer domain forces the subsequent inner domain, and only the innermost domain contains the wind turbines. As a consequence, the simulation of wind farms using periodic boundary conditions and large-scale forcing is enabled, but avoids the recirculation of the turbine wakes, which would occur when using a single periodic domain [205]. Other large-scale forcing approaches in literature avoided the assumption of horizontal homogeneity made for GRASP by not relying on periodic boundary conditions; however, in doing so, they also limited the range of permitted wind directions [206].

### 4.2.2 OpenFAST

The wind turbine dynamics are simulated using the open-source tool OpenFAST developed by the National Renewable Energy Laboratory (NREL), USA [125]. OpenFAST follows a

modular modelling approach where each module calculates a part of the turbine dynamics. The different modules include aerodynamics, hydrodynamics, control and structural dynamics. The overarching OpenFAST glue code manages the coupling of the modules and enables the integrated simulation of nonlinear aero-hydro-servo-elastic wind turbine dynamics. OpenFAST also offers a C++ API in order to link it to external programs. In this work, we utilise this API to develop a coupling between OpenFAST and the LES code GRASP. In addition, the present study employs the following physics modules of OpenFAST:

1. AeroDyn: Calculates the aerodynamic loading of the wind turbine. The blades and tower are discretised using analysis nodes spread along actuator lines. AeroDyn is provided by OpenFAST with the instantaneous orientation, position and flow velocity for each analysis node. Blade element theory, relying on two-dimensional airfoil data, is then used to calculate the local drag force, lift force and pitching moment.

2. ElastoDyn: Calculates the structural dynamics of the turbine. The turbine's desired degrees of freedom for blades, tower, generator and nacelle are set in this module. ElastoDyn receives the aerodynamic loads and controller commands as input. Based on this input, the resulting displacements, structural velocities/accelerations and reaction loads are calculated.

3. ServoDyn: This module covers all control aspects of the turbine, including pitch, generator/torque and yaw control. In addition, ServoDyn offers a bladed-style DISCON controller interface. This interface allows for a simple integration of external turbine controllers.

### 4.2.3 The LES-OpenFAST coupling

This section describes the newly developed coupling between GRASP and OpenFAST. GRASP calculations are carried out on the GPU, but through its API ASPIRE it is possible to couple plugins running on central processing units (CPUs). The coupling is realised with a new ASPIRE plugin written in C++, which is called AspFAST. AspFAST tasks are to synchronise the LES and OpenFAST simulations, to exchange information between the two main codes (forces, velocity, turbine blade position/orientation) and to perform the calculations for the ALM/FALM that are not covered by OpenFAST. A schematic of the resulting simulation environment is shown in Figure 4.1. It is important to note that in

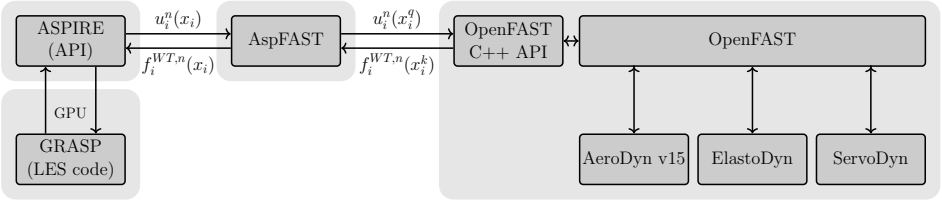


Figure 4.1: Schematic of the new simulation environment. The ASPIRE plugin AspFAST manages the communication between the LES code and the OpenFAST C++ API at each time step $t^n$. In addition, it implements the sampling of the LES velocity at the actuator points, the projection of the point forces back to the LES grid and optionally the calculation of the FALM correction.

OpenFAST the blade is discretised with both $N_F$ force actuator and $N_V$ velocity actuator points, where in general $N_F \neq N_V$. The number of points $N_F$ is flexible and is specified in AspFAST. The number of points $N_V$, on the other hand, is determined by the number of blade stations which are set in the AeroDyn blade specification file. An increase in velocity actuator points thus requires the interpolation of the initial blade input data to the desired value of $N_V$ points. The outline of the ALM and FALM below uses the following notation for the discretised solution. The subscript $(\cdots)_i$ still refers to the Einstein summation convention, denoting the spatial direction with respect to the corresponding coordinate system. In addition, we introduce the superscripts $x^k$ and $x^q$ to denote the kth force and qth velocity actuator point, respectively. The discrete solution at time step $t^n$ is indicated with the superscript $(\cdots)^n$.

During initialisation, the user input data (number of turbines, turbine positions, $N_F$) is read by AspFAST and communicated to OpenFAST. At each subsequent time step $t^n$, AspFAST receives the full LES velocity field $u_i^n(x_i)$ from GRASP and the current blade point positions $x_i^k$ and $x_i^q$ from OpenFAST. The LES velocity at the current velocity actuator point $u_i^n(x_i^q)$ is sampled using linear interpolation from the nearest LES grid point $x_i$ and then sent to OpenFAST. Provided with the LES velocity input, OpenFAST advances the turbine model by one time step. In a minimum configuration, this step entails the calculation of the aerodynamic loads by AeroDyn and the update of the actuator point locations. Note that the wake/induction model in AeroDyn is disabled since these effects are resolved by the LES. In particular, AeroDyn calculates the spanwise distribution of the aerodynamic forces acting on the blade using blade element theory based on two-dimensional airfoil look-up tables for drag and lift coefficients [207]. Using the local velocity magnitude

$$U_{Rel}^n(x_i^q) = \sqrt{(u_{ax}^n(x_i^q))^2 + (\Omega^n r^q - u_\theta^n(x_i^q))^2}, \tag{4.5}$$

the local inflow angle at each blade element can be determined as

$$\phi^n(x_i^q) = \tan^{-1}\left(\frac{u_{ax}^n(x_i^q)}{\Omega^n r^q - u_\theta^n(x_i^q)}\right), \tag{4.6}$$

where the velocities are expressed in a blade-aligned coordinate system given by $(x_1, x_2, x_3) = (r, \theta, ax)$. The rotor speed is denoted by $\Omega$. The local angle of attack is obtained by subtracting the sum of the local twist angle and the blade pitch angle (their sum is denoted as $\gamma$)

$$\alpha^n(x_i^q) = \phi^n(x_i^q) - \gamma^n(x_i^q). \tag{4.7}$$

The local lift and drag forces are then obtained utilising the airfoil look-up tables for lift coefficient $C_L = C_L(\alpha, Re)$ and drag coefficient $C_D = C_D(\alpha, Re)$ dependent on Reynolds number $Re$ and angle of attack

$$\frac{F_L^n(x_i^q)}{\Delta r(x_i^q)} = \frac{1}{2}\rho(U_{Rel}^n(x_i^q))^2 c(x_i^q) C_L^n(x_i^q), \tag{4.8}$$

$$\frac{F_D^n(x_i^q)}{\Delta r(x_i^q)} = \frac{1}{2}\rho(U_{Rel}^n(x_i^q))^2 c(x_i^q) C_D^n(x_i^q), \tag{4.9}$$

where the density $\rho$ is specified in the AeroDyn input file, $\Delta r(x_i^q)$ denotes the spanwise extent of the blade element associated with the actuator point and $c$ is the local chord length. The resultant force vector is transformed back into the Cartesian LES coordinate system and communicated to AspFAST at the force actuator point locations $x_i^k$. This point force $f_i^{WT,n}(x_i^k)$ is spread across multiple LES grid points using a convolution with a constant Gaussian kernel $\eta_\epsilon$ with kernel width $\epsilon$

$$\eta_\epsilon = \frac{1}{\epsilon^3 \pi^{3/2}} \exp\left(\frac{-(x_i - x_i^k)^2}{\epsilon^2}\right), \tag{4.10}$$

$$f_i^{WT,n}(x_i) = f_i^{WT,n}(x_i^k) \otimes \eta_\epsilon, \tag{4.11}$$



thereby ensuring that singular behaviour is avoided and the resulting force distribution is smooth. The resultant body force distribution $f_i^{WT,n}$ is then applied as an additional force term in the flow domain (i.e. in Equation 4.2). The ALM, as outlined above, follows the traditional ALM formulation as developed by Sørensen and Shen [137].

As outlined in the introduction, the ALM in its traditional form suffers from overpredicted blade torque and thus power generation if the Gaussian kernel width is chosen larger than the value found to be optimal $\epsilon > \epsilon^{Opt}$. However, the requirement for the optimal value of the Gaussian kernel is very restrictive since it leads to very fine grid resolutions, which are infeasible for LES simulations on the wind farm scale. Therefore, Martínez-Tossas and Meneveau [149] proposed a subfilter correction applied to the sampled LES velocity. This method, labelled as filtered actuator line model (FALM), aims to remedy the issue of torque overprediction for cases where $\epsilon > \epsilon^{Opt}$. In the following, the formulation of FALM and its implementation in the LES-OpenFAST coupling are described.

For the implementation in AspFAST, forces and velocities are kept in vector form throughout the calculation; thus, the same is done for the outline of the equations below. The usage of $\epsilon > \epsilon^{Opt}$ for LES leads to the underestimation of induced velocity. This reduced strength of the induced velocity causes larger angles of attack along the blade than would have occurred with $\epsilon^{Opt}$. The main idea of FALM is to determine the resolved and the missing part of the induced velocity in order to correct the sampled LES velocity for the effect of a suboptimal kernel size $\epsilon^{LES}$

$$\hat{u}_i(x_i) = u_i(x_i) + [u_{i,ind}(x_i; \epsilon^{Opt}) - u_{i,ind}(x_i; \epsilon^{LES})]. \tag{4.12}$$

The numerical procedure to obtain this subfilter correction can be summarised as follows. The calculation of the correction requires knowledge of the freestream velocity, excluding the effects of induced velocity. This velocity can be approximated as

$$U_{i,\infty}^n(x_i^k) = u_i^n(x_i^k) - u_{i,ind}^n(x_i^k; \epsilon^{LES}). \tag{4.13}$$

The lift force at each blade element acts perpendicular to $U_{i,\infty}^n(x_i^k)$. Since OpenFAST only returns the resultant force vector, the lift force is not directly available. However, the lift

force can be recovered using the local unperturbed inflow velocity

$$G_i^{n-1}(x_i^k) = \frac{1}{2} c(x_i^k) C_L(x_i^k) U_{j,\infty}(x_i^k) U_{j,\infty}(x_i^k)$$
$$= \frac{1}{\rho \Delta x^k} \left( f_i^{WT,n-1}(x_i^k) - U_{i,\infty}(x_i^k) \frac{f_j^{WT,n-1}(x_i^k) U_{j,\infty}(x_i^k)}{U_{j,\infty}(x_i^k) U_{j,\infty}(x_i^k)} \right). \tag{4.14}$$

Furthermore, the gradient of $G_i^{n-1}$ along the blade span is obtained using finite differences

$$k = 1: \quad \Delta G_i^{n-1}(x_i^1) = G_i^{n-1}(x_i^1) \tag{4.15}$$

$$k \in (2, N_F - 1): \quad \Delta G_i^{n-1}(x_i^k) = \frac{1}{2}[G_i^{n-1}(x_i^{k+1}) - G_i^{n-1}(x_i^{k-1})] \tag{4.16}$$

$$k = N_F: \quad \Delta G_i^{n-1}(x_i^1) = -G_i^{n-1}(x_i^{N_F}). \tag{4.17}$$

Using the lift gradient, one can then calculate the resulting induced velocity at the kth actuator point for a given kernel width $\epsilon$

$$u_{i,ind}^n(x_i^k; \epsilon) \approx -\sum_{l=1}^{N_F} \frac{1}{\sqrt{U_{j,\infty}(x_i^l) U_{j,\infty}(x_i^l)}} \frac{1}{4\pi(x_i^k - x_i^l)} \Delta G_i^{n-1}(x_i^l)$$
$$\times \left( 1 - \exp\left( \frac{-(x_i^k - x_i^l)^2}{\epsilon^2} \right) \right). \tag{4.18}$$

At each time step, Equation 4.18 is evaluated twice per actuator point. The first evaluation uses the kernel size $\epsilon = \epsilon^{LES}$ to obtain the part of the induced velocity which is already resolved by the LES. The second evaluation sets $\epsilon = \epsilon^{Opt}$, which results in the induced velocity which would have been observed in a highly resolved ALM-LES simulation, allowing for $\epsilon^{LES} = \epsilon^{Opt}$. Finally, under-relaxation is applied to determine the updated subfilter velocity correction, accounting for the difference in resolved and optimal induced velocity

$$\Delta u_{i,ind}^n(x_i^k) = f_u[u_{i,ind}^n(x_i^k; \epsilon^{Opt}) - u_{i,ind}^n(x_i^k; \epsilon^{LES})]$$
$$+ (1 - f_u)[u_{i,ind}^{n-1}(x_i^k; \epsilon^{Opt}) - u_{i,ind}^{n-1}(x_i^k; \epsilon^{LES})], \tag{4.19}$$

which is added to the sampled LES velocity

$$\hat{u}_i^n(x_i^k) = u_i^n(x_i^k) + \Delta u_{i,ind}^n(x_i^k). \tag{4.20}$$

A factor $f_u = 0.1$ is recommended for the under-relaxation [149]. It is noted that AspFAST receives the force vectors from OpenFAST always at the force actuator points. Therefore, the entire FALM calculations are carried out at the force actuator point locations, and only the final corrected LES velocities are interpolated to the velocity actuator points before they are sent to OpenFAST. The entire coupling algorithm with the optional application of the FALM is shown in Algorithm 1 in Appendix 4.A.

## 4.3 Case Setup of the numerical simulations

The new simulation environment is employed to study a total of three cases. The first case serves the objective of cross-verifying the ALM implementation with four other popular research LES codes (Section 4.3.1). The remaining two cases concern the objective of testing the FALM implementation and assessing its performance compared to the ALM. In the second case, the FALM is applied to a translating constant chord wing (Section 4.3.2), whereas in Section 4.3.3 the FALM is applied to the NREL 5-MW reference wind turbine. For both turbine cases, the focus is on modelling the rotor since the reference data in Section 3.1 only includes the rotor forces, and the aim in Section 3.3 is to study the impact of the FALM on the rotor performance in isolation. Modelling the tower and nacelle with an immersed boundary method [208] or including the nacelle by means of an anisotropic Gaussian body force [209] would further improve the accuracy of especially the near wake predictions.



All cases use uniform inflow with a specified reference velocity $u_i^{ref} = (U_\infty, 0, 0)$. The boundary conditions in the streamwise and lateral directions are periodic. In order to ensure a uniform inflow with the desired reference velocity, a fringe region is included in the inlet/outlet region of the domain. Within the fringe region, an additional source term is added to the momentum equations, which drives the flow again toward $u_i^{ref}$

$$f_i^{Fringe} = \rho_b \left( \frac{\partial u_i}{\partial t} \right)^{Fringe} = -\rho_b \frac{\alpha(x,y,z)\eta}{\Delta t} (u_i - u_i^{ref}). \tag{4.21}$$

The strength of the forcing is controlled with the fringe factor $\eta$. The relaxation strength $\alpha(x,y,z)\eta/\Delta t$ is an inverse time scale, where $\alpha$ is a weighting function varying from a value of one at the inlet/outlet to a value of zero at the boundary of the fringe region according to a second order polynomial. The maximum fringe strength and extent are chosen as small as possible while still ensuring that the uniform inflow profile is recovered. The top boundary condition (BC) at $z = L_z$ enforces a vanishing vertical velocity component and vanishing gradient for the streamwise and lateral velocity components. The bottom boundary condition (at $z = 0$) in GRASP is currently only designed for the simulation of the atmospheric boundary layer; thus, it does not offer a zero-shear-stress bottom BC, yet. For the purpose of this study, an approximately zero-friction velocity $u^*$ is specified for the surface scheme of the bottom BC. This approach, in combination with the relatively coarse grid resolution, ensures that there is no boundary layer forming above the bottom boundary surface. The constraint is kept in mind for the analysis of the wake results. The chosen time step for all simulations ensures that the local Courant-Friedrich-Levy number (CFL) is kept below a value of one [190].

### 4.3.1 ALM: Cross-Verification

The implementation of the new coupling is cross-verified by performing an ALM simulation of a popular reference case, which has already been used previously to compare four research LES codes and their ALM implementation [210]. This case considers a single NREL 5-MW turbine [211] ($D = 126\,\mathrm{m}$) which is placed in a uniform laminar inflow of $U_\infty = 8\,\mathrm{m/s}$. The turbine blades are considered as rigid, and the rotational speed of the rotor is set to a constant value of $\Omega = 9.155\,\mathrm{rpm}$. At this set point, the turbine is operating

at its optimal power coefficient. The density is set to $\rho = 1\,\mathrm{kg/m^3}$. The tilt angle of the rotor is set to zero in the OpenFAST model of the turbine in order to ensure a streamwise aligned wake. As noted in Martínez et al. [210], there are two different approaches on how to obtain the blade specifications for the actuator points located between the last defined point of the NREL 5-MW turbine and the tip of the blade. Data can be either extrapolated from the last two defined data points or interpolated based on a zero chord assumption at the tip of the blade. For the present case, the latter approach is chosen, whereas the former approach is applied in Section 4.3.3, demonstrating the impact of this choice.

Initial tests with a streamwise domain length equal to the reference case ($L_x = 24\,\mathrm{D}$) showed that the forcing of the fringe region influenced the wake recovery. Therefore, the GRASP domain is extended by a factor of approximately two compared to the reference case in order to account for the length and the influence of the fringe region at the domain outflow. The coefficient for the Smagorinsky subgrid model is chosen as $C_s = 0.16$ to be consistent with the reference. For a summary of the simulation parameters, see Table 4.1. It is noted that the chosen resolution of the reference case cannot be exactly reproduced due to the current limitations of the maximum available GPU memory (using one NVIDIA A100 40GB GPU).



Table 4.1: Parameter settings for the ALM cross-verification case including the hub position of the turbine $L_{x,Hub}$, $L_{y,Hub}$, $L_{z,Hub}$, the domain size $L_x \times L_y \times L_z$, the number of actuator points for force and velocity nodes $N_F/N_V$, the non-dimensional spreading $\epsilon/D$, grid resolution $\epsilon/\Delta x$ and simulation time $T_{Sim}U_\infty/L_x$.

| $L_{x,Hub}$, $L_{y,Hub}$, $L_{z,Hub}$ | $L_x \times L_y \times L_z$ | $N_F$ | $N_V$ | $\epsilon/D$ | $\epsilon/\Delta x$ | $T_{Sim}U_\infty/L_x$ |
|---|---|---|---|---|---|---|
| 4.5D, 3D, 3D | 53.25D × 6D × 6D | 64 | 19 | 0.079 | 3.39 | ≈ 2 |

### 4.3.2 FALM: Translating Wing Test Case

The implementation of the FALM is first tested for a translating wing under uniform inflow. This case was already used in previous studies for the testing of the FALM [149, 192] and the development of an ALM tip correction [150]. A constant chord wing is placed inside the domain, centred with respect to all three axes. The spanwise direction of the wing is parallel to the y-axis. The angle of attack is $\alpha = 6^\circ$. The airfoil is of type NACA64A17, which is also used for the outermost part of the blade of the NREL 5-MW turbine. The objective is to simulate these case specifications with an unmodified version of the newly developed LES-OpenFAST coupling. To this end, the OpenFast model of the NREL 5-MW turbine is simplified to represent the single constant chord wing. In particular, the number of blades is reduced to one, the AeroDyn blade input file is modified to contain only the NACA64A17 airfoil type along the entire span of the wing, the rotor speed is set to zero and azimuth/pitch angles are adjusted to ensure the desired angle of attack $\alpha = 6^\circ$ with respect to the incoming flow. The employed subgrid model is the standard Smagorinsky model with $C_S = 0.16$. The effect of the subgrid model was found to be not crucial for this test case [149]. Calculations are carried out with the ALM and FALM for three different spreading parameters $\epsilon/c$ and two different grid resolutions $\epsilon/\Delta x$. In total, this results in a set of 12 simulations (see Table 4.2).

Table 4.2: Parameter settings for the translating wing test case, including the wing span $S$, the domain size $L_x \times L_y \times L_z$, the number of actuator points for force and velocity nodes $N_F/N_V$, the non-dimensional spreading $\epsilon/c$, grid resolution $\epsilon/\Delta x$ and simulation time $T_{Sim}U_\infty/L_x$.

| $S$ | $L_x \times L_y \times L_z$ | $N_F$ | $N_V$ | $\epsilon/c$ | $\epsilon/\Delta x$ | $T_{Sim}U_\infty/L_x$ |
|---|---|---|---|---|---|---|
| 12.5c | 2.5S × 2.5S × 2.5S | 300 | 100 | {1;2;4} | {4;8} | 3.2 |

### 4.3.3 FALM versus ALM: NREL 5-MW Turbine

After cross-verifying the basic ALM for the NREL 5-MW turbine and the FALM for the translating wing, the study concludes with a performance comparison of the ALM and FALM applied to the NREL 5-MW turbine. The case setup is identical to the one presented in Section 4.3.1. In total, four simulations are performed considering two different choices of the Gaussian spreading parameter for both ALM and FALM. The chosen values of the Gaussian spreading are typical for the simulation of a wind farm using LES/ALM on a coarse grid and therefore allow the quantification of the dependence of ALM and FALM results on $\epsilon$ in these practical use cases. The setup maintains a ratio of $\epsilon/\Delta x \approx 3$ and a constant grid spacing in x, y and z. This results in slightly different streamwise domain lengths $L_x$ since the number of grid points in GRASP has to be an integer multiple of 32. The chosen resolution is a trade-off between the available computational resources for practical applications of the ALM on wind farm scale and the full convergence of the results. It fulfils the requirement $\epsilon/\Delta x > 2$ in order to avoid numerical oscillations [190], but is below the ratio of $\epsilon/\Delta x = 5$, which has been found necessary for fully converged results [147]. Compared to the initial ALM simulations, the number of actuator points has to be significantly increased when using the FALM. Only then are the large lift gradients at the blade tip resolved, which are crucial for the calculation of the FALM correction term. A summary of the parameter settings for this case is shown in Table 4.3.

Table 4.3: Parameter settings for the ALM cross-verification case, including the hub position of the turbine $L_{x,Hub}, L_{y,Hub}, L_{z,Hub}$, the domain size $L_x \times L_y \times L_z$, the number of actuator points for force and velocity nodes $N_F/N_V$, the non-dimensional spreading $\epsilon/D$, grid resolution $\epsilon/\Delta x$ and simulation time $T_{Sim}U_\infty/L_x$.

| $L_{x,Hub}, L_{y,Hub}, L_{z,Hub}$ | $L_x \times L_y \times L_z$ | $N_F$ | $N_V$ | $\epsilon/D$ | $\epsilon/\Delta x$ | $T_{Sim}U_\infty/L_x$ |
|---|---|---|---|---|---|---|
| 4.5D, 3D, 3D | {53.1; 52.8}D × 6D × 6D | 307 | 307 | {0.079;0.11} | ≈ 3 | ≈ 2 |

## 4.4 Results

This section presents the results obtained with the GRASP-OpenFAST coupling for the test and verification cases presented in Section 4.3. Firstly, the results of the ALM cross-verification are shown in Section 4.4.1. Secondly, the FALM verification using the translating wing test case is presented in Section 4.4.2. We conclude with the comparison of

the FALM and ALM performance in Section 4.4.3. For the performance assessment of the new simulation environment, it is referred to Appendix 4.B.

### 4.4.1 ALM: Cross-Verification

The new coupling of GRASP and OpenFAST via an ALM is cross-verified by comparing the predictions for the NREL 5-MW reference turbine in uniform inflow to the ALM results of four other research LES codes. The codes considered for the comparison are LESGO (Johns Hopkins University: JHU), SOWFA (National Renewable Energy Laboratory: NREL), SP-Wind (KU Leuven: KUL) and EllipSys3D (Technical University of Denmark: DTU). The codes are compared in terms of predictions for the blade and wake quantities. Temporal averaging of the results of the four reference codes is done for one to two flow-through times $T_F$, excluding the initial flow-through time during which the flow develops. For GRASP it is found that the initial transient development takes slightly longer than $T_F$ = 1, and averaging is done across an interval of 1.85 $T_F$ starting at $t_{Sim}$ = 1.3 $T_F$ where $T_F$ is calculated with the streamwise length of the reference case ($L_x$ = 24 D) and not the extended GRASP domain. As mentioned previously, it is found that the location of the laminar-turbulent transition in the wake and its recovery in GRASP are sensitive to the strength of the fringe in the outflow region. However, even for very weak fringe forcing, mean quantities in the far wake are modified as soon as the initially created wake reaches the outflow boundary. In the present study, this influence is mitigated by choosing a very long domain length of $L_x$ = 53.25 D, which allows for a sufficiently long averaging interval before the initial wake interacts with the fringe forcing.

The five ALM implementations are first compared in terms of their predictions for mean quantities along the spanwise direction of the blade. The mean distributions of angle of attack $\overline{\alpha}$, axial velocity $\overline{u}_x/U_\infty$ and drag/lift force are shown in Figure 4.2, where forces are non-dimensionalized with the rotor diameter D, the fluid density $\rho$, the inflow wind speed $U_\infty$ and the spanwise width $\Delta r$ of the respective blade segment. The four reference LES codes show overall similar distributions for angle of attack and drag/lift forces. However, the previous study of Martínez-Tossas et al. [210], which compared the four reference ALM implementations, also pointed out two main reasons for deviations between the results. The first one is the treatment of the actuator points close to the tip of the blade, whereas the second one concerns the treatment of the transitions between different airfoil types along the blade. The GRASP results are obtained from OpenFAST at the $N_V$ velocity actuator point locations, where the most outer specified point in the AeroDyn blade input file is located precisely at the blade tip. The specifications for this actuator point are not uniquely defined since the last documented point of the NREL 5-MW turbine is located further inward. For this comparison, the assumption of vanishing chord length at the blade tip is used. As a consequence, the drag and lift distributions obtained with GRASP tend toward zero at $r = R$. The second possible choice of extrapolating the chord length specified for the most outer actuator point from the two neighbouring inner points is demonstrated later in Section 4.4.3. The second cause of deviations (especially for the axial velocity profile) is the possibility of interpolating the drag and lift tables when the airfoil type is changed between two blade sections. This approach is only implemented in the EllipSys3D code, which thereby obtains smooth distributions along the blade. The remaining four codes show discontinuities at locations where the airfoil type changes. It

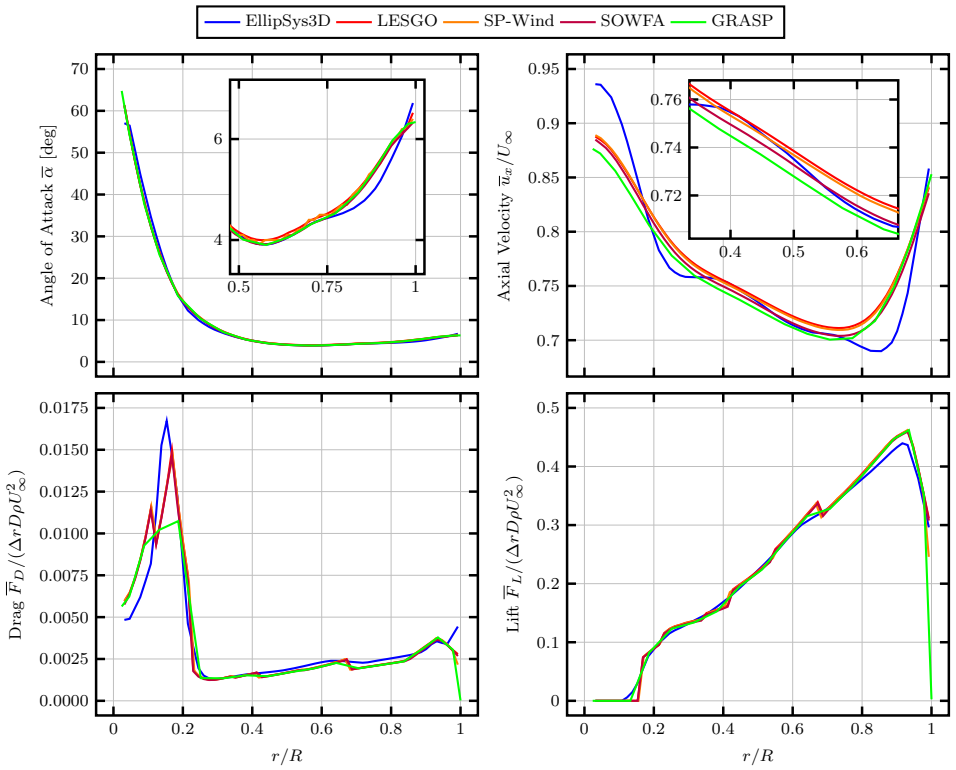


Figure 4.2: Comparison of mean angle of attack $\overline{\alpha}$, axial velocity $\overline{u}_x/U_\infty$, drag and lift per unit length along the blade span.

should be noted that the GRASP-OpenFAST coupling uses $N_F = 64$ force actuator points, as the other four codes, but in fact, the shown blade quantities are obtained at the $N_V = 19$ velocity actuator points, thus leading to coarser profiles. The blade quantities nevertheless show good agreement with the four references. The only exception is the non-resolved peak of the drag force near $r/R = 0.175$. The second notable deviation of the GRASP results is the prediction of smaller axial velocities $\overline{u}_x/U_\infty$ compared to the other three codes, which choose not to interpolate between airfoil types. This deviation is most likely due to the fact that the GRASP simulation only reaches a resolution of $\epsilon/\Delta x \approx 3.39$, which is limited by the size of the GPU memory, whereas the references use $\epsilon/\Delta x \approx 5$. Additional tests with smaller domains but refined grids show that the GRASP solution shifts towards the three references.

The small differences in the implementation of the ALM also have an effect on the wake. In Figures 4.3 and 4.4, velocity $\overline{u}_x(z)/U_\infty$ and streamwise Reynolds stress $\overline{u_x' u_x'}(z)/U_\infty^2$ profiles are shown at seven locations downstream of the turbine. The former quantity is of main concern for the power production of a hypothetical downstream turbine, whereas the latter one indicates the onset of transition in the wake. The codes predict similar velocity profiles for the laminar region of the wake $x/D \approx (0, 6)$. The only exception is the

EllipSys3D code, which already shows a stronger shear layer gradient in the rotor plane. This stronger gradient persists in the near wake region and causes the wake to transition earlier than the other two second-order finite difference codes SOWFA and GRASP (see locations $x/D = \{9; 12\}$). The two remaining codes (LESGO and SP-Wind) use pseudo-spectral discretisation for the horizontal directions, which leads to the earlier onset of laminar-turbulent transition and faster recovery of the wakes [210]. These differences become less pronounced far downstream ($x/D = 15$) when the wakes are turbulent for all codes. In the turbulent far wake at $x/D = 15$, the vertical velocity profile calculated by GRASP shows a slight asymmetry with respect to the centre axis of the wake. This asymmetry is not present for the velocity profile in the lateral direction (shown as reference in Figure 4.3 with a dashed green line) and is likely to be caused by the fact that GRASP currently does not offer a zero shear stress (slip wall) BC for the bottom boundary as explained in Section 4.3. To confirm this hypothesis, future testing with newly implemented BCs for the vertical direction is necessary.



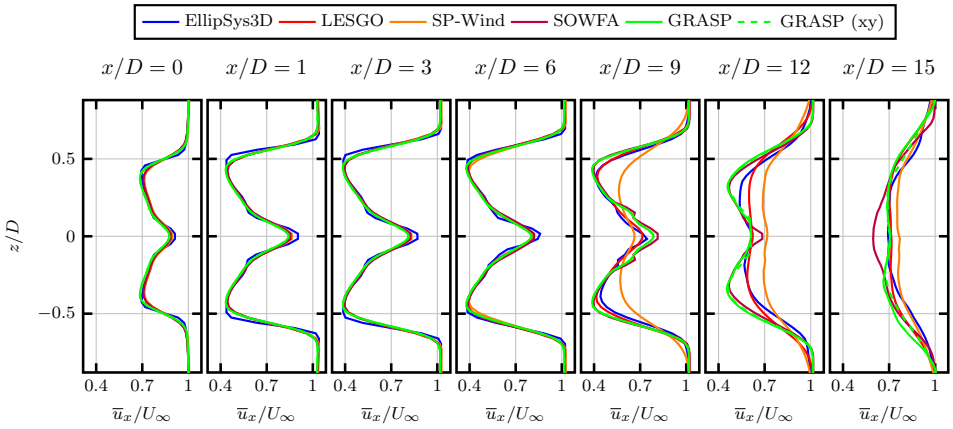


Figure 4.3: Comparison of mean streamwise velocity profiles $\overline{u}_x/U_\infty$ at seven locations in the wake downstream of the turbine. For Grasp, the profiles in the lateral direction (labelled xy) are shown in addition to the vertical profiles.

An overall comparison of the wake structure is facilitated by analysing two-dimensional contours of the mean streamwise velocity and Reynolds stress in a vertical x-z plane (see Figure 4.5 and 4.6, respectively). The Reynolds stress magnitude clearly indicates that transition is triggered the earliest in SP-Wind ($x/D \approx 5.5$), followed by EllipSys3D and LESGO. For both SOWFA and GRASP, the onset of transition is the furthest downstream at $x/D \approx 10$. GRASP uses a spatially staggered grid, which improves the accuracy of the second-order finite difference discretisation compared to the collocated grid arrangement employed in SOWFA [212]. Consequently, one would expect the onset of turbulence to occur earlier for GRASP since high wave number modes, which trigger turbulence, are less damped [210]. However, as discussed previously, the present GRASP study can only achieve a resolution of $\epsilon/\Delta x \approx 3.39$; therefore, the gain in accuracy achieved by the grid arrangement is again lost due to the coarser grid resolution. This current limitation also affects the magnitude of the Reynolds stress predicted by GRASP, which is smaller through-

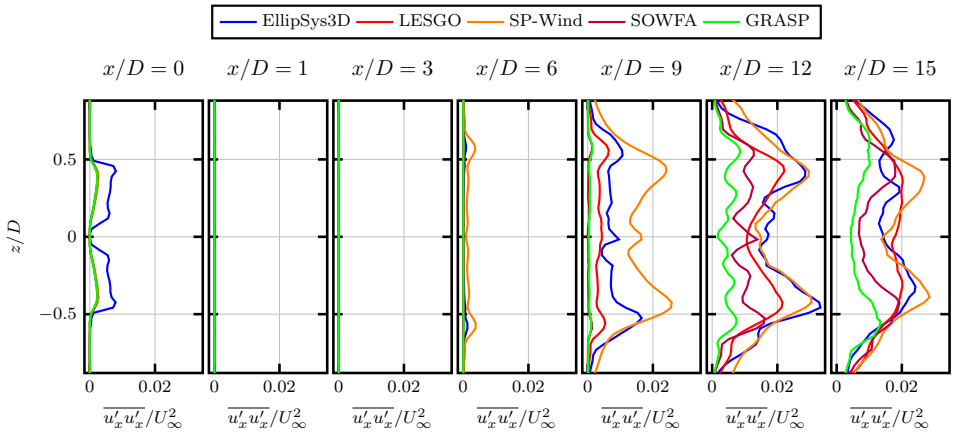


Figure 4.4: Comparison of streamwise Reynolds stress profiles $\overline{u'_x u'_x}/U_\infty^2$ at seven locations in the wake downstream of the turbine.

out the wake. Multi-GPU parallelisation of GRASP is currently under development and will enable future comparisons with finer grid resolutions.

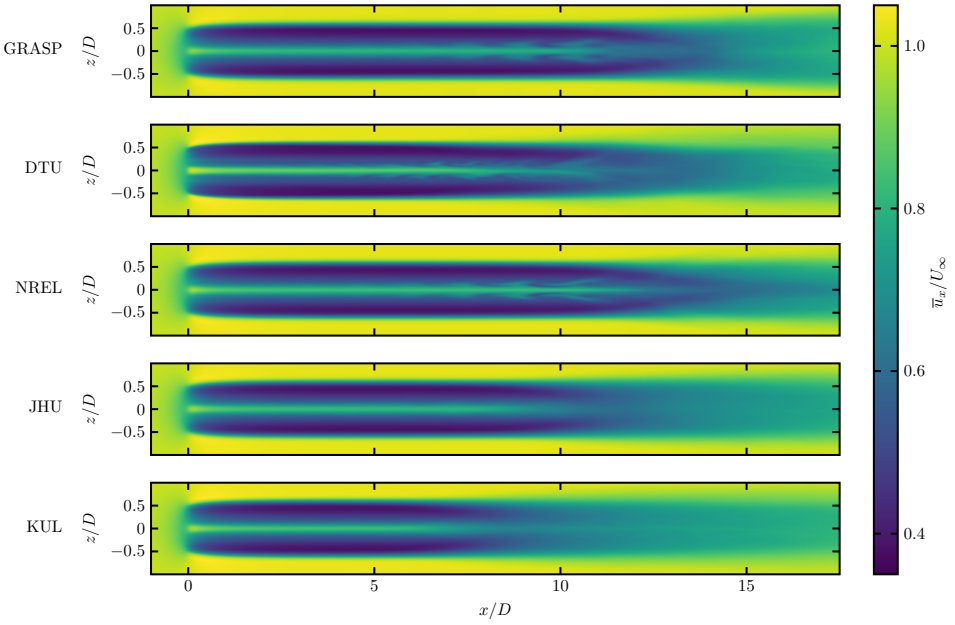


Figure 4.5: Comparison of mean streamwise velocity contours $\overline{u}_x/U_\infty$ for the five LES codes. The rotor is located at $x/D = 0$.

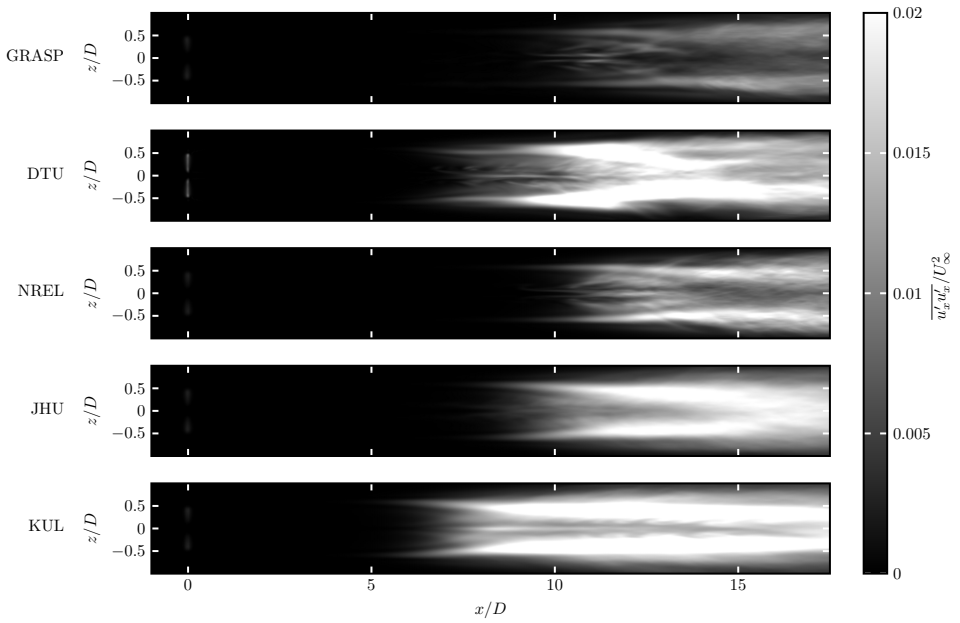


Figure 4.6: Comparison of streamwise Reynolds stress contours $\overline{u'_x u'_x}/U_\infty^2$ for the five LES codes. The rotor is located at $x/D = 0$.

### 4.4.2 FALM: Translating Wing Test Case

In addition to the introduced ALM implementation, the GRASP-OpenFAST coupling also offers an FALM extension that can improve the ALM performance on coarse grids. The implementation of the FALM is first tested using a translating wing in uniform inflow before applying it to an entire wind turbine rotor (see Section 4.3.2 for a description of the case setup). The resulting flow field forming around the wing is shown in Figure 4.7 (a). The vorticity magnitude displays the typical horseshoe shape associated with the bound circulation along the wing span and the shed vorticity at the tips of the finite-span constant chord wing. The contour of vertical velocity clearly indicates the regions of upwash and downwash present in the proximity of the wing and in its wake. Figures 4.7 (b) and (c) show a comparison of ALM and FALM results for the streamwise vorticity $\omega_x$ and lateral vorticity $\omega_y$ at the wing location $x/S = 0$ where the bound vortex $\omega_y$ is located and in the wake at $x/S = 0.25$ where only the tip vortices $\omega_x$ remain. It is important to note that there are only minor differences between the two models since the FALM also uses the same coarse $\epsilon$ to project the actuator point forces onto the LES grid. The FALM thus mainly affects the local quantities along the wing (like induced velocity and lift), on which we focus in the following.

The wing is simulated using both ALM and FALM for a set of different kernel widths $\epsilon/c = \{1; 2; 4\}$ and grid resolutions $\epsilon/\Delta x = \{4; 8\}$. The reference study of Martínez-Tossas and Meneveau [149] ran the simulations for all choices of the kernel width with the same very high grid resolution. In their study, even the smallest kernel width $\epsilon/c = 0.25$ corresponded

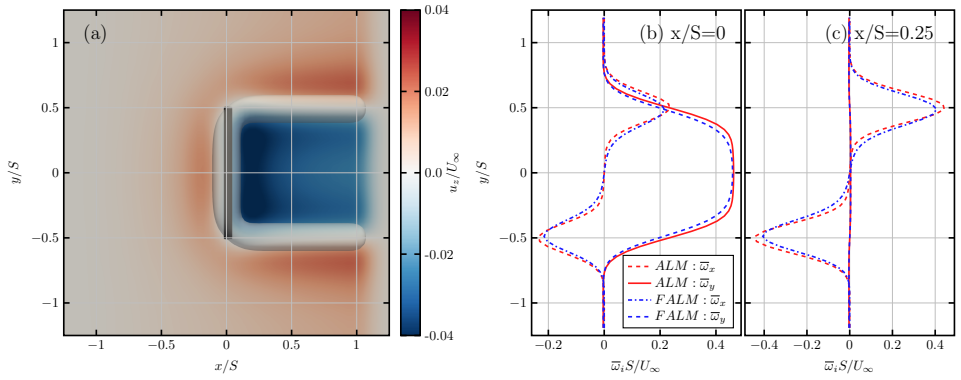


Figure 4.7: Vertical velocity field $u_z/U_\infty$ and isosurface of the non-dimensional vorticity magnitude $\overline{(\omega_i\omega_i)^{1/2}}S/U_\infty \approx 0.31$ around the translating wing used for testing of the FALM implementation (a). Comparison of the streamwise vorticity $\omega_x$ and lateral vorticity $\omega_y$ at the wing location $x/S = 0$ (b) and in the wake $x/S = 0.25$ (c) as obtained with the ALM and FALM. All the results are obtained for the parameter choice $\epsilon/c = 2$ and $\epsilon/\Delta x = 4$.

to a relative resolution of $\epsilon/\Delta x \approx 13$. In the present study, we choose to follow another approach since the application of FALM for full wind turbine rotors involves significantly smaller ratios $\epsilon/\Delta x < 5$. Otherwise, the advantage of the FALM, which is to enable coarser grid resolutions, would be lost. Instead, we choose to study the convergence of the results for lift coefficient and subfilter velocity correction on two coarser grids for each kernel width $\epsilon/c$.

Figure 4.8 shows the magnitude of the subfilter correction $|\overline{\Delta u}_{ind}|$ along the span of the wing. Large magnitudes are limited to the proximity of the wing tips, where the correction is needed to add the missing downwash, which is not resolved by LES due to a suboptimal kernel width $\epsilon^{LES} > \epsilon^{Opt}$. While for kernel widths of $\epsilon/c = \{1; 2\}$ the correction is essentially zero in the midsection of the wing, the largest width $\epsilon/c = 4$ requires a correction of the results for all spanwise locations. The amount of downwash resolved by the LES increases with decreasing LES kernel width, thus leading to a lowered magnitude of the subfilter correction along the entire span of the wing. As can be seen in the inset of Figure 4.8, the subfilter correction is already converged for a grid resolution of $\epsilon/\Delta x = 4$ for all three choices of the kernel width $\epsilon/c = \{1; 2; 4\}$. This finding is in agreement with previous results, which reported that convergence of the solution can be expected for grid resolutions of $\epsilon/\Delta x > 2.8$ [149]. The corresponding convergence behavior of the lift coefficient $C_L$ is shown in Figure 4.9 for both the ALM and FALM, where the additional black dots denote the ALM reference solution obtained for $\epsilon^{LES} = \epsilon^{Opt} = 0.25c$ (taken from Martínez-Tossas and Meneveau [149]). In general, the lift distributions obtained with both models already indicate convergence for the coarser grid resolution of $\epsilon/\Delta x = 4$ for all three choices of $\epsilon/c$. It is noted, though, that convergence is slightly slower for smaller kernel widths. This delay can be observed most clearly for the ALM results obtained with $\epsilon/c = 1$ in the region of the two local minima of the lift distribution.

The behaviour of the FALM is now studied explicitly for the results obtained with

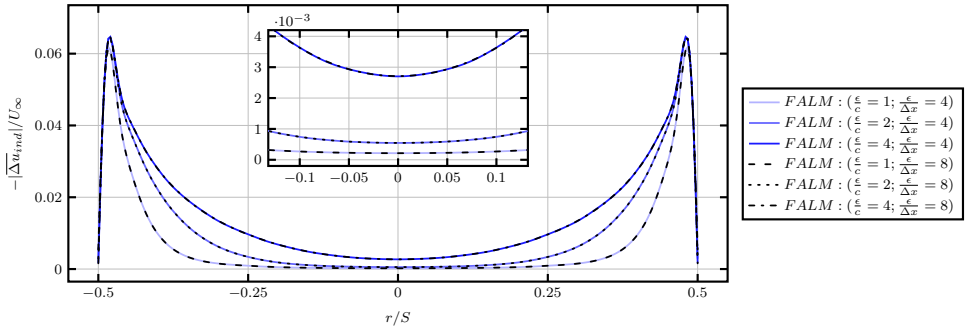


Figure 4.8: Convergence of the magnitude of the FALM subfilter correction $|\overline{\Delta u_{ind}}|$ along the span of the wing for different kernel widths $\epsilon/c$.

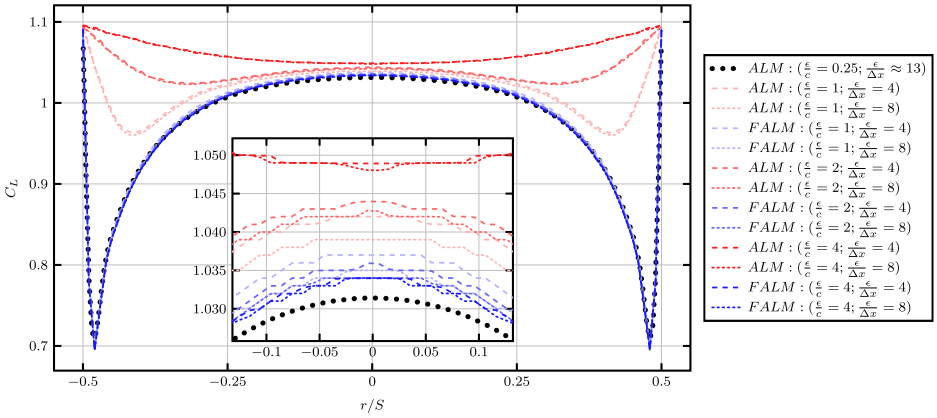


Figure 4.9: Convergence of the lift coefficient $C_L$ along the span of the wing for different kernel widths $\epsilon/c$ using both ALM and FALM. The black dots denote the ALM reference solution obtained for $\epsilon^{LES} = \epsilon^{Opt} = 0.25c$ (taken from Martínez-Tossas and Meneveau [149]).

$\epsilon/\Delta x = 8$. Figure 4.10 shows the resolved induced velocity $|\overline{u}_{ind}^{LES}|$ and the subfilter correction $|\overline{\Delta u}_{ind}|$ for varying kernel widths. Smaller LES kernel widths $\epsilon^{LES}$ lead to larger lift gradients at the tip (see Figure 4.9), which in turn create stronger tip vortices. The consequences are stronger induced velocities along the wing span, especially in the proximity of the tip. In contrast, a wide kernel of $\epsilon/c = 4$ is insufficient to resolve the peaks in downwash close to the tips. It leads to a monotonic distribution of the downwash with respect to the half-wing length, only showing one maximum at the wing centre. Furthermore, the distribution of optimal induced downwash $|\overline{u}_{ind}^{Opt}|$ does not depend on the LES kernel width $\epsilon^{LES}$. Therefore, smaller LES kernel widths require a smaller subfilter correction, as is to be expected. The main benefit of the FALM is clearly visible in Figure 4.9. Even the smallest of the three studied kernel widths exceeds the optimal value of $\epsilon^{Opt}/c = 0.25$ by a factor of four. As a result, the lift distribution along the wing span varies strongly with the LES kernel width when using the ALM without correction. Further, the lift is significantly

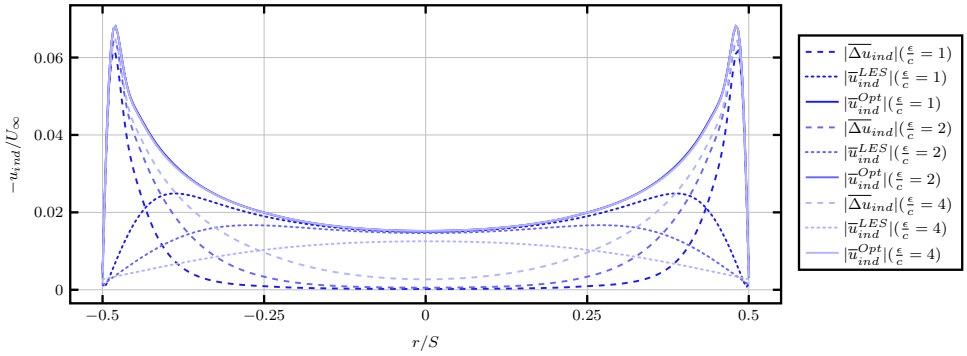


Figure 4.10: Dependence of the induced velocities $u_{ind}$ on the kernel width $\epsilon/c$ for a grid resolution of $\epsilon/\Delta x = 8$.

4

overpredicted near the tips due to underpredicted downwash. In contrast, the FALM captures the strong decrease in lift near the tips and, importantly, displays a solution that is independent of kernel width even for kernel widths exceeding the optimum value by a factor of sixteen. The epsilon-independent solution further matches the reference ALM lift profile obtained with $\epsilon^{Opt}$. At this point, it should be noted that the performance of the FALM relies on the numerically calculated lift gradient (recall equation 4.18). An accurate calculation of the gradient is only possible with a large number of actuator points. For the present wing test case, a value of $N_F = 300$ is found to be necessary to obtain the correct magnitude and shape of the lift profiles. This undesirable effect could be at least partially compensated for by using a non-uniform actuator point spacing with high resolution only in the proximity of the wing tips.

### 4.4.3 FALM versus ALM: NREL 5-MW Turbine

After testing the implementation of the FALM with the translating wing example, its performance for a wind turbine is now compared to the ALM. The studied case is identical to the one used for the cross-verification of the ALM, i.e. the NREL 5-MW reference turbine in uniform inflow (case parameters are shown in Section 4.3.3). Both ALM and FALM simulations are carried out for $\epsilon/D = \{0.079; 0.11\}$ while maintaining a grid resolution of $\epsilon/\Delta x = 3$ for each case. The aim is to study the differences in blade quantities and wake behaviour for these larger Gaussian spreading widths and coarser grids since they are of practical importance when simulating an entire wind farm, but also cause a significant overprediction of the generated power if no additional correction like the FALM is employed [213]. For the present comparison, both models use $N_F = N_V = 307$ to eliminate any possible influence of the number of actuator points. However, the required number of actuator points for the ALM and FALM is, in general, different, and it is referred to Appendix 4.C for a detailed convergence study.

The FALM computes a subfilter correction added to the sampled LES velocity based on the optimal induced velocity and its resolved part along the blade. The mean profiles of these three velocities are shown in Figure 4.11. As observed in the previous section for the translating wing, large magnitudes of the induced velocities are limited to the inner and outer parts of the blade, where the root and tip vortices cause strong induction.

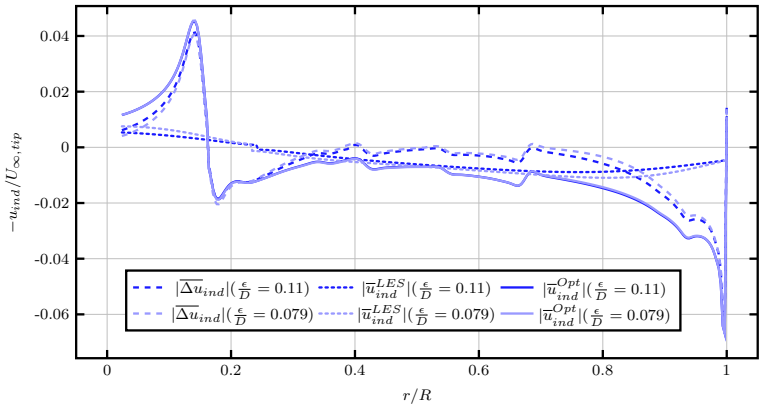


Figure 4.11: Magnitudes of the induced velocities $u_{ind}$ along the blade span of the NREL 5-MW turbine shown for two different Gaussian kernel widths. All velocities are normalised with the magnitude of the unperturbed incoming velocity at the blade tip $U_{\infty,tip}$. The signs are determined by computing the alignment with respect to the lift force.

In the middle section of the blade the coarse resolution and large spreading widths are sufficient to resolve the major share of the induced velocities, whereas toward the tip, the ratio of optimal and resolved induced velocity attains a ratio as large as $|\overline{u}^{Opt}_{ind}|/|\overline{u}^{LES}_{ind}| \approx 12$. The smaller Gaussian spreading $\epsilon/D = 0.079$ results in larger resolved induced velocity, especially in the interval $r/R = (0.7, 0.9)$, but still relies strongly on the subfilter correction in order to obtain the optimal downwash distribution. Further, it should be noted that the inflexion points visible in the profiles of the correction and the optimal velocity are due to the discontinuities of the lift force distribution caused by the sudden changes of the airfoil type along the blade (see right centre panel in Figure 4.12). The lift force profile also explains the sign change of the optimal induced velocity at $r/R \approx 0.16$. The inner part of the blade of the NREL 5-MW turbine ($r/R < 0.16$) consists of circular airfoils, which do not provide any lift. Therefore, the positive velocity correction found close to the blade root is the upwash induced by the shed vorticity in the proximity of the strong lift gradient at $r/R \approx 0.16$.

The resulting profiles of angle of attack, axial velocity and forces along the blade are presented in Figure 4.12. It is important to note that for this section, the second possible approach to obtain the blade specifications at the tip is employed, illustrating its impact on the results (data are now extrapolated from the two neighbouring inner blade points instead of interpolated based on a zero chord assumption). This user choice modifies the lift profile at the blade tip. It is important to keep this source of possible deviations between different ALM implementations in mind (compare with the other approach shown in Figure 4.2). As can be seen in the inset shown in the top left corner of Figure 4.12, the FALM correction results in a reduced angle of attack for $r/R > 0.75$. This change, in turn, leads to a lower lift force, which translates to reduced tangential and normal forces, ultimately decreasing the generated torque/power and thrust force. This finding is confirmed quantitatively in Table 4.4, where comparisons of ALM and FALM predictions for the rotor's

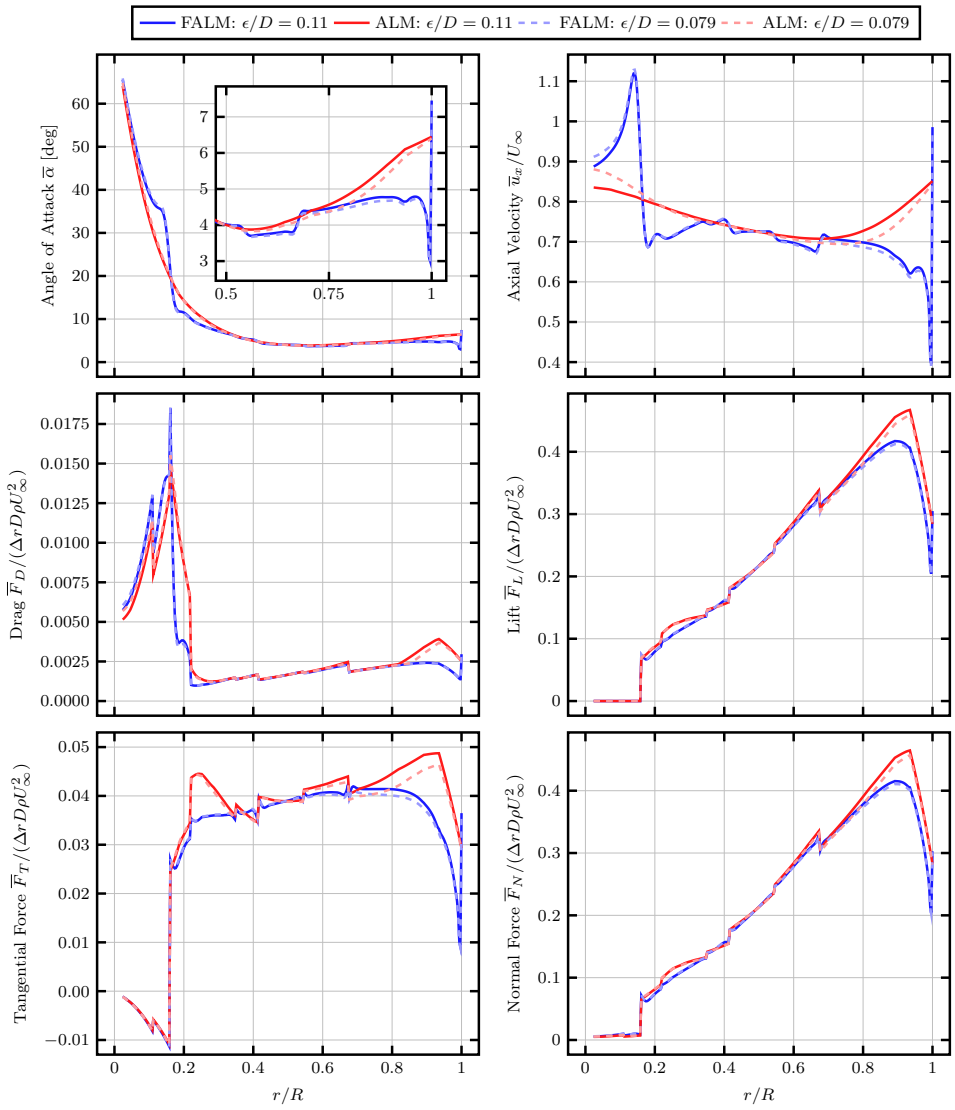


Figure 4.12: ALM versus FALM: Comparison of mean angle of attack $\overline{\alpha}$, axial velocity $\overline{u}_x/U_\infty$, drag, lift, tangential and normal force per unit length along the blade span. The forces are non-dimensionalised in the same manner as done for the ALM results (see Section 4.4.1).

thrust coefficient $C_T$ and aerodynamic power coefficient $C_P$ are shown. From the force profiles as well as the integral rotor quantities, it can be concluded that the FALM is successful in reducing the dependence of the solution on the width of the Gaussian spreading on coarse grids but cannot provide a fully independent solution (in terms of $\epsilon$ and $\Delta x$). This finding is confirmed by the study of Blaylock et al. [193] who compared the dependence of

the FALM solution on varying coarse meshes using a resolution of $\epsilon/\Delta x = 2$ instead of the $\epsilon/\Delta x = 3$ employed in this study. We expect that increasing $\epsilon/\Delta x$ would lead to improved convergence. Furthermore, it should be noted that the preceding analysis focused on the modelling error inherent to the ALM for different $\epsilon^{LES}$ rather than comparing the error with another model like the blade element momentum (BEM) model, which relies on very different simplifying assumptions. This focus is motivated by the fact that the FALM aims to correct the ALM results towards the mathematical solution of the underlying model equations solved for the optimal $\epsilon^{Opt}$ and thus its effectiveness should be judged in this context.

Table 4.4: Comparison of ALM and FALM predictions for the aerodynamic power and thrust coefficients of the NREL 5-MW rotor. For both models, absolute values are shown for $\epsilon/D = 0.079$ and, in addition, relative increases for the coarser $\epsilon/D = 0.11$.



| **Power** | |
|---|---|
| $C_P(\epsilon/D = 0.079)$ [-] | $100 * \left( \frac{C_P(\epsilon/D=0.11)}{C_P(\epsilon/D=0.079)} - 1 \right)$ [%] |
| ALM: 0.569 | ALM: +3.51% |
| FALM: 0.514 | FALM: +1.56% |
| **Thrust** | |
| $C_T(\epsilon/D = 0.079)$ [-] | $100 * \left( \frac{C_T(\epsilon/D=0.11)}{C_T(\epsilon/D=0.079)} - 1 \right)$ [%] |
| ALM: 0.838 | ALM: +1.31% |
| FALM: 0.805 | FALM: +0.50% |

We conclude this study with an assessment of how the wake development is influenced by the application of the FALM. In Figure 4.13, mean streamwise velocity profiles are shown in the wake downstream of the turbine, ranging from $x/D = 0$ to $x/D = 15$. It is possible to identify two main trends. Firstly, the wake is more stable for the case of larger spreading width $\epsilon/D = 0.11$. In fact, the first signs of wake recovery are only visible for the location furthest downstream at $x/D = 15$. This is likely to be caused by the smaller gradient of the shear layer, which is smoothed out by the larger width of the Gaussian spreading. In addition, the coarser resolution associated with this case delays the onset of transition as discussed in Section 4.4.1. Secondly, even for the same choices of $\epsilon$ and $\epsilon/\Delta x$, the wake differs between ALM and FALM. The reduced normal loading of the blades when using the FALM leads to both less induction and a less steep shear layer in the rotor plane at $x/D = 0$. As a result, the application of the FALM delays the laminar-turbulent transition for both choices of $\epsilon$. This conclusion is limited to laminar inflow scenarios, and further investigations are necessary to determine whether this finding holds true for turbulent inflow.

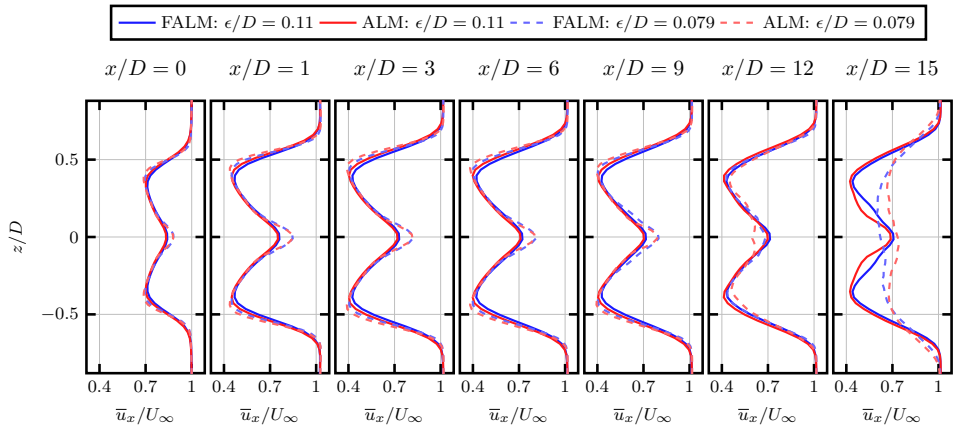


Figure 4.13: ALM versus FALM: Comparison of mean streamwise velocity profiles $\overline{u}_x/U_\infty$ at seven locations in the wake downstream of the turbine.

## 4.5 Conclusions

The objective of this work was the development and subsequent verification of a new simulation environment that can give combined insights into the respective dynamics of the flow and individual turbines in a wind farm. Such an environment could then be further utilised to develop new dynamic wind farm control strategies, which require simultaneous knowledge about the development of the turbine wakes, the loads acting on the turbines and the generated power. Additionally, the new environment should enable the use of GPU computing resources.

This aim was achieved by developing a new coupling between the GPU-resident LES code GRASP and the multi-physics turbine simulation tool OpenFAST. The coupling was implemented via an ALM and optionally offers the FALM extension. The ALM implementation was cross-verified with four other popular research LES codes with an ALM by comparing their performance in terms of blade and wake quantities for the NREL 5-MW turbine in uniform inflow. The new coupling predicted similar results for the lift/drag forces along the blade and showed a good agreement for the near wake behaviour when compared to the other four codes, thus confirming a successful implementation of the new ALM. Differences were found for the far wake development predicted by GRASP — in particular, the magnitude of the Reynolds stresses was lower than for the four references, and the mean streamwise velocity showed a slight asymmetry. The former finding was attributed to the coarser grid resolution used for GRASP compared to the references, whereas the latter was expected to be caused by the limitation that GRASP currently does not offer a slip wall BC for the bottom boundary. The implementation of the FALM was tested with a simple translating wing, and its performance was subsequently compared to the ALM for the NREL 5-MW turbine. The FALM proved to be successful in reducing the dependence of the blade loads and the generated power on the width of the Gaussian kernel used to project the point forces onto the LES grid. Furthermore, the wake predicted with the FALM was shown to transition later than for the traditional ALM when

considering uniform inflow.

Future work will be oriented toward two objectives. Firstly, the development of a multi-GPU version of GRASP can enable the study of cases with larger domains and higher resolution. Secondly, the new simulation environment can be utilised to study new wind farm control strategies, including the turbulent ABL.

# 4.A GRASP-OpenFAST Coupling via the (filtered) Actuator Line Model

**Algorithm 1**

**while** $n < n_{tmax}$ **do**
  **ASPIRE**: Transfer LES velocity data from GPU to CPU
  **for** $m \longleftarrow 1$ to $N_{Blades}$ **do**
    **for** $k \longleftarrow 1$ to $N_{V,F}$ **do**
      **if** FALM **then**
        **AspFAST**: Sample LES velocity at force actuator point
        **AspFAST**: Compute the new subgrid velocity correction:
          Equations 4.14, 4.15, 4.16, 4.17, 4.18 and 4.19
        **AspFAST**: Correct the sampled LES velocity: Equation 4.20
        **OpenFAST**: Interpolate velocity from force to velocity actuator point
      **else**
        **AspFAST**: Sample LES velocity at velocity actuator point
      **end if**
      **OpenFast**: Compute velocity magnitude: Equation 4.5
      **OpenFast**: Compute angle of attack: Equations 4.6, 4.7
      **OpenFast**: Compute actuator point force: Equations 4.8, 4.9
      **if** FALM **then**
        **AspFAST**: Store actuator point force
      **end if**
    **end for**
  **end for**
  **AspFAST**: Project point forces onto LES grid: Equations 4.10, 4.11
  **ASPIRE**: Transfer the wind turbine body force data from CPU to GPU
  **GRASP**: Advance the governing LES equations (Equations 4.1 and 4.2) by one time step
  $n+ = 1$
**end while**

# 4.B Performance Assessment

This appendix provides an overview of the computational speed associated with the different configurations of the new simulation environment. In particular, it is distinguished between three configurations: the LES code operating in isolation, the LES code coupled

one-way to OpenFAST (only velocities are sampled from the LES and passed on) and coupled two-way to OpenFAST (exchange of velocities and forces). To this end, a test case based on the ALM cross-verification from Section 4.3.1 is designed considering three different grid resolutions ($\Delta x/D$ = 1/63, $\Delta x/D$ = 2/63 and $\Delta x/D$ = 4/63), which results in a total of nine cases. The domain size is $L_x \times L_y \times L_z = (8.12D)^3$ with the turbine hub centred within the cubic domain. For all cases, the number of actuator points is kept constant as $N_F$=$N_V$ = 64 and the ratio of Gaussian kernel width to grid spacing is fixed as $\epsilon/\Delta x$ = 2. All nine cases are advanced for 3000 steps in time to collect robust wall time estimates. In addition, the wall time results from Section 4.3.1, 4.3.3 and Appendix 4.C are collected to present a complete overview of the computational performance in Figure 4.14. Simulations are performed on two different computing platforms. Firstly, utilising a single GPU node on an HPC cluster equipped with one NVIDIA A100-SXM4-40GB GPU and 12 Intel(R) Xeon(R) CPU @ 2.20GHz (abbreviated as A100 in 4.14). Secondly, utilising a standalone GPU machine equipped with one NVIDIA GeForce RTX 3090-24GB GPU and a total availability of 64 Intel(R) Xeon(R) CPU E7-4809 v4 @ 2.10GHz (abbreviated as GTX in 4.14). It should be noted that the three large test cases using $\Delta x/D$ = 1/63 are not permitted by the 24GB memory of the smaller GeForce RTX GPU. For the six cases permitted by both GPU memories, the single HPC node equipped with the A100 leads to better performance for all cases.

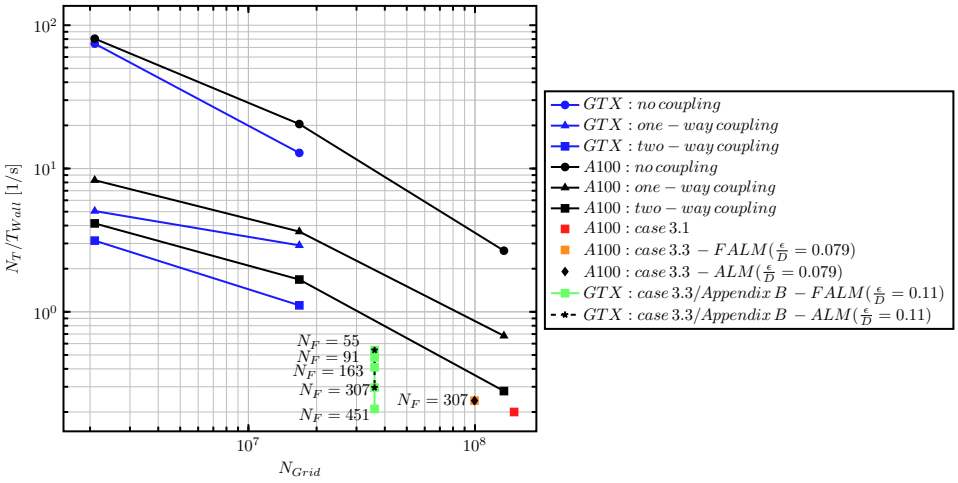


Figure 4.14: Scaling of the computational speed in terms of computed time steps per wall clock second with increasing problem size $N_{Grid}$. Results are shown for the standalone LES code (no coupling), one-way and two-way coupling. Furthermore, the results from Section 4.3.1, 4.3.3 and Appendix 4.C are presented. The number of actuator points is $N_F$ = 64 except if specifically noted otherwise in the plot next to the corresponding marker.

Furthermore, the differences between the different coupling configurations and the additional expense of the FALM can be assessed. The standalone LES code is approximately one order of magnitude faster than the two-way coupled code for the medium and large test cases. This is to be expected as the calculations performed by AspFAST and OpenFAST are both carried out on CPUs and also require additional data transfer between the

GPU and the CPU. The one-way coupling only performs the sampling of the velocities at the actuator points and the OpenFAST internal calculations, but does not require the projection of the body force onto the LES grid, which results in approximately two times faster speed compared to the two-way coupling. The simulation from Section 4.3.1 (red square in Figure 4.14) does not reach the speed of the test case for two reasons: Firstly, the number of grid cells $(N_x, N_y, Nz)$ are not integer powers of two, which leads to a suboptimal division of the problem on the GPU. Secondly, the $\epsilon/\Delta x$ ratio is equal to five rather than two which requires the projection of the body force onto more LES grid points (as the projection is only calculated for grid points where the strength of the Gaussian kernel $\eta_\epsilon$ is larger than 0.1% of its center value).

To conclude, the computational overhead added by the FALM is assessed. The additional computation of the subgrid velocity correction (Equations 4.14- 4.20) is found to be negligible (black diamond matches orange square and black stars match the green squares in Figure 4.14). The added overhead is rather determined by the required number of actuator points $N_F$ for the FALM. The convergence of the FALM results is studied in Appendix 4.B, concluding that at least $N_F$ = 150 is required compared to well-converged ALM results with $N_F$ = 55. The FALM with $N_F$ = 163 reduces $N_T/T_{Wall}$ by about 25% compared to the ALM with $N_F$ = 55.



## 4.C Convergence of the FALM results

The quality of the FALM results relies on the accurate calculation of both the resolved and optimal induced velocity along the blade in Equation 4.18. The smallest length scales across which the resolved/optimal induced velocities can vary are given by the widths of the Gaussian kernels $\epsilon^{LES}$ and $\epsilon^{Opt}$, respectively. Since in general $\epsilon^{LES} \gg \epsilon^{Opt}$, the latter one imposes the requirement of finer actuator point spacing along the blade compared to the traditional ALM. This fact becomes apparent in Figure 4.15 (a) where the convergence of the lift force near the blade tip is studied as a function of the number of actuator points (using the FALM $\epsilon/D$ = 0.11 case defined in Section 4.3.3).

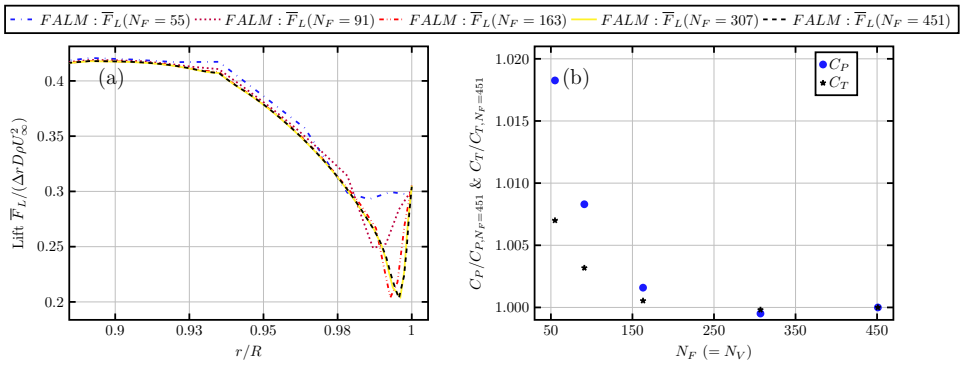


Figure 4.15: Convergence of the FALM results ($\epsilon/D$ = 0.11) for the NREL 5-MW turbine with increasing number of actuator points ($N_F = N_V$) shown for the lift force per unit length in the outer region of the blade (a) and the aerodynamic thrust and power coefficients of the rotor normalized with their respective values obtained for $N_F$ = 451 (b).

It can be seen that the FALM using $N_F = 55$ is incapable of predicting the sharp drop of the lift force at the blade tip due to the presence of the tip vortex. While the accurate prediction of the magnitude of this drop requires at least $N_F = 163$ points, full convergence of the lift profile is only obtained for $N_F \approx 300$. The aerodynamic power and thrust coefficients $C_P$ and $C_T$ of the rotor further confirm these findings (Figure 4.15 (b)), where the percentage differences between the power and thrust coefficients obtained for $N_F = 55$ and $N_F = 307$ are $\approx 1.8\%$ and $\approx 0.7\%$. In contrast, the differences for the ALM are only $\approx 0.014\%$ and $\approx 0.011\%$, indicating convergence of the ALM results with $N_F = 55$.

# 5

# Unsteady aerodynamic loads on pitching airfoils represented by Gaussian body force distributions



*The actuator line method (ALM) is an approach commonly used to represent lifting and dragging devices like wings and blades in large-eddy simulations (LES). The crux of the ALM is the projection of the actuator point forces onto the LES grid by means of a Gaussian regularisation kernel. The minimum width of the kernel is constrained by the grid size; however, for most practical applications like LES of wind turbines, this value is an order of magnitude larger than the optimal value, which maximises accuracy. This discrepancy motivated the development of corrections for the actuator line, which, however, neglect the effect of unsteady spanwise shed vorticity. In this work, we develop a model for the impact of spanwise shed vorticity on the unsteady loading of an airfoil modelled as a Gaussian body force distribution, where the model is applicable within the regime of unsteady attached flow. The model solution is derived both in the time and frequency domain and features an explicit dependence on the Gaussian kernel width. We verify the model with ALM-LES for both pitch steps and periodic pitching. The model solution is compared to Theodorsen theory and validated with both computational fluid dynamics (CFD) using body-fitted grids and experiment. It is concluded that the optimal kernel width for unsteady aerodynamics is approximately* 40% *of the chord. The ALM is able to predict the magnitude of the unsteady loading up to a reduced frequency of* $k \approx 0.2$.

This chapter is based on the following publication:

[159] E. Taschner, G. Deskos, M. B. Kuhn, J. W. van Wingerden, and L. A. Martínez-Tossas. "Unsteady aerodynamic loads on pitching airfoils represented by Gaussian body force distributions". In: *Accepted for publication in Journal of Fluid Mechanics* (2025)

# 5.1 Introduction

Today's wind energy generation relies on large-scale wind farms operating optimally in the lower (surface) part of the atmospheric boundary layer (ABL) [21, 185]. Optimal performance of wind farms requires accurate prediction of the aerodynamic characteristics of the individual turbines and their interaction with wakes and the ambient atmospheric flow. The unsteady ABL flow is commonly computed using large-eddy simulation (LES), where wind turbines are parameterised with actuator models like actuator disks or actuator lines [131].

The actuator line model (ALM), initially developed by Sørensen et al. [137], represents lifting and dragging devices, such as blades and wings, as discrete lines. It allows for the distribution of body forces along these lines, effectively simulating the influence of solid bodies on the flow. As such, when the ALM is utilised to model a wind turbine rotor, it is capable of capturing the footprint of the individual blades and the associated vortex system composed of the bound, tip and root vortices [214, 190, 57, 147]. Nevertheless, the ALM is still relatively simple to implement thanks to its suitability with Cartesian grids. This balance between simplicity, physical accuracy, and computational cost has contributed to the ALM's ongoing popularity more than twenty years after its inception [141, 131]. During these years, the ALM has enabled many advancements in wind energy and beyond, for example, the study of ABL-turbine interaction [215, 108], the analysis of near-wake vortex dynamics like the tip vortex instability [59, 216, 217, 218], the study of novel wake control strategies [71, 73], or the simulation of vertical axis wind turbines [219] and complex wing configurations [220].



## 5.1.1 Gaussian force regularisation and smearing corrections for the actuator line model

The accuracy of the ALM approach depends on the force projection from the discrete lines onto the LES grid using a regularisation kernel, $\eta_\epsilon$. In its most general form in three-dimensional space, the regularisation of a single discrete actuator point force $\boldsymbol{f}^{Act}$ across the volume $\Omega$ takes the following form,

$$\boldsymbol{f}^{Reg} = \iiint_{\Omega} \boldsymbol{f}^{Act} \eta_\epsilon \, \mathrm{d}\boldsymbol{x}, \, \boldsymbol{x} \in \Omega \text{ with } \eta_\epsilon = \frac{1}{\pi^{3/2}\epsilon^3} e^{-(|\boldsymbol{x}-\boldsymbol{x}^{Act}|)^2/\epsilon^2}, \tag{5.1}$$

where $\epsilon$ is the Gaussian kernel width and $\boldsymbol{x}^{Act}$ the actuator point location. The need for calculating a convolution of the actuator forces with a regularisation kernel was introduced in the foundational ALM work by Sørensen et al. [137] in order to avoid singular behaviour, which would result from direct application of the actuator point forces on the LES grid. In their work, the shape of the regularisation kernel was chosen to be an isotropic Gaussian as introduced above, where the kernel width is constant along the entire span of the blade. Motivated by the idea that the actuator forces are ultimately supposed to model the dimension and shape of the wing or blade and the associated airfoils, a comprehensive body of literature exists aiming to improve the force regularisation accordingly [146, 191, 221, 222, 223, 224]. However, independent of the employed kernel type and shape, the minimal allowable kernel width is dictated by the grid size, $\Delta x$, employed in LES, and arguments of a minimum allowable ratio, $\epsilon/\Delta x$, have been made in order to avoid numerical

oscillations and obtain convergence. Its proposed value ranges from $\epsilon/\Delta x = 2$ [190] to $\epsilon/\Delta x \geq 4$ [225] and $\epsilon/\Delta x \geq 5$ [147].

The resulting kernel widths from grid size considerations are often an order of magnitude larger than the optimal kernel width. Martínez-Tossas et al. [146] found the optimal kernel width by maximising the agreement between the two-dimensional flow solution around an airfoil with chord, $c$, modelled as a Gaussian body force akin to the ALM, and the corresponding potential flow solution. They concluded that the optimal kernel width is of the order of $\epsilon_{Opt}/c = \mathcal{O}(10^{-1})$, which is in agreement with the earlier proposed range of $\epsilon_{Opt}/c \in [1/8, 1/4]$ [225]. Martínez-Tossas et al. [146] further noted that the optimal kernel width is not a function of the angle of attack and that the dependence on the type of lifting surface (e.g. airfoil camber and thickness) is weak. For the context of this work, it is also important to note that the conclusions of Martínez-Tossas et al. [146] regarding the optimal kernel width were drawn considering steady-state conditions.

In practice, the existing discrepancy between the conditions for the optimal and numerically allowable kernel width is the reason why the standard ALM, when employed on coarse LES grids, fails to accurately reproduce the loading in the proximity of the wing and blade tips. One of the earliest proposals to address this issue was made by Shen et al. [226] who introduced a tip loss correction for the ALM similar to the ones employed for blade element momentum theory. Progress has been made on this issue by Dağ et al. [151] (originally [227]), who observed that the bound vortex created by the ALM is also of Gaussian shape and thus similar to the shape of a Lamb-Oseen vortex. This observation was shown to be a mathematical consequence of the Gaussian force regularisation by Forsythe et al. [228] for the bound vortex and by Martínez-Tossas et al. [149] for the vorticity shed by an actuator line.

These insights enable the correction of ALM results based on the mismatch between the induced velocities along the actuator line as they result from shed Lamb-Oseen vortices, with the kernel width dictated by numerical considerations and from a reference considered optimal [150, 149, 151, 152]. These corrections—also often labelled as smearing corrections —were applied to wind turbine rotors, for example, by Meyer Forsting et al. [229], Stanly et al. [192] and Taschner et al. [158]. Meyer Forsting et al. [150] and Kleine et al. [152] also tested their corrections for unsteady operating conditions, namely the NREL 5MW turbine subject to a step in blade pitch or operating in sheared inflow. In these conditions, spanwise vorticity would also be shed in response to the varying strength of the bound vortex. The effect of this additional unsteady vorticity component is not captured by the previously mentioned corrections, which also neglect the influence of drag. Kleine et al. [152] pointed out in their work that a better understanding of drag and unsteady effects and their relation to the error caused by Gaussian regularisation with large kernel widths could help to further decrease associated errors. The impact of drag was already studied in the work of Caprace et al. [230] who developed an immersed lifting and dragging line method, which captures streamwise/spanwise and normal/spanwise shed vorticity for lift and drag forcing, respectively.

### 5.1.2 Unsteady aerodynamics in the context of the ALM

The previous outline shows that progress has been made on developing the ALM, and theoretical insights lead to corrections for practically employed kernel widths. These devel-

opments mostly focused on steady and quasi-steady conditions. The operating conditions of a wind turbine are, however, subject to various periodic and aperiodic sources of unsteadiness like shear, veer and high-frequency turbulence fluctuations in the atmospheric inflow; body motion due to flexible structures; tower shadow effects; and interaction of the blades with wakes generated by upstream turbines [231]. There also exists a variety of wind farm control strategies to mitigate wake effects on downstream turbines. These wake control strategies utilise the turbine's yaw, rotational and pitch degrees of freedom, often introducing additional sources of unsteadiness [45].

The body force approach of the ALM is at the core of its simplicity, and therefore it may not resolve phenomena associated with boundary-layer dynamics, e.g., flow separation/reattachment, laminar-turbulent transition and dynamic stall effects. Their effect on the unsteady lift and drag can only be included by means of additional models, e.g., the dynamic stall model from Leishman et al. [232]. However, even for flow scenarios corresponding to unsteady attached flow, the question remains of how Gaussian force regularisation with sub-optimal large kernel widths may impact the unsteady loading. When using sub-optimal large kernel widths, the vorticity shed in response to the wake suffers from an excess of smearing, similar to the steady case, affecting its feedback to the angle of attack (induction) and thus the loading on the blades. The role of shed unsteady spanwise vorticity has so far been neglected from previous ALM corrections [149, 150, 151, 152], and therefore it is the focus of this study.



We begin by tackling the unsteady two-dimensional incompressible, inviscid flow over a Gaussian body force, similar to the successive theoretical advancements of the ALM in steady conditions [146]. This approach links the unsteady two-dimensional ALM (or actuator point rather than actuator line) to the wealth of foundational work on the unsteady incompressible, inviscid thin-airfoil problem [233, 234, 155]. Unsteady inviscid solutions can be traced back to the pioneering work of Prandtl [235]. They noted that unsteady airfoil loading implies the shedding of circulation into the wake and suggested a first-order solution to the problem of a flapping airfoil. Birnbaum [236] solved this problem by utilising a series approximation and quantified the degree of unsteadiness with the so-called reduced frequency, $k$, a non-dimensional number given by the ratio of the time scales of the unsteady phenomena and the time needed by the flow to travel across the airfoil's semi-chord length. Since a number of solutions have been derived to address the unsteady thin-airfoil problem, it is helpful to categorise them based on two criteria [155]: firstly, whether the solution is derived in the time or frequency domain, and secondly, whether the source of unsteadiness is the inflow (e.g. sinusoidal gusts of the normal velocity) or the airfoil motion, e.g., translatory oscillation (heave) and/or rotational oscillation (pitching). Wagner [237] and Küssner [238] derived time domain solutions for the cases of unsteady body motion and unsteady inflow, respectively. Corresponding frequency domain solutions were derived by Theodorsen [239] for the case of airfoil motion and by Sears [240] for gusts.

In either case, the lift can be split into three contributions: (i) quasi-steady, (ii) apparent-mass, and (iii) wake-induced [233, 240]. The computation of contribution (iii) is based on the transfer functions $C(k)$ and $S(k)$ for Theodorsen's and Sears's solutions, respectively. These transfer functions incorporate the frequency-dependent phase and magnitude modulation of the unsteady lift caused by the shed vorticity in the wake. In principle, the

ALM inherently captures the wake-induced unsteady loading since it is modelled by the LES. However, this also raises three fundamental questions, namely

1. Does the optimal kernel width determined for steady-state conditions still apply to the unsteady case?

2. How does the error in the unsteady loading depend on $\epsilon_*$ and $k$ when employing sub-optimal large kernel widths?

3. Beyond which reduced frequencies does the ALM fail to accurately model unsteady aerodynamics even when employing the optimal kernel width and considering attached flow conditions below stall?

### 5.1.3 Objective

The present work tackles these questions for the case of unsteady attached flow over a pitching airfoil modelled as a two-dimensional Gaussian body force, i.e. the unsteady two-dimensional ALM. The detailed contributions are



1. The development of a first-order model capable of reproducing two-dimensional unsteady ALM results without relying on the use of LES. The model is formulated in the time and the frequency domain, akin to the aerodynamic models of Wagner [237] and Theodorsen [239], but stems from a formulation of the governing equations which is consistent with the ALM.

2. The establishment of a range for the optimal Gaussian kernel width for the ALM in the case of unsteady aerodynamics by comparing the model with inviscid computational fluid dynamics (CFD) using body-fitted grids and Theodorsen theory.

3. The identification of a threshold reduced frequency beyond which the ALM fails to accurately capture the unsteady airfoil loading even when employing the optimal kernel width for unsteady conditions from (ii). This identification is based on numerical and experimental validation data and a detailed comparison with Theodorsen theory.

The remainder of the paper is organised as follows. We start by formulating the unsteady two-dimensional problem and derive its general solution in terms of vorticity in Section 5.2. In Section 5.3, we then utilise the derived unsteady vorticity solution to obtain the corresponding induced velocity solution at the airfoil location by means of the Biot-Savart law. Section 5.4 builds upon the induced velocity solutions to obtain a model for the unsteady airfoil loading both in the time and the frequency domain, where the latter is compared in detail to Theodorsen theory. We verify the model predictions for the airfoil's unsteady loading by comparing them to ALM-LES in Section 5.5 and discuss the impact of neglecting non-linear contributions for the model derivation in Section 5.6. In Section 5.7, the model is validated with numerical and experimental benchmarks to establish the range of the optimal kernel width for unsteady aerodynamics and identify the limits of the ALM's applicability. We conclude with Section 5.8, where the findings are summarised and an outlook of future work is provided.

## 5.2 Flow over an unsteady two-dimensional Gaussian body force

We start by deriving the general solution for the unsteady vorticity field that forms around an airfoil represented by a two-dimensional Gaussian body force. For the derivations, we assume incompressible flow in the infinite Reynolds number limit. Following the work of Martínez-Tossas et al. [146], but retaining the time derivative term, our starting point is the two-dimensional unsteady Euler equation in non-dimensional form. We use the free stream velocity, $U_\infty$, the fluid density, $\rho$, and the airfoil's chord length, $c$, as the characteristic velocity, density and length scales, respectively, and define the dimensionless time and space coordinates $t_* = tU_\infty/c$, $x_* = x/c$, $y_* = y/c$, $\epsilon_* = \epsilon/c$, velocities $u_* = u/U_\infty$, $v_* = v/U_\infty$, pressure $p_* = p/(\rho U_\infty^2)$ and vorticity $\omega_* = \omega c/U_\infty$ to obtain

$$\frac{\partial \boldsymbol{u}_*}{\partial t_*} + \boldsymbol{u}_* \cdot \nabla_* \boldsymbol{u}_* = -\nabla_* p_* - \frac{C_x \boldsymbol{i} + C_y \boldsymbol{j}}{2\pi\epsilon_*^2} e^{-(x_*^2+y_*^2)/\epsilon_*^2}, \tag{5.2}$$

where $\boldsymbol{u}_* = (u_*, v_*)^\top$ is the velocity vector and $\boldsymbol{i}$ and $\boldsymbol{j}$ represent the streamwise and normal unit vectors. Here, the non-dimensional streamwise forcing, $C_x$, and normal forcing, $C_y$, model the impact of the airfoil on the flow, akin to the ALM. The force coefficients are functions of the time-dependent angle of attack $\alpha(t_*)$ and are regularised with a Gaussian kernel of width, $\epsilon_*$, centred at the actuator point located at $\boldsymbol{x}_*^{Act} = (x_*^{Act}, y_*^{Act})^\top = (0,0)^\top$. By taking the *curl* of equation 5.2, the pressure term can be eliminated, and one obtains a transport equation for the vorticity,

$$\frac{\partial \omega_*}{\partial t_*} + \boldsymbol{u}_* \cdot \nabla_* \omega_* = \frac{-y_* C_x + x_* C_y}{\pi\epsilon_*^4} e^{-(x_*^2+y_*^2)/\epsilon_*^2}. \tag{5.3}$$

Equation 5.3 may further be simplified by considering a linear perturbation analysis around $\omega_* = 0$, and thus $C_x = C_y = 0$ such that $\boldsymbol{u}_* = \boldsymbol{i} + \boldsymbol{u}_*^p$, $\omega_* = \omega_*^p$, $C_x = C_x^p$, $C_y = C_y^p$ and $\boldsymbol{u}_* \cdot \nabla_* \omega_* \approx \partial\omega_*^p/\partial x_*$. After these approximations, equation 5.3 becomes,

$$\frac{\partial \omega_*^p}{\partial t_*} + \frac{\partial \omega_*^p}{\partial x_*} = \frac{-y_* C_x^p + x_* C_y^p}{\pi\epsilon_*^4} e^{-(x_*^2+y_*^2)/\epsilon_*^2}. \tag{5.4}$$

For the remainder of this paper, the superscripts $^p$ are omitted for all variables, and it is understood that they refer to their respective perturbation values. It should be noted that the linearisation point of $\omega_* = 0$ implicitly assumes an infinitesimally thin non-cambered drag-free airfoil at zero mean angle of attack such that the wake of the airfoil lies on the $x$-axis at $y_* = 0$ parallel to the free stream velocity $U_\infty$. Thus, applying the derived solutions to airfoils with a non-zero base loading, camber, or thickness is an approximation since the influence of mean-flow deflection on the vorticity transport is neglected. The first effect will be observed when compared to the non-linear LES reference in Section 5.5, whereas the latter two aspects are inherently not captured by the ALM and thus also not present in the non-linear LES results. More advanced second-order approaches would be needed to take those effects into account, as for example in the Sears problem [241, 242]. The impact of the simplifying assumptions made here to arrive at the linearised vorticity transport equation 5.4 is discussed in Section 5.6. It should be noted that the made

assumptions are shared with the theory of Theodorsen [239] (see e.g. [243]). In particular, the modelling approach taken here is valid as long as the considered flow conditions correspond to unsteady attached flow across the airfoil.

Using the streamwise and normal perturbation velocities, one can define the flow angle at the actuator point $\phi = \arctan(v_*/(1+u_*))$. The flow angle is related to the angle of attack via the pitch angle $\beta$ as $\alpha = \phi + \beta$, where we consider in this work the unsteady forcing to stem from a time-dependent pitch angle, $\beta(t_*)$. It should be stressed that the angle of attack not only depends on the pitch angle, but also via the flow angle/the perturbation velocities on the unsteady vorticity field $\omega_*(x_*, y_*, t_*)$, i.e. the solution of equation 5.4. Hence, the unsteady forcing term on the right-hand side of equation 5.4 is not known a priori. It instead follows from solving the underlying feedback problem between the unsteady loading and the unsteady shed vorticity in the airfoil wake, which can be formulated in terms of the flow angle as we will show in Section 5.4. The flow angle furthermore allows us to determine the streamwise and normal force coefficients from the airfoil-specific tabulated lift $C_L$ and drag $C_D$ coefficients according to the projections

$$\begin{aligned} C_x &= -C_L \sin(\phi) + C_D \cos(\phi), \\ C_y &= \phantom{-}C_L \cos(\phi) + C_D \sin(\phi). \end{aligned} \tag{5.5}$$



While the force coefficient time histories are determined by a look-up operation from a static airfoil-specific table using the instantaneous angle of attack, the unsteadiness enters the problem via the aforementioned feedback problem, whose solution determines the angle of attack time history. This is consistent with the approach taken in Theodorsen theory, where the unsteady circulatory lift follows from the quasi-steady one via a modified angle of attack due to the unsteady shed vorticity [239]. For Theodorsen theory, the underlying employed static lift coefficient taken as input is that of the flat plate airfoil, $C_L = 2\pi\alpha$, which follows from thin airfoil theory and, in particular, the use of the Kutta condition and the Kutta-Joukowski theorem [244, 245]. The problem setup together with the definitions of the coordinate system, the velocity vector, the angles and the force projection are visualised in Figure 5.1.

Equation 5.4 is a linear non-homogeneous partial differential equation and can be solved using the method of characteristics (see Appendix 5.A). The solution for $t_* \geq 0$ is given by

$$\begin{aligned} \omega_*(x_*, y_*, t_*) = \omega_*^{IC}(x_* - t_*, y_*) \\ + \underbrace{\int_0^{t_*} \frac{-y_* C_x(s) + (x_* + s - t_*) C_y(s)}{\pi \epsilon_*^4} e^{-((x_*+s-t_*)^2+y_*^2)/\epsilon_*^2} \, \mathrm{d}s}_{\omega_*^{us}(x_*, y_*, t_*)}. \end{aligned} \tag{5.6}$$

The solution comprises two terms. The first term, $\omega_*^{IC}$, is the initial condition representing a spatio-temporal shift, $x_* - t_* = (x - U_\infty t)/c$, due to vorticity being advected by the free stream velocity, $U_\infty$, and the second term, $\omega_*^{us}$, captures the generation of shed vorticity due to the fluctuations of the unsteady forcing term (unsteady streamwise and normal Gaussian body forces). Equation 5.6 allows us to solve for the two-dimensional time-dependent vorticity field. However, if one is interested in a solution not expressed in

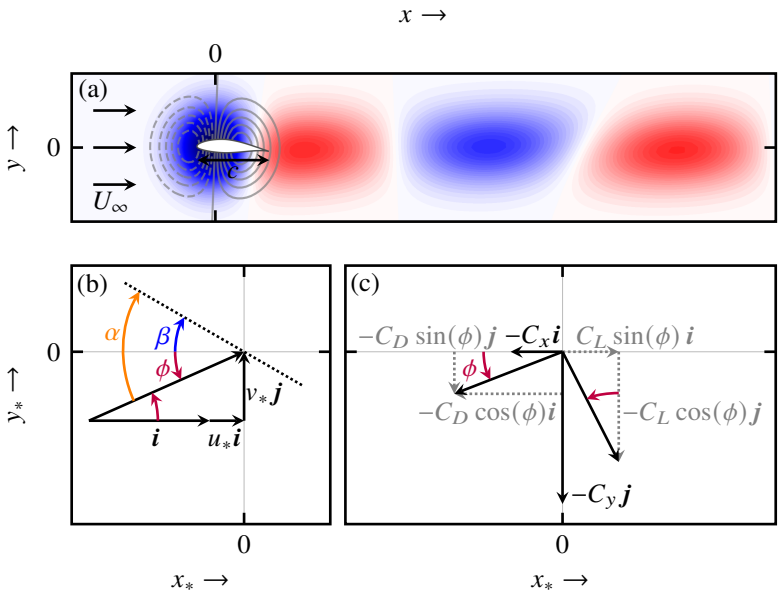


Figure 5.1: (a) The problem setup with the pitching airfoil (chord $c$) represented by a two-dimensional Gaussian body force in a free stream flow of speed $U_\infty$. The resulting unsteady vorticity source term (right-hand side of the vorticity transport equation 5.4) is illustrated by the grey dashed/solid (negative/positive vorticity source term) contour lines. The small tilt angle of the contour is caused by the source term contribution of the streamwise forcing $C_x$. The blue/red (negative/positive vorticity) contours illustrate the resulting bound vortex and shed vorticity. Note that the vorticity source term and the vorticity are time-dependent, and thus their signs and magnitudes at a given spatial location can change. (b) Definition of the angle of attack, $\alpha$, the pitch angle, $\beta$, the flow angle, $\phi$, and the velocity vector at the actuator point, $(x_*^{Act}, y_*^{Act})^\top = (0,0)^\top$. (c) Definition of the streamwise $C_x$ and normal $C_y$ force coefficients and their relation to the lift $C_L$ and drag $C_D$ coefficients. Note that all force coefficients are expressed as forces acting from the body on the fluid. Furthermore, the magnitude of the drag force is exaggerated to aid the visual presentation of the projection.

terms of a time integral, the forcing needs to be expressed in terms of a given set of basis functions. In Appendix 5.B, we derive such a solution by expressing the forcing in terms of a Fourier series. However, we here turn our attention towards deriving solutions for the induced velocity along the wake centre line $(x_*, y_* = 0)^\top$ since the knowledge of the induced velocity at the actuator point $(x_*^{Act}, y_*^{Act})^\top = (0,0)^\top$ is sufficient to compute the unsteady loading on the airfoil.

## 5.3 The induced velocity due to unsteady forcing

The solution for the induced velocity at location $\boldsymbol{x} = (x_*, y_*)^\top$ due to vorticity residing at $\boldsymbol{x'} = (x_*', y_*')^\top$ can be derived by applying the Biot-Savart law [246] to the general unsteady

vorticity solution (equation 5.6), which for the given two-dimensional flow reads as

$$(u_*, v_*)^\top = \frac{1}{2\pi} \int_{-\infty}^{+\infty} \int_{-\infty}^{+\infty} \omega_*(x'_*, y'_*, t_*) \frac{-(y_* - y'_*)\boldsymbol{i} + (x_* - x'_*)\boldsymbol{j}}{(x_* - x'_*)^2 + (y_* - y'_*)^2} \, \mathrm{d}x'_* \mathrm{d}y'_*. \tag{5.7}$$

We note that when seeking a solution restricted to the wake centre line for the linearised equations, the streamwise forcing only induces streamwise velocity perturbations, and the normal forcing only induces normal velocity perturbations. Hence, for each forcing direction, only one velocity component of the Biot-Savart integral needs to be evaluated.

### 5.3.1 Induced velocity due to normal forcing

The normal induced velocity along the wake centre line $(x_*, y_* = 0)^\top$ is obtained by solving the normal component of the Biot-Savart integral given in equation 5.7 for a generic normal forcing $C_y(t_*)$. First, we focus here on the contribution from the second term of the unsteady vorticity solution $\omega_*^{us}$ (the time integral in equation 5.6). By switching the order of temporal and spatial integration, we may obtain,

$$v_*^{us}(x_*, 0, t_*) = \int_0^{t_*} \frac{1}{2\pi} \int_{-\infty}^{+\infty} \int_{-\infty}^{+\infty} \frac{(x_* - x'_*)(x'_* + s - t_*)}{(x_* - x'_*)^2 + (-y'_*)^2} \frac{C_y(s)}{\pi \epsilon_*^4} e^{-((x'_* + s - t_*)^2 + y'^2_*)/\epsilon_*^2} \, \mathrm{d}x'_* \mathrm{d}y'_* \mathrm{d}s, \tag{5.8}$$

which is the normal perturbation velocity induced by the vorticity shed as a result of the unsteady forcing in the time interval $t_* \in [0, t_*]$. Integration in the two spatial directions leads to (see Appendix 5.C.1)

$$v_*^{us}(x_*, 0, t_*) = \int_0^{t_*} \frac{-C_y(s)}{2\pi} \left[ \frac{e^{-(x_* + s - t_*)^2/\epsilon_*^2}}{\epsilon^2} + \frac{e^{-(x_* + s - t_*)^2/\epsilon_*^2} - 1}{2(x_* + s - t_*)^2} \right] \mathrm{d}s. \tag{5.9}$$

We note that the integrand in the limit $(x_* + s - t_*) \longrightarrow 0$ tends to $-C_y(s)/(4\pi\epsilon_*^2)$, i.e., it is not singular. The derived solution shows the identical structure as the formula obtained by Martínez-Tossas et al. [247] for their generalised steady three-dimensional filtered lifting line theory. This equivalence stems from the fact that the two problems are similar upon applying a rotation of 90° to their coordinate system and replacing the spatial convolution integral in their solution with a spatio-temporal convolution as in equation 5.9. So far, only the contribution from the second term of the vorticity solution $\omega_*^{us}$ has been considered. Thus the induced velocity solution in equation 5.9 has to be complemented with a term $v_*^{IC}(x_*, 0, t_*)$, accounting for the velocity induced by the initial vorticity field in case $\omega_*^{IC} \neq 0$ in equation 5.6. If we assume that the initial condition is given by the steady-state solution of the flow over a Gaussian body force, one can take the initial condition derived by Martínez-Tossas et al. [146], i.e., the velocity field induced by a Lamb-Oseen vortex with core size $\epsilon_*$ advected downstream by the background flow

$$v_*^{IC}(x_* - t_*, 0) = \frac{-C_y(t_* = 0)}{4\pi} \frac{1 - e^{-((x_* - t_*)/\epsilon_*)^2}}{x_* - t_*}. \tag{5.10}$$

The complete solution for the normal induced velocity along the wake centre line follows by combining equations 5.9 and 5.10 as

$$v_*(x_*, 0, t_*) = v_*^{IC}(x_* - t_*, 0) + v_*^{us}(x_*, 0, t_*). \tag{5.11}$$

While for numerical implementation purposes the structure of the solution in equation 5.9 is beneficial since it does not require the calculation of the temporal gradient of $C_y(t_*)$, it is insightful to rewrite the time integral using integration by parts,

$$v_*^{us}(x_*, 0, t_*) = -\left[\frac{C_y(s)}{4\pi}\frac{1 - e^{-((x_*+s-t_*)/\epsilon_*)^2}}{x_* + s - t_*}\right]_{s=0}^{s=t_*} + \int_0^{t_*} \frac{1}{4\pi}\frac{\mathrm{d}C_y(s)}{\mathrm{d}s}\frac{1 - e^{-((x_*+s-t_*)/\epsilon_*)^2}}{x_* + s - t_*}\,\mathrm{d}s, \tag{5.12}$$

where we define the indicial response function as

$$\varphi(x_* + s - t_*) = \frac{1 - e^{-((x_*+s-t_*)/\epsilon_*)^2}}{x_* + s - t_*}. \tag{5.13}$$

5

In the steady case ($\mathrm{d}C_y/\mathrm{d}s = 0$), the time integral vanishes, and the term in the first brackets evaluated for the lower bound $s = 0$ cancels the initial condition in equation 5.10. Thus, the only remaining term is the first term evaluated at the upper integration bound, which represents the induced velocity of the bound vortex, e.g., one recovers the solution of the steady problem.

When combining the contributions of the vorticity initial condition (equation 5.10) and the vorticity due to unsteady forcing (equation 5.12) to the normal induced velocity at the actuator point as $v_*(0, 0, t_*) = v_*^{IC}(0 - t_*, 0) + v_*^{us}(0, 0, t_*)$, one obtains the solution

$$v_*(0, 0, t_*) = -\int_0^{t_*} \frac{1}{4\pi}\frac{\mathrm{d}C_y(s)}{\mathrm{d}s}\varphi(t_* - s)\,\mathrm{d}s, \tag{5.14}$$

where we exploit the fact that $\varphi(x_* + s - t_*)$ for $x_* = 0$ is an anti-symmetric function and $\varphi(0) = 0$. This solution is a Duhamel's integral with the indicial response function $\varphi$ [155]. The induced velocity at the actuator point at time $t_*$ due to the unsteady Gaussian forcing is then obtained as the superposition of all indicial responses to the forcing in the time interval $s \in [0, t_*]$. Wagner [237] derived an indicial response function for the response of a thin airfoil to a step change of the angle of attack, which has been shown by Garrick [248] to be directly related to Theodorsen's function $C(k)$ in the frequency domain [239]. In our case, the indicial response function for an unsteady Gaussian forcing is parameterised with the Gaussian kernel width $\epsilon_*$, and from equation 5.13 it can be seen that the indicial response function is given by the shape representative for the induced velocity of a Lamb-Oseen vortex with core size $\epsilon_*$ located at the streamwise location $x_* = t_* - s$.

### 5.3.2 Induced velocity due to streamwise forcing

The streamwise induced velocity along the wake centre line $(x_*, y_* = 0)^\top$ is obtained by solving the streamwise component of the Biot-Savart integral given in equation 5.7 for a generic streamwise forcing $C_x(t)$. We first focus again on the contribution from the

second term of the unsteady vorticity solution $\omega_*^{us}$ (the time integral in equation 5.6). By switching the order of temporal and spatial integration, it follows that

$$u_*^{us}(x_*,0,t_*) = -\int_0^{t_*} \frac{1}{2\pi} \int_{-\infty}^{+\infty}\int_{-\infty}^{+\infty} \frac{(-y_*')}{(x_*-x_*')^2+(-y_*')^2} \frac{-y_*' C_x(s)}{\pi\epsilon_*^4} \times e^{-((x_*'+s-t_*)^2+y_*'^2)/\epsilon_*^2} \mathrm{d}x_*' \mathrm{d}y_*' \mathrm{d}s, \tag{5.15}$$

and the two integrals in $x_*'$ and $y_*'$ can be solved analytically to obtain (see Appendix 5.C.2)

$$u_*^{us}(x_*,0,t_*) = \int_0^{t_*} \frac{C_x(s)}{4\pi}\left[\frac{e^{-(x_*+s-t_*)^2/\epsilon_*^2}-1}{(x_*+s-t_*)^2}\right]\mathrm{d}s. \tag{5.16}$$

It should be noted that in the limit case of a vanishing spatio-temporal shift $x_*+s-t_* \longrightarrow 0$, the integrand tends to $-C_x(s)/(4\pi\epsilon_*^2)$.

Furthermore, given the assumption of constant streamwise forcing $C_x \neq C_x(t_*)$, one can recover the induced velocity solution of the steady two-dimensional problem derived by Martínez-Tossas et al. [146]. We derive here the solution valid for any $x_*$, but restricted to $y_* = 0$. To this end, equation 5.16 is integrated for general $t_*$ but constant $C_x$, which yields

$$u_*^{us}(x_*,0,t_*) = \frac{C_x}{4\pi}\left[\frac{1-e^{-(x_*+s-t_*)^2/\epsilon_*^2}}{(x_*+s-t_*)} - \frac{\sqrt{\pi}}{\epsilon_*}\,\mathrm{erf}\left(\frac{(x_*+s-t_*)}{\epsilon_*}\right)\right]_{s=0}^{s=t_*}. \tag{5.17}$$

The steady-state solution along the curve $(x_*, y_*=0)^\top$ is obtained in the limit $t_* \longrightarrow \infty$ using the rule of l'Hôpital

$$u_*^{st}(x_*,0) = \frac{C_x}{4\pi}\left[\frac{1-e^{-x_*^2/\epsilon_*^2}}{x_*} - \frac{\sqrt{\pi}}{\epsilon_*}\,\mathrm{erf}\left(\frac{x_*}{\epsilon_*}\right) - \frac{\sqrt{\pi}}{\epsilon_*}\right]. \tag{5.18}$$

In the case of $x_* \longrightarrow \infty$, the first term vanishes and the error function tends to one which leads to a limit value of $u_*^{st}(y_*=0) = -C_x/(2\sqrt{\pi}\epsilon_*)$ far downstream, which is exactly the result derived by Martínez-Tossas et al. [146]. Furthermore, at the actuator point, the solution is exactly half of the limit value far downstream, i.e., $u_*^{st}(y_*=0) = -C_x/(4\sqrt{\pi}\epsilon_*)$. Similar to the normal forcing case, the solution in equation 5.18 can also be used as an initial condition in order to account for a non-zero initial vorticity field $\omega_*^{IC}(x_*-t_*, y_*)$ due to streamwise forcing, i.e.,

$$u_*^{IC}(x_*-t_*,0) = \frac{C_x(t_*=0)}{4\pi}\left[\frac{1-e^{-(x_*-t_*)^2/\epsilon_*^2}}{x_*-t_*} - \frac{\sqrt{\pi}}{\epsilon_*}\,\mathrm{erf}\left(\frac{x_*-t_*}{\epsilon_*}\right) - \frac{\sqrt{\pi}}{\epsilon_*}\right]. \tag{5.19}$$

The complete solution for the normal induced velocity along the wake centre line then follows by combining equations 5.16 and 5.19 as

$$u_*(x_*,0,t_*) = u_*^{IC}(x_*-t_*,0) + u_*^{us}(x_*,0,t_*). \tag{5.20}$$

5

## 5.4 A model for the unsteady airfoil loading

In Sections 5.3.1 and 5.3.2 the time-dependent solutions for the normal and streamwise induced velocity due to an unsteady Gaussian body force are derived, which allow us to define the velocity sampled at the actuator point $(x_*^{Act}, y_*^{Act})^\top = (0,0)^\top$. These formulas will now be used to combine the velocity solutions with the forcing time histories. The forcing time histories $C_x(t_*)$ and $C_y(t_*)$ are functions of the external pitch angle input and of the induced velocities since they change the flow angle and thus, in turn, the forcing. This feedback turns the velocity solutions given by equation 5.11 and 5.20 into integral equations. The associated feedback problem can be formulated in terms of the flow angle, and its solution can be found in either the time (Section 5.4.1) or frequency (Section 5.4.2) domain in order to obtain a model for the unsteady loading of the airfoil modelled as a Gaussian body force.

### 5.4.1 Time domain solution: The root-finding problem

We now seek to obtain the time history of both the forcing and the velocity at the actuator point as a function of time using equations 5.11 and 5.20. We write the time history of the velocity at the actuator point with a single equation in terms of the flow angle, as done by Ning [249] and Martinez-Tossas et al. [250]. The tangent of the flow angle at the actuator point is defined by

$$\tan(\phi(t_*)) = \frac{v_*(0,0,t_*)}{1+u_*(0,0,t_*)}, \tag{5.21}$$

where $u_*$ and $v_*$ can both be written in terms of $\phi$; thus, this is an implicit equation where the time history, $\phi(t_*)$, is the only unknown. Rearranging equation 5.21 yields

$$R(\phi) = v_*(0,0,t_*)\cos(\phi) - (1+u_*(0,0,t_*))\sin(\phi) = 0. \tag{5.22}$$

Given a guess for $\phi(t_*)$ as input, the following algorithm provides the steps to compute equation 5.22:

1. Compute the angle of attack using the known pitch input, $\beta(t_*)$:

$$\alpha(t_*) = \phi(t_*) + \beta(t_*).$$

2. This effective angle of attack, which incorporates the effect of the shed vorticity, allows for the evaluation of the lift, $C_L(\alpha(t_*))$, and drag, $C_D(\alpha(t_*))$, coefficients from tabulated airfoil data, which can be subsequently converted into the corresponding streamwise and normal forcing coefficients using the projection based on the flow angle given in equation 5.5:

$$C_x(t_*) = -C_L(t_*)\sin(\phi(t_*)) + C_D(t_*)\cos(\phi(t_*)),$$
$$C_y(t_*) = C_L(t_*)\cos(\phi(t_*)) + C_D(t_*)\sin(\phi(t_*)).$$

3. The integral equations for the induced velocities are solved via numerical integration:

$$u_*(0,0,t_*) = u_*^{IC}(0-t_*,0) + \int_0^{t_*} \frac{C_x(s)}{4\pi}\left[\frac{e^{-(s-t_*)^2/\epsilon_*^2}-1}{(s-t_*)^2}\right] \mathrm{d}s,$$

$$v_*(0,0,t_*) = v_*^{IC}(0-t_*,0) + \int_0^{t_*} -\frac{C_y(s)}{2\pi}\left[\frac{e^{-(s-t_*)^2/\epsilon_*^2}}{\epsilon_*^2} + \frac{e^{-(s-t_*)^2/\epsilon_*^2}-1}{2(s-t_*)^2}\right] \mathrm{d}s.$$

4. Finally, the residual is computed:

$$R(\phi) = v_*(0,0,t_*)\cos(\phi) - (1+u_*(0,0,t_*))\sin(\phi).$$

A multidimensional root-finding algorithm then iteratively evaluates steps (i)–(iv) to compute the $\phi(t_*)$ that solves $R(\phi(t_*)) = 0$. The resulting $\phi(t_*)$ is the full solution to the problem that provides the time history of forcing at the actuator point. The algorithm above is implemented based on the python scipy.optimize.root() function [251] using the derivative-free spectral algorithm for non-linear equations (DF-SANE) by La Cruz et al. [252].

### 5.4.2 Frequency domain solution: The closed-loop transfer function

The time domain solution from Section 5.4.1 can be compared to results from ALM-LES. However, it is insightful to also formulate the feedback problem in the frequency domain since it allows for a concise analysis of the Gaussian kernel width's influence on the phase and magnitude modulation of the unsteady loading through a closed-loop transfer function. This connection is analogous to the one that can be obtained between Theodorsen's frequency domain solution for unsteady airfoil motion [239] and Wagner's time domain solution [237] as shown by Garrick [248].

In order to derive the transfer function from the quasi-steady to the unsteady lift, we explicitly need to linearise the projection of the lift and drag coefficients onto the streamwise and normal directions (equation 5.5), which is not necessary for the time domain solution. When doing so, one obtains $C_y \approx C_L + C_D\phi$, and since $C_D$ is at least an order of magnitude smaller than $C_L$ in the operating regime of interest for this study, it is consistent to neglect the drag because $C_D\phi$ is a higher-order term. The linearised lift coefficient is then described by its value at the linearisation point, $C_L(\beta^0)$, and the corresponding lift slope $\mathrm{d}C_L/\mathrm{d}\alpha(\beta^0)$. For a given sinusoidal pitch input signal $\beta(t_*) = \beta^0 + \Delta\beta\sin(2kt_*)$ with amplitude $\Delta\beta$, the quasi-steady and unsteady lift coefficients are then, after the decay of any transient, given by

$$C_L^{qs}(t_*;k) = C_L(\beta^0) + \Delta\beta\sin(2kt_*)\left.\frac{\mathrm{d}C_L}{\mathrm{d}\alpha}\right|_{\beta^0}, \tag{5.23}$$

$$C_L^{us}(t_*;k) = C_L(\beta^0) + \Delta\beta|G(k)|\sin(2kt_* + \angle G(k))\left.\frac{\mathrm{d}C_L}{\mathrm{d}\alpha}\right|_{\beta^0}, \tag{5.24}$$

where $|G|$ and $\angle G$ are the magnitude and phase of the corresponding closed-loop transfer function $G$ mapping from the quasi-steady to the unsteady lift. This transfer function can be derived from the system's block diagram shown in Figure 5.2, where we invoke the small-angle approximation for the flow angle $\phi \approx v_*$. Calculating the Laplace transform of the individual blocks, the transfer function follows from block diagram algebra. It should be noted that the Laplace transform has the convenient property that the convolution of two functions in the time domain reduces simply to a multiplication in the Laplace

domain. Denoting the Laplace transform of the indicial response function $\varphi$ for the normal induced velocity defined in equation 5.13 as $\Phi(ik)$, the closed-loop transfer function for the feedback problem then reads as

$$G(k) = \frac{\Delta C_L^{us}(k)}{\Delta C_L^{qs}(k)} = \frac{1}{1 - 2ki\,\frac{\mathrm{d}C_L}{\mathrm{d}\alpha}\Big|_{\beta^0}\,\Phi(ik)}, \tag{5.25}$$

with $i$ denoting the imaginary unit (not to be confused with the streamwise unit vector $\boldsymbol{i}$). The full expression for the Laplace transform of the indicial response function $\varphi$ is given by

$$\begin{aligned}\Phi(ik) = \frac{1}{16\pi}\Big[&2\gamma - 2\pi\,\mathrm{erfi}(ik\epsilon_*) - 2\log(1/\epsilon_*^2) \\ &+ 4\log(2ki) + (2\epsilon_* ki)^2\,{}_2F_2((1,1);(3/2,2);(ik\epsilon_*)^2)\Big],\end{aligned} \tag{5.26}$$

where $\gamma$ is Euler's constant and ${}_pF_q(a;b;z)$ is the generalised hypergeometric function. Unsteady aerodynamics problems are commonly classified using the reduced frequency $k = \pi f c/U_\infty$, which is based on the semi-chord length [155]. Recalling that the non-dimensional variables in this work are based on the chord length and the free stream velocity, it follows that the angular frequency is given by $\sigma_* = 2k$, which explains the added factor of 2 when writing the frequency in terms of the reduced frequency $k$.

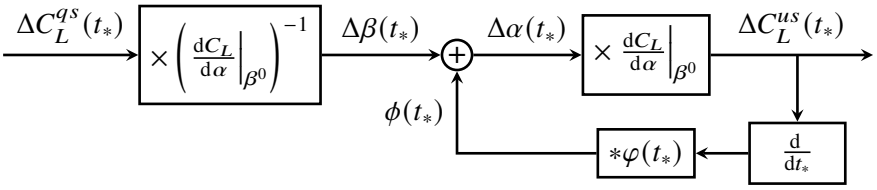


Figure 5.2: Schematic block diagram of the feedback problem for the unsteady lift experienced by a pitching airfoil with $C_D = 0$ at a linearised operating point $\beta^0$. The convolution operator is denoted by $*$, and $\varphi$ is the indicial response function for the normal induced velocity (defined in equation 5.13).

### 5.4.3 Relation between $G(k)$ and Theodorsen theory

Theodorsen [239] derived a transfer function $T(k)$ from quasi-steady to unsteady lift for a flat plate airfoil modelled as a line distribution of point vortices. For an airfoil in pure pitching motion, it consists of two non-circulatory (apparent mass) $T_{NC}(k)$ and two circulatory $T_C(k)$ contributions given by

$$\begin{aligned}T(k) = \frac{\Delta C_L^{us}(k)}{\Delta C_L^{qs}(k)} = T_{NC}(k) + T_C(k) &= \left[T_{NC}^{\dot\beta}(k) + T_{NC}^{\ddot\beta}(k)\right] + \left[T_C^{\beta}(k) + T_C^{\dot\beta}(k)\right] \\ &= \frac{\left[\pi ik + \pi ak^2\right] + 2\pi C(k)\left[1 + ik(\frac{1}{2} - a)\right]}{2\pi},\end{aligned} \tag{5.27}$$

where $a \in [-1, 1]$ (from leading to trailing edge) is the location of the rotation axis of the pitching motion, and the complex Theodorsen function $C(k)$ is given by

$$C(k) = \frac{K_1(ik)}{K_0(ik) + K_1(ik)}. \tag{5.28}$$

Here, $K_0$ and $K_1$ denote modified Bessel functions of the second kind. The superscripts $(\cdot)^{\beta}$, $(\cdot)^{\dot{\beta}}$ and $(\cdot)^{\ddot{\beta}}$ denote terms depending on the pitch angle, pitch rate and pitch acceleration, respectively. In the frequency domain, these dependencies translate to terms scaling proportionally to 1, $k$, and $k^2$, respectively. The classical ALM, as it was proposed by Sørensen et al. [137] and as it is also used in this work, only models the $T_C^{\beta}(k)$ term. The remaining three terms, which are proportional to either $k$ or $k^2$, are not captured by the ALM. It follows that the derived transfer function $G(k)$ is the equivalent of the Theodorsen function $C(k)$ consistent with the mathematical formulation of the ALM.

The ALM (for $\epsilon_* \in [0.125, 16.0]$) and Theodorsen frequency domain solutions are compared in the complex plane in Figure 5.3 and as Bode plot in Figure 5.4 up to a reduced frequency of $k = 0.6$. The magnitude of the transfer function is always $|G| \leq 1$, whereas the phase can be both positive or negative depending on the considered kernel width and the reduced frequency. In general, it can be seen that smaller kernel widths lead to larger damping. The phase of $G(k)$ (see Figure 5.4(b)) first decreases with increasing $k$ before a characteristic phase inversion point is approached where the phase switches from negative to positive. This phase inversion point occurs for larger $k$ as the kernel width decreases. The magnitude $|C|(k)$ closely follows $|G|(k; \epsilon_* = 0.375)$ for $k < 0.4$. Adding the second circulatory term $T_C^{\dot{\beta}}(k)$ which is proportional to the pitch rate shows that the circulatory Theodorsen solution $|T_C|(k)$ departs from $|G|(k; \epsilon_* = 0.375)$ for $k > 0.2$. Finally, also adding the two non-circulatory terms leads to an additional deviation between the ALM and the complete Theodorsen solution $|T|(k)$ for $k > 0.4$. The phase $\angle C(k)$ closely follows $\angle G(k; \epsilon_* = 0.375)$ for $k < 0.4$. In contrast to the magnitude, adding the second circulatory and eventually the two non-circulatory terms both leads to immediate deviations in phase compared to $\angle G(k; \epsilon_* = 0.375)$ for any $k$ rather than the two distinct points of departure of $k = 0.2$ and $k = 0.4$ observed for the magnitude.

These results suggest that when taking Theodorsen theory as a reference, the classical ALM can capture the unsteady damping of the lift accurately up to a reduced frequency of $k = 0.2$, whereas errors in phase are immediately encountered as soon as $k > 0$. However, these phase errors are relatively small and at $k = 0.2$ the difference in phase predicted by the ALM and the complete Theodorsen theory is $T(k = 0.2) - G(k = 0.2) \approx 19^{\circ}$. The model validation shown later in Section 5.7 will further support these identified bounds of the ability of the ALM to capture unsteady aerodynamic effects. For the purpose of further elucidating in Section 5.7 the impact of the ALM not capturing the terms $T_C^{\dot{\beta}}$, $T_{NC}^{\dot{\beta}}$ and $T_{NC}^{\ddot{\beta}}$ we also define the extended closed-loop transfer function $G_{Ext}(k)$ for the ALM. The extended ALM transfer function incorporates the three missing terms compared to Theodorsen theory in an *ad-hoc* approach and then is defined accordingly as

$$G_{Ext}(k) = \frac{\Delta C_L^{us}(k)}{\Delta C_L^{qs}(k)} = \frac{\left[\pi ik + \pi a k^2\right] + \frac{\mathrm{d}C_L}{\mathrm{d}\alpha} G(k) \left[1 + ik(\frac{1}{2} - a)\right]}{\frac{\mathrm{d}C_L}{\mathrm{d}\alpha}}, \tag{5.29}$$

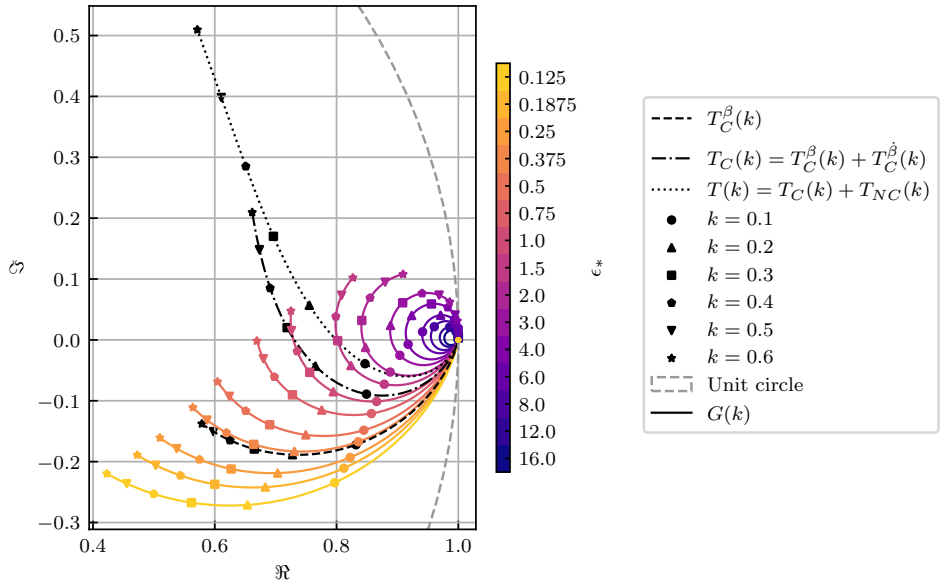


Figure 5.3: The closed-loop transfer function, $G(k)$, for a pitching flat plate, ($\mathrm{d}C_L/\mathrm{d}\alpha = 2\pi$), in the complex plane. The function is shown for fifteen different Gaussian kernel widths. The Theodorsen function, $T_C^\beta(k) = C(k)$, the circulatory component of Theodorsen's transfer function, $T_C(k)$, and Theodorsen's complete transfer function, $T(k)$, are shown for reference, where the airfoil pitches around the quarter-chord point ($a = -1/2$).

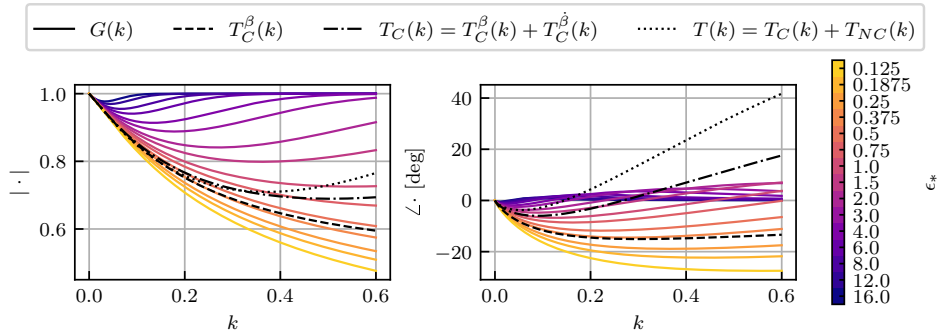


Figure 5.4: Magnitude (left) and phase (right) of $G(k)$ for a pitching flat plate, ($\mathrm{d}C_L/\mathrm{d}\alpha = 2\pi$), for fifteen different Gaussian kernel widths. The Theodorsen function, $T_C^\beta(k) = C(k)$, the circulatory component of Theodorsen's transfer function, $T_C(k)$, and Theodorsen's complete transfer function, $T(k)$, are shown for reference, where the airfoil pitches around the quarter-chord point ($a = -1/2$).

where $G(k)$ effectively replaces the Theodorsen function $C(k)$. It should be stressed that the current comparison between Theodorsen theory and the ALM is based on the classical ALM model relying on point velocity sampling. An integral velocity sampling approach as introduced by Churchfield et al. [191] could influence the transfer function and should

be explored in future work.

## 5.5 Verification: Model versus ALM-LES

In the previous three sections, we have derived a model for the unsteady loading on an airfoil modelled as a two-dimensional Gaussian body force. In this section, we verify this model by comparing it with ALM-LES data to establish the bounds of its accuracy and model limitations.

### 5.5.1 Investigated cases

The range of investigated cases is chosen such that a range of operating points, types of actuation, reduced frequencies and the interplay between streamwise and normal forcing are explored. All cases are conducted using the NACA64-A17 airfoil, which is, for example, also used for the outer part of the blade of the NREL 5MW reference turbine [211]. The airfoil's tabulated lift and drag coefficients are shown in Figure 5.5. Each investigated



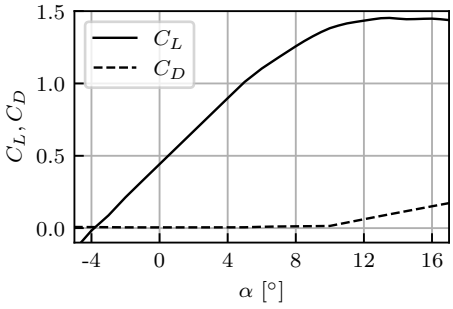


Figure 5.5: Tabulated lift, $C_L(\alpha)$, and drag, $C_D(\alpha)$, coefficients of the NACA64-A17 airfoil.

case is analysed for the set of Gaussian kernel widths $\epsilon_* \in \{0.25, 0.5, 1.0, 2.0, 4.0\}$. The lower limit is chosen here on the order of the steady-state optimal kernel width [146], while the upper limit corresponds to coarse grid ALM-LES simulations conducted for wind energy purposes. An overview of all cases and their acronyms is provided in Table 5.1. In the following, the different cases are explained in more detail.

In order to characterise the obtained theoretical solutions and their scaling with the kernel width, we begin by considering two cases with a step in pitch angle. Both cases start from an initial condition of zero vorticity, $\omega^{IC} = 0$, i.e., zero forcing. This choice ensures that there is no mismatch between the initial conditions used for the model and LES. The simulation start thus corresponds to a sudden step actuation to reach the operating pitch angle $\beta^0$ for $t_* \geq 0$. The considered operating points are $\beta^0 = 0^\circ$ (A0-Cxy-S4) and $\beta^0 = 8^\circ$ (A8-Cxy-S12). The same cases are also repeated without applying any normal forcing (A0-Cx-S4 and A8-Cx-S12). It should be noted that the frequency content of a step function is proportional to the inverse of the frequency ($|\hat{\beta}| \propto 1/k$) and thus tests the model simultaneously across the entire frequency range. The step case A14-Cxy-S18 is only conducted for $\epsilon_* = 0.25$ to obtain the largest forcing magnitudes. This case is used to perform

a grid and domain size convergence study for the LES setup.

The second set of cases considers the same initial step but additionally superposes continuous periodic pitch actuation with an amplitude of $\Delta\beta = 3^\circ$ and reduced frequencies of $k = 0.1$, $k = 0.2$, $k = 0.3$ and $k = 0.6$ (indicated by the endings -k01, -k02, -k03 and -k06 of the case acronyms). The periodic pitch actuation is of the form $\beta(t_*) = \Delta\beta \sin(2kt_*)$. It is applied at the operating point $\beta^0 = 0^\circ$ (A0-Cxy-P3-k...). This second set of cases is well suited to test the predictions of the derived closed-loop transfer function for an isolated frequency component after the initial transient decayed.

| Case acronym | Operating point $\beta^0$ | Forcing $C_x$ | Forcing $C_y$ | Actuation type | Magnitude $\Delta\alpha$ (Step) | Amplitude $\Delta\beta$ (Periodic) | Frequency $k$ (Periodic) |
|---|---|---|---|---|---|---|---|
| A0-Cx-S4 | $0^\circ$ | Yes | No | Step | $4^\circ$ | - | - |
| A0-Cxy-S4 | $0^\circ$ | Yes | Yes | Step | $4^\circ$ | - | - |
| A8-Cx-S12 | $8^\circ$ | Yes | No | Step | $12^\circ$ | - | - |
| A8-Cxy-S12 | $8^\circ$ | Yes | Yes | Step | $12^\circ$ | - | - |
| A14-Cxy-S18 | $14^\circ$ | Yes | Yes | Step | $18^\circ$ | - | - |
| A0-Cxy-P3-k01 | $0^\circ$ | Yes | Yes | Step + Periodic | $4^\circ$ | $3^\circ$ | $k = 0.1$ |
| A0-Cxy-P3-k02 | $0^\circ$ | Yes | Yes | Step + Periodic | $4^\circ$ | $3^\circ$ | $k = 0.2$ |
| A0-Cxy-P3-k03 | $0^\circ$ | Yes | Yes | Step + Periodic | $4^\circ$ | $3^\circ$ | $k = 0.3$ |
| A0-Cxy-P3-k06 | $0^\circ$ | Yes | Yes | Step + Periodic | $4^\circ$ | $3^\circ$ | $k = 0.6$ |

Table 5.1: Overview of the investigated cases. The initial condition for all cases is $\omega^{IC} = 0$, corresponding to a situation without initial forcing. The step magnitude is defined as the difference between the pitch angle after the step (given by the operating point $\beta^0$) and the angle of attack, which results in approximately zero lift force for the cambered airfoil $\Delta\alpha = \beta^0 - \alpha^{C_L=0}$ ($\alpha^{C_L=0} \approx -4^\circ$). The periodic component of the actuation is of the form $\beta(t_*) = \Delta\beta \sin(2kt_*)$. The step components contain a continuous frequency spectrum where the magnitude of the Fourier transform of the step scales as $|\hat{\beta}| \propto 1/k$.

### 5.5.2 Employed numerical code and simulation setup

Numerical non-linear reference results for the assessment of the developed model are obtained by means of LES using the open-source code AMR-Wind. AMR-Wind solves the three-dimensional incompressible Navier-Stokes equations on block-structured Cartesian grids and is specifically designed for wind energy applications. For details on the numerical schemes employed in AMR-Wind, the reader is referred to Almgren et al. [253], Sharma et al. [113], and Kuhn et al. [112]. For the purpose of verifying the developed model, which is based on the Euler equations, the governing equations are solved in the limit of infinite Reynolds number by setting the molecular viscosity to zero. Throughout the simulations, the inflow and the wake flow behind the actuator points remain laminar, removing the need for explicit turbulence modelling.

This work utilises AMR-Wind's implementation of the ALM for straight translating wings. AMR-Wind does not allow for strictly two-dimensional simulations; rather, we simulate the airfoil in a three-dimensional domain as an infinite wing, i.e., periodic boundary conditions are imposed in the spanwise direction. The lower and upper boundary condition in the normal direction is a slip wall ($y$-direction). In the streamwise direction ($x$-direction), a constant inflow velocity of $\boldsymbol{u} = U_\infty \boldsymbol{i}$ is imposed at the upstream boundary (which in non-dimensional units corresponds to $\boldsymbol{u}_* = \boldsymbol{i}$), and a pressure outflow boundary condition is applied at the downstream boundary. The wing spans two actuator points located on the spanwise boundaries of the domain at which the actuator forces are applied. The forces are regularised with a two-dimensional isotropic Gaussian kernel of width $\epsilon_*$. The velocity used for the actuator force calculation is the known inflow velocity (see Appendix 5.D).

The convergence of LES results with domain size and grid resolution is studied in Appendix 5.E for the A14-Cxy-S18 case using $\epsilon_* = 0.25$. Based on this convergence study, all simulations are conducted with a semi-domain height $L_{y_*} = 256$ and an upstream fetch of $L_{x_*}^{upstr} = 256$ between the inflow boundary and the actuator point. The streamwise distance from the actuator point to the outlet is $L_{x_*}^{downstr} = T_* + L_{y_*}$, where $T_*$ is the maximum simulated time. The grid resolution on the coarsest grid level is constant for all simulations; however, depending on the studied kernel width, four ($\epsilon_* = 4$) to eight ($\epsilon_* = 0.25$) refinement levels are added such that on the finest grid around the actuator point, the resolution is always $\epsilon_*/\Delta x_* = 8$. The grid resolution between two adjacent grid levels varies with a constant factor of 2. The size of the finest grid level is dependent on the kernel width. Its extent in the $x$ and $y$-directions is $-4\epsilon_* < x_* < 16 + 4\epsilon_*$ and $-4\epsilon_* < y_* < 4\epsilon_*$, respectively. Letting the index $m$ denote the grid level (the finest being $m = 0$), the extent of all other refinement levels ($m > 0$) in $x$ and $y$ is given by $-4\epsilon_* 2^m < x_* < T_* + 4\epsilon_* 2^m$ and $-4\epsilon_* 2^m < y_* < 4\epsilon_* 2^m$. The time step size $\Delta t_{*,\mathrm{LES}}$ is chosen such that the Courant-Friedrichs-Levy (CFL) number defined on the finest grid level is $CFL < 0.5$ at all times. Step cases are simulated up to $T_* = 128$, whereas the step cases followed by periodic actuation are simulated up to $T_* = 256$. These long simulation times provide enough time for the actuator loading to reach the new steady state (step cases) or periodic limit cycle (step+periodic cases) after the decay of the initial transient. The simulation time-dependent streamwise domain length ensures that no vorticity is truncated at the outlet. The simulation time for the periodic cases is chosen twice as long in order to collect a large number of actuation periods, even for the smallest frequency $k = 0.1$. The LES setup is visualised in Figure 5.6.

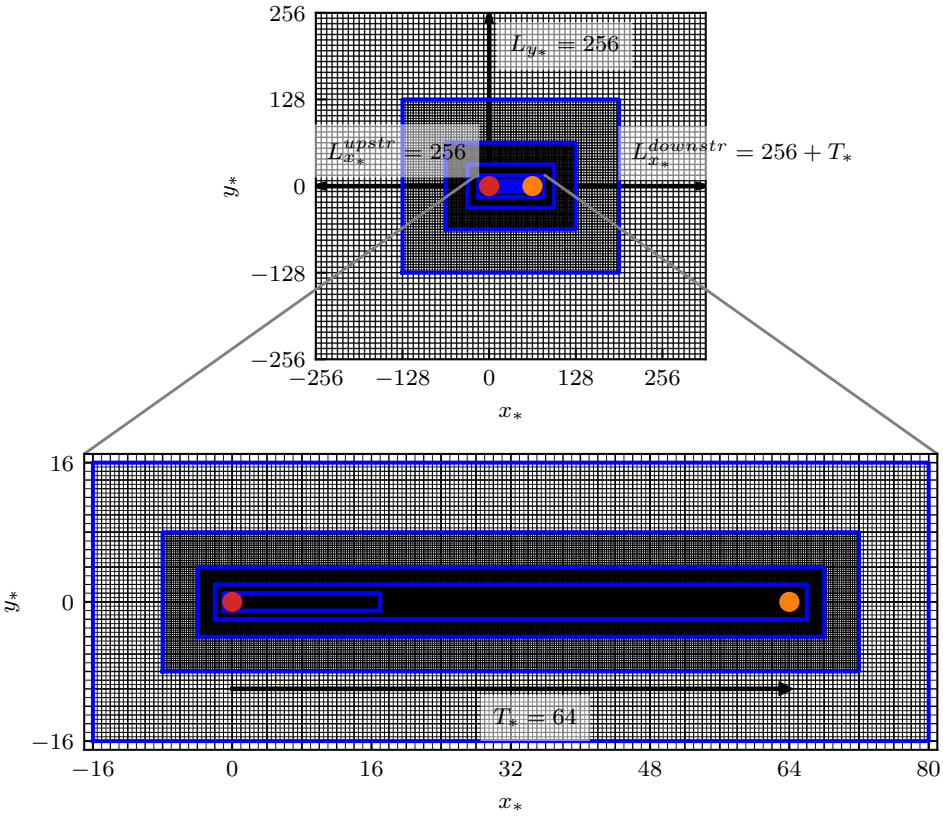


Figure 5.6: LES domain and grid refinement structure for the Gaussian kernel width $\epsilon_* = 0.25$ with the resolution on the finest grid level being $\epsilon_*/\Delta x = 8$. Note that the domain here is configured for a simulation time of $T_* = 64$ in order to keep the aspect ratio limited for visual clarity. The actual simulations are performed for $T_* = 128$ (steps) and $T_* = 256$ (periodic). The red dot marks the actuator point. The orange dot marks the approximate downstream location of the start-up vortex at time $t_* = T_*$.

### 5.5.3 Response to pitch step actuation

We start by probing the developed model for two pitch step actuation cases within the linear regime of the lift curve. Their respective operating points are $\beta^0 = 0^\circ$ (A0-Cxy-S4) and $\beta^0 = 8^\circ$ (A8-Cxy-S12). The initial condition is chosen as an undisturbed free stream flow, i.e., no forcing is active. Consequently, the two operating points correspond to effective angle of attack steps of $\Delta\alpha = 4^\circ$ and $\Delta\alpha = 12^\circ$ upon simulation start (the lift coefficient of the cambered airfoil is approximately zero at $\alpha \approx -4^\circ$).

The vorticity distribution around the airfoil and in the wake as predicted by the model (see Appendix 5.B), with $\epsilon_* = 0.25$ is shown in Figure 5.7 for the larger pitch step case A8-Cxy-S12. Around the airfoil, a bound vortex forms in response to the non-zero loading after $t_* > 0$. The bound vortex is accompanied by the formation of a start-up vortex, which ensures conservation of the overall vorticity. Since the model assumes the advection speed

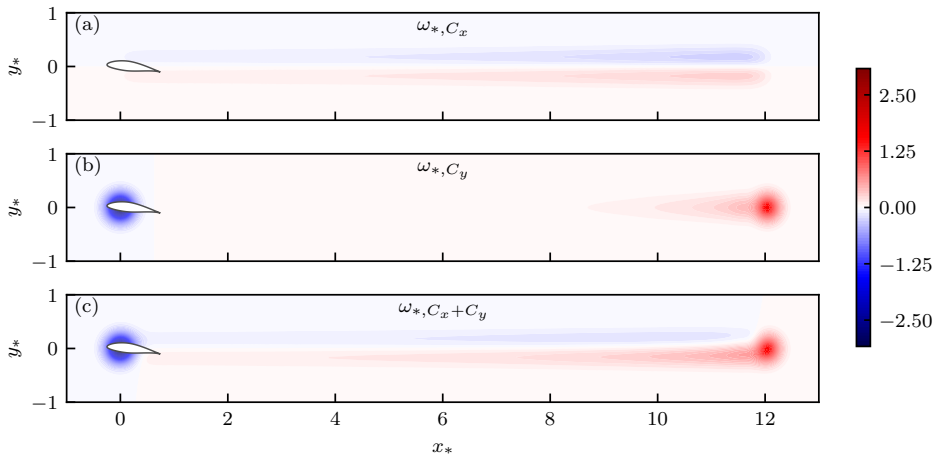


Figure 5.7: Model solution for the vorticity field of the A8-Cxy-S12 case with the kernel width $\epsilon_* = 0.25$ at time instance $t_* = 12$. The vorticity created by streamwise $C_x$ and normal $C_y$ forcing is shown in (a) and (b), respectively. The total resultant vorticity field is shown in (c). The airfoil modelled by the Gaussian body force is shown in white with black outline. The airfoil's quarter-chord point is located at the actuator point $(x_*^{Act}, y_*^{Act})^\top = (0,0)^\top$.

in the wake to match the free stream velocity, the start-up vortex is located at $x_* = 12$ in the wake at the shown time instance $t_* = 12$. Furthermore, it is seen that the wake centre line $(x_*, y_* = 0)^\top$ is the symmetry axis for both the vorticity due to streamwise and the vorticity due to normal forcing (Figure 5.7a/b). The vorticity due to streamwise forcing exhibits an anti-symmetric distribution around this symmetry axis, whereas the normal forcing contribution is distributed symmetrically around the wake centre line. These distributions stem from the symmetry properties of the forcing terms in the linearised vorticity transport equation 5.4.

The formation of the start-up vortex and its subsequent advection downstream causes a dynamic angle of attack response. A comparison of the model and the LES solution for this response is shown in Figure 5.8 for the small pitch step case A0-Cxy-S4. The start-up vortex induces velocity at the actuator point, which in turn alters the angle of attack. As it is advected further downstream, its influence on the angle of attack fades, which leads the angle of attack to converge towards the new steady-state operating point $\alpha = \beta^0 = 0^\circ$ (Figure 5.8a). The initial modulation of the angle of attack depends on the kernel width since it sets the local strength of the applied forcing and thus also the strength of the start-up vortex. Furthermore, the core size of the start-up vortex is also set by the kernel width. The core size determines the time period between $t_* = 0$ and the time instance when the angle of attack reaches its minimum. The minimum angle of attack is attained faster with a smaller kernel width and thus core size.

The model error compared to the LES reference is presented in Figure 5.8b. The very initial relative angle of attack error is as large as 3.4% and then subsequently drops to the order of tenths of a per cent. The relative error starts approaching zero after the actuator point no longer lies within the vortex core region of the start-up vortex. The relative error

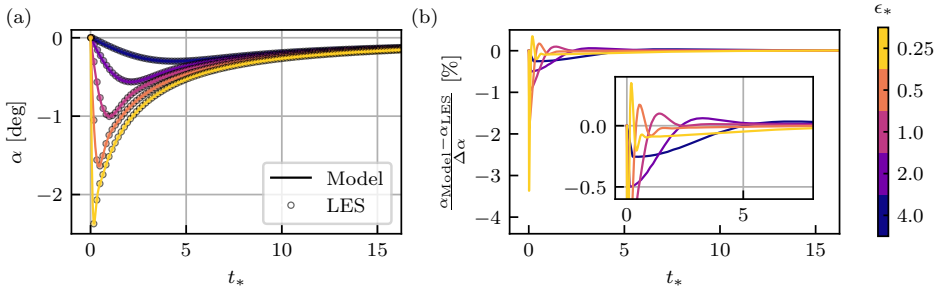


Figure 5.8: Comparison of the model solution and LES reference for the initial time evolution of the angle of attack (a) and the corresponding relative error (b) for the pitch step actuation case A0-Cxy-S4. Reference data points are only shown in steps of $4\Delta t_{*,\text{LES}}/\epsilon_*$.

is larger for smaller kernel widths as long as there is overlap between the vortex core and the actuator point. This is the case because the velocity induced by the bound and start-up vortex both reach their absolute maximum values in proximity to their respective core boundary, where the maximum values increase with decreasing kernel width. Thus after the time instance $t_* > |x_*^{Act} - t_*| \approx |0 - \epsilon_*| = \epsilon_*$ the impact of the bound vortex on the trajectory of the start-up vortex as well as the impact of the start-up vortex on the angle of attack at the actuator point start to decrease. Hence, the effect of modelling errors also decreases as soon as $t_* \approx \epsilon_*$. The larger pitch step case A8-Cxy-S12 shown in Figure 5.9 follows the previous observations made apart from the relative error evolution for $\epsilon_* = 0.25$. In this case, the error also persists after the vortex core no longer overlaps with the actuator point and only fades at $t_* \approx 10$. The larger pitch step combined with the smallest kernel width makes for a stronger bound vortex, increasingly challenging the model, which is based on a linearisation around the vorticity-free background flow. The detailed impact of the error due to the linearisation will be explored in the following Section 5.6.

We explore the two pitch step cases further by turning our attention towards the load-

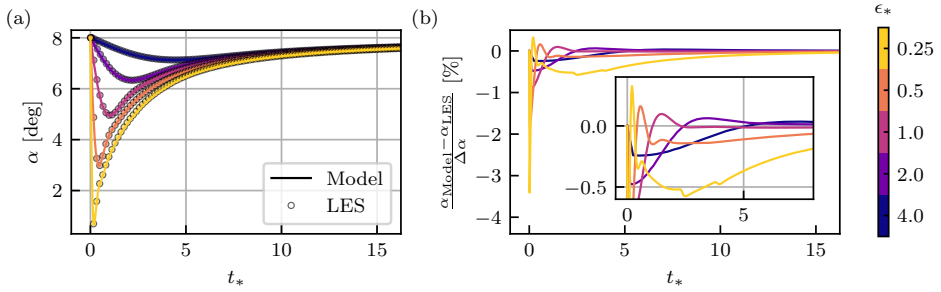


Figure 5.9: Comparison of the model solution and LES reference for the initial time evolution of the angle of attack (a) and the corresponding relative error (b) for the pitch step actuation case A8-Cxy-S12. Reference data points are only shown in steps of $4\Delta t_{*,\text{LES}}/\epsilon_*$.

ing, which the model ultimately should predict. The model is able to accurately reproduce the time evolution of the streamwise, $C_x$, and normal, $C_y$, force coefficients for both the small (Figure 5.10b/d) and the large (Figure 5.11b/d) pitch step cases. In particular, the transient drop in normal forcing and peak in streamwise forcing caused by the start-up vortex are captured. It is also worthwhile to study the induced velocities at the actuator point, which induce the change in flow angle and thus angle of attack (panels a/c of Figures 5.10 and 5.11). The model matches the LES prediction for the normal induced velocity, $v_*$, for both pitch step magnitudes, but discrepancies are apparent for the streamwise induced velocity, $u_*$, which become more pronounced for smaller kernel widths and the larger pitch step (compare Figures 5.10a and 5.11a). This discrepancy also matches the previous observation that the angle of attack error of the A8-Cxy-S12 case for $\epsilon_* = 0.25$ persists for a longer time. Since we deal with small perturbation velocities, the flow angle is small and thus approximately given by $\phi \approx v_*$. Thus, the error in streamwise induced velocity does not affect the quality of the streamwise and normal force coefficients as long as the small perturbation assumption is justified. In fact, $u_*$ is a measure of the system's non-linearity and is relevant for the flow angle calculation given larger induced velocities. However, larger induced velocities start to challenge the linearisation of the vorticity transport equation for the model derivation. Thus, the mismatch for $u_*$ and its increase for stronger forcing are consistent. In Section 5.6, we show that the observed streamwise velocity residual is explained by the vorticity residual obtained from the difference between the model (linear) and the LES reference (non-linear) solution. However, the two pitch



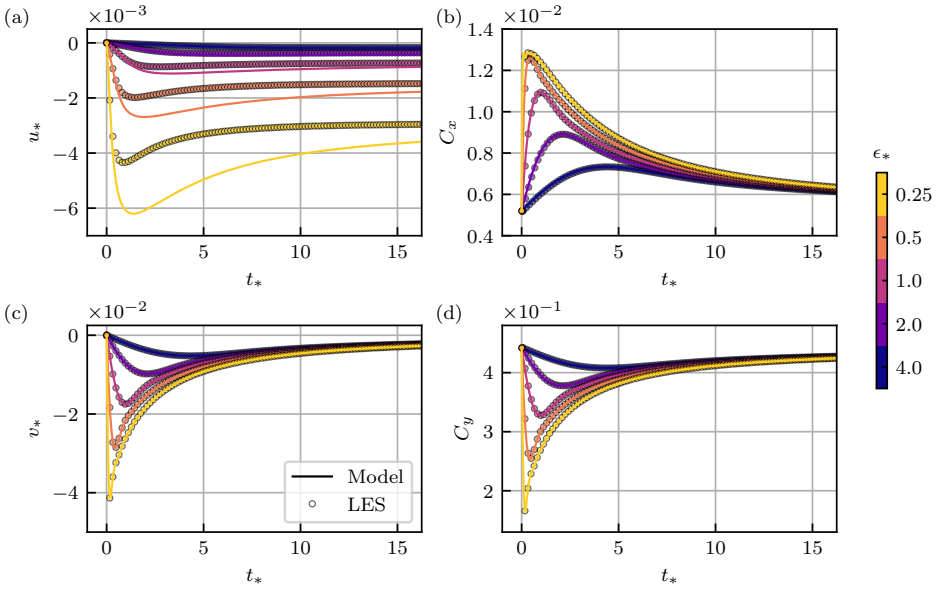


Figure 5.10: Comparison of the model solution and LES reference for the initial time evolution of the streamwise (a) and normal (c) induced velocity and the streamwise (b) and normal (d) force coefficients for the pitch step actuation case A0-Cxy-S4. Reference data points are only shown in steps of $4\Delta t_{*,\mathrm{LES}}/\epsilon_*$.

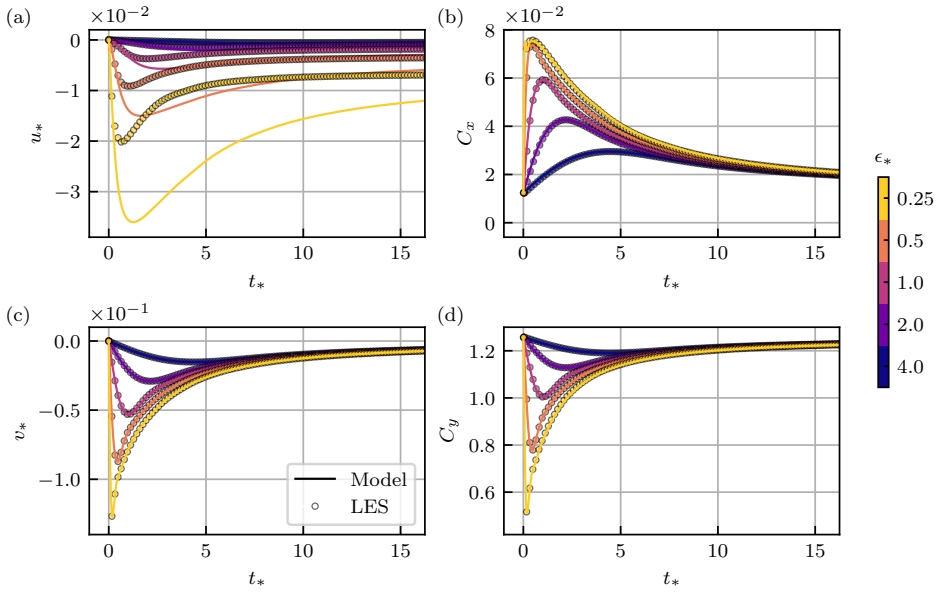


Figure 5.11: Comparison of the model solution and LES reference for the initial time evolution of the streamwise (a) and normal (c) induced velocity and the streamwise (b) and normal (d) force coefficients for the pitch step actuation case A8-Cxy-S12. Reference data points are only shown in steps of $4\Delta t_{*,\mathrm{LES}}/\epsilon_*$.

step cases show that the developed model can predict the loading on the airfoil in the linear regime of the lift curve despite the mismatch in $u_*$. The cases also illustrate the importance of the kernel width. The largest studied kernel width of $\epsilon_* = 4.0$ barely modifies the normal force coefficient, while the kernel width $\epsilon_* = 0.25$, which is of the order of the steady-state optimal value, results in a transient drop of more than 50% (see Figure 5.11d).

Motivated by the mismatch of the streamwise induced velocity, we also conduct the pitch step cases with an absent normal force $C_y = 0$ (the cases labelled A0-Cx-S4 and A8-Cx-S12). The resulting evolution of $u_*$ and the corresponding absolute model error are shown in Figure 5.12 for the large pitch step case. In the absence of normal forcing, the previously observed mismatch between the model and the LES reference vanishes, and the model error after the initial time steps is 2 orders of magnitude smaller than $u_*$. This highlights the impact of the assumptions made when linearising the vorticity transport equation for the model derivation. Neglecting the non-linear transport terms, which include the induced velocity, causes the model to miss the normal displacement of the start-up vortex as it is advected in the induced normal velocity field of the bound vortex, which is maximal at the wake centre line ($x_*, y_* = 0$). This lack of vertical displacement is also apparent in the previously shown model solution for the vorticity field (Figure 5.7). Switching off the normal forcing, $C_y$, removes its anti-symmetric contribution to the induced velocity field. Thus, as long as the streamwise induced velocity remains small, the model can now correctly predict $u_*$, too. It can also be noted that the induced streamwise velocity after the decay of the transient tends towards the steady-state limit given by $u_* = -C_x/(4\sqrt{\pi}\epsilon_*)$,

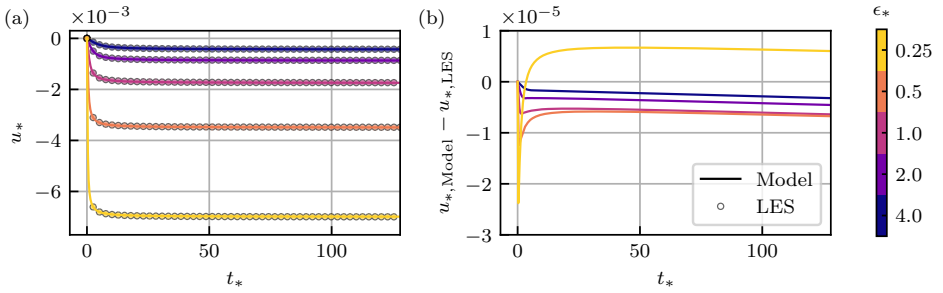


Figure 5.12: Comparison of the model solution and LES reference for the time evolution of the streamwise induced velocity (a) and the corresponding absolute error (b) for the pitch step actuation case A8-Cx-S12. Reference data points are only shown in steps of $64\Delta t_{*,\mathrm{LES}}/\epsilon_*$.

which was also derived by Martínez-Tossas et al. [146].

5

### 5.5.4 Response to periodic pitch actuation

After characterising the developed model with pitch steps we now move on towards signals which are more present in reality, i.e., smooth signals and, in particular, periodic signals with sinusoidal shape. The solution to the latter can also be used to construct the solution for more complex forcing signals via their representation in terms of a Fourier series. In the following, we consider the four cases A0-Cxy-P3-k01, A0-Cxy-P3-k02, A0-Cxy-P3-k03 and A0-Cxy-P3-k06, which initially possess the same pitch step as the A0-Cxy-S4 case but then proceed with a continuous sinusoidal pitch actuation of amplitude $\Delta\beta = 3^\circ$. The four different cases vary in terms of the actuation frequency; namely, the four reduced frequencies $k = 0.1$, $k = 0.2$, $k = 0.3$ and $k = 0.6$ are considered.

Representative angle of attack evolutions obtained for these four reduced frequencies are shown for the case of $k = 0.3$ in Figure 5.13. The angle of attack now varies periodically, where its initial evolution shows a transient due to the influence of the start-up vortex, which initially is still present. After the transient, the angle of attack attains a limit cycle. For reference, Figure 5.13 shows horizontal lines indicating the angle of attack amplitude predicted by the model closed-loop transfer function (given by $|G(k)|\Delta\beta$). The frequency domain solution in terms of the transfer function is able to predict the limit cycle amplitude modulation since the peaks of the angle of attack time series converge towards the horizontal lines. Therefore, the effect of increasingly smaller kernel widths is a successive reduction of the angle of attack amplitude compared to the quasi-steady reference ($\Delta\beta = 3^\circ$) and a successive increase in phase lag. For the given airfoil and reduced frequency of $k = 0.3$, the reduction in effective angle of attack amplitude is as large as 35% for the smallest studied kernel width $\epsilon_* = 0.25$, which is of the order of the steady-state optimal kernel width. The evolution of the induced velocities and the force coefficients corresponding to the previous angle of attack evolution of the A0-Cxy-P3-k03 case are shown in Figure 5.14. Similar to the step cases, the model cannot predict the correct streamwise induced velocity, $u_*$, in the presence of combined streamwise and normal forcing, where the error increases with decreasing kernel width. After the decay of the initial transient, it is

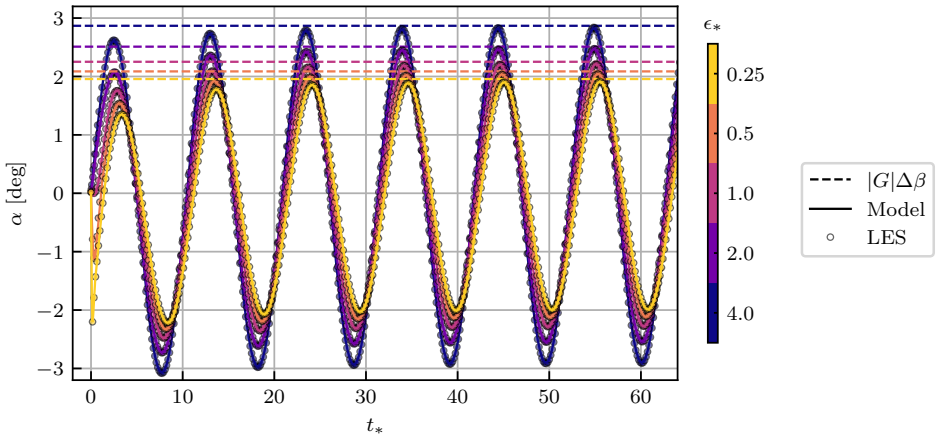


Figure 5.13: Comparison of the model solution and LES reference for the initial time evolution of the angle of attack for the periodic pitch actuation case A0-Cxy-P3-k03. Reference data points are only shown in steps of $4\Delta t_{*,\mathrm{LES}}/\epsilon_*$. The horizontal coloured dashed lines indicate the unsteady angle of attack amplitudes $|G(k)|\Delta\beta$ predicted by the model closed-loop transfer function $G(k)$.

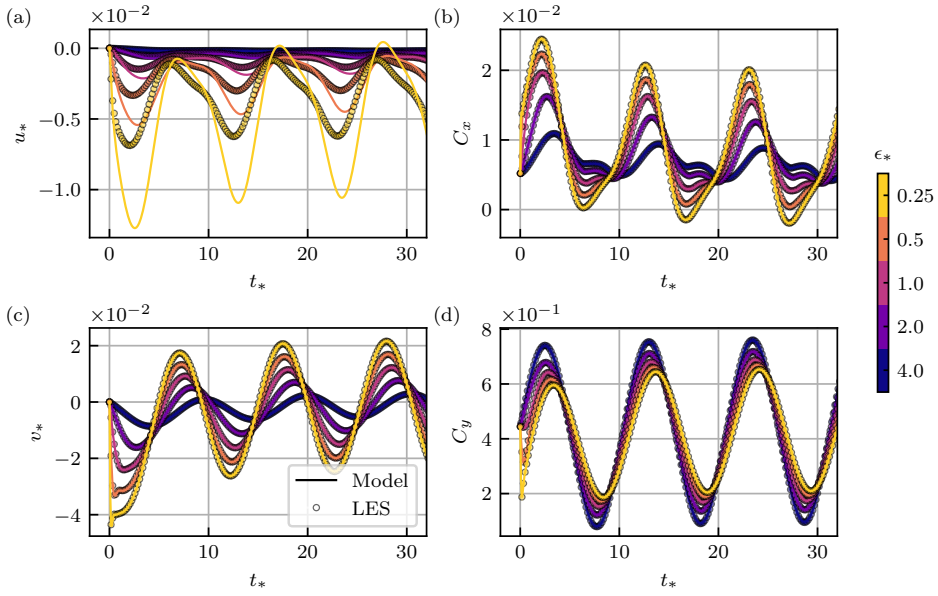


Figure 5.14: Comparison of the model solution and LES reference for the initial time evolution of the streamwise (a) and normal (c) induced velocity and the streamwise (b) and normal (d) force coefficients for the periodic pitch actuation case A0-Cxy-P3-k03. Reference data points are only shown in steps of $4\Delta t_{*,\mathrm{LES}}/\epsilon_*$.

convenient to represent the force coefficients in terms of hysteresis plots (Figure 5.15). The

grey reference lines in this plot show the quasi-steady force coefficients, i.e., the forcing as it would be obtained when the instantaneous angle of attack matches the instantaneous pitch angle. However, the velocity induced by the shed vorticity in the wake causes a non-zero flow angle, and it is $\alpha \neq \beta$, which causes the unsteady force coefficients to differ from the quasi-steady ones both in terms of magnitude and phase. These differences between unsteady and quasi-steady force coefficients depend on the kernel width. For the shown case of $k = 0.3$ in Figure 5.15b, it can be seen that smaller kernel widths cause stronger hysteresis, e.g., the minor axis of the ellipse for $C_y$ is larger (phase modulation). Furthermore, the major axis of the ellipse becomes increasingly tilted towards the horizontal axis, i.e., the force amplitude is damped compared to the quasi-steady case (amplitude modulation). For the streamwise forcing, $C_x$, smaller kernel widths also lead to more pronounced hysteresis as observed for $C_y$ (Figure 5.15a). However, the trend for the amplitude modulation is different compared to $C_y$ in the sense that the unsteady solution for $C_x$, compared to the quasi-steady reference, shows an increase in amplitude rather than a decrease. This amplitude increase is larger for smaller kernel widths because for these cases, the normal induced velocity reaches larger values (Figure 5.14c), and thus the same follows for the flow angle $\phi$. Since the streamwise force coefficient in the linear regime of the lift curve is dominated by the $C_L$ contribution, it attains its maximum when the product $-C_L(\alpha)\sin(\phi)$ becomes maximal, which in addition to large $C_L$ also requires flow angles close to their maximal negative value since $C_L$ and $v_*$ are approximately half a period out of phase (compare panels c and d of Figure 5.14). Given the dominance of the normal

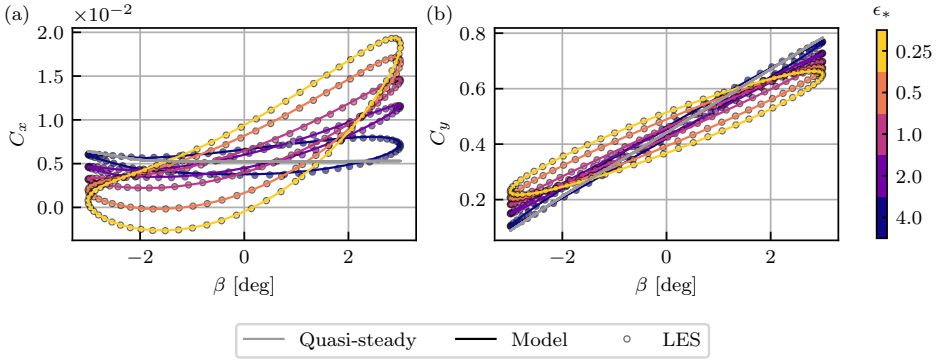


Figure 5.15: Comparison of the model solution and LES reference for the hysteresis of the streamwise (a) and normal (b) force coefficient (periodic pitch actuation case A0-Cxy-P3-k03). The quasi-steady references $C_x(\beta)$ and $C_y(\beta)$ are shown in grey.

forcing in the linear regime of the lift curve for which the present model is developed, the observations regarding the phase and amplitude modulations made from the time series and hysteresis curves can be concisely summarised in a Bode plot. Figure 5.16a/b shows the Bode magnitude and Bode phase plot of the model closed-loop transfer function $G(k)$, which was derived assuming $C_D = 0$. $G(k)$ is here computed using the linearised value of the lift slope of the NACA64-A17 airfoil at the operating point $\beta^0 = 0^\circ$, matching the operating point of the periodic actuation cases. The model solution is presented for the set

of kernel widths $\epsilon_* \in \{0.25, 0.5, 1.0, 2.0, 4.0\}$ in the range $k \in [0, 0.75]$. In addition, the phase and amplitude modulation are extracted from the last period of the LES reference data for the cases A0-Cxy-P3-k01 ($k = 0.1$), A0-Cxy-P3-k02 ($k = 0.2$), A0-Cxy-P3-k03 ($k = 0.3$) and A0-Cxy-P3-k06 ($k = 0.6$), which are shown as dots in the plot. The transfer function solution matches the LES reference for all four reduced frequencies.

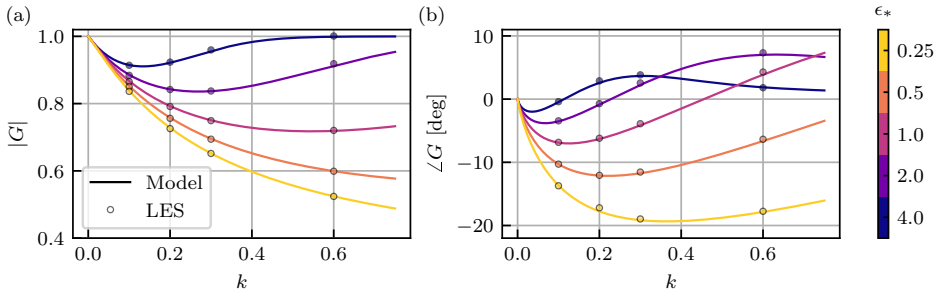


Figure 5.16: The magnitude (a) and phase (b) of the model closed-loop transfer function $G(k)$ for the NACA64-A17 airfoil at the linearisation point $\beta^0 = 0^\circ$. Dots indicate the corresponding amplitude and phase modulations extracted from the last period of the LES reference cases A0-Cxy-P3-k01, A0-Cxy-P3-k02, A0-Cxy-P3-k03 and Cxy-P3-k06.

For reduced frequencies $k \leq 0.3$, magnitude and phase trends are monotone for varying kernel width at a given constant frequency. However, the magnitude and phase variation with frequency for a constant kernel width are not monotone. The magnitude reaches a minimum, after which it again approaches $|G| = 1$ for further increasing $k$. The convergence to $|G| = 1$ happens for smaller $k$, the larger the kernel width, and for the shown relevant frequency range, it is only visible for $\epsilon_* = 4.0$. In this limit, the unsteady lift magnitude again approaches the quasi-steady solution. Also, the phase tends towards a common limit of $\angle G = 0^\circ$ for all kernel widths as $k \longrightarrow \infty$, although this convergence happens for $k > 0.75$ except for the largest studied kernel width. Consequently, for a chosen kernel width representing the airfoil, the maximum reduction of the quasi-steady lift amplitude $\min(|G(k;\epsilon_*)|)$ and maximum phase lag $\min(\angle G(k;\epsilon_*))$ occur for an intermediate reduced frequency $0 < k < \infty$. Further, the maximum phase lag occurs for smaller $k$ than does the maximum amplitude reduction. Within the range of relevant $k$, smaller kernel widths lead to larger damping. Comparing $\epsilon_* = 0.25$, which is of the order of the steady-state optimal kernel width, with $\epsilon_* = 4$, which corresponds to a value encountered for coarse grid ALM-LES for wind energy purposes, one would miss about $\Delta(|G|) \approx 0.3$ of damping and $\Delta(\angle G) \approx 23^\circ$ of phase lag at a reduced frequency of $k = 0.3$. This difference is the unsteady equivalent of the steady-state lift error observed for suboptimal large kernel widths, which motivated the development of smearing corrections [149, 150, 151, 152].

The source of the unsteady error due to large kernel widths can also be made apparent by comparing the topology of the shed vorticity in the wake for varying $\epsilon_*$ (Figure 5.17). The regularisation with the Gaussian kernel conserves both the integrated force as well as the integrated vorticity. That is assuming the magnitude of the point force would not be affected by the induced velocities, which in reality it is. But even neglecting this ef-

fect, the conservation on an integral level can still be achieved by locally very different vorticity distributions. The vorticity for small kernel widths is more localised, and thus integral conservation directly implies locally higher vorticity magnitudes in proximity of the airfoil and the wake centre line. In turn, large kernel widths spread the vorticity across a larger area, reducing its local magnitude. Since the induced velocity scales with the inverse of the distance outside of the vortex core, this directly implies smaller induced velocities at the actuator point. Finally, the phase error is also apparent from the vorticity distributions. To this end, one can track the vertical band of zero vorticity, which is located between the bound vortex (blue) and the neighbouring positive vorticity patch (red) directly downstream of the airfoil. Its location is closest to the airfoil for $\epsilon_* = 0.25$ and then shifts continuously farther downstream for larger kernel widths, i.e., the larger the kernel width, the further ahead the phase.

Summarising the model verification presented in this section, we conclude that the developed model matches the ALM-LES predictions for the unsteady loading on the airfoil within the considered operating regime, which is the linear part of the lift curve. The step and periodic actuation cases demonstrated the frequency-dependent impact of the Gaussian kernel width on the unsteady loading, both in terms of lift reduction and added phase lag.



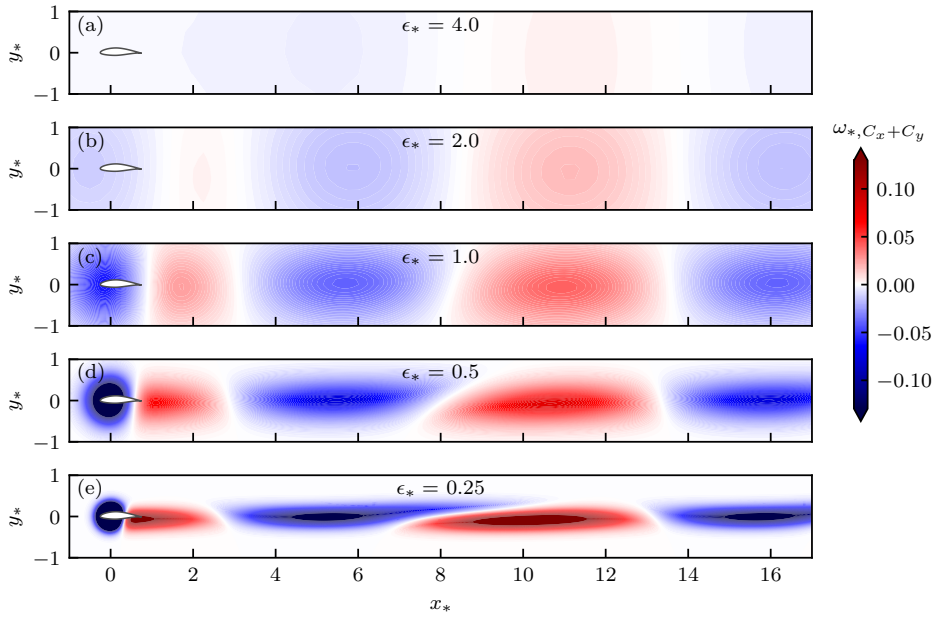


Figure 5.17: Model solution for the total resultant vorticity field of the A0-Cxy-P3-k03 case at time instance $t_* = 32$. The panels (a) to (e) show the solution for the Gaussian kernel widths $\epsilon \in \{4.0, 2.0, 1.0, 0.5, 0.25\}$. The airfoil modelled by the Gaussian body force is shown in white with black outline. The airfoil's quarter-chord point is located at the actuator point $(x_*^{Act}, y_*^{Act})^\top = (0,0)^\top$.

## 5.6 Discussion: Assessing the model error with respect to LES-ALM

The preceding verification results show that within the linear regime of the lift curve, the derived model solutions match the ALM-LES predictions of the unsteady loading on the airfoil. However, it also became clear that even within this regime the model cannot reproduce the correct streamwise induced velocity in the presence of combined forcing in the streamwise and normal directions. This deficiency does not affect the accuracy of the results as long as the small-angle approximation for the flow angle is valid. Nevertheless, due to this observation, we already pointed out in Section 5.5.3 towards the fact that there is a coupling between the two forcing directions, which is neglected for the derivations in this work. We derive here the exact form of the neglected terms and assess their magnitude and spatial localisation with respect to the reference LES data.

The vorticity transport equation for the two-dimensional problem was introduced in equation 5.3 and reads in expanded form as

$$\frac{\partial \omega_*}{\partial t_*} + \frac{\partial \omega_*}{\partial x_*} + \underbrace{u_* \frac{\partial \omega_*}{\partial x_*} + v_* \frac{\partial \omega_*}{\partial y_*}}_{\mathcal{N}(\boldsymbol{u}_*, \omega_*)} = \underbrace{\frac{-y_* C_x + x_* C_y}{\pi \epsilon_*^4} e^{-(x_*^2 + y_*^2)/\epsilon_*^2}}_{F(x_*, y_*, t_*)}. \tag{5.30}$$

In order to arrive at the final linearised equation 5.4 as introduced in Section 5.2, one needs to assume that the non-linear term $\mathcal{N}(\boldsymbol{u}_*, \omega_*)$ can be neglected, which means that if the other remaining terms are all of order $\mathcal{O}(1)$, the non-linear term should be at maximum of order $\mathcal{N} = \mathcal{O}(1/10)$. An increasing magnitude of the forcing $F(x_*, y_*, t_*)$ increasingly challenges this linearisation. Analysis of the forcing shows that it is locally linearly proportional to the magnitude of the force coefficients $F \propto C_i$ ($i \in x, y$), but inversely proportional to the fourth power of the kernel width $F \propto 1/\epsilon_*^4$. However, in addition the Gaussian contribution, the forcing term attains a maximum value of $\max(x_* \exp(-x_*^2/\epsilon_*^2)) \approx 0.43\epsilon_*$ at $x = \epsilon_*/\sqrt{2}$. Neglecting the effect of the kernel on the strength of the forcing via the induced velocity, this scaling shows that within the linear region of the lift curve, doubling the angle of attack only doubles the local forcing magnitude, whereas halving the Gaussian kernel width leads to an eightfold increase in local forcing (i.e. $F \propto 1/\epsilon_*^3$).

Based on this scaling analysis, we focus the error analysis on the smallest kernel width of $\epsilon_* = 0.25$. Figure 5.18a/b shows the vorticity solution for the large pitch step case A8-Cxy-S12 obtained both from the model and the LES at time instance $t_* = 12$. The LES which solves for all terms present in equation 5.30 predicts a roll-up and normal displacement of the start-up vortex. Furthermore, the non-linear terms break the (anti-) symmetric vorticity distribution of the model with respect to the wake centre line. In contrast, the model cannot capture these effects since it neglects $\mathcal{N}$. Figure 5.18c/d shows the resulting (relative) error with respect to the LES reference. In proximity of the start-up vortex, the maximum relative error reaches more than 30%, but it remains of the order of a few per cent in the remaining wake region between the bound and start-up vortex. We now show that this vorticity error accounts for the discrepancy of the streamwise induced velocity at the actuator point, which is observed in Figure 5.11a. To this end, we numerically evaluate the Biot-Savart law of the vorticity residual $\omega_{*,\mathrm{LES}} - \omega_{*,\mathrm{Model}}$ to obtain the velocity residuals $u_{*,\mathrm{Res}}$ and $v_{*,\mathrm{Res}}$.

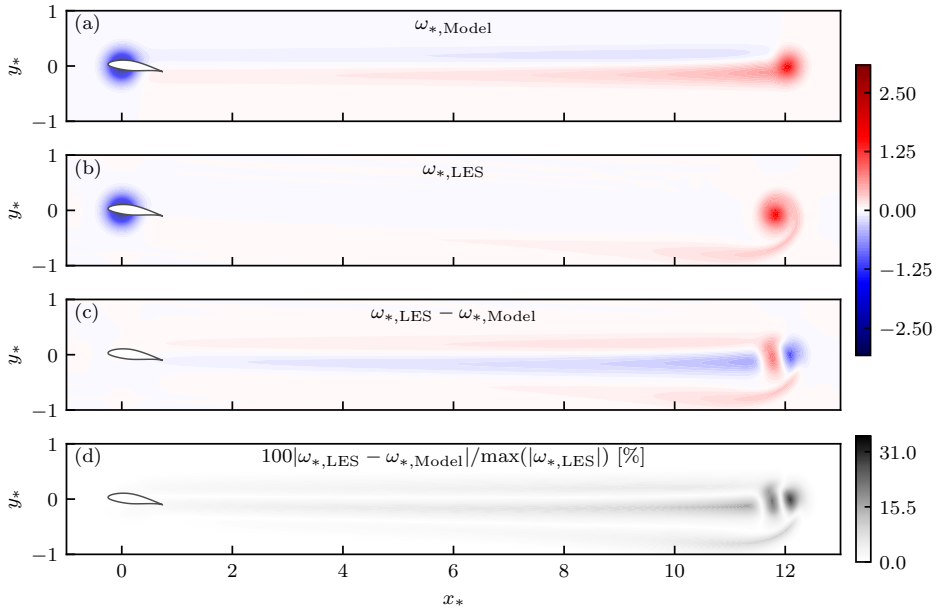


Figure 5.18: Model (a) and LES (b) solution for the total vorticity field of the A8-Cxy-S12 case for $\epsilon_* = 0.25$ at time instance $t_* = 12$. The difference between the model and LES solution is shown in (c). The relative error is shown in (d) where the reference for the normalisation of the error is the maximum value of the absolute vorticity in the $x_* - y_*$ plane. The airfoil modelled by the Gaussian body force is shown with a grey outline. The airfoil's quarter-chord point is located at the actuator point $(x_*^{Act}, y_*^{Act})^\top = (0, 0)^\top$.

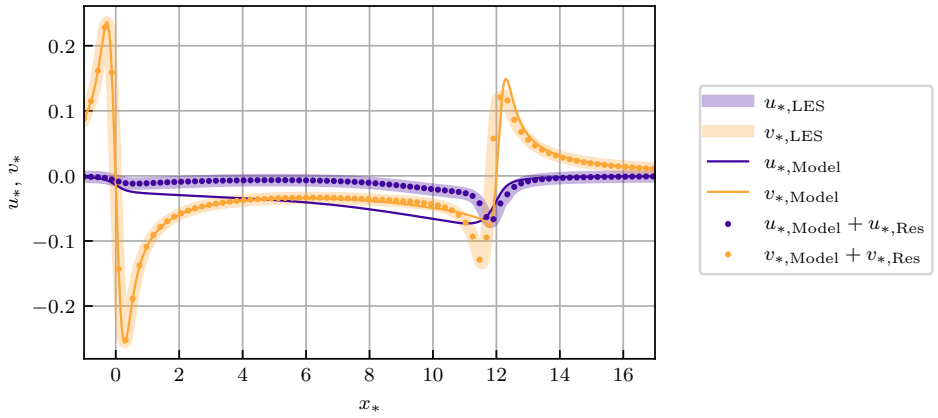


Figure 5.19: Comparison of the model and the LES solution for the streamwise and normal induced velocity along the curve $(x_*, y_* = 0)^\top$ for $\epsilon_* = 0.25$ at time instance $t_* = 12$ (A8-Cxy-S12 case). The black markers show the sum of the model solution and the velocity induced by the vorticity residual shown in Figure 5.18c. The residual contribution is obtained by numerical evaluation of the Biot-Savart integral.

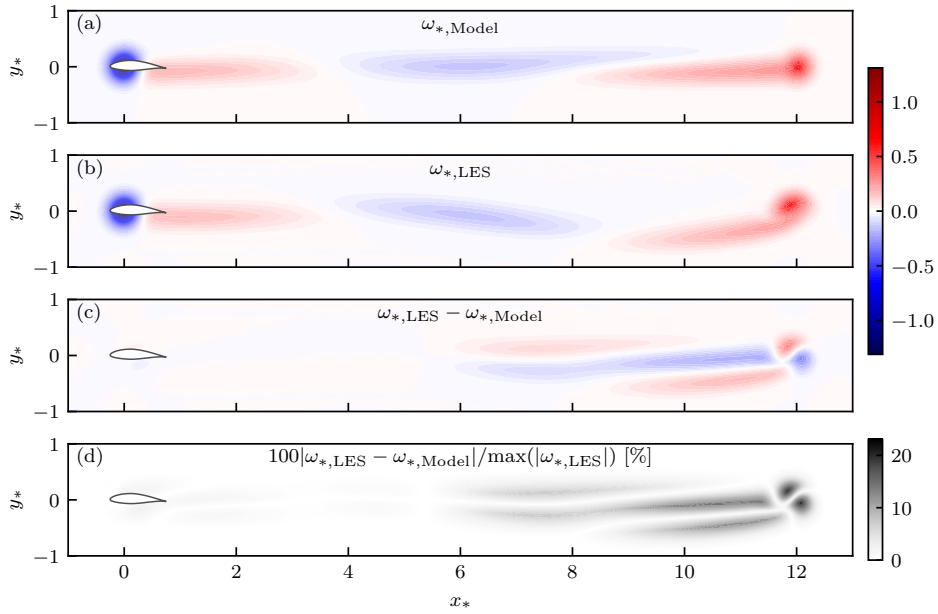


Figure 5.20: Model (a) and LES (b) solution for the total vorticity field of the A0-Cxy-P3-k03 case for $\epsilon_* = 0.25$ at time instance $t_* = 12$. The difference between the model and LES solution is shown in (c). The relative error is shown in (d) where the reference for the normalisation of the error is the maximum value of the absolute vorticity in the $x_* - y_*$ plane. The airfoil modelled by the Gaussian body force is shown with a grey outline. The airfoil's quarter-chord point is located at the actuator point $(x_*^{Act}, y_*^{Act})^\top = (0,0)^\top$.

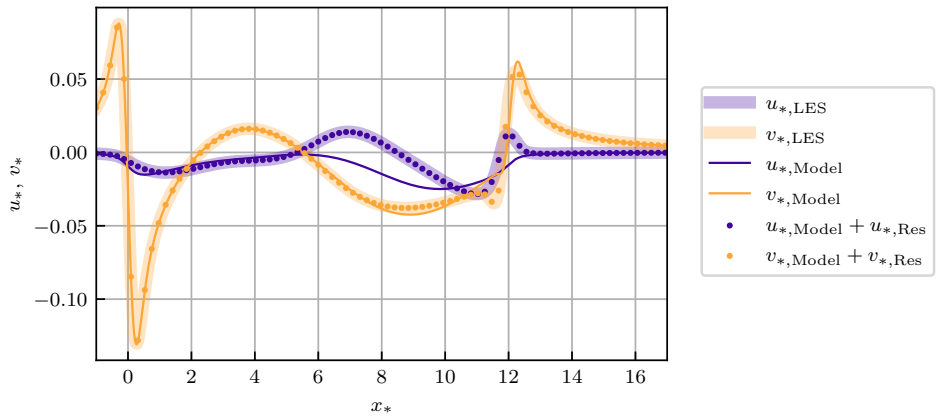


Figure 5.21: Comparison of the model and the LES solution for the streamwise and normal induced velocity along the curve $(x_*, y_* = 0)^\top$ for $\epsilon_* = 0.25$ at time instance $t_* = 12$ (A0-Cxy-P3-k03 case). The black markers show the sum of the model solution and the velocity induced by the vorticity residual shown in Figure 5.20c. The residual contribution is obtained by numerical evaluation of the Biot-Savart integral.

Figure 5.19 shows the streamwise and normal induced velocity along the wake centre line both for the model and the LES. The model correctly predicts $v_*$ near the actuator point and in the near wake, but deviations occur farther downstream near the start-up vortex. The streamwise component $u_*$ also deviates already in the proximity of the actuator point, as observed previously. However, adding the numerically computed residual velocities to the model solution recovers the LES solution. This finding shows that the derived model solutions for the induced velocity (equations 5.9 and 5.16) and the vorticity (equations 5.38 and 5.41) are consistent and that neglecting the term $\mathcal{N}$ explains the observed model error.

The same error analysis is also conducted for the A0-Cxy-P3-k03 case in Figure 5.20, which features a continuous change of bound vorticity and thus also a continuous band of shed vorticity. The (relative) error shown in panels c and d of this Figure is constrained to a region starting downstream of $x_* = 6$. This localisation shows that the previously observed absence of large errors in the near wake of the pitch step case are not simply due to the absence of vorticity (the start-up vortex was already advected further downstream), but that the linearised vorticity transport equation is capable of predicting an accurate trajectory of the shed vorticity in the near wake. This observation also manifests in the induced velocity distributions along the centre line shown in Figure 5.21. The model captures the normal induced velocity accurately up to $x_* = 6$. The deviations farther downstream and in general for the streamwise induced velocity are again shown to be accounted for by the contribution of the vorticity residual between LES and the model.



## 5.7 Numerical and experimental model validation

In the two preceding sections, we verified the developed model with the corresponding non-linear ALM-LES results and quantified the error due to using the linearised governing equations for the model derivation. However, there are additional physical effects which are inherently not captured by the ALM and thus are also ignored by the derived model, which is intended to reproduce the ALM predictions. The comparison with Theodorsen theory in Section 5.4.3 showed that the classical ALM neglects the non-circulatory contributions to the unsteady lift and also does not take into account the circulatory contribution from the pitch rate. Furthermore, Theodorsen theory itself assumes inviscid flow, approximates the airfoil with a simple representation in terms of point vortices, neglects the airfoil thickness and assumes the trajectory of the shed vorticity in the wake to be solely determined by the free stream velocity (linearisation). In order to probe the impact of these model assumptions, we validate the developed model for the ALM with numerical and experimental reference data, which (partially) do not rely on the above assumptions (Table 5.2). Doing so allows us to find answers to the two questions raised earlier, namely, is the steady-state optimal kernel width still applicable for the unsteady case, and further, when does the ALM fail to predict the unsteady loading even when using the optimal kernel width?

### 5.7.1 Validation with inviscid (Euler) computational fluid dynamics

We first compare the model with numerical reference data from Motta et al. [254]. They employ a finite-volume Euler solver for moving, overset, multi-block grids to compute the loads on symmetric airfoils in response to sinusoidal pitching motion around the quarter-

| Study | Airfoil | Re | $\beta^0$ | $\Delta\beta$ | $k$ |
|---|---|---|---|---|---|
| Motta et al. [254] | NACA 00{04/12/18/24} | $\infty$ | $0^\circ$ | $1^\circ$ | 0.01 – 0.75 |
| Ōtomo et al. [255] | NACA 0018 | $3.2 \cdot 10^4$ | $0^\circ$ | $\{4, 8\}^\circ$ | $\{0.22, 0.44, 0.66\}$ |

Table 5.2: Overview of the numerical and experimental data sets employed for the model validation. The type of airfoil is shown together with the studied chord-based Reynolds numbers Re, operating points $\beta^0$, pitch amplitudes $\Delta\beta$ and the reduced frequencies $k$.

chord point ($a = -0.5$). The pitching motion is characterised by an operating point of $\beta^0 = 0^\circ$, a pitch amplitude of $\Delta\beta = 1^\circ$ and considers the range of reduced frequencies $k \in [0.01, 0.75]$. The flow is approximately incompressible with a Mach number of $Ma = 0.117$. Four different NACA airfoils (0004, 0012, 0018, 0024) were simulated to study the impact of airfoil thickness on the unsteady loads and the results were compared to Theodorsen theory.

We compare in Figure 5.22 the ALM transfer function, $G(k)$, for the unsteady lift with the results from Motta et al. [254] obtained for their thinnest studied airfoil (NACA 0004). In addition, the Theodorsen transfer function, $T(k)$, is shown. It should be noted that Motta et al. [254] chose to present their results in terms of the unsteady lift coefficient normalised with the pitch amplitude ($\Delta C_L^{us}(k)/\Delta\beta$) and thus the transfer function $G(k)$ and $T(k)$ need to be multiplied with the airfoil lift slope ($\mathrm{d}C_L/\mathrm{d}\alpha = 2\pi$ for the flat plate) in order to obtain the appropriate scaling. Furthermore, it should be noted that the transfer function $G(k)$ for the ALM is also computed based on the flat plate lift slope to be consistent with Theodorsen theory. The reference data for the NACA 0004 airfoil closely match the magnitude and phase of $T(k)$. Because of the good match between the thin airfoil CFD results and $T(k)$ the conclusions reached in Section 5.4.3 regarding the limits of the ALM's applicability to model unsteady aerodynamics apply to the validation with the CFD data. A Gaussian kernel width of $\epsilon_* \approx 0.4$ closely matches the magnitude of the unsteady lift up to $k < 0.2$, whereas deviations in phase occur as soon as $k > 0$.

In section 5.4.3, we also showed that the three remaining terms modelled by Theodorsen theory, but neglected by the ALM, can be incorporated into an extended ALM transfer function $G_{Ext}(k)$ (equation 5.29). In Figure 5.23, the previous comparison with the reference data from Motta et al. [254] for the NACA 0004 airfoil is repeated for $G_{Ext}(k)$. It can be seen that $G_{Ext}(k; \epsilon_* = 0.4)$ closely reproduces the prediction from Theodorsen theory and thus also leads to an accurate magnitude and phase prediction compared to the CFD reference. While the objective of the present study is to reproduce the behaviour of the classical ALM with a simple model, this result highlights avenues for future work to incorporate the non-circulatory terms, $T_{NC}^{\dot{\beta}}$ and $T_{NC}^{\ddot{\beta}}$, and the pitch rate dependent circulatory term, $T_C^{\dot{\beta}}$, into the ALM formulation in order to increase the bounds of the ALM's applicability to unsteady aerodynamics beyond $k = 0.2$.

The presented comparison with inviscid CFD and Theodorsen theory leads to recommendations regarding the optimal kernel width in order to accurately capture unsteady aerodynamic effects with the classical ALM based on point velocity sampling. We find that the reference data are closely matched up to $k < 0.2$ for a kernel width in the range $\epsilon_* \in [0.3, 0.5]$. Based on the validation of the extended ALM transfer function $G_{Ext}(k)$ a ker-

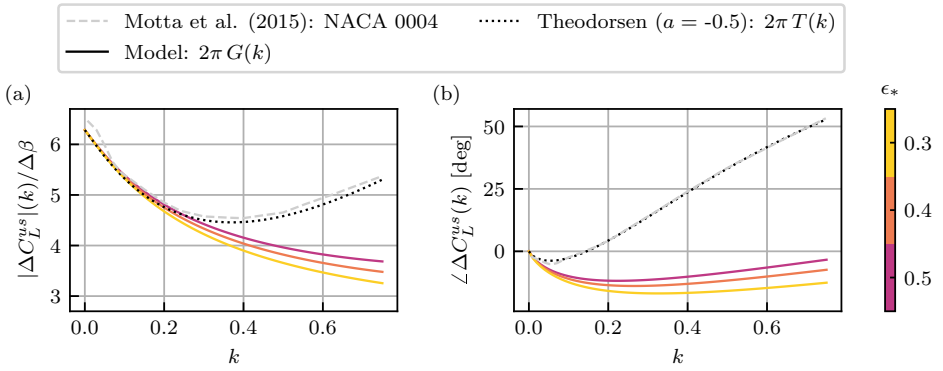


Figure 5.22: Magnitude (a) and phase (b) of the unsteady lift coefficient normalised with the actuation pitch amplitude $\Delta\beta$ as function of reduced frequency $k$. The predictions of the model frequency domain solution assuming the lift slope of a flat plate are compared with the unsteady lift predicted by Theodorsen theory and inviscid CFD results from Motta et al. [254] for a NACA 0004 airfoil.



nel width of $\epsilon_* \approx 0.4$ provides a good match with Theodorsen theory and CFD throughout the frequency range $k \in [0, 0.75]$. These identified values for the optimal unsteady kernel width are slightly higher than the range of the optimal kernel width found for steady conditions $\epsilon_{*,Opt} \in [1/8, 1/4]$ [225, 146]. However, we note that when using a Gaussian kernel with different widths in the chord and thickness directions, Martínez-Tossas et al. [146] found that the optimal width along the chord direction is approximately $\epsilon_* \approx 0.3$ for thin airfoils. Since the chord is the principal direction in the unsteady problem, it is reasonable for the optimal width to scale accordingly. Given that practical ALM-LES for wind turbine/farm modelling typically operate with kernel widths which are an order of magnitude larger, the difference between the identified optimal kernel width for steady and unsteady aerodynamics is rather small. Nevertheless, future work should explore if this difference persists when considering an advanced ALM formulation based on integral velocity sampling as proposed by Churchfield et al. [191].

Lastly, Motta et al. [254] also studied the unsteady loads on NACA 0012, 0018 and 0024 airfoils and showed that the increasing non-dimensional airfoil thickness of up to $d/c = 24\%$ challenges the flat plate assumption made by Theodorsen theory. Figure 5.24 shows that this equally applies to the ALM model. Figure 5.24(a) shows that the steady lift magnitude, $|\Delta C_L^{us}|(k = 0)$, continuously increases with the airfoil thickness. In fact the term $\Delta C_L^{us}(k = 0)/\Delta\beta$ is the lift slope of the airfoil, which can be approximated with the relation $\mathrm{d}C_L/\mathrm{d}\alpha = 2\pi(1 + 0.77\,d/c)$ [254]. The only way the airfoil thickness enters the ALM is via the lift(-slope) input. Thus, we use the relation between thickness and lift slope given above to determine varying lift slope inputs for $G_{Ext}(k)$ in order to model the impact of increasing airfoil thickness. Comparing the unsteady lift magnitude in Figure 5.24(a) shows that the $G_{Ext}(k)$ now more closely matches the CFD results in proximity of $k = 0$ than when using the flat plate lift slope to ensure consistency with Theodorsen theory (compare with Figure 5.23). However, these deviations are small compared to the deviations between the CFD and ALM results for larger airfoil thicknesses of 12 – 24%. The increased damping of

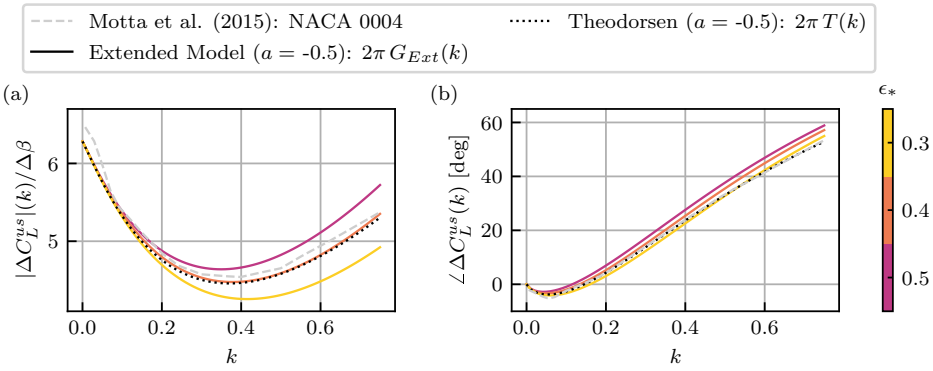


Figure 5.23: Magnitude (a) and phase (b) of the unsteady lift coefficient normalised with the actuation pitch amplitude $\Delta\beta$ as function of reduced frequency $k$. The predictions of the extended model frequency domain solution assuming the lift slope of a flat plate are compared with the unsteady lift predicted by Theodorsen theory and inviscid CFD results from Motta et al. [254] for a NACA 0004 airfoil.



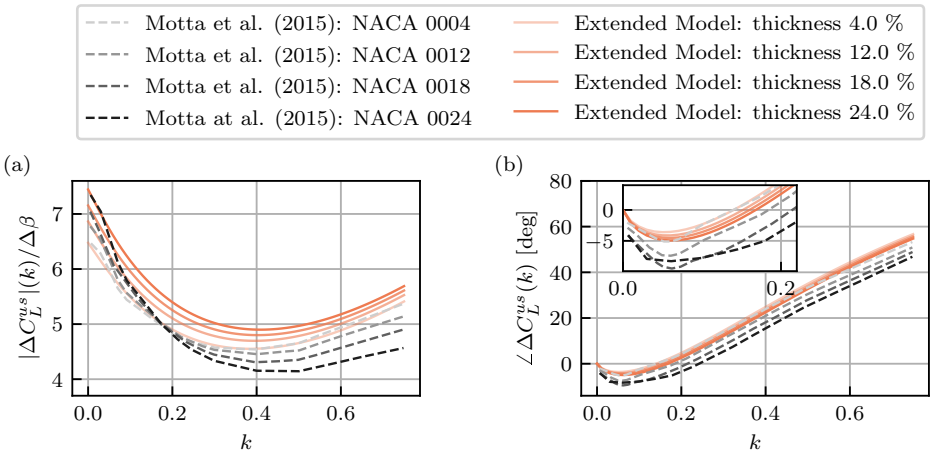


Figure 5.24: Magnitude (a) and phase (b) of the unsteady lift coefficient normalised with the actuation pitch amplitude $\Delta\beta$ as function of reduced frequency $k$. The predictions of the extended model frequency domain solution are shown for $\epsilon_* = 0.4$. The employed lift slope varies with the airfoil thickness according to $\mathrm{d}C_L/\mathrm{d}\alpha = 2\pi(1 + 0.77\,d/c)$. Results are compared to inviscid CFD results from Motta et al. [254] for the NACA 0004, NACA 0012, NACA 0018 and NACA 0024 airfoils.

the lift magnitude predicted by CFD is not captured by the ALM, in particular, as soon as $k >$ 0.05. Similar conclusions are found for the phase in Figure 5.24(b). The CFD results predict a shift of the phase inversion point to larger $k$ as the thickness increases. This trend is only qualitatively captured by the ALM, but both the maximum phase lag and the reduced frequency corresponding to the phase inversion point are quantitatively underestimated.

### 5.7.2 Validation with experiment at $Re = 32\,000$

Lastly, we validate the ALM predictions with the experimental data set from Ōtomo et al. [255]. They studied a NACA 0018 airfoil with periodic smoothed triangular pitching kinematics at $Re = 32\,000$. Hence, this validation data set also probes the model assumption of inviscid flow, and furthermore, the model is tested for actuation signals which are more complex than mono-frequency sinusoids. The triangular pitching kinematics are characterised by an operating point of $\beta^0 = 0^\circ$, pitch amplitudes of $\Delta\beta \in \{4^\circ, 8^\circ\}$ and periods corresponding to the reduced frequencies $k \in \{0.22, 0.44, 0.66\}$. The location of the pitching axis is the quarter-chord point ($a = -0.5$). Ōtomo et al. [255] compared their experimental results also to predictions from Theodorsen theory by considering the superposition of the individual Theodorsen solutions corresponding to the twenty leading Fourier harmonics.

The temporal evolution of the unsteady lift coefficient in response to the smoothed triangular pitching kinematics is shown for one period $T_{p*}$ in Figure 5.25, and the corresponding maxima of the lift coefficient are summarised in Figure 5.26. The experimental data and the Theodorsen solution are compared with the time domain solution of the de-



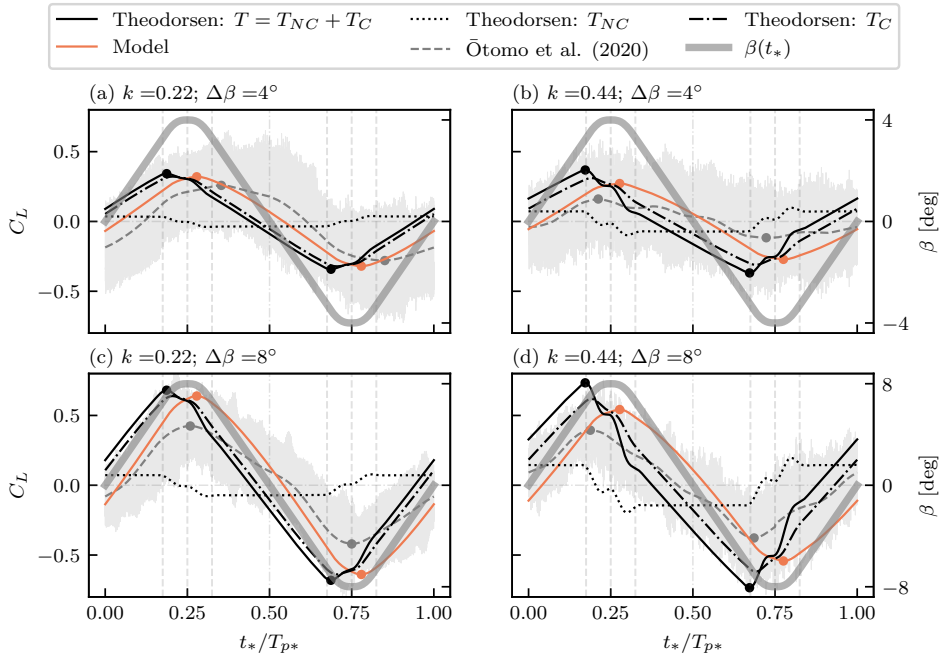


Figure 5.25: One period of the unsteady lift coefficient in response to smoothed triangular pitching kinematics with $k = 0.22$ (a)/(c) and $k = 0.44$ (b)/(d) with actuation amplitudes of $\Delta\beta = 4^\circ$ and $\Delta\beta = 8^\circ$. The predictions of the model time domain solution are shown for $\epsilon_* = 0.4$ using the lift coefficient of a flat plate. For reference, the experimental results from Ōtomo et al. [255] are shown (the shaded grey area denotes the 95% confidence interval). In addition the predictions of Theodorsen theory are shown, where the non-circulatory and circulatory contributions are also shown separately. The thick semi-transparent line indicates the time series of the pitch actuation signal. Dots mark the maxima and minima of the signals.

veloped model. The model solution is computed for the kernel width $\epsilon_* = 0.4$, which was determined as the recommended kernel width for unsteady conditions in the previous validation section. We start by focusing on the case $k = 0.22/\Delta\beta = 4^\circ$ (Figure 5.25(a)), which can be seen as the limit case for the ALM's applicability to unsteady aerodynamics given the preceding comparison with Theodorsen theory and the CFD results from Motta et al. [254] in Section 5.7.1. The Theodorsen solution is also shown split into the non-circulatory and circulatory contributions to visualise their relative importance. The non-circulatory term proportional to the pitch acceleration is zero within the linear parts of the pitch actuation signal due to the constant pitch rate and thus only contributes close to the extreme values of the pitch. It can be seen that the ALM predicts a slightly smaller unsteady lift magnitude than Theodorsen theory, which can be attributed to the observation that the non-circulatory terms neglected by the ALM reduce the damping of the unsteady lift (also recall Figure 5.4). Due to the inclusion of the non-circulatory terms, the Theodorsen theory predicts a positive phase shift with respect to the pitch actuation signal with the fundamental frequency of $k = 0.22$, whereas the ALM still predicts a small phase lag. The experimental data shows the overall largest damping and phase lag. Motta et al. [254] also studied the effect of including viscosity in their CFD study such that $Re = 10^6$ for a NACA 0018 airfoil. They observed a reduced maximum lift coefficient for the viscous results compared to the inviscid reference. Furthermore, experiments conducted by Mackowski et al. [256] for a NACA 0012 airfoil subject to sinusoidal pitching at $Re = 16\,600$ also showed stronger damping, i.e. smaller peak lift coefficient values, compared to Theodorsen theory for the pitch amplitudes $\Delta\beta \in \{2, 4, 8\}^\circ$ in the range $k \in [0, 1]$. The increased deviation between the inviscid ALM and Theodorsen solutions compared to the experimental data from Ōtomo et al. [255] is thus in agreement with the observations made in the two aforementioned studies. It should be further pointed out that one should not conclude from the comparison with the experiment that the ALM prediction is more accurate than Theodorsen theory. The closer match between the ALM and the experiment is rather likely due to fortunate cancellation of the modelling errors due to neglecting viscosity, but in addition also the three terms $T_{NC}^{\dot{\beta}}$, $T_{NC}^{\ddot{\beta}}$ and $T_C^{\dot{\beta}}$ which in turn are captured by Theodorsen theory.

Doubling the pitch amplitude (the case $k = 0.22/\Delta\beta = 8^\circ$ shown in Figure 5.25(c)) leads to doubled lift magnitudes predicted by ALM and Theodorsen theory, which is consistent with their linear nature. In contrast, the increase in lift magnitude seen in the experiment is only 60%. Furthermore, phase predictions of the linear models are unaltered, whereas the experiment shows a gain in phase such that the unsteady lift is almost in phase with the pitch actuation. Further increasing the fundamental frequency of the pitch actuation to $k = 0.44$ increases the importance of the non-circulatory terms, where the unsteady lift signals from Theodorsen theory and experiment now are ahead of the pitch actuation (Figure 5.25(b)/(d)).

As a summary of the observations made above, the maximum lift coefficients for ALM, Theodorsen theory and experiment are shown as a function of the reduced frequency $k$ in Figure 5.26. It can be concluded that for the case of $k = 0.22/\Delta\beta = 4^\circ$ both ALM and Theodorsen theory still provide reasonable lift predictions despite the low Reynolds number $Re = 32\,000$ of the experiment. In this light, the observed errors can be seen as an upper bound, given that for wind energy purposes, where the ALM finds its most use, chord-

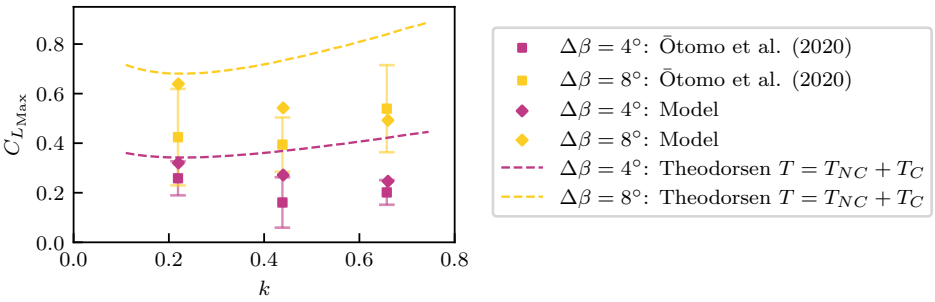


Figure 5.26: Maximum unsteady lift coefficient resulting from the smoothed triangular pitching kinematics with amplitude $\Delta\beta = 4^\circ$ and $\Delta\beta = 8^\circ$. The predictions of the model time domain solution are shown for $\epsilon_* = 0.4$ using the lift coefficient of a flat plate. For reference, the experimental results of Ōtomo et al. [255] are shown (error bars denote the 95% confidence interval). In addition the predictions of Theodorsen theory are shown.

5

based Reynolds numbers are two orders of magnitude larger. It should be again stressed that the apparent better match between ALM and experiment compared to Theodorsen theory is expected to stem from the lack of modelling the terms $T_{NC}^{\dot{\beta}}$, $T_{NC}^{\ddot{\beta}}$ and $T_C^{\dot{\beta}}$. Thus the experimental validation affirms the conclusions drawn from the ALM-Theodorsen comparison (Section 5.4.3) and from the validation with inviscid CFD results (Section 5.7.1), namely that the ALM can capture unsteady aerodynamic effects up to $k \approx 0.2$ given that the Gaussian kernel width is close to the determined optimum $\epsilon_* \approx 0.4$; the airfoil thickness is limited; and errors in phase of approximately twenty degrees can be accepted.

## 5.8 Conclusions

In this study, we assessed the ability of the actuator line model to capture the unsteady aerodynamic effects of induced velocity due to shed vorticity. We focused on the simplified two-dimensional problem of an airfoil represented by an unsteady Gaussian body force. The objective was to determine the unsteady loading on the airfoil in response to generic unsteady pitch actuation with an explicit dependence on the Gaussian kernel width. This problem formulation thereby links the ALM to the theories developed by Theodorsen [239] and Wagner [237] for the unsteady inviscid thin-airfoil problem. A linearised vorticity transport equation was obtained from the Euler equations subject to an unsteady Gaussian body force, which enabled the derivation of theoretical solutions for the induced velocity along the wake centre line and the complete two-dimensional vorticity field. The former solution takes the form of a Duhamel's integral involving an indicial response function. Based on the theoretical velocity solutions, a model for the unsteady airfoil loading was derived. Its solution was obtained in the time domain by solving a root-finding problem for the flow angle, as well as in the frequency domain by deriving the system's closed-loop transfer function mapping from the quasi-steady to the unsteady lift force. The closed-loop transfer function is parameterised by the Gaussian kernel width and thus explicitly shows its impact on the amplitude modulation and phase lag of the unsteady lift as a function of the reduced frequency.

The model was verified with non-linear reference data obtained by means of ALM-LES. The verification study considered both pitch step and periodic pitch actuation cases, where the model was tested within the linear region of the airfoil's lift curve. The relative errors for the angle of attack were on the order of tenths of a per cent. The model was shown to accurately capture the time evolution of the induced normal velocity, the angle of attack and the streamwise and normal force coefficients within the considered range of kernel widths $\epsilon_* \in [0.25, 4.0]$ and reduced frequencies $k \in \{0.1, 0.2, 0.3, 0.6\}$. However, a mismatch between ALM-LES and the model was observed for the streamwise induced velocity in the case of combined streamwise and normal forcing. This mismatch was shown to be a direct consequence of the linearisation of the vorticity transport equation during the model derivation by computing the induced velocity corresponding to the vorticity residual between the non-linear ALM-LES results and the theoretical vorticity solution.

The derived model was then used to validate the ALM's ability to model unsteady aerodynamics in attached flow conditions below stall. The comparison with Theodorsen theory showed that the ALM does not capture the contributions of the non-circulatory terms and the circulatory contribution of the pitch rate. This conclusion was confirmed by further validating with reference results obtained by means of inviscid CFD using body-fitted grids. Two main conclusions were drawn from this validation. Firstly, the optimal kernel width for modelling unsteady aerodynamics with the classical ALM based on point velocity sampling is $\epsilon_* \approx 0.4$. This value is still on the order $\epsilon_* = \mathcal{O}(10^{-1})$, but slightly larger than the range $\epsilon_* \in [1/8, 1/4]$ previously identified for the optimal steady-state isotropic Gaussian kernel width. Secondly, the ALM can accurately predict the magnitude of the unsteady loading up to reduced frequencies of $k \approx 0.2$ when employing a kernel width on the order of the identified optimum for unsteady aerodynamics. However, small errors in phase occur as soon as $k > 0$, where the error is about twenty degrees at $k = 0.2$. Finally, validation with experimental data for an airfoil executing smoothed triangular pitching kinematics at $Re = 32\,000$ further pointed towards the previously identified threshold frequency of $k \approx 0.2$ beyond which the ALM is not sufficient to capture unsteady effects.

Based on the results, we have identified three key directions for future work. Firstly, the model derivation is currently based on a linearisation point equivalent to undisturbed (vorticity-free) flow. Incorporating a flexible linearisation point by using the corresponding steady-state solution could improve the model's capabilities of predicting the trajectory of the shed vorticity in the wake. A second path is to extend the model to three dimensions, e.g., to obtain an unsteady three-dimensional filtered lifting line solution, extending the steady-state solution derived by Martínez-Tossas et al. [149]. Finally, this unsteady three-dimensional filtered lifting line solution could then be employed as a correction for coarse grid ALM-LES.



## 5.A Solving the linearised vorticity transport equation

In order to solve equation 5.4, one can exploit its advection character by considering solutions along spatio-temporal curves given by $X(s) = x_* + s$ and $T(s) = t_* + s$ (neglecting the $y_*$ dependence, which is not relevant for the derivation). Differentiation of the solution

along these curves yields

$$\frac{d}{ds}\omega_*(X(s),T(s)) = \frac{\partial\omega_*}{\partial x}\frac{dX}{ds} + \frac{\partial\omega_*}{\partial t}\frac{dT}{ds} = \frac{\partial\omega_*}{\partial x} + \frac{\partial\omega_*}{\partial t} = F(X(s),T(s)) \tag{5.31}$$

where $F(X(s),T(s))$ represents the right-hand side of equation 5.4. Subsequent integration from $T(s=-t_*)=0$ to $T(s=0)=t_*$ provides

$$\int_{-t_*}^{0}\frac{d}{ds}\omega_*(X(s),T(s))\,\mathrm{d}s = \omega_*(x_*,t_*) - \omega_*(x_*-t_*,0) = \int_{-t_*}^{0}F(x_*+s,t_*+s)\,\mathrm{d}s. \tag{5.32}$$

Using the transformation $s' = t_* + s$ ($ds' = ds$) and subsequently denoting $s'$ again as $s$, the solution with the explicit $y_*$ dependence is obtained as shown in equation 5.6.

5

## 5.B The vorticity field created by an unsteady Gaussian body force

The derivations in Section 5.3 bypass the need to calculate an explicit vorticity solution and thus avoid the need for expressing the forcing in terms of a given set of basis functions. This approach allows the computation of the unsteady loading on an airfoil subject to a generic pitch actuation, as shown in Section 5.4. However, it is instructive to study not only the influence of the Gaussian kernel width on the unsteady loading but also the unsteady vorticity field forming around the airfoil for the following two reasons: First, the vorticity field offers an explanation for the magnitude and phase modulation introduced to the unsteady loading for a given Gaussian kernel width and reduced frequency. Second, the vorticity solution can be utilised to assess the spatial and temporal nature of the modelling error caused by linearising the vorticity transport equation (equation 5.3) by computing the non-linear vorticity residual with respect to the reference LES data.

Thus, in the following an unsteady vorticity solution for equation 5.4 is derived, which requires expressing the forcing time histories $C_x(t_*)$ and $C_y(t_*)$ as a Fourier series. Then, the solution from Section 5.4.1 can be utilised as a starting point to obtain the forcing time histories for a given pitch actuation signal defined on $t_* \in [0, T_*]$, incorporating the feedback effect of the shed vorticity. Subsequently, the forcing time histories are expressed as discrete Fourier series

$$C_x(t_*) = C_x^0 + \sum_{n=1}^{N}\left(\alpha_x^n\cos\left(2\pi n t_*/T_*\right) + \beta_x^n\sin\left(2\pi n t_*/T_*\right)\right), \tag{5.33}$$

$$C_y(t_*) = C_y^0 + \sum_{n=1}^{N}\left(\alpha_y^n\cos\left(2\pi n t_*/T_*\right) + \beta_y^n\sin\left(2\pi n t_*/T_*\right)\right), \tag{5.34}$$

where $\alpha_x^n$, $\beta_x^n$, $\alpha_y^n$ and $\beta_y^n$ are the real Fourier coefficients for the streamwise and normal forcing, respectively. By exploiting the linearity of equation 5.4, one may consider the solution for each Fourier basis function separately and obtain the complete solution by

superposition. To this end, consider the combined streamwise and normal forcing term (right-hand side of equation 5.4) for a single frequency component to be

$$F^n(x_*, y_*, t_*) = \frac{-y_*(\alpha_x^n \cos(\sigma_*^n t_*) + \beta_x^n \sin(\sigma_*^n t_*))}{\pi \epsilon_*^4} e^{-(x_*^2+y_*^2)/\epsilon_*^2} + \frac{x_*(\alpha_y^n \cos(\sigma_*^n t_*) + \beta_y^n \sin(\sigma_*^n t_*))}{\pi \epsilon_*^4} e^{-(x_*^2+y_*^2)/\epsilon_*^2}, \tag{5.35}$$

where $\sigma_*^n = 2\pi n t_*/T_*$ is the harmonic angular frequency.

The complete vorticity solution is then obtained by superposing three contributions: the unsteady vorticity contributions from each non-zero frequency $\omega_*^n$, the contributions $\omega_*^0$ from the zero frequency components $C_x^0$ and $C_y^0$, and, if applicable, the contribution from the initial vorticity field $\omega_*^{IC}$, which in this work is considered to be the vorticity field corresponding to the steady state solution (equations (8) and (15) from [146]). In the following, we derive the missing solutions for the first two contributions for normal and streamwise forcing and assemble the complete solutions.



## 5.B.1 Vorticity due to normal forcing

The vorticity solution accounting for the unsteady non-zero frequency contributions ($n > 0$) of the normal forcing is obtained by inserting the normal forcing component of equation 5.35 into the integral in equation 5.6 to obtain

$$\omega_*^n = \int_{x_*-t_*}^{x_*} \xi \frac{\alpha_y^n \cos[\sigma_*^n(\xi - x_* + t_*)] + \beta_y^n \sin[\sigma_*^n(\xi - x_* + t_*)]}{\pi \epsilon_*^4} e^{-(\xi^2+y_*^2)/\epsilon_*^2} \mathrm{d}\xi, \tag{5.36}$$

where the transformation $\xi = x_* + (s - t_*)$ ($\mathrm{d}\xi = \mathrm{d}s$) is used. The analytical solution for this integral is derived in Appendix 5.B.3. The solution corresponding to the zero frequency component of the unsteady forcing ($n = 0$) is obtained by inserting the forcing $C_y^0$ instead of the trigonometric functions into the integral in equation 5.6, which then can readily be solved to obtain

$$\omega_*^0 = -\frac{C_y^0}{2\pi\epsilon_*^2} e^{-(x_*^2+y_*^2)/\epsilon_*^2} + \frac{C_y^0}{2\pi\epsilon_*^2} e^{-[(x_*-t_*)^2+y_*^2]/\epsilon_*^2}. \tag{5.37}$$

Finally, all three vorticity contributions can be combined to end up with the vorticity solution given an unsteady normal forcing $C_y(t_*)$ and subject to the assumption that $C_y(t_*)$

can be expressed as a discrete Fourier series:

$$
\begin{aligned}
\omega(x_*, y_*, t_*) =& \omega_*^{IC} + \omega_*^0 + \omega_*^n \\
=& -\frac{C_y^{IC}}{2\pi\epsilon_*^2} e^{-[(x_*-t_*)^2+y_*^2]/\epsilon_*^2} \\
& - \frac{C_y^0}{2\pi\epsilon_*^2} e^{-(x_*^2+y_*^2)/\epsilon_*^2} + \frac{C_y^0}{2\pi\epsilon_*^2} e^{-[(x_*-t_*)^2+y_*^2]/\epsilon_*^2} \\
& + \sum_{n=1}^{N} \Bigg\{ -\frac{\alpha_y^n \cos(\sigma_*^n t_*) + \beta_y^n \sin(\sigma_*^n t_*)}{2\pi\epsilon_*^2} e^{-(x_*^2+y_*^2)/\epsilon_*^2} \\
& \qquad + \frac{\alpha_y^n}{2\pi\epsilon_*^2} e^{-[(x_*-t_*)^2+y_*^2]/\epsilon_*^2} \\
& \qquad + \frac{\sigma_*^n}{4\pi\epsilon_*^2} e^{-y_*^2/\epsilon_*^2} \Bigg\{ (\alpha_y^n i + \beta_y^n) e^{i\sigma_*^n(-x_*+t_*)} \left( -\frac{1}{2} i \sqrt{\pi} \epsilon_* e^{-1/4(\sigma_*^n)^2\epsilon_*^2} \right) \times \\
& \qquad\quad \left[ \operatorname{erfi}\left( \frac{\sigma_*^n \epsilon_*}{2} + \frac{i x_*}{\epsilon_*} \right) - \operatorname{erfi}\left( \frac{\sigma_*^n \epsilon_*}{2} + \frac{i(x_*-t_*)}{\epsilon_*} \right) \right] \\
& \qquad + (-\alpha_y^n i + \beta_y^n) e^{-i\sigma_*^n(-x_*+t_*)} \left( \frac{1}{2} i \sqrt{\pi} \epsilon_* e^{-1/4(\sigma_*^n)^2\epsilon_*^2} \right) \times \\
& \qquad\quad \left[ \operatorname{erfi}\left( \frac{\sigma_*^n \epsilon_*}{2} - \frac{i x_*}{\epsilon_*} \right) - \operatorname{erfi}\left( \frac{\sigma_*^n \epsilon_*}{2} - \frac{i(x_*-t_*)}{\epsilon_*} \right) \right] \Bigg\} \Bigg\}.
\end{aligned}
\tag{5.38}
$$

It can be noted that in the case of a constant forcing and an already established bound vortex (i.e., $C_y^{IC} = C_y^0$) the solution simply reduces to the steady state solution derived in [146].

## 5.B.2 Vorticity due to streamwise forcing

The vorticity solution accounting for the unsteady non-zero frequency contributions ($n > 0$) of the streamwise forcing is obtained by inserting the streamwise forcing component of equation 5.35 into the integral in equation 5.6. Making use again of the transformation $\xi = x_* + (s - t_*)$, the integral reads as

$$
\omega_*^n = -\frac{y_*}{\pi\epsilon_*^4} \int_{x_*-t_*}^{x_*} (\alpha_x^n \cos[\sigma_*^n(\xi - x_* + t_*)] + \beta_x^n \sin[\sigma_*^n(\xi - x_* + t_*)]) e^{-(\xi^2+y_*^2)/\epsilon_*^2} \, \mathrm{d}\xi, \tag{5.39}
$$

and its solution is derived in Appendix 5.B.4. The solution corresponding to the zero frequency component ($n = 0$) of the unsteady forcing is obtained by inserting the forcing $C_x^0$ instead of the trigonometric functions into the integral in equation 5.6, which can then be solved to obtain

$$
\omega_*^0 = \frac{C_x^0}{2\sqrt{\pi}\epsilon_*^3} y_* e^{-y_*^2/\epsilon_*^2} \left[ \operatorname{erf}\left( \frac{x_* - t_*}{\epsilon_*} \right) - \operatorname{erf}\left( \frac{x_*}{\epsilon_*} \right) \right]. \tag{5.40}
$$

Combining all three contributions leads to the complete vorticity solution resulting from periodic streamwise forcing $C_x(t_*)$:

$$\begin{aligned}
\omega(x_*, y_*, t_*) =& \omega_*^{IC} + \omega_*^0 + \omega_*^n \\
=& -\frac{C_x^{IC}}{2\sqrt{\pi}\epsilon_*^3} y_* e^{-y_*^2/\epsilon_*^2} \left[1 + \operatorname{erf}\left(\frac{x_* - t_*}{\epsilon_*}\right)\right] \\
&+ \frac{C_x^0}{2\sqrt{\pi}\epsilon_*^3} y_* e^{-y_*^2/\epsilon_*^2} \left[\operatorname{erf}\left(\frac{x_* - t_*}{\epsilon_*}\right) - \operatorname{erf}\left(\frac{x_*}{\epsilon_*}\right)\right] \\
&+ \sum_{n=1}^{N} \Bigg\{ -\frac{y_*}{2\pi\epsilon_*^4} e^{-y_*^2/\epsilon_*^2} \Bigg\{ (\alpha_x^n - i\beta_x^n) e^{i\sigma_*^n(-x_*+t_*)} \left(-\frac{1}{2} i\sqrt{\pi}\epsilon_* e^{-1/4(\sigma_*^n)^2\epsilon_*^2}\right) \times \\
&\qquad \left[\operatorname{erfi}\left(\frac{\sigma_*^n\epsilon_*}{2} + \frac{ix_*}{\epsilon_*}\right) - \operatorname{erfi}\left(\frac{\sigma_*^n\epsilon_*}{2} + \frac{i(x_*-t_*)}{\epsilon_*}\right)\right] \\
&\quad + (\alpha_x^n + i\beta_x^n) e^{-i\sigma_*^n(-x_*+t_*)} \left(\frac{1}{2} i\sqrt{\pi}\epsilon_* e^{-1/4(\sigma_*^n)^2\epsilon_*^2}\right) \times \\
&\qquad \left[\operatorname{erfi}\left(\frac{\sigma_*^n\epsilon_*}{2} - \frac{ix_*}{\epsilon_*}\right) - \operatorname{erfi}\left(\frac{\sigma_*^n\epsilon_*}{2} - \frac{i(x_*-t_*)}{\epsilon_*}\right)\right] \Bigg\} \Bigg\}.
\end{aligned} \tag{5.41}$$

An observation similar to the normal forcing case can be made. In the case of constant forcing and an already established vorticity (i.e., $C_x^{IC} = C_x^0$), the solution simply reduces to the steady state solution derived in [146].

## 5.B.3 Intermediate steps: Normal forcing

Equation 5.36 can be integrated by parts to obtain

$$\begin{aligned}
\mathcal{I} =& -\int_{x_*-t_*}^{x_*} \frac{\alpha_y^n \cos[\sigma_*^n(\xi - x_* + t_*)] + \beta_y^n \sin[\sigma_*^n(\xi - x_* + t_*)]}{2\pi\epsilon_*^2} \frac{\mathrm{d}}{\mathrm{d}\xi}\left[e^{-(\xi^2+y_*^2)/\epsilon_*^2}\right] \mathrm{d}\xi \\
=& \mathcal{I}_1 + \mathcal{I}_2 + \mathcal{I}_3 \\
=& -\frac{\alpha_y^n \cos(\sigma_*^n t_*) + \beta_y^n \sin(\sigma_*^n t_*)}{2\pi\epsilon_*^2} e^{-(x_*^2+y_*^2)/\epsilon_*^2} + \frac{\alpha_y^n}{2\pi\epsilon_*^2} e^{-[(x_*-t_*)^2+y_*^2]/\epsilon_*^2} \\
&+ \int_{x_*-t_*}^{x_*} \frac{-\alpha_y^n\sigma_*^n \sin[\sigma_*^n(\xi - x_* + t_*)] + \beta_y^n\sigma_*^n \cos[\sigma_*^n(\xi - x_* + t_*)]}{2\pi\epsilon_*^2} e^{-(\xi^2+y_*^2)/\epsilon_*^2} \mathrm{d}\xi.
\end{aligned} \tag{5.42}$$

The last integral is computed with the help of the imaginary error function $\operatorname{erfi}(z) = 1/i \operatorname{erf}(iz)$. To this end, the trigonometric functions are replaced with their representation in terms of complex exponentials

$$\sin[\sigma_*^n(\xi - x_* + t_*)] = \frac{1}{2i}\left[e^{i\sigma_*^n(\xi-x_*+t_*)} - e^{-i\sigma_*^n(\xi-x_*+t_*)}\right] \tag{5.43a}$$

$$\cos[\sigma_*^n(\xi - x_* + t_*)] = \frac{1}{2}\left[e^{i\sigma_*^n(\xi-x_*+t_*)} + e^{-i\sigma_*^n(\xi-x_*+t_*)}\right] \tag{5.43b}$$

which leads to the modified integral

$$\mathcal{I}_3 = \frac{\sigma_*^n}{\epsilon_*^2} e^{-y_*^2/\epsilon_*^2} \Bigg[ (\alpha_y^n i + \beta_y^n) e^{i\sigma_*^n(-x_*+t_*)} \int_{x_*-t_*}^{x_*} e^{i\sigma_*^n \xi - \xi^2/\epsilon_*^2} \mathrm{d}\xi + (-\alpha_y^n i + \beta_y^n) e^{-i\sigma_*^n(-x_*+t_*)} \int_{x_*-t_*}^{x_*} e^{-i\sigma_*^n \xi - \xi^2/\epsilon_*^2} \mathrm{d}\xi \Bigg]. \tag{5.44}$$

The two remaining integrals can be solved analytically and are given by

$$\int_{x_*-t_*}^{x_*} e^{i\sigma_*^n \xi - \xi^2/\epsilon_*^2} \mathrm{d}\xi = -\frac{1}{2} i \sqrt{\pi} \epsilon_* e^{-1/4(\sigma_*^n)^2 \epsilon_*^2} \left[ \mathrm{erfi}\left( \frac{\sigma_*^n \epsilon_*}{2} + \frac{i x_*}{\epsilon_*} \right) - \mathrm{erfi}\left( \frac{\sigma_*^n \epsilon_*}{2} + \frac{i(x_* - t_*)}{\epsilon_*} \right) \right], \tag{5.45a}$$

$$\int_{x_*-t_*}^{x_*} e^{-i\sigma_*^n \xi - \xi^2/\epsilon_*^2} \mathrm{d}\xi = \frac{1}{2} i \sqrt{\pi} \epsilon_* e^{-1/4(\sigma_*^n)^2 \epsilon_*^2} \left[ \mathrm{erfi}\left( \frac{\sigma_*^n \epsilon_*}{2} - \frac{i x_*}{\epsilon_*} \right) - \mathrm{erfi}\left( \frac{\sigma_*^n \epsilon_*}{2} - \frac{i(x_* - t_*)}{\epsilon_*} \right) \right]. \tag{5.45b}$$

Thus, the remaining integral $\mathcal{I}_3$ in equation 5.42 is solved, and one obtains the non-zero frequency contributions ($n > 0$) of the normal forcing to the vorticity solution given in equation 5.38.

## 5.B.4 Intermediate steps: Streamwise forcing

Equation 5.39 can be rewritten using the exponential expressions for the trigonometric functions as done for the derivation of the normal vorticity, and the resulting integral is given by

$$\omega_*^n = -\frac{y_*}{2\pi\epsilon_*^4} e^{-y_*^2/\epsilon_*^2} \Bigg[ (\alpha_x^n - i\beta_x^n) e^{i\sigma_*^n(-x_*+t_*)} \int_{x_*-t_*}^{x_*} e^{i\sigma_*^n \xi - \xi^2/\epsilon_*^2} \mathrm{d}\xi + (\alpha_x^n + i\beta_x^n) e^{-i\sigma_*^n(-x_*+t_*)} \int_{x_*-t_*}^{x_*} e^{-i\sigma_*^n \xi - \xi^2/\epsilon_*^2} \mathrm{d}\xi \Bigg]. \tag{5.46}$$

It is noted that this solution only differs from its normal forcing counterpart (equation 5.44) in terms of the pre-factors of the integrals. The solutions to the integrals themselves are the same as derived in the previous section for the normal forcing. Thus, one obtains the non-zero frequency contributions ($n > 0$) of the streamwise forcing to the vorticity solution given in equation 5.41.

# 5.C Derivation of the induced velocity solutions

## 5.C.1 Normal induced velocity

Starting from equation 5.8, integration of the portion of the integral with $y_*'$ dependence yields

$$\int_{-\infty}^{+\infty} \frac{(x_* - x_*')}{(x_* - x_*')^2 + (-y_*')^2} e^{-y_*'^2/\epsilon_*^2} \, \mathrm{d}y_* = \mathrm{sgn}(x_* - x_*')\pi \left[1 - \mathrm{erf}\left(\frac{|x_* - x_*'|}{\epsilon_*}\right)\right] e^{(x_* - x_*')^2/\epsilon_*^2}, \quad (5.47)$$

which can then be combined with the portion of the integral with $x_*'$ dependence to obtain

$$v_*^{us}(x_*, 0, t_*) = \int_0^{t_*} \frac{C_y(s)}{2\pi\epsilon_*^4} \int_{-\infty}^{+\infty} \mathrm{sgn}(x_* - x_*')(x_*' + s - t_*) \left[1 - \mathrm{erf}\left(\frac{|x_* - x_*'|}{\epsilon_*}\right)\right] e^{(-(x_*' + s - t_*)^2 + (x_* - x_*')^2)/\epsilon_*^2} \, \mathrm{d}x_*' \mathrm{d}s. \quad (5.48)$$

The argument of the exponential function can be rewritten as $-2(x_* + s - t_*)x_*' + x_*^2 - (s - t_*)^2$, and with the transformation $x_*'' = x_* - x_*'$ ($\mathrm{d}x_*'' = -\mathrm{d}x_*'$), one obtains

$$v_*^{us}(x_*, 0, t_*) = \int_0^{t_*} \frac{C_y(s)}{2\pi\epsilon_*^4} \int_{+\infty}^{-\infty} (-1)\mathrm{sgn}(x_*'')(-x_*'' + x_* + s - t_*) \left[1 - \mathrm{erf}\left(\frac{|x_*''|}{\epsilon_*}\right)\right] \times e^{(2(x_* + s - t_*)x_*'' - 2(x_*^2 + x_*(s - t_*)) + (x_*^2 - (s - t_*)^2))/\epsilon_*^2} \, \mathrm{d}x_*'' \mathrm{d}s. \quad (5.49)$$

The factor of $(-1)$ can be cancelled by switching the integration limits. Furthermore, the change in sign at $x_*'' = 0$ can be handled by splitting the integral and using the fact that the error function is an odd function ($\mathrm{erf}(-x_*'') = -\mathrm{erf}(x_*'')$) in order to eliminate the absolute value in the argument of the error function, which yields

$$\begin{aligned} v_*^{us}(x_*, 0, t_*) = \int_0^{t_*} \frac{C_y(s)}{2\pi\epsilon_*^4} \Bigg[ & \int_0^{+\infty} (-x_*'' + x_* + s - t_*) \left[1 - \mathrm{erf}\left(\frac{x_*''}{\epsilon_*}\right)\right] \times \\ & e^{(2(x_* + s - t_*)x_*'' - 2(x_*^2 + x_*(s - t_*)) + (x_*^2 - (s - t_*)^2))/\epsilon_*^2} \, \mathrm{d}x_*'' \\ & + \int_{-\infty}^{0} (-1)(-x_*'' + x_* + s - t_*) \left[1 + \mathrm{erf}\left(\frac{x_*''}{\epsilon_*}\right)\right] \times \\ & e^{(2(x_* + s - t_*)x_*'' - 2(x_*^2 + x_*(s - t_*)) + (x_*^2 - (s - t_*)^2))/\epsilon_*^2} \, \mathrm{d}x_*'' \Bigg] \mathrm{d}s. \end{aligned} \quad (5.50)$$

Subsequent integration in $\mathrm{d}x_*''$ yields the solution for the normal induced velocity (equation 5.9).

### 5.C.2 Streamwise induced velocity

The solution for the portion of the integral in equation 5.15 which depends on $y'_*$ is given by

$$-\int_{-\infty}^{+\infty} \frac{y_*'^2}{(x_*-x'_*)^2+(-y'_*)^2} e^{-y_*'^2/\epsilon_*^2}\,\mathrm{d}y'_* = \\ -\sqrt{\pi}\epsilon_* - \pi|x_*-x'_*|(\mathrm{erf}(|x_*-x'_*|/\epsilon_*)-1)e^{(x_*-x'_*)^2/\epsilon_*^2}, \tag{5.51}$$

and thus we are left with

$$u_*^{us}(x_*,0,t_*) = \\ -\int_0^{t_*} \frac{C_x(s)}{2\pi^2\epsilon_*^4} \int_{-\infty}^{+\infty} \left(\sqrt{\pi}\epsilon_* + \pi|x_*-x'_*|(\mathrm{erf}(|x_*-x'_*|/\epsilon_*)-1)e^{(x_*-x'_*)^2/\epsilon_*^2}\right) e^{-(x'_*+s-t_*)^2/\epsilon_*^2}\,\mathrm{d}x'_*\,\mathrm{d}s. \tag{5.52}$$

5

The argument of the exponential simplifies to $-2x'_*(x_*+s-t_*)+x_*^2-(s-t_*)^2$. The absolute values are handled by splitting the integral in two parts, and we further transform the integrals by substituting $x''_* = x_* - x'_*$ ($\mathrm{d}x''_* = -\mathrm{d}x'_*$) to obtain

$$u_*^{us}(x_*,0,t_*) = -\int_0^{t_*} \frac{C_x(s)}{2\pi^2\epsilon_*^4} \int_0^{+\infty} \left(\sqrt{\pi}\epsilon_* e^{-(x_*-x''_*+s-t_*)^2/\epsilon_*^2}\right) + (\pi x''_*(\mathrm{erf}(x''_*/\epsilon_*)-1)\times \\ e^{(2x''_*(x_*+s-t_*)-2x_*(x_*+s-t_*)+x_*^2-(s-t_*)^2)/\epsilon_*^2})\,\mathrm{d}x''_*\,\mathrm{d}s \\ + \int_{-\infty}^{0} \left(\sqrt{\pi}\epsilon_* e^{-(x_*-x''_*+s-t_*)^2/\epsilon_*^2}\right) + (\pi(-1)x''_*(-\mathrm{erf}(x''_*/\epsilon_*)-1)\times \\ e^{(2x''_*(x_*+s-t_*)-2x_*(x_*+s-t_*)+x_*^2-(s-t_*)^2)/\epsilon_*^2})\,\mathrm{d}x''_*\,\mathrm{d}s, \tag{5.53}$$

where we exploited the fact that $\mathrm{erf}(-x''_*) = -\mathrm{erf}(x''_*)$. Integration then yields equation 5.16.

## 5.D A note on velocity sampling in the ALM

Both the time and frequency domain solutions of the developed model compute the forcing based on the flow angle determined at the actuator point. This approach was introduced in the foundational ALM work by Sørensen et al. [137]. Nevertheless, there is a difference in the definition of the velocity magnitude used for the force calculation between the derived theoretical solutions and the common ALM implementation in LES codes. In principle, the lift and drag coefficients used in step (ii) of the algorithm outlined in Section 5.4.1 are defined for the free stream velocity $U_\infty$. Since the characteristic velocity scale to non-dimensionalise the equations in this work is chosen to be $U_\infty$, the derived solutions are consistent with this definition. However, common ALM implementations in LES codes

not only use the local velocity $\boldsymbol{u}_*^{LES}$ at the actuator point to determine the flow angle for evaluation of the force coefficients but also use its magnitude to directly compute the force, e.g., for the lift force one would have $F_L^{LES} \propto |\boldsymbol{u}_*^{LES}|^2 C_L(\alpha)$. This velocity is affected by the induced velocities such that $|\boldsymbol{u}_*^{LES}| = ((1 + u_*^{LES}(0,0,t_*))^2 + v_*^{LES}(0,0,t_*)^2)^{1/2}$ and thus in case of a non-zero drag coefficient or shed vorticity, it is $|\boldsymbol{u}_*^{LES}| \neq 1$, where it should be noted that for small induced velocities $|\boldsymbol{u}_*^{LES}| \approx |1 + u_*^{LES}(0,0,t_*)|$. However, the force calculation should be based on the free stream velocity according to $F_L \propto C_L(\alpha)$.

Martínez-Tossas et al. [146] and Caprace et al. [230] proposed corrections which are used to determine an estimate of the free stream velocity solely based on the locally sampled velocity at the actuator point. Specifically for this work this would mean that equation 5.20 for $u_*$ at the actuator point would be employed to obtain the estimate

$$U_\infty^{Est} \approx |\boldsymbol{u}^{LES} - u_*(0,0,t_*)\boldsymbol{i}|. \tag{5.54}$$

In the present work, this issue can be circumvented for the reference LES simulations carried out in Section 5.5, since the free stream velocity $U_\infty$ is known and thus can be directly used for the force calculation. If, on the other hand, the LES the force coefficients would be directly evaluated with the locally sampled velocity magnitude, an additional error between model and LES would be introduced as $F_L^{LES}/F_L = |\boldsymbol{u}^{LES}|^2 \approx (1 + u_*^{LES}(0,0,t_*))^2$.



# 5.E Grid and domain size convergence of the LES setup

This appendix motivates the chosen LES setup in Section 5.5.2 by studying the convergence of the angle of attack time history at the actuator point both with grid and domain size. For this purpose, we choose a case with a stronger forcing magnitude than any case studied in the validation section (A14-Cxy-S18 for $\epsilon_* = 0.25$). The stronger magnitude results in steeper gradients and thus a more conservative setup choice.

The domain size is completely determined by the simulation time $T_*$ and the length $L_{y_*}$, which is the semi-domain height, but also sets the upstream and downstream fetch. All runs for the convergence study are conducted for $T_* = 256$, which is the longest simulation time used for the model validation. The angle of attack time dependence on $L_{y_*}$ is shown in Figure 5.27, where the grid size of the most inner refinement is $\epsilon_*/\Delta x_* = 4$ and spans $-4\epsilon_* < x_* < T_* + 4\epsilon_*$ and $-4\epsilon_* < y_* < 4\epsilon_*$. It can be seen that the angle of attack evolution is only smooth up to the time instance $t_*$ where the start-up vortex reaches the location $x_* \approx L_{y_*}$ and its induced velocity field, which scales with the inverse of the distance to the vortex core, is altered by the slip boundary conditions applied at the domain top and bottom. Consequently, we choose $L_{y_*} = 256$ since we conduct validation LES runs with $T_* = 256$. The relative error compared to an even larger domain with $L_{y_*} = 512$ (Figure 5.27b) slowly increases with time but does not exceed 0.1%, even at the final time instance $t_* = T_*$.

Furthermore, the resolution of the most inner refinement is varied between $\epsilon_*/\Delta x_* = 2$, $\epsilon_*/\Delta x_* = 4$ and $\epsilon_*/\Delta x_* = 8$ using the chosen $L_{y_*} = 256$. Note that the resolution of the base grid is constant, and the resolution is varied by adding additional refinement levels around the actuator point and the wake region. The normal extent of the most inner refinement is always $-4\epsilon_* < y_* < 4\epsilon_*$. The streamwise extent of the two coarser resolutions is $-4\epsilon_* < x_* < T_* + 4\epsilon_*$, whereas the highest resolution case only adds an additional refinement level between $-4\epsilon_* < x_* < 16 + 4\epsilon_*$. The evolution of the angle of attack on these three different

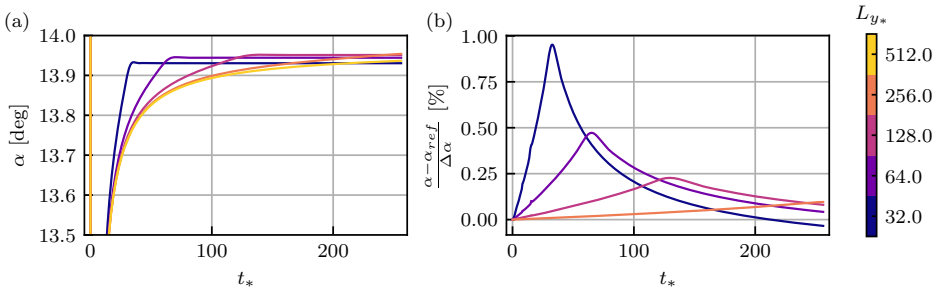


Figure 5.27: Domain size convergence study for case A14-Cxy-S18 using $\epsilon_* = 0.25$. The simulation time is $T_* = 256$, and the resolution of the most inner refinement is $\epsilon_*/\Delta x_* = 4$. (a) Angle of attack for the range of semi-domain heights $L_{y_*} = 32$ to $L_{y_*} = 512$ where the upstream and downstream fetch are scaled accordingly as described in Section 5.5.2. (b) Relative error based on the angle of attack step magnitude $\Delta\alpha = 18^\circ$. The reference case for the calculation of the error is $L_{y_*} = 512$.

5

grid resolutions is shown in Figure 5.28. Contrary to the domain size convergence, the relative angle of attack error for the grid resolution convergence stays constant after the start-up phase. This is the case because it is governed by the strength of the start-up vortex, which is determined during the initial phase of the step response. The relative error for the $\epsilon_*/\Delta x_* = 4$ case is below 0.25% after the first few time steps (Figure 5.28b). We conservatively choose here a resolution of $\epsilon_*/\Delta x_* = 8$ for all model validation runs, which ensures fully converged LES results.

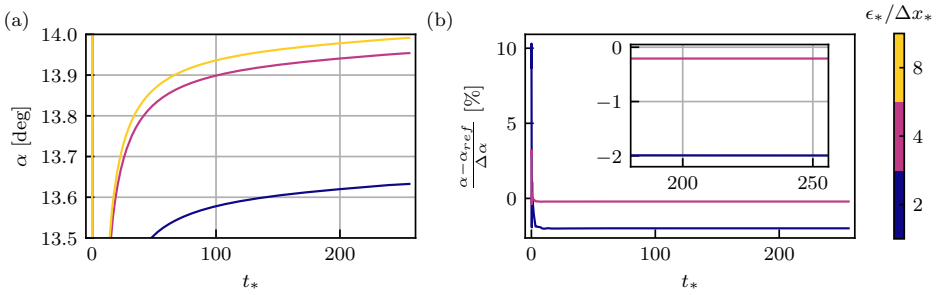


Figure 5.28: Grid size convergence study for case A14-Cxy-S18 using $\epsilon_* = 0.25$. The simulation time is $T_* = 256$ and the semi-domain height is $L_{y_*} = 256$. (a) Angle of attack for the range of grid resolutions $\epsilon_*/\Delta x_* = 2$ to $\epsilon_*/\Delta x_* = 8$ (for the most inner refinement). The semi-domain height for all three cases is $L_{y_*} = 256$. (b) Relative error based on the angle of attack step magnitude $\Delta\alpha = 18^\circ$. The reference case for the calculation of the error is $\epsilon_*/\Delta x_* = 8$.

# 6

# Conclusions and Recommendations

In the following, we return to the individual conclusions of each chapter and subsequently formulate the overall conclusion of this thesis (Section 6.1). We conclude by presenting the recommendations for future work (Section 6.2).

## 6.1 Conclusions



In this thesis, we set out with the following overall objective:

> Assess the performance of helix active wake control in quasi-steady atmospheric boundary layers and develop actuator line model capabilities for its study in coarse grid real weather large-eddy simulations.

This objective was approached in two steps. In a first step, which comprises Chapters 2 and 3, we focused on large-eddy simulations of helix active wake control in quasi-steady atmospheric boundary layers in order to address two objectives: On the one hand, the trade-off between power gain and added loading for helix active wake control in terms of its sensitivity to the actuation amplitude; and on the other hand, the comparison of helix active wake control with wake steering control. In a second step, comprising Chapters 4 and 5, we then implemented an actuator line model into an atmospheric LES code using the filtered lifting line correction to improve force predictions on coarse grids. Finally, we took the dynamic individual pitch actuation underlying helix active wake control as inspiration to explore the unsteady aerodynamic response as it is captured by the actuator line model.

### The trade-off between power gain and load for the helix

> Quantify the sensitivity of helix active wake control to the pitch amplitude control input in terms of the trade-off between wind farm power gain and structural turbine loading.

Helix active wake control was deployed on the upstream turbine of a small two-turbine wind farm operating in a conventionally neutral boundary layer with turbulence intensity

of 3 – 5% across the rotor. The pitch actuation amplitude was varied between $\beta \in [1^\circ, 6^\circ]$ while the actuation frequency was fixed at $St = 0.25$. We found that the power gain did not saturate within the considered range of pitch amplitudes. After a small region of non-linear scaling, the overall relative power gain for pitch amplitudes of $\beta > 2^\circ$ scaled approximately linearly. The power loss at the actuated turbine was caused by the airfoils operating mainly at sub-optimal angles of attack away from the design point achieved by the baseline greedy control at $\max(C_L/C_D)$. The wake of the first turbine showed elevated levels of turbulence kinetic energy compared to baseline greedy control throughout the wake between $x/D = 1 - 4$ with up to fourfold levels in the upper wake shear layer in the near wake at one diameter downstream. In conjunction, the mean streamwise velocity in the wake indicated accelerated wake recovery, which led to a maximum relative power gain of 74.6% at the downstream turbine for a pitch amplitude of $\beta = 6^\circ$. The phase-averaged wake centre trajectory for cases with helix actuation followed close to circular paths in cross-stream planes where the radius increased with pitch amplitude. This footprint of the helix in the wake caused the control to be not only present with a frequency peak at $1P + St$ in the out-of-plane blade moments of the actuated turbine, but also with a peak at $St$ at the downstream turbine, which indicates that there is still actuation induced coherent motion remaining at $x/D = 5$, which could be exploited for deploying the control also on downstream turbines. The achieved power gain came at the cost of similar increases of the pitch bearing damage and the DELs of the actuated turbine, in particular for the blade root flapwise and the tower top side-side and fore-aft channels. The DEL increases on the downstream turbine were, in comparison, marginal.



## Comparison of helix and wake steering control

> Compare the robustness of power gains achieved with helix active wake control to variations in turbine spacing and wake overlap with static wake steering.

To this end, a LES setup was developed, which made the comparison of helix and wake steering control across a wide range of turbine spacing and wake overlap computationally tractable. For wake steering, the optimal yaw offset was selected from the interval $\gamma \in [-30, 30]^\circ$ while for the helix, only a single case with $St = 0.3$ and a pitch amplitude of $\beta = 3^\circ$ was considered. Two main conclusions were drawn. Firstly, wake steering outperformed the chosen helix control in terms of power gain for all operating scenarios except the situation of full wake overlap combined with dense turbine spacing of approximately less than six turbine diameters. Here, it needs to be noted that this conclusion was obtained using a single atmospheric condition with turbulence intensity levels of 3 – 5% and $4^\circ$ of veer across the rotor. Furthermore, this conclusion holds for a constant wind direction without any uncertainty. Secondly, the optimal yaw offset for wake steering featured a discontinuity at the wind direction corresponding to full wake overlap. This discontinuity became important when considering non-zero wind direction uncertainty in terms of wind direction fluctuations around full wake overlap, to which the turbines cannot timely adjust their optimal control setpoint. For this case, helix control provided a power gain which is more robust to the occurring unintentional additional yaw offset, which is further achieved without modification of the control setpoint. This finding thus also implies that, from a

sole power gain perspective, the simultaneous use of helix and wake steering control could outperform either of them applied in isolation.

## Combining atmospheric LES with aero-hydro-servo-elastic wind turbine modelling

> Develop a simulation environment to enable large-eddy simulations of helix active wake control in realistic weather scenarios, which ensures an accurate turbine response also on coarse grids.

This objective was tackled by coupling the atmospheric LES code ASPIRE with the aero-hydro-servo-elastic wind turbine simulation code OpenFAST. The coupling between ASPIRE and OpenFAST was done via an ALM, which allows for capturing azimuthal variations in the thrust distribution, e.g. caused by helix active wake control. The use of OpenFAST allows for the convenient inclusion of turbine controllers for WFFC via the ServoDyn module of OpenFAST. The ALM implementation was cross-verified with four other commonly used research LES codes for a single NREL 5-MW turbine operating in uniform inflow. The predicted lift and drag forces along the blade matched the reference data from the other codes. Furthermore, the predicted wake profiles were consistent up to $x/D = 6$ downstream. Hence, these results indicated a correct implementation of the ALM. To improve the predicted blade forces and thus also the estimate of the turbine's generated power, which is important for the evaluation of WFFC strategies, the filtered lifting line correction was implemented. The correction reduced the ALM's power and thrust overprediction when using sub-optimal large Gaussian kernel widths. However, the implemented version of the correction required more than 150 actuator points uniformly spaced along the blade for convergence, which entailed a significant computational slowdown.



## Unsteady aerodynamics within the mathematical framework of the actuator line model

> Derive a semi-analytical model, which quantifies the ability of the actuator line model to capture unsteady aerodynamic effects and identify bounds for its validity.

The widespread application of the ALM in unsteady operating conditions, like continuous blade pitching for helix active wake control, led us to investigate to what degree unsteady aerodynamics are captured by the model. While due to its inherent model structure, the ALM cannot take into account the effect of unsteady separated flow, it was also unclear how the force regularisation impacts the unsteady response in attached flow conditions below stall. To this end, a semi-analytical model for the simplified two-dimensional ALM problem was developed and verified with ALM-LES. Validation of the model with Theodorsen theory, inviscid CFD using body fitted grids and experimental data led to three main conclusions for the thin airfoils studied here. Firstly, the chosen value of the Gaussian kernel width has a strong impact on both the magnitude and phase of the unsteady loading. Further, for a given constant kernel width, its impact on the unsteady loading depends on the reduced frequency. Secondly, the optimal Gaussian kernel width for the force regularisation in the unsteady case is approximately 40% of the chord. Thirdly, the

ALM can capture the magnitude of the unsteady lift up to reduced frequencies of $k \approx 0.2$ given that the optimal kernel width is used. For larger reduced frequencies, the predictions deteriorate since the ALM does not capture the unsteady terms accounting for added-mass and pitch rate effects.

## The bigger picture

While at first glance, the four topics above might seem only loosely related, they are four pieces of the same puzzle, which could be named *"new control strategies challenge our current models"*. Studying helix active wake control with LES proved challenging due to the added relevance of shorter temporal scales on the order of the turbine's rotational speed and smaller spatial scales on the order of individual airfoils. For the small wind farms studied in Chapters 2 and 3, this added complexity could still be handled by accepting the additional computational burden. However, solely relying on the availability of large computing resources seems restrictive. We attempted to relax the grid resolution requirements for ALM-LES by the implementation and use of the filtered lifting line correction. The correction improved accuracy, but the version used in Chapters 3 and 4 of this thesis still caused a significant increase in simulation wall time due to the increased number of required actuator points. However, this issue can be circumvented by using a non-uniform actuator point distribution in future implementations. Further, the correction was not derived for the complete unsteady problem. In Chapter 5, we showed that on coarse grids, which necessitate large sub-optimal Gaussian kernel widths for the ALM, the damping of the unsteady lift is underestimated. It is fortunate that for the 1st harmonic of the helix actuation, this underestimation might not be a pressing issue for the outer part of the newest turbine blade designs, which also contribute the most to the power generation (recall the reduced frequencies resulting from the helix shown in Figure 1.9 in the introduction). However, further blade inwards and for higher harmonics in general, this underestimation can most likely not be neglected, thus highlighting the need for a complete unsteady three-dimensional actuator line correction.



The helix's amplitude sensitivity studied in Chapter 2 showed that there will always be a price to pay for any power gain and that, unfortunately, there is no such thing as a free lunch. Combined with the superior performance of wake steering for most of the effective wind farm layouts (Chapter 3), it is likely that the helix needs to be seen as one option available in a more comprehensive toolbox of WFFC strategies. The selection and switching between control strategies from such a toolbox will require prior high fidelity modelling going beyond small wind farms operating in quasi-stationary ABLs, as important questions will be firstly the robustness of each WFFC strategy to transients in the ABL and secondly the performance potential on the scale of entire modern offshore wind farms. From these observations, we saw the need for transferring ALM capabilities and the associated corrections to atmospheric LES codes as done in Chapter 4. While in its current form, the developments of Chapter 4 are only a proof-of-concept and its application to wind farm ALM-LES at the time of conducting the research was hindered by the missing multi-GPU capabilities of the used LES code, it is believed that these issues can be overcome in the future. In fact, the utilised LES code is nowadays multi-GPU ready, and it is hoped that it will be of use for future studies of WFFC strategies like helix active wake control in realistic weather conditions.

## 6.2 Recommendations

Based on the conclusions reached above, we arrive at the following recommendations for directions of future research.

### Testing helix active wake control in "real weather" LES

As indicated in the conclusions, the filtered lifting line correction in the developed ALM-LES environment (Chapter 4) should be adapted to allow for non-uniform actuator point spacing, which allows for increased accuracy at reduced computational cost. In the meantime, during the preparation of the present thesis, a multi-GPU version of the LES code employed in Chapter 4 became available. This feature would now enable simulations using grid resolutions small enough for the ALM, but simultaneously reaching domain sizes suitable to capture entire wind farms. With the former changes, the simulation environment from Chapter 4 could be employed to test and optimise helix active wake control in realistic non-stationary ABL conditions.

### Towards a toolbox of wind farm flow control strategies

The comparison between helix and wake steering control in this thesis showed that the two different WFFC strategies might excel for different effective turbine layouts, which are determined by the wind direction. Recent research further suggests that the selection of the optimal control strategy depends on the ABL state, namely the levels of shear, veer and turbulence intensity [85, 86]. Hence, it is suggested to compare and assess the robustness of various WFFC strategies in more detail for realistic transient ABLs. Based on these results, one could develop a wind farm flow controller with a switching logic, which activates the most beneficial control strategy in response to the varying ABL state and the relative position of each turbine in the farm.



### Development of a helix wake model for optimisation

Linking back to the discussion about model fidelity in the introduction of this thesis, the employed high fidelity LES modelling was useful to obtain an understanding of the fundamental behaviour of helix active wake control and the impact of the actuation parameters. However, as a next step, there is a need for a helix wake model with low computational cost, which can capture the wake in its dynamic or at least mean evolution and depends on the actuation amplitude and frequency. The most recent research results also suggest that veer and shear effects should be included [85, 86], although neglecting them might be a tempting assumption for the model derivation. Among others, there are three interesting use cases for variants of such a model. Firstly, optimisation spanning the entire turbine lifetime (see the last recommendation) will require such a model in order to assess the power and load impact of the helix for a plethora of operating conditions at low computational cost. Secondly, there are efforts to consider the optimisation of wind farm layout and WFFC not as two separate matters conducted during the wind farm planning and operation stage, respectively. Rather, the deployment of WFFC strategies can be considered in a co-design approach to wind farm layout optimisation [180]. Here, a simplified helix wake model could allow for the consideration of the helix for this optimisation. Thirdly, the deployment of the helix in the field might ask for an optimisation of the dynamic

activation/deactivation strategy of the control given knowledge about the future wind direction. For such an optimisation, a dynamic fast-running helix wake model would be an important ingredient.

### An unsteady three-dimensional solution for the actuator line model

The present thesis highlighted the important role of corrections for the ALM, in particular on coarse LES grids. So far, a complete unsteady three-dimensional actuator line correction, which captures the impact of all vorticity components, is not available. Hence, it is suggested to extend the theoretical developments for the two-dimensional unsteady problem from Chapter 5 to three dimensions. Such a development could address three additional points. Firstly, one could incorporate a non-zero linearisation point into the semi-analytical ALM model, which could improve the assumed trajectory of the shed vorticity in the wake and thus, in particular, the drag force prediction. Secondly, in Chapter 5 it appeared that including additional terms from Theodorsen theory can improve the ALM prediction and could enable the use of the ALM for larger reduced frequencies. Lastly, we found that the optimal kernel width to model unsteady aerodynamics differs from the previously identified optimal value for steady-state conditions. Hence, future work towards an unsteady three-dimensional correction should also address the question of what is the true optimal kernel width to best represent blades with an actuator point/line model.



### Co-design of wind turbines and optimisation over lifetime for the deployment of helix active wake control

Hypothetically, helix active wake control could be deployed on any wind turbine which has individual blade pitch capabilities. In practice, however, the specific turbine might not have been designed having continuous individual pitch actuation for WFFC purposes in mind. Hence, pitch bearings and actuators might not allow for active control with the desired amplitudes and frequencies during all operating conditions, which would be, in principle, favourable for the activation of helix active wake control. Further, even when the actuators could realise the control actuation, the load impact of the helix may be reduced by developing the turbine and the control in conjunction, i.e. by following the co-design principle which optimises the structural design for the loads created by the helix. This principle could also be applied to the aerodynamic blade design, where airfoils would be selected/designed with long continuous intervals of pitch actuation in mind, or the helix actuation could be potentially even completely realised without relying on blade pitch actuation, but rather using dynamically actuated flaps along the blade. Ultimately, a more holistic approach is needed to optimise the deployment of helix active wake control. The power gain will most likely always come at the expense of some degree of load increase. Hence, an optimisation spanning the entire lifetime of the turbine is needed. Such an optimisation would then move from power to, e.g. the return over turbine lifetime as the variable to be maximised. This will be highly challenging since it requires assumptions about the development of the electricity price, material costs, wind conditions and many other factors for time frames of 20 to 30 years.

# Bibliography


[1] United Nations Environment Programme. *Emissions Gap Report 2024: No more hot air … please! With a massive gap between rhetoric and reality, countries draft new climate commitments*. Tech. rep. 2024.

[2] S. Bouckaert, A. F. Pales, C. McGlade, U. Remme, B. Wanner, L. Varro, D. D'Ambrosio, and T. Spencer. *Net zero by 2050: A roadmap for the global energy sector*. Tech. rep. Paris: International Energy Agency, 2021.

[3] International Energy Agency. *World Energy Outlook 2024*. Tech. rep. Paris, 2024.

[4] International Energy Agency. *Global Energy Review 2025*. Tech. rep. Paris, 2025.

[5] K. Sanderson. "COP28 climate summit signals the end of fossil fuels — but is it enough?" In: *Nature* 624.7992 (2023), pp. 484–485.

[6] A. Cherp, V. Vinichenko, J. Tosun, J. A. Gordon, and J. Jewell. "National growth dynamics of wind and solar power compared to the growth required for global climate targets". In: *Nature Energy* 6.7 (2021), pp. 742–754.

[7] Y. Wang et al. "Global spatiotemporal optimization of photovoltaic and wind power to achieve the Paris Agreement targets". In: *Nature Communications* 16.1 (2025), p. 2127.

[8] F. Wiese et al. "The key role of sufficiency for low demand-based carbon neutrality and energy security across Europe". In: *Nature Communications* 15.1 (2024), p. 9043.

[9] C. L. Archer and M. Z. Jacobson. "Evaluation of global wind power". In: *Journal of Geophysical Research: Atmospheres* 110.D12 (2005).

[10] X. Lu, M. B. McElroy, and J. Kiviluoma. "Global potential for wind-generated electricity". In: *Proceedings of the National Academy of Sciences* 106.27 (2009), pp. 10933–10938.

[11] M. Z. Jacobson and C. L. Archer. "Saturation wind power potential and its implications for wind energy". In: *Proceedings of the National Academy of Sciences* 109.39 (2012), pp. 15679–15684.

[12] K. Eurek, P. Sullivan, M. Gleason, D. Hettinger, D. Heimiller, and A. Lopez. "An improved global wind resource estimate for integrated assessment models". In: *Energy Economics* 64 (2017), pp. 552–567.

[13] L. Sedefian. "On the Vertical Extrapolation of Mean Wind Power Density". In: *Journal of Applied Meteorology and Climatology* 19.4 (1980), pp. 488–493.

[14] M. J. Dvorak, C. L. Archer, and M. Z. Jacobson. "California offshore wind energy potential". In: *Renewable Energy* 35.6 (2010), pp. 1244–1254.

[15] L. Hong and B. Möller. "Offshore wind energy potential in China: Under technical, spatial and economic constraints". In: *Energy* 36.7 (2011), pp. 4482–4491.

[16] A. R. Henderson, C. Morgan, B. Smith, H. C. Sørensen, R. J. Barthelmie, and B. Boesmans. "Offshore Wind Energy in Europe— A Review of the State-of-the-Art". In: *Wind Energy* 6.1 (2003), pp. 35–52.

[17] P. Veers et al. "Grand challenges in the design, manufacture, and operation of future wind turbine systems". In: *Wind Energy Science* 8.7 (2023), pp. 1071–1131.

[18] R. Green and N. Vasilakos. "The economics of offshore wind". In: *Energy Policy*. Special Section on Offshore wind power planning, economics and environment 39.2 (2011), pp. 496–502.

[19] P. E. Morthorst and L. Kitzing. "2 - Economics of building and operating offshore wind farms". In: *Offshore Wind Farms*. Ed. by C. Ng and L. Ran. Woodhead Publishing, 2016, pp. 9–27.

[20] I. Galparsoro, I. Menchaca, J. M. Garmendia, Á. Borja, A. D. Maldonado, G. Iglesias, and J. Bald. "Reviewing the ecological impacts of offshore wind farms". In: *npj Ocean Sustainability* 1.1 (2022), p. 1.

[21] P. Veers et al. "Grand challenges in the science of wind energy". In: *Science* 366.6464 (2019).

[22] S. Pope. *Turbulent Flows*. Cambridge University Press, 2001.

[23] J. C. Wyngaard. "Atmospheric Turbulence". In: *Annual Review of Fluid Mechanics* 24.Volume 24, 1992 (1992), pp. 205–234.

[24] R. A. Pielke. *Mesoscale meteorological modeling*. Third edition. International geophysics series; volume 98. Amsterdam: Elsevier, 2013.

[25] J. Sanz Rodrigo, R. A. Chávez Arroyo, P. Moriarty, M. Churchfield, B. Kosović, P.-E. Réthoré, K. S. Hansen, A. Hahmann, J. D. Mirocha, and D. Rife. "Mesoscale to microscale wind farm flow modeling and evaluation". In: *WIREs Energy and Environment* 6.2 (2017), e214.

[26] R. J. Stevens and C. Meneveau. "Flow Structure and Turbulence in Wind Farms". In: *Annual Review of Fluid Mechanics* 49.1 (2017), pp. 311–339.

[27] C. B. Hasager, N. G. Nygaard, and G. S. Poulos. "Wind Farm Blockage Revealed by Fog: The 2018 Horns Rev Photo Case". In: *Energies* 16.24 (2023), p. 8014.

[28] L. P. Chamorro and F. Porté-Agel. "A Wind-Tunnel Investigation of Wind-Turbine Wakes: Boundary-Layer Turbulence Effects". In: *Boundary-Layer Meteorology* 132.1 (2009), pp. 129–149.

[29] L. P. Chamorro and F. Porté-Agel. "Effects of Thermal Stability and Incoming Boundary-Layer Flow Characteristics on Wind-Turbine Wakes: A Wind-Tunnel Study". In: *Boundary-Layer Meteorology* 136.3 (2010), pp. 515–533.

[30] M. Abkar and F. Porté-Agel. "Influence of atmospheric stability on wind-turbine wakes: A large-eddy simulation study". In: *Physics of Fluids* 27.3 (2015), p. 035104.

[31] D. Allaerts and J. Meyers. "Large eddy simulation of a large wind-turbine array in a conventionally neutral atmospheric boundary layer". In: *Physics of Fluids* 27.6 (2015), p. 065108.

[32] K. S. Heck and M. F. Howland. “Coriolis effects on wind turbine wakes across neutral atmospheric boundary layer regimes”. In: *Journal of Fluid Mechanics* 1008 (2025), A7.

[33] R. J. Barthelmie et al. “Modelling and measuring flow and wind turbine wakes in large wind farms offshore”. In: *Wind Energy* 12.5 (2009), pp. 431–444.

[34] R. J. Barthelmie and L. E. Jensen. “Evaluation of wind farm efficiency and wind turbine wakes at the Nysted offshore wind farm”. In: *Wind Energy* 13.6 (2010), pp. 573–586.

[35] R. J. Barthelmie, S. C. Pryor, S. T. Frandsen, K. S. Hansen, J. G. Schepers, K. Rados, W. Schlez, A. Neubert, L. E. Jensen, and S. Neckelmann. “Quantifying the Impact of Wind Turbine Wakes on Power Output at Offshore Wind Farms”. In: *Journal of Atmospheric and Oceanic Technology* 27.8 (2010), pp. 1302–1317.

[36] J. C. Y. Lee and M. J. Fields. “An overview of wind-energy-production prediction bias, losses, and uncertainties”. In: *Wind Energy Science* 6.2 (2021), pp. 311–365.

[37] J. Bleeg, M. Purcell, R. Ruisi, and E. Traiger. “Wind Farm Blockage and the Consequences of Neglecting Its Impact on Energy Production”. In: *Energies* 11.6 (2018), p. 1609.

[38] D. Allaerts and J. Meyers. “Boundary-layer development and gravity waves in conventionally neutral wind farms”. In: *Journal of Fluid Mechanics* 814 (2017), pp. 95–130.

[39] J. Newman, J. Lebron, C. Meneveau, and L. Castillo. “Streamwise development of the wind turbine boundary layer over a model wind turbine array”. In: *Physics of Fluids* 25.8 (2013), p. 085108.

[40] D. Allaerts and J. Meyers. “Gravity Waves and Wind-Farm Efficiency in Neutral and Stable Conditions”. In: *Boundary-Layer Meteorology* 166.2 (2018), pp. 269–299.

[41] T. Nishino and T. D. Dunstan. “Two-scale momentum theory for time-dependent modelling of large wind farms”. In: *Journal of Fluid Mechanics* 894 (2020), A2.

[42] P. Baas, R. Verzijlbergh, P. Van Dorp, and H. Jonker. “Investigating energy production and wake losses of multi-gigawatt offshore wind farms with atmospheric large-eddy simulation”. In: *Wind Energy Science* 8.5 (2023), pp. 787–805.

[43] A. Kirby, T. Nishino, L. Lanzilao, T. D. Dunstan, and J. Meyers. “Turbine- and farm-scale power losses in wind farms: an alternative to wake and farm blockage losses”. In: *Wind Energy Science* 10.2 (2025), pp. 435–450.

[44] J. Herbert-Acero, O. Probst, P.-E. Réthoré, G. Larsen, and K. Castillo-Villar. “A Review of Methodological Approaches for the Design and Optimization of Wind Farms”. In: *Energies* 7.11 (2014), pp. 6930–7016.

[45] J. Meyers, C. Bottasso, K. Dykes, P. Fleming, P. Gebraad, G. Giebel, T. Göçmen, and J. W. van Wingerden. “Wind farm flow control: prospects and challenges”. In: *Wind Energy Science* 7.6 (2022), pp. 2271–2306.

[46] L. Lanzilao and J. Meyers. “Set-point optimization in wind farms to mitigate effects of flow blockage induced by atmospheric gravity waves”. In: *Wind Energy Science* 6.1 (2021), pp. 247–271.

[47] T. Burton, N. Jenkins, D. Sharpe, and E. Bossanyi. *Wind energy handbook*. John Wiley & Sons, 2011.

[48] J. Liew, K. S. Heck, and M. F. Howland. "Unified momentum model for rotor aerodynamics across operating regimes". In: *Nature Communications* 15.1 (2024).

[49] E. Gaertner, J. Rinker, L. Sethuraman, F. Zahle, B. Anderson, G. E. Barter, N. J. Abbas, F. Meng, P. Bortolotti, W. Skrzypinski, et al. *IEA Wind TCP Task 37: Definition of the IEA 15-Megawatt Offshore Reference Wind Turbine*. Tech. rep. National Renewable Energy Lab. (NREL), Golden, CO (United States), 2020.

[50] L. A. Martínez-Tossas, E. Branlard, K. Shaler, G. Vijayakumar, S. Ananthan, P. Sakievich, and J. Jonkman. "Numerical investigation of wind turbine wakes under high thrust coefficient". In: *Wind Energy* 25.4 (2022), pp. 605–617.

[51] D. R. Houck. "Review of wake management techniques for wind turbines". In: *Wind Energy* 25.2 (2022), pp. 195–220.

[52] M. Steinbuch, W. W. de Boer, O. H. Bosgra, S. A. W. M. Peters, and J. Ploeg. "Optimal control of wind power plants". In: *Journal of Wind Engineering and Industrial Aerodynamics* 27.1 (1988), pp. 237–246.

[53] P. Parkin, R. Holm, and D. Medici. "The application of PIV to the wake of a wind turbine in yaw". In: 2001, pp. 155–162.

[54] Á. Jiménez, A. Crespo, and E. Migoya. "Application of a LES technique to characterize the wake deflection of a wind turbine in yaw". In: *Wind Energy* 13.6 (2009), pp. 559–572.

[55] M. Bastankhah and F. Porté-Agel. "Experimental and theoretical study of wind turbine wakes in yawed conditions". In: *Journal of Fluid Mechanics* 806 (2016), pp. 506–541.

[56] M. F. Howland, J. B. Quesada, J. J. P. Martínez, F. P. Larrañaga, N. Yadav, J. S. Chawla, V. Sivaram, and J. O. Dabiri. "Collective wind farm operation based on a predictive model increases utility-scale energy production". In: *Nature Energy* 7.9 (2022), pp. 818–827.

[57] S. Ivanell, R. Mikkelsen, J. N. Sørensen, and D. Henningson. "Stability analysis of the tip vortices of a wind turbine". In: *Wind Energy* 13.8 (2010), pp. 705–715.

[58] J. N. Sørensen. "Instability of helical tip vortices in rotor wakes". In: *Journal of Fluid Mechanics* 682 (2011), pp. 1–4.

[59] S. Sarmast, R. Dadfar, R. F. Mikkelsen, P. Schlatter, S. Ivanell, J. N. Sørensen, and D. S. Henningson. "Mutual inductance instability of the tip vortices behind a wind turbine". In: *Journal of Fluid Mechanics* 755 (2014), pp. 705–731.

[60] K. Brown, D. Houck, D. Maniaci, C. Westergaard, and C. Kelley. "Accelerated Wind-Turbine Wake Recovery Through Actuation of the Tip-Vortex Instability". In: *AIAA Journal* 60.5 (2022), pp. 3298–3310.

[61] L. E. M. Lignarolo, D. Ragni, F. Scarano, C. J. Simão Ferreira, and G. J. W. van Bussel. "Tip-vortex instability and turbulent mixing in wind-turbine wakes". In: *Journal of Fluid Mechanics* 781 (2015), pp. 467–493.

[62] X. Mao and J. N. Sørensen. "Far-wake meandering induced by atmospheric eddies in flow past a wind turbine". In: *Journal of Fluid Mechanics* 846 (2018), pp. 190–209.

[63] D. Foti, X. Yang, and F. Sotiropoulos. "Similarity of wake meandering for different wind turbine designs for different scales". In: *Journal of Fluid Mechanics* 842 (2018), pp. 5–25.

[64] M. Heisel, J. Hong, and M. Guala. "The spectral signature of wind turbine wake meandering: A wind tunnel and field-scale study". In: *Wind Energy* 21.9 (2018), pp. 715–731.

[65] K. Kimura, Y. Tanabe, Y. Matsuo, and M. Iida. "Forced wake meandering for rapid recovery of velocity deficits in a wind turbine wake". In: *AIAA Scitech 2019 Forum*. San Diego, California: American Institute of Aeronautics and Astronautics, 2019.

[66] W. Munters and J. Meyers. "Dynamic Strategies for Yaw and Induction Control of Wind Farms Based on Large-Eddy Simulation and Optimization". In: *Energies* 11.1 (2018), p. 177.

[67] V. L. Okulov, I. V. Naumov, R. F. Mikkelsen, I. K. Kabardin, and J. N. Sørensen. "A regular Strouhal number for large-scale instability in the far wake of a rotor". In: *Journal of Fluid Mechanics* 747 (2014), pp. 369–380.

[68] G. V. Iungo, F. Viola, S. Camarri, F. Porté-Agel, and F. Gallaire. "Linear stability analysis of wind turbine wakes performed on wind tunnel measurements". In: *Journal of Fluid Mechanics* 737 (2013), pp. 499–526.

[69] L. C. Cheung, K. A. Brown, D. R. Houck, and N. B. deVelder. "Fluid-Dynamic Mechanisms Underlying Wind Turbine Wake Control with Strouhal-Timed Actuation". In: *Energies* 17.4 (2024), p. 865.

[70] J. P. Goit and J. Meyers. "Optimal control of energy extraction in wind-farm boundary layers". In: *Journal of Fluid Mechanics* 768 (2015), pp. 5–50.

[71] A. E. Yılmaz and J. Meyers. "Optimal dynamic induction control of a pair of inline wind turbines". In: *Physics of Fluids* 30.8 (2018), p. 085106.

[72] W. Munters and J. Meyers. "Towards practical dynamic induction control of wind farms: analysis of optimally controlled wind-farm boundary layers and sinusoidal induction control of first-row turbines". In: *Wind Energy Science* 3.1 (2018), pp. 409–425.

[73] J. A. Frederik, B. M. Doekemeijer, S. P. Mulders, and J. W. van Wingerden. "The helix approach: Using dynamic individual pitch control to enhance wake mixing in wind farms". In: *Wind Energy* 23.8 (2020), pp. 1739–1751.

[74] H. Korb, H. Asmuth, and S. Ivanell. "The characteristics of helically deflected wind turbine wakes". In: *Journal of Fluid Mechanics* 965 (2023), A2.

[75] M. Coquelet, J. Gutknecht, J. W. van Wingerden, M. Duponcheel, and P. Chatelain. "Dynamic individual pitch control for wake mitigation: Why does the helix handedness in the wake matter?" In: *Journal of Physics: Conference Series* 2767.9 (2024), p. 092084.

[76] G. Bir. "Multi-Blade Coordinate Transformation and its Application to Wind Turbine Analysis". In: *46th AIAA Aerospace Sciences Meeting and Exhibit*. Reno, Nevada: American Institute of Aeronautics and Astronautics, 2008.

[77] J. Gutknecht, E. Taschner, M. Coquelet, A. Viré, and J. W. van Wingerden. "The impact of coherent large-scale vortices generated by helix active wake control on the recovery process of wind turbine wakes". In: *Physics of Fluids* 37.6 (2025).

[78] D. van der Hoek, B. V. den Abbeele, C. Simao Ferreira, and J. W. van Wingerden. "Maximizing wind farm power output with the helix approach: Experimental validation and wake analysis using tomographic particle image velocimetry". In: *Wind Energy* 27.5 (2024), pp. 463–482.

[79] F. V. Mühle, F. M. Heckmeier, F. Campagnolo, and C. Breitsamter. "Wind tunnel investigations of an individual pitch control strategy for wind farm power optimization". In: *Wind Energy Science* 9.5 (2024), pp. 1251–1271.

[80] H. Korb, H. Asmuth, M. Stender, and S. Ivanell. "Exploring the application of reinforcement learning to wind farm control". In: *Journal of Physics: Conference Series* 1934.1 (2021), p. 012022.

[81] L. J. Huang, S. P. Mulders, E. Taschner, and J. W. van Wingerden. "Enhancing Wake Mixing in Wind Farms by Multi-Sine Signals in the Helix Approach". In: *2023 American Control Conference (ACC)*. 2023, pp. 824–830.

[82] D. Van Der Hoek, C. S. Ferreira, and J. W. van Wingerden. "Experimental comparison of induction control methods for wind farm power maximization on a scaled two-turbine setup". In: *Journal of Physics: Conference Series* 2767.9 (2024), p. 092064.

[83] J. A. Frederik and J. W. van Wingerden. "On the load impact of dynamic wind farm wake mixing strategies". In: *Renewable Energy* 194 (2022), pp. 582–595.

[84] A. A. Van Vondelen, S. T. Navalkar, D. R. Kerssemakers, and J. W. van Wingerden. "Enhanced wake mixing in wind farms using the Helix approach: A loads sensitivity study". In: *2023 American Control Conference (ACC)*. 2023, pp. 831–836.

[85] J. A. Frederik, E. Simley, K. A. Brown, G. R. Yalla, L. C. Cheung, and P. A. Fleming. "Comparison of wind farm control strategies under realistic offshore wind conditions: turbine quantities of interest". In: *Wind Energy Science* 10.4 (2025), pp. 755–777.

[86] K. Brown, G. Yalla, L. Cheung, J. Frederik, D. Houck, N. deVelder, E. Simley, and P. Fleming. "Comparison of wind-farm control strategies under realistic offshore wind conditions: wake quantities of interest". In: *Wind Energy Science Discussions* (2025), pp. 1–39.

[87] J. Gutknecht, M. Becker, C. Muscari, T. Lutz, and J. W. van Wingerden. "Scaling DMD modes for modeling Dynamic Induction Control wakes in various wind speeds". In: *2023 IEEE Conference on Control Technology and Applications (CCTA)*. 2023, pp. 574–580.

[88] G. R. Yalla, K. Brown, L. Cheung, D. Houck, N. deVelder, and N. Hamilton. "Spectral proper orthogonal decomposition of active wake mixing dynamics in a stable atmospheric boundary layer". In: *Wind Energy Science Discussions* (2025), pp. 1–36.

[89] L. Cheung, G. Yalla, P. Mohan, A. Hsieh, K. Brown, N. deVelder, D. Houck, and M. Henry de Frahan. "Modeling the effects of active wake mixing on wake behavior through large scale coherent structures". In: *Wind Energy Science Discussions* (2024), pp. 1–26.

[90] A. A. W. van Vondelen, M. Coquelet, S. T. Navalkar, and J. W. van Wingerden. "Synchronized Helix Wake Mixing Control". In: *Wind Energy Science Discussions* (2025), pp. 1–36.

[91] D. V. D. Berg, D. D. Tavernier, and J. W. van Wingerden. "Using The Helix Mixing Approach On Floating Offshore Wind Turbines". In: *Journal of Physics: Conference Series* 2265.4 (2022), p. 042011.

[92] D. van den Berg, D. de Tavernier, D. Marten, J. Saverin, and J. W. van Wingerden. "Wake Mixing Control For Floating Wind Farms: Analysis of the Implementation of the Helix Wake Mixing Strategy on the IEA 15-MW Floating Wind Turbine". In: *IEEE Control Systems* 44.5 (2024), pp. 81–105.

[93] S. Boersma, B. Doekemeijer, P. Gebraad, P. Fleming, J. Annoni, A. Scholbrock, J. Frederik, and J. W. van Wingerden. "A tutorial on control-oriented modeling and control of wind farms". In: *2017 American Control Conference (ACC)*. 2017, pp. 1–18.

[94] P. Gebraad, J. J. Thomas, A. Ning, P. Fleming, and K. Dykes. "Maximization of the annual energy production of wind power plants by optimization of layout and yaw-based wake control: Maximization of wind plant AEP by optimization of layout and wake control". In: *Wind Energy* 20.1 (2017), pp. 97–107.

[95] M. Becker, D. Allaerts, and J. W. van Wingerden. "FLORIDyn - A dynamic and flexible framework for real-time wind farm control". In: *Journal of Physics: Conference Series* 2265.3 (2022), p. 032103.

[96] M. Becker, M. J. v. d. Broek, D. Allaerts, and J. W. van Wingerden. "Closed-loop model-predictive wind farm flow control under time-varying inflow using FLORIDyn". In: *arXiv* (2025).

[97] J. R. Beattie, C. Federrath, R. S. Klessen, S. Cielo, and A. Bhattacharjee. "The spectrum of magnetized turbulence in the interstellar medium". In: *Nature Astronomy* (2025), pp. 1–11.

[98] R. B. Stull. *An introduction to boundary layer meteorology*. Atmospheric sciences library. Dordrecht: Kluwer Academic Publishers Dordrecht, 1988.

[99] P. Sagaut. *Large eddy simulation for incompressible flows: an introduction*. 3rd ed. Scientific computation. Berlin ; New York: Springer, 2006.

[100] M. Calaf, C. Meneveau, and J. Meyers. "Large eddy simulation study of fully developed wind-turbine array boundary layers". In: *Physics of Fluids* 22.1 (2010), p. 015110.

[101] M. Calaf, M. B. Parlange, and C. Meneveau. "Large eddy simulation study of scalar transport in fully developed wind-turbine array boundary layers". In: *Physics of Fluids* 23.12 (2011), p. 126603.

[102] M. Abkar and F. Porté-Agel. "Influence of the Coriolis force on the structure and evolution of wind turbine wakes". In: *Physical Review Fluids* 1.6 (2016), p. 063701.

[103] O. Maas and S. Raasch. "Wake properties and power output of very large wind farms for different meteorological conditions and turbine spacings: a large-eddy simulation case study for the German Bight". In: *Wind Energy Science* 7.2 (2022), pp. 715–739.

[104] J. Gutknecht, M. Becker, E. Taschner, S. Stipa, D. Allaerts, A. Viré, and J. W. van Wingerden. "Active Cluster Wake Mixing". In: *Journal of Physics: Conference Series* 2767.9 (2024), p. 092052.

[105] P. A. Fleming, P. M. Gebraad, S. Lee, J. W. van Wingerden, K. Johnson, M. Churchfield, J. Michalakes, P. Spalart, and P. Moriarty. "Evaluating techniques for redirecting turbine wakes using SOWFA". In: *Renewable Energy* 70 (2014), pp. 211–218.

[106] M. F. Howland, A. S. Ghate, S. K. Lele, and J. O. Dabiri. "Optimal closed-loop wake steering – Part 1: Conventionally neutral atmospheric boundary layer conditions". In: *Wind Energy Science* 5.4 (2020), pp. 1315–1338.

[107] M. F. Howland, A. S. Ghate, J. B. Quesada, J. J. Pena Martínez, W. Zhong, F. P. Larrañaga, S. K. Lele, and J. O. Dabiri. "Optimal closed-loop wake steering – Part 2: Diurnal cycle atmospheric boundary layer conditions". In: *Wind Energy Science* 7.1 (2022), pp. 345–365.

[108] M. J. Churchfield, S. Lee, J. Michalakes, and P. J. Moriarty. "A numerical study of the effects of atmospheric and wake turbulence on wind turbine dynamics". In: *Journal of Turbulence* 13 (2012), N14.

[109] S. Stipa, A. Ajay, D. Allaerts, and J. Brinkerhoff. "TOSCA – an open-source, finite-volume, large-eddy simulation (LES) environment for wind farm flows". In: *Wind Energy Science* 9.2 (2024), pp. 297–320.

[110] N. N. Sørensen. "General purpose flow solver applied to flow over hills". Ph.D. Thesis. DTU, 1995.

[111] J. A. Michelsen. *Basis3D-a Platform for Development of Multiblock PDE Solvers: β-release.* Tech. rep. AFM 92-05. DTU, 1992.

[112] M. B. Kuhn et al. "AMR-Wind: A Performance-Portable, High-Fidelity Flow Solver for Wind Farm Simulations". In: *Wind Energy* 28.5 (2025), e70010.

[113] A. Sharma et al. "ExaWind: Open-source CFD for hybrid-RANS/LES geometry-resolved wind turbine simulations in atmospheric flows". In: *Wind Energy* 27.3 (2024), pp. 225–257.

[114] Y.-T. Wu and F. Porté-Agel. "Large-Eddy Simulation of Wind-Turbine Wakes: Evaluation of Turbine Parametrisations". In: *Boundary-Layer Meteorology* 138.3 (2011), pp. 345–366.

[115] H. Korb, H. Asmuth, and S. Ivanell. "Validation of a Lattice Boltzmann Solver Against Wind Turbine Response and Wake Measurements". In: *Journal of Physics: Conference Series* 2505.1 (2023), p. 012008.

[116] V. Kumar, J. Kleissl, C. Meneveau, and M. B. Parlange. "Large-eddy simulation of a diurnal cycle of the atmospheric boundary layer: Atmospheric stability and scaling issues". In: *Water Resources Research* 42.6 (2006).

[117] D. Muñoz-Esparza, J. K. Lundquist, J. A. Sauer, B. Kosović, and R. R. Linn. "Coupled mesoscale-LES modeling of a diurnal cycle during the CWEX-13 field campaign: From weather to boundary-layer eddies". In: *Journal of Advances in Modeling Earth Systems* 9.3 (2017), pp. 1572–1594.

[118] C. Talbot, E. Bou-Zeid, and J. Smith. "Nested Mesoscale Large-Eddy Simulations with WRF: Performance in Real Test Cases". In: *Journal of Hydrometeorology* 13.5 (2012), pp. 1421–1441.

[119] B. Maronga et al. "Overview of the PALM model system 6.0". In: *Geoscientific Model Development* 13.3 (2020), pp. 1335–1372.

[120] J. A. Sauer and D. Muñoz-Esparza. "The FastEddy® Resident-GPU Accelerated Large-Eddy Simulation Framework: Model Formulation, Dynamical-Core Validation and Performance Benchmarks". In: *Journal of Advances in Modeling Earth Systems* 12.11 (2020).

[121] T. Heus et al. "Formulation of the Dutch Atmospheric Large-Eddy Simulation (DALES) and overview of its applications". In: *Geoscientific Model Development* 3.2 (2010), pp. 415–444.

[122] J. Schalkwijk, E. J. Griffith, F. H. Post, and H. J. J. Jonker. "High-Performance Simulations of Turbulent Clouds on a Desktop PC: Exploiting the GPU". In: *Bulletin of the American Meteorological Society* 93.3 (2012), pp. 307–314.

[123] J. Schalkwijk, H. J. J. Jonker, A. P. Siebesma, and E. Van Meijgaard. "Weather Forecasting Using GPU-Based Large-Eddy Simulations". In: *Bulletin of the American Meteorological Society* 96.5 (2015), pp. 715–723.

[124] F. Vorpahl, H. Schwarze, T. Fischer, M. Seidel, and J. Jonkman. "Offshore wind turbine environment, loads, simulation, and design". In: *WIREs Energy and Environment* 2.5 (2013), pp. 548–570.

[125] J. Jonkman. "The New Modularization Framework for the FAST Wind Turbine CAE Tool". In: *51st AIAA Aerospace Sciences Meeting including the New Horizons Forum and Aerospace Exposition*. Grapevine (Dallas/Ft. Worth Region), Texas: American Institute of Aeronautics and Astronautics, 2013.

[126] T. J. Larsen and A. M. Hansen. *How 2 HAWC2 the User'sManual*. Technical Report Risø-R-1597(ver. 12.7)(EN). Denmark: Risø National Laboratory for Sustainable Energy, 2019.

[127] N. J. Abbas, D. S. Zalkind, L. Pao, and A. Wright. "A reference open-source controller for fixed and floating offshore wind turbines". In: *Wind Energy Science* 7.1 (2022), pp. 53–73.

[128] B. J. Jonkman. *TurbSim User's Guide v2.00.00*. Tech. rep. National Renewable Energy Laboratory, 2014.

[129] K. Thomsen and P. Sørensen. "Fatigue loads for wind turbines operating in wakes". In: *Journal of Wind Engineering and Industrial Aerodynamics* 80.1-2 (1999), pp. 121–136.

[130] A. N. Robertson, K. Shaler, L. Sethuraman, and J. Jonkman. "Sensitivity analysis of the effect of wind characteristics and turbine properties on wind turbine loads". In: *Wind Energy Science* 4.3 (2019), pp. 479–513.

[131] S.-P. Breton, J. Sumner, J. N. Sørensen, K. S. Hansen, S. Sarmast, and S. Ivanell. "A survey of modelling methods for high-fidelity wind farm simulations using large eddy simulation". In: *Philosophical Transactions of the Royal Society A: Mathematical, Physical and Engineering Sciences* 375.2091 (2017), p. 20160097.

[132] M. P. Van Der Laan, O. García-Santiago, M. Kelly, A. Meyer Forsting, C. Dubreuil-Boisclair, K. Sponheim Seim, M. Imberger, A. Peña, N. N. Sørensen, and P.-E. Réthoré. "A new RANS-based wind farm parameterization and inflow model for wind farm cluster modeling". In: *Wind Energy Science* 8.5 (2023), pp. 819–848.

[133] S. Stipa, A. Ajay, and J. Brinkerhoff. "The actuator farm model for large eddy simulation (LES) of wind-farm-induced atmospheric gravity waves and farm–farm interaction". In: *Wind Energy Science* 9.12 (2024), pp. 2301–2332.

[134] R. E. Froude. "On the part played in propulsion by differences of fluid pressure". In: *Trans. Inst. Naval Architects* 30 (1889), p. 390.

[135] J. N. Sørensen and A. Myken. "Unsteady actuator disc model for horizontal axis wind turbines". In: *Journal of Wind Engineering and Industrial Aerodynamics* 39.1-3 (1992), pp. 139–149.

[136] A. Jimenez, A. Crespo, E. Migoya, and J. Garcia. "Large-eddy simulation of spectral coherence in a wind turbine wake". In: *Environmental Research Letters* 3.1 (2008), p. 015004.

[137] J. N. Sørensen and W. Z. Shen. "Numerical Modeling of Wind Turbine Wakes". In: *Journal of Fluids Engineering* 124.2 (2002), pp. 393–399.

[138] R. C. Storey, S. E. Norris, and J. E. Cater. "An actuator sector method for efficient transient wind turbine simulation". In: *Wind Energy* 18.4 (2015), pp. 699–711.

[139] W. Z. Shen, J. H. Zhang, and J. N. Sørensen. "The Actuator Surface Model: A New Navier–Stokes Based Model for Rotor Computations". In: *Journal of Solar Energy Engineering* 131.1 (2009), p. 011002.

[140] C. Sibuet Watters, S. Breton, and C. Masson. "Application of the actuator surface concept to wind turbine rotor aerodynamics". In: *Wind Energy* 13.5 (2010), pp. 433–447.

[141] B. Sanderse, S. Pijl, and B. Koren. "Review of computational fluid dynamics for wind turbine wake aerodynamics: Review of CFD for wind turbine wake aerodynamics". In: *Wind Energy* 14.7 (2011), pp. 799–819.

[142] N. Sorensen and M. Hansen. "Rotor performance predictions using a Navier-Stokes method". In: *1998 ASME Wind Energy Symposium*. Reno,NV,U.S.A.: American Institute of Aeronautics and Astronautics, 1998.

[143] M. Moens, M. Coquelet, F. Trigaux, and P. Chatelain. "Handling Individual Pitch Control within an Actuator Disk framework: verification against the Actuator Line method and application to wake interaction problems". In: *Journal of Physics: Conference Series* 2265.2 (2022), p. 022053.

[144] M. Coquelet, M. Moens, M. Duponcheel, J. W. van Wingerden, L. Bricteux, and P. Chatelain. “Simulating the helix wake within an actuator disk framework: verification against discrete-blade type simulations”. In: *Journal of Physics: Conference Series* 2505.1 (2023), p. 012017.

[145] B. De Vos, B. M. Harder, T. A. Huisman, J. Gutknecht, and J. W. van Wingerden. “Mimicking the Helix with a porous disc for wind tunnel testing”. In: *Journal of Physics: Conference Series* 2767.9 (2024), p. 092063.

[146] L. A. Martínez-Tossas, M. J. Churchfield, and C. Meneveau. “Optimal smoothing length scale for actuator line models of wind turbine blades based on Gaussian body force distribution”. In: *Wind Energy* 20.6 (2017), pp. 1083–1096.

[147] L. A. Martínez-Tossas, M. J. Churchfield, and S. Leonardi. “Large eddy simulations of the flow past wind turbines: actuator line and disk modeling”. In: *Wind Energy* 18.6 (2015), pp. 1047–1060.

[148] W. Z. Shen, R. Mikkelsen, J. N. Sørensen, and C. Bak. “Tip loss corrections for wind turbine computations”. In: *Wind Energy* 8.4 (2005), pp. 457–475.

[149] L. A. Martínez-Tossas and C. Meneveau. “Filtered lifting line theory and application to the actuator line model”. In: *Journal of Fluid Mechanics* 863 (2019), pp. 269–292.

[150] A. R. Meyer Forsting, G. R. Pirrung, and N. Ramos-García. “A vortex-based tip/smearing correction for the actuator line”. In: *Wind Energy Science* 4.2 (2019), pp. 369–383.

[151] K. O. Dağ and J. N. Sørensen. “A new tip correction for actuator line computations”. In: *Wind Energy* 23.2 (2020), pp. 148–160.

[152] V. G. Kleine, A. Hanifi, and D. S. Henningson. “Non-iterative vortex-based smearing correction for the actuator line method”. In: *Journal of Fluid Mechanics* 961 (2023), A29.

[153] F. Trigaux, T. Villeneuve, G. Dumas, and G. Winckelmans. “Near-tip correction functions for the actuator line method to improve the predicted lift and drag distributions”. In: *Journal of Fluid Mechanics* 989 (2024), A1.

[154] H. Korb and E. Taschner. “Coarse, fast, and still accurate? Comparing corrections for the actuator line model”. In: *Journal of Physics: Conference Series* 3016.1 (2025), p. 012051.

[155] J. G. Leishman. *Principles of helicopter aerodynamics*. 1st pbk. ed. Cambridge aerospace series; Cambridge aerospace series; 12. Cambridge: Cambridge University Press, 2002.

[156] E. Taschner, A. van Vondelen, R. Verzijlbergh, and J. W. van Wingerden. “On the performance of the helix wind farm control approach in the conventionally neutral atmospheric boundary layer”. In: *Journal of Physics: Conference Series* 2505.1 (2023), p. 012006.

[157] E. Taschner, M. Becker, R. Verzijlbergh, and J. W. van Wingerden. “Comparison of helix and wake steering control for varying turbine spacing and wind direction”. In: *Journal of Physics: Conference Series* 2767.3 (2024), p. 032023.

[158] E. Taschner, M. Folkersma, L. A. Martínez-Tossas, R. Verzijlbergh, and J. W. van Wingerden. "A new coupling of a GPU-resident large-eddy simulation code with a multiphysics wind turbine simulation tool". In: *Wind Energy* 27.11 (2024), pp. 1152–1172.

[159] E. Taschner, G. Deskos, M. B. Kuhn, J. W. van Wingerden, and L. A. Martínez-Tossas. "Unsteady aerodynamic loads on pitching airfoils represented by Gaussian body force distributions". In: *Accepted for publication in Journal of Fluid Mechanics* (2025).

[160] A. Croce, S. Cacciola, M. Montero Montenegro, S. Stipa, and R. Praticó. "A CFD-based analysis of dynamic induction techniques for wind farm control applications". In: *Wind Energy* 26.3 (2023), pp. 325–343.

[161] D. van der Hoek, J. Frederik, M. Huang, F. Scarano, C. Simao Ferreira, and J. W. van Wingerden. "Experimental analysis of the effect of dynamic induction control on a wind turbine wake". In: *Wind Energy Science* 7.3 (2022), pp. 1305–1320.

[162] C. Muscari, P. Schito, A. Viré, A. Zasso, D. van der Hoek, and J. W. van Wingerden. "Physics informed DMD for periodic Dynamic Induction Control of Wind Farms". In: *Journal of Physics: Conference Series* 2265.2 (2022), p. 022057.

[163] S. S. Zilitinkevich and I. N. Esau. "On Integral Measures Of The Neutral Barotropic Planetary Boundary Layer". In: *Boundary-Layer Meteorology* 104.3 (2002), pp. 371–379.

[164] C.-H. Moeng. "A Large-Eddy-Simulation Model for the Study of Planetary Boundary-Layer Turbulence". In: *Journal of the Atmospheric Sciences* 41.13 (1984), pp. 2052–2062.

[165] L. Cheung, M. J. Brazell, A. Hsieh, S. Ananthan, G. Vijayakumar, and N. deVelder. "Computation and comparison of the stable Northeastern US marine boundary layer". In: *AIAA Scitech 2021 Forum*. Virtual Event: American Institute of Aeronautics and Astronautics, 2021.

[166] T. Chatterjee, J. Li, S. Yellapantula, B. Jayaraman, and E. Quon. "Wind farm response to mesoscale-driven coastal low level jets: a multiscale large eddy simulation study". In: *Journal of Physics: Conference Series* 2265.2 (2022), p. 022004.

[167] A. A. W. van Vondelen, S. T. Navalkar, A. Iliopoulos, D. C. van der Hoek, and J. W. van Wingerden. "Damping identification of offshore wind turbines using operational modal analysis: a review". In: *Wind Energy Science* 7.1 (2022), pp. 161–184.

[168] G. Hayman. *MLife theory manual for version 1.00*. Tech. rep. Golden, CO: National Renewable Energy Laboratory, 2012, p. 106.

[169] *61400-3-1: 2019 Part 3-1: Design Requirements for Fixed Offshore Wind Turbines*. Geneva, Switzerland, 2019.

[170] M. Stammler, A. Reuter, and G. Poll. "Cycle counting of roller bearing oscillations – case study of wind turbine individual pitching system". In: *Renewable Energy Focus* 25 (2018), pp. 40–47.

[171] P. K. Taylor and M. J. Yelland. "The Dependence of Sea Surface Roughness on the Height and Steepness of the Waves". In: *Journal of Physical Oceanography* 31.2 (2001), pp. 572–590.

[172] G. T. Csanady. "Equilibrium theory of the planetary boundary layer with an inversion lid". In: *Boundary-Layer Meteorology* 6.1-2 (1974), pp. 63–79.

[173] R. A. Brost, D. H. Lenschow, and J. C. Wyngaard. "Marine Stratocumulus Layers. Part 1: Mean Conditions". In: *Journal of Atmospheric Sciences* 39.4 (1982), pp. 800–817.

[174] G. Rampanelli and D. Zardi. "A Method to Determine the Capping Inversion of the Convective Boundary Layer". In: *Journal of Applied Meteorology* 43.6 (2004), pp. 925–933.

[175] H. Wurps, G. Steinfeld, and S. Heinz. "Grid-Resolution Requirements for Large-Eddy Simulations of the Atmospheric Boundary Layer". In: *Boundary-Layer Meteorology* 175.2 (2020), pp. 179–201.

[176] A. S. Hsieh, K. A. Brown, N. B. deVelder, T. G. Herges, R. C. Knaus, P. J. Sakievich, L. C. Cheung, B. C. Houchens, M. L. Blaylock, and D. C. Maniaci. "High-fidelity wind farm simulation methodology with experimental validation". In: *Journal of Wind Engineering and Industrial Aerodynamics* 218 (2021), p. 104754.

[177] S. Zilitinkevich, I. Esau, and A. Baklanov. "Further comments on the equilibrium height of neutral and stable planetary boundary layers". In: *Quarterly Journal of the Royal Meteorological Society* 133.622 (2007), pp. 265–271.

[178] J. Park and K. H. Law. "Cooperative wind turbine control for maximizing wind farm power using sequential convex programming". In: *Energy Conversion and Management* 101 (2015), pp. 295–316.

[179] W. Munters and J. Meyers. "Optimal dynamic induction and yaw control of wind farms: effects of turbine spacing and layout". In: *Journal of Physics: Conference Series* 1037 (2018), p. 032015.

[180] A. P. J. Stanley, C. J. Bay, and P. Fleming. "Enabling control co-design of the next generation of wind power plants". In: *Wind Energy Science* 8.8 (2023), pp. 1341–1350.

[181] H. Olivares-Espinosa and J. Arnqvist. "Modelling of wind turbine wakes over forests along the diurnal cycle". In: *Journal of Physics: Conference Series* 2505.1 (2023), p. 012043.

[182] F. Scheurich, P. B. Enevoldsen, H. N. Paulsen, K. K. Dickow, M. Fiedel, A. Loeven, and I. Antoniou. "Improving the Accuracy of Wind Turbine Power Curve Validation by the Rotor Equivalent Wind Speed Concept". In: *Journal of Physics: Conference Series* 753.7 (2016), p. 072029.

[183] A. C. Hansen and C. P. Butterfield. "Aerodynamics of Horizontal-Axis Wind Turbines". In: *Annual Review of Fluid Mechanics* 25.1 (1993), pp. 115–149.

[184] J. N. Sørensen. "Aerodynamic Aspects of Wind Energy Conversion". In: *Annual Review of Fluid Mechanics* 43.1 (2011), pp. 427–448.

[185] F. Porté-Agel, M. Bastankhah, and S. Shamsoddin. “Wind-Turbine and Wind-Farm Flows: A Review”. In: *Boundary-Layer Meteorology* 174.1 (2020), pp. 1–59.

[186] E. A. Bossanyi. “Wind Turbine Control for Load Reduction”. In: *Wind Energy* 6.3 (2003), pp. 229–244.

[187] L. E. Andersson, O. Anaya-Lara, J. O. Tande, K. O. Merz, and L. Imsland. “Wind farm control - Part I: A review on control system concepts and structures”. In: *IET Renewable Power Generation* 15.10 (2021), pp. 2085–2108.

[188] H. Lu and F. Porté-Agel. “Large-eddy simulation of a very large wind farm in a stable atmospheric boundary layer”. In: *Physics of Fluids* 23.6 (2011), p. 065101.

[189] D. Mehta, A. van Zuijlen, B. Koren, J. Holierhoek, and H. Bijl. “Large Eddy Simulation of wind farm aerodynamics: A review”. In: *Journal of Wind Engineering and Industrial Aerodynamics* 133 (2014), pp. 1–17.

[190] N. Troldborg, J. N. Sorensen, and R. Mikkelsen. “Numerical simulations of wake characteristics of a wind turbine in uniform inflow”. In: *Wind Energy* 13.1 (2010), pp. 86–99.

[191] M. J. Churchfield, S. J. Schreck, L. A. Martinez, C. Meneveau, and P. R. Spalart. “An Advanced Actuator Line Method for Wind Energy Applications and Beyond”. In: *35th Wind Energy Symposium*. Grapevine, Texas: American Institute of Aeronautics and Astronautics, 2017.

[192] R. Stanly, L. A. Martínez-Tossas, S. H. Frankel, and Y. Delorme. “Large-Eddy Simulation of a wind turbine using a Filtered Actuator Line Model”. In: *Journal of Wind Engineering and Industrial Aerodynamics* 222 (2022), p. 104868.

[193] M. L. Blaylock, L. Martinez-Tossas, P. Sakievich, B. C. Houchens, L. Cheung, K. Brown, A. Hsieh, D. C. Maniaci, and M. J. Churchfield. “Validation of Actuator Line and Actuator Disk Models with Filtered Lifting Line Corrections Implemented in Nalu-Wind Large Eddy Simulations of the Atmospheric Boundary Layer”. In: *AIAA SCITECH 2022 Forum*. San Diego, CA & Virtual: American Institute of Aeronautics and Astronautics, 2022.

[194] R. C. Storey, S. E. Norris, K. A. Stol, and J. E. Cater. “Large eddy simulation of dynamically controlled wind turbines in an offshore environment”. In: *Wind Energy* 16.6 (2013), pp. 845–864.

[195] J. C. Heinz, N. N. Sørensen, and F. Zahle. “Fluid-structure interaction computations for geometrically resolved rotor simulations using CFD: Fluid-structure interaction computations for geometrically resolved rotor simulations using CFD”. In: *Wind Energy* 19.12 (2016), pp. 2205–2221.

[196] S. Krüger, G. Steinfeld, M. Kraft, and L. J. Lukassen. “Validation of a coupled atmospheric–aeroelastic model system for wind turbine power and load calculations”. In: *Wind Energy Science* 7.1 (2022), pp. 323–344.

[197] M. A. Sprague, S. Boldyrev, P. Fischer, R. Grout, W. I. Gustafson Jr., and R. Moser. *Turbulent Flow Simulation at the Exascale: Opportunities and Challenges Workshop: August 4-5, 2015, Washington, D.C.* Tech. rep. NREL/TP–2C00-67648, 1338668. U.S. Department of Energy, Office of Science, Advanced Scientific Computing Research, 2017.

[198] M. A. Sprague, S. Ananthan, G. Vijayakumar, and M. Robinson. "ExaWind: A multifidelity modeling and simulation environment for wind energy". In: *Journal of Physics: Conference Series* 1452.1 (2020), p. 012071.

[199] S. J. Böing, H. J. J. Jonker, A. P. Siebesma, and W. W. Grabowski. "Influence of the Subcloud Layer on the Development of a Deep Convective Ensemble". In: *Journal of the Atmospheric Sciences* 69.9 (2012), pp. 2682–2698.

[200] J. Smagorinsky. "General circulation experiments with the primitive equations: I. The basic experiment". In: *Monthly Weather Review* 91.3 (1963), pp. 99–164.

[201] L. J. Wicker and W. C. Skamarock. "Time-Splitting Methods for Elastic Models Using Forward Time Schemes". In: *Monthly Weather Review* 130.8 (2002), pp. 2088–2097.

[202] C. Gilbert, J. W. Messner, P. Pinson, P.-J. Trombe, R. Verzijlbergh, P. Dorp, and H. Jonker. "Statistical post-processing of turbulence-resolving weather forecasts for offshore wind power forecasting". In: *Wind Energy* 23.4 (2020), pp. 884–897.

[203] G. Schepers, P. van Dorp, R. Verzijlbergh, P. Baas, and H. Jonker. "Aeroelastic loads on a 10 MW turbine exposed to extreme events selected from a year-long large-eddy simulation over the North Sea". In: *Wind Energy Science* 6.4 (2021), pp. 983–996.

[204] J. Schalkwijk, H. J. J. Jonker, A. P. Siebesma, and F. C. Bosveld. "A Year-Long Large-Eddy Simulation of the Weather over Cabauw: An Overview". In: *Monthly Weather Review* 143.3 (2015), pp. 828–844.

[205] L. Vollmer, G. Steinfeld, and M. Kühn. "Transient LES of an offshore wind turbine". In: *Wind Energy Science* 2.2 (2017), pp. 603–614.

[206] C. Santoni, E. J. García-Cartagena, U. Ciri, L. Zhan, G. Valerio Iungo, and S. Leonardi. "One-way mesoscale-microscale coupling for simulating a wind farm in North Texas: Assessment against SCADA and LiDAR data". In: *Wind Energy* 23.3 (2020), pp. 691–710.

[207] J. M. Jonkman, G. J. Hayman, B. J. Jonkman, R. R. Damiani, and R. E. Murray. *AeroDyn v15 User's Guide and Theory Manual.* Tech. rep. Golden, Colorado, USA: NREL, 2017, p. 46.

[208] C. Santoni, K. Carrasquillo, I. Arenas-Navarro, and S. Leonardi. "Effect of tower and nacelle on the flow past a wind turbine: Effect of tower and nacelle on the flow past a wind turbine". In: *Wind Energy* 20.12 (2017), pp. 1927–1939.

[209] Z. Gao, Y. Li, T. Wang, W. Shen, X. Zheng, S. Pröbsting, D. Li, and R. Li. "Modelling the nacelle wake of a horizontal-axis wind turbine under different yaw conditions". In: *Renewable Energy* 172 (2021), pp. 263–275.

[210] L. A. Martínez-Tossas, M. J. Churchfield, A. E. Yilmaz, H. Sarlak, P. L. Johnson, J. N. Sørensen, J. Meyers, and C. Meneveau. "Comparison of four large-eddy simulation research codes and effects of model coefficient and inflow turbulence in actuator-line-based wind turbine modeling". In: *Journal of Renewable and Sustainable Energy* 10.3 (2018), p. 033301.

[211] J. Jonkman, S. Butterfield, W. Musial, and G. Scott. *Definition of a 5-MW Reference Wind Turbine for Offshore System Development*. Tech. rep. NREL/TP-500-38060. Golden, CO: National Renewable Energy Laboratory, 2009, NREL/TP–500–38060, 947422.

[212] P. Moin and R. Verzicco. "On the suitability of second-order accurate discretizations for turbulent flow simulations". In: *European Journal of Mechanics - B/Fluids* 55 (2016), pp. 242–245.

[213] R. J. Stevens, L. A. Martínez-Tossas, and C. Meneveau. "Comparison of wind farm large eddy simulations using actuator disk and actuator line models with wind tunnel experiments". In: *Renewable Energy* 116 (2018), pp. 470–478.

[214] N. Troldborg. "Actuator Line Modeling of Wind Turbine Wakes". PhD Thesis. 2009.

[215] N. Troldborg, G. C. Larsen, H. A. Madsen, K. S. Hansen, J. N. Sørensen, and R. Mikkelsen. "Numerical simulations of wake interaction between two wind turbines at various inflow conditions". In: *Wind Energy* 14.7 (2011), pp. 859–876.

[216] J. N. Sørensen, R. F. Mikkelsen, D. S. Henningson, S. Ivanell, S. Sarmast, and S. J. Andersen. "Simulation of wind turbine wakes using the actuator line technique". In: *Philosophical Transactions of the Royal Society A: Mathematical, Physical and Engineering Sciences* 373.2035 (2015), p. 20140071.

[217] E. Kleusberg, S. Benard, and D. S. Henningson. "Tip-vortex breakdown of wind turbines subject to shear". In: *Wind Energy* 22.12 (2019), pp. 1789–1799.

[218] A. Hodgkin, S. Laizet, and G. Deskos. "Numerical investigation of the influence of shear and thermal stratification on the wind turbine tip-vortex stability". In: *Wind Energy* 25.7 (2022), pp. 1270–1289.

[219] V. Mendoza, P. Bachant, C. Ferreira, and A. Goude. "Near-wake flow simulation of a vertical axis turbine using an actuator line model". In: *Wind Energy* 22.2 (2019), pp. 171–188.

[220] V. G. Kleine, A. Hanifi, and D. S. Henningson. "Simulating Airplane Aerodynamics with Body Forces: Actuator Line Method for Nonplanar Wings". In: *AIAA Journal* 61.5 (2023), pp. 2048–2059.

[221] P. K. Jha and S. Schmitz. "Actuator curve embedding – an advanced actuator line model". In: *Journal of Fluid Mechanics* 834 (2018), R2.

[222] D.-G. Caprace, P. Chatelain, and G. Winckelmans. "Lifting Line with Various Mollifications: Theory and Application to an Elliptical Wing". In: *AIAA Journal* 57.1 (2019), pp. 17–28.

[223] M. Schollenberger, T. Lutz, and E. Krämer. “Boundary Condition Based Actuator Line Model to Simulate the Aerodynamic Interactions at Wingtip Mounted Propellers”. In: *New Results in Numerical and Experimental Fluid Mechanics XII*. Ed. by A. Dillmann, G. Heller, E. Krämer, C. Wagner, C. Tropea, and S. Jakirlić. Cham: Springer International Publishing, 2020, pp. 608–618.

[224] L. Liu, L. Franceschini, D. F. Oliveira, F. C. Galeazzo, B. S. Carmo, and R. J. A. M. Stevens. “Evaluating the accuracy of the actuator line model against blade element momentum theory in uniform inflow”. In: *Wind Energy* 25.6 (2022), pp. 1046–1059.

[225] M. Shives and C. Crawford. “Mesh and load distribution requirements for actuator line CFD simulations”. In: *Wind Energy* 16.8 (2013), pp. 1183–1196.

[226] W. Z. Shen, J. N. Sørensen, and R. Mikkelsen. “Tip Loss Correction for Actuator/Navier–Stokes Computations”. In: *Journal of Solar Energy Engineering* 127.2 (2005), pp. 209–213.

[227] K. O. Dağ. “Combined pseudo-spectral / actuator line model for wind turbine applications”. PhD Thesis. 2017.

[228] J. R. Forsythe, E. Lynch, S. Polsky, and P. Spalart. “Coupled Flight Simulator and CFD Calculations of Ship Airwake using Kestrel”. In: *53rd AIAA Aerospace Sciences Meeting*. AIAA SciTech Forum. American Institute of Aeronautics and Astronautics, 2015.

[229] A. R. Meyer Forsting, G. R. Pirrung, and N. Ramos-García. “The wake of an actuator line with a vortex-basedtip/smearing correction in uniform and turbulent inflow”. In: *Journal of Physics: Conference Series* 1256.1 (2019), p. 012020.

[230] D.-G. Caprace, G. Winckelmans, and P. Chatelain. “An immersed lifting and dragging line model for the vortex particle-mesh method”. In: *Theoretical and Computational Fluid Dynamics* 34.1 (2020), pp. 21–48.

[231] J. G. Leishman. “Challenges in modelling the unsteady aerodynamics of wind turbines”. In: *Wind Energy* 5.2-3 (2002), pp. 85–132.

[232] J. G. Leishman and T. S. Beddoes. “A Semi-Empirical Model for Dynamic Stall”. In: *Journal of The American Helicopter Society* 34 (1989), pp. 3–17.

[233] T. von Kármán and W. R. Sears. “Airfoil Theory for Non-Uniform Motion”. In: *Journal of the Aeronautical Sciences* 5.10 (1938), pp. 379–390.

[234] R. Bisplinghoff, H. Ashley, and R. Halfman. *Aeroelasticity*. Mineola, New York: Dover Publications, 1996.

[235] L. Prandtl. “Über die Entstehung von Wirbeln in der idealen Flüssigkeit, mit Anwendung auf die Tragflügeltheorie und andere Aufgaben”. In: *Vorträge aus dem Gebiete der Hydro- und Aerodynamik (Innsbruck 1922)*. Ed. by T. v. Kármán and T. Levi-Civita. Berlin, Heidelberg: Springer Berlin Heidelberg, 1924, pp. 18–33.

[236] W. Birnbaum. “Das ebene Problem des schlagenden Flügels”. In: *ZAMM - Journal of Applied Mathematics and Mechanics / Zeitschrift für Angewandte Mathematik und Mechanik* 4.4 (1924), pp. 277–292.

[237] H. Wagner. "Über die Entstehung des dynamischen Auftriebes von Tragflügeln". In: *ZAMM - Journal of Applied Mathematics and Mechanics / Zeitschrift für Angewandte Mathematik und Mechanik* 5.1 (1925), pp. 17–35.

[238] H. G. Küssner. "Zusammenfassender Bericht über den instationären Auftrieb von Flügeln". In: *Luftfahrtforschung* 13 (1936), pp. 410–424.

[239] T. Theodorsen. *General Theory of Aerodynamic Instability and the Mechanism of Flutter*. Tech. rep. 496. National Advisory Committee for Aeronautics, 1935.

[240] W. R. Sears. "Some Aspects of Non-Stationary Airfoil Theory and Its Practical Application". In: *Journal of the Aeronautical Sciences* 8.3 (1941), pp. 104–108.

[241] M. E. Goldstein and H. Atassi. "A complete second-order theory for the unsteady flow about an airfoil due to a periodic gust". In: *Journal of Fluid Mechanics* 74.4 (1976), pp. 741–765.

[242] H. M. Atassi. "The Sears problem for a lifting airfoil revisited - new results". In: *Journal of Fluid Mechanics* 141 (1984), pp. 109–122.

[243] E. J. Limacher. "Towards a general theory of accelerating foils in the attached-flow regime". In: *Journal of Fluid Mechanics* 1012 (2025), R1.

[244] G. K. Batchelor. *An Introduction to fluid dynamics*. Cambridge: Cambridge Univ. Press, 1967.

[245] L. M. Milne-Thomson. *Theoretical aerodynamics*. 4th ed. New York: Dover Publications, 1973.

[246] P. Saffman. *Vortex dynamics*. Cambridge monographs on mechanics and applied mathematics. Cambridge, UK: Cambridge University Press, 1992.

[247] L. A. Martínez-Tossas, P. Sakievich, M. J. Churchfield, and C. Meneveau. "Generalized filtered lifting line theory for arbitrary chord lengths and application to wind turbine blades". In: *Wind Energy* 27.1 (2024), pp. 101–106.

[248] I. Garrick. *On Some Reciprocal Relations in the Theory of Nonstationary Flows*. Tech. rep. 629. National Advisory Committee for Aeronautics, 1938.

[249] S. A. Ning. "A simple solution method for the blade element momentum equations with guaranteed convergence". In: *Wind Energy* 17.9 (2014), pp. 1327–1345.

[250] L. A. Martinez-Tossas, D. Allaerts, E. Branlard, and M. J. Churchfield. "A Solution Method for the Filtered Lifting Line Theory". In: *Journal of Fluids Engineering* 147.011502 (2024).

[251] P. Virtanen et al. "SciPy 1.0: fundamental algorithms for scientific computing in Python". In: *Nature Methods* 17.3 (2020), pp. 261–272.

[252] W. La Cruz, J. M. Martinez, and M. Raydan. "Spectral residual method without gradient information for solving large-scale nonlinear systems of equations". In: *Mathematics of computation* 75.255 (2006), pp. 1429–1448.

[253] A. S. Almgren, J. B. Bell, P. Colella, L. H. Howell, and M. L. Welcome. "A Conservative Adaptive Projection Method for the Variable Density Incompressible Navier–Stokes Equations". In: *Journal of Computational Physics* 142.1 (1998), pp. 1–46.

[254] V. Motta, A. Guardone, and G. Quaranta. “Influence of airfoil thickness on unsteady aerodynamic loads on pitching airfoils”. In: *Journal of Fluid Mechanics* 774 (2015), pp. 460–487.

[255] S. Ōtomo, S. Henne, K. Mulleners, K. Ramesh, and I. M. Viola. “Unsteady lift on a high-amplitude pitching aerofoil”. In: *Experiments in Fluids* 62.1 (2020), p. 6.

[256] A. W. Mackowski and C. H. K. Williamson. “Direct measurement of thrust and efficiency of an airfoil undergoing pure pitching”. In: *Journal of Fluid Mechanics* 765 (2015), pp. 524–543.

# Acronyms

**ABL** atmospheric boundary layer

**ADM** actuator disk model

**AEP** annual energy production

**ALM** actuator line model

**AWC** active wake control

**CFD** computational fluid dynamics

**CNBL** conventionally neutral atmospheric boundary layer

**CPU** central processing unit

**DEL** damage equivalent load

**DIC** dynamic induction control

**DNS** direct numerical simulation

**FLLC** filtered lifting line correction

**GPU** graphical processing unit

**IPC** individual pitch control

**LES** large-eddy simulation

**NSE** Navier-Stokes equations

**NWP** numerical weather prediction

**PBD** pitch bearing damage

**RANS** Reynolds-averaged Navier–Stokes equations

**RL** reinforcement learning

**WFFC** wind farm flow control

# Curriculum Vitæ

## Emanuel Taschner

| | |
|---|---|
| 2021 — 2025 | Doctor of Philosophy (Ph.D.)<br>Delft University of Technology<br>Delft, The Netherlands<br>Thesis: *Large-Eddy Simulations of Helix Active Wake Control — Sensitivity, Robustness and Advanced Actuator Line Modelling*<br>Promotor: Prof. dr. ir. J.W. van Wingerden<br>Promotor: Dr. ir. R.A. Verzijlbergh |
| 9/2023 — 10/2023 | Visiting Ph.D. Researcher<br>National Renewable Energy Laboratory<br>Boulder, Colorado, US |
| 2019 — 2021 | Master of Science in Engineering Mechanics (Fluid Mechanics)<br>KTH Royal Institute of Technology<br>Stockholm, Sweden |
| 10/2018 — 02/2019 | Student Apprentice: R&D Process Department<br>Linde<br>Munich, Germany |
| 2015 — 2019 | Bachelor of Science in Mechanical Engineering<br>Karlsruhe Institute of Technology<br>Karlsruhe, Germany |
| 2007 — 2015 | Albert-Schweitzer-Gymnasium<br>Leonberg, Germany |
| 1997 | Born 14$^{th}$ April 1997<br>Leonberg, Germany |

# List of Publications

**Journal Papers:**

1. E. Taschner, M. Folkersma, L. A. Martínez-Tossas, R. Verzijlbergh, and J. W. van Wingerden. "A new coupling of a GPU-resident large-eddy simulation code with a multiphysics wind turbine simulation tool". In: *Wind Energy* 27.11 (2024), pp. 1152–1172

2. E. Taschner, G. Deskos, M. B. Kuhn, J. W. van Wingerden, and L. A. Martínez-Tossas. "Unsteady aerodynamic loads on pitching airfoils represented by Gaussian body force distributions". In: *Accepted for publication in Journal of Fluid Mechanics* (2025)

3. J. Gutknecht, E. Taschner, M. Coquelet, A. Viré, and J. W. van Wingerden. "The impact of coherent large-scale vortices generated by helix active wake control on the recovery process of wind turbine wakes". In: *Physics of Fluids* 37.6 (2025)

4. J. Gutknecht, E. Taschner, M. Becker, A. Viré & J. W. van Wingerden. "Mitigating wind theft from neighboring wind farms through farm-wide coordinated control" (working title). *In Preparation*

**Conference Papers:**

1. E. Taschner, A. van Vondelen, R. Verzijlbergh, and J. W. van Wingerden. "On the performance of the helix wind farm control approach in the conventionally neutral atmospheric boundary layer". In: *Journal of Physics: Conference Series* 2505.1 (2023), p. 012006

2. L. J. Huang, S. P. Mulders, E. Taschner, and J. W. van Wingerden. "Enhancing Wake Mixing in Wind Farms by Multi-Sine Signals in the Helix Approach". In: *2023 American Control Conference (ACC)*. 2023, pp. 824–830

3. E. Taschner, M. Becker, R. Verzijlbergh, and J. W. van Wingerden. "Comparison of helix and wake steering control for varying turbine spacing and wind direction". In: *Journal of Physics: Conference Series* 2767.3 (2024), p. 032023

4. J. Gutknecht, M. Becker, E. Taschner, S. Stipa, D. Allaerts, A. Viré, and J. W. van Wingerden. "Active Cluster Wake Mixing". In: *Journal of Physics: Conference Series* 2767.9 (2024), p. 092052

5. H. Korb and E. Taschner. "Coarse, fast, and still accurate? Comparing corrections for the actuator line model". In: *Journal of Physics: Conference Series* 3016.1 (2025), p. 012051

Included in this thesis.

## Patent Application:

J. Gutknecht, M. Becker, E. Taschner & J. W. van Wingerden. "Wind turbine cluster control for improved cluster wake mixing". *World Intellectual Property Organization*, WO 2025/051959 A1 (2025)

## Conference Presentations:

1. E. Taschner*, M. Folkersma, L. A. Martínez-Tossas, R. Verzijlbergh & J. W. van Wingerden. "A new coupling of a GPU-resident large-eddy simulation code with a multiphysics wind turbine simulation tool". *Presented at the 2022 NAWEA-WindTech Conference*, Newark, Delaware, USA

2. E. Taschner*, R. Verzijlbergh & J. W. van Wingerden. "The helix wind farm control approach in the conventionally neutral atmospheric boundary layer: Strouhal number scaling and wake response". *Presented at the 2023 Wind Energy Science Conference (WESC)*, Glasgow, Scotland, UK

3. E. Taschner*, A. van Vondelen, R. Verzijlbergh & J. W. van Wingerden. "On the performance of the helix wind farm control approach in the conventionally neutral atmospheric boundary layer". *Presented at the 2023 Wake Conference*, Visby, Gotland, Sweden

4. E. Taschner*, J. Gutknecht, A. van Vondelen, R. Verzijlbergh & J. W. van Wingerden. "Assessing the potential of the helix wind farm control approach — Dependence on atmospheric boundary layer conditions and the level of wake overlap". *Presented at the 2023 NAWEA-WindTech Conference*, Boulder, Colorado, USA

5. E. Taschner*, M. Becker, R. Verzijlbergh & J. W. van Wingerden. "Comparison of helix and wake steering control for varying turbine spacing and wind direction". *Presented at the 2024 TORQUE Conference*, Florence, Italy

6. E. Taschner, G. Deskos, M. Kuhn, J. W. van Wingerden & L. A. Martínez-Tossas*. "On the unsteady aerodynamics of two-dimensional Gaussian body forces". *Presented at the 2024 NAWEA-WindTech Conference*, New Brunswick, New Jersey, USA

7. E. Taschner*, G. Deskos, M. Kuhn, J. W. van Wingerden & L. A. Martínez-Tossas. "On the unsteady aerodynamics of two-dimensional Gaussian body forces". *Presented at the 2025 Wind Energy Science Conference (WESC)*, Nantes, France

* Presenter